



UNIVERSITY OF READING

**An Integrated Approach to
Modelling Cancer Metastasis**

PhD

School of Biological Sciences

Shirley Keeton

June 2016

Dedication

This work is dedicated to my father,

John Michael Keeton,

without whom neither I nor this would have been possible,

but who did not live to see its completion.

Declaration

I confirm that this is my own work and the use of all material from other sources has been properly and fully acknowledged.

Signed:

Acknowledgements

Dr Phil Dash – for supervision and discussion throughout my PhD studies.

Dr Steve Ray – for discussion and ideas on behalf of the industrial sponsor, Natural Biosciences.

Dr Mark Cranfield, for technical support and help with decellularization of tissues, on behalf of industrial sponsor, Natural Biosciences.

Dash Lab members: Dr Ibrahim Barnawi, Dr Mahmoud Chawsheen, Dr Godwin Ponuwei, Ana Wass, Jonathan Rudge, Zhiyao Huang and Jordi Lambert for their assistance, support and help during my PhD studies.

Dr Munira Batarfi – chick embryo assay.

Dr Graham Luke – chick embryo assay and microscopy.

Dr Alan Burns and Dr Jean Marie Delalande – development of the CAM assay.

Dr Immy Smith – for advice regarding three dimensional cell culture.

Miss Amanpreet Kaur - EM Lab, Scanning Electron Microscopy work.

Dr Elizabeth Lander - assistance with molecular techniques.

Professor Ketan Patel and lab members: Dr Robert Mitchell, Taryn Morash, Dr Henry Collins-Hooper, for materials, assistance and support in the laboratory.

Dr James Foster and Dr Ricardo Gouveia – for initial assistance with compressed collagen production.

Dr Keith Foster, Dr Helen Foster, Dr Wouter Eilers, Dr Damilola Pinheiro-Fadeyi, Dr Graeme Cottrell for provision of plasmids and resources to produce the Green Fluorescent Protein expressing lentivirus and in help producing and testing the product.

Professor Simon Andrews for advice and guidance.

And with thanks to my long suffering family and friends who have loved and supported me throughout my PhD studies.

Abstract

The spread of cancer to distant sites, metastasis, is responsible for the majority of cancer related deaths. Metastasis is a complex process comprising a number of steps and mechanisms which take place over time. Due to the temporal and extemperaneous nature of metastasis it has proved difficult to study. Current models are limited in their application and there is a need to develop new models which provide a better and more meaningful biological context for the study of metastasis.

Taking a tissue engineering approach, this project has sought to develop a set of *in vitro* models for the exploration of cancer metastasis in three dimensions. Two collagen based assays were developed to allow the exploration of metastasis in a three dimensional (3D) environment. A simple collagen based assay was developed to create multiple regions of interest, allowing the study of cell migration, invasion and colonization in two dimensions, three dimensions and at border zones. Compression of collagen was used to construct a stiffer more elastic 3D *in vitro* context and this assay was developed to provide multiple regions of interest for the study of metastasis in a more structured and biologically relevant environment.

The chick chorioallantoic membrane (CAM) assay was explored as an *in vivo* model for the study of metastasis however this allowed only a short time period for study. However, the decellularization of CAM tissue provided a novel and useful 3D context which could be used for the study of metastatic mechanisms in direct comparison to the *in vivo* model but over longer time periods.

Decellularized CAM was successfully used in conjunction with the other two assays to explore the differential expression of intermediate filaments across different 3D environments, confirming the need to use different assays and approaches when investigating metastatic mechanisms.

Table of Contents

	Page
Acknowledgements.....	iv
Abstract.....	v
Table of Contents.....	vii
Abbreviations.....	xvi
Publications and Presentations.....	xviii
Papers.....	xviii
Posters presented.....	xviii
Table of Figures.....	xix
Table of Tables.....	xxvi
1. Introduction.....	1
1.1. Cancer.....	1
1.2. Metastasis.....	4
1.3. Epithelial-Mesenchymal Transition (EMT).....	7
1.4. Cell migration.....	10
1.5. Metastasis in context.....	16
1.5.1. The Tumour Microenvironment (TME).....	16
1.5.2. The Extracellular Matrix (ECM).....	18
1.5.3. The premetastatic niche.....	19

1.6.	Modelling cell migration and metastasis	21
1.7.	Project aims	26
2.	Materials and Methods	27
2.1.	Cell culture	27
2.1.1.	HT1080 human fibrosarcoma cells	27
2.1.2.	MDA-MB-231 human adenocarcinoma cells.....	28
2.1.3.	MCF7 human adenocarcinoma cells.....	29
2.2.	Cell culture materials	30
2.2.1.	Matrigel preparation.....	30
2.2.2.	Collagen preparation	30
2.2.3.	Fibronectin preparation	30
2.3.	Development of permanently expressing Green Fluorescent Protein (GFP+) cell lines	31
2.3.1.	Myristoylated GFP+ cell lines.....	31
2.3.2.	Lentiviral GFP+ cell lines	33
2.4.	Fixing and staining cells.....	39
2.4.1.	Embedding and sectioning samples.....	41
2.5.	Microscopy	42
2.5.1.	Phase contrast time-Lapse.....	42
2.5.2.	Epifluorescence microscopy	43

2.5.3. Confocal microscopy	43
2.6. Statistical analysis.....	44
2.6.1. Quantification of sample size.....	44
2.6.2. Statistical analysis of experimental results.....	44
3. Modelling Metastasis <i>In Vitro</i>	46
3.1. Introduction.....	46
3.2. Materials and methods	49
3.2.1. 2D cell migration assays.....	49
3.2.2. 3D collagen cell migration assay.....	50
3.2.3. 3D collagen and fibronectin cell migration assay.....	51
3.2.4. Compressed Collagen (CC) assay	51
3.2.5. 2D/3D invasion assay.....	53
3.3. Results	55
3.3.1. Cell migration on coated 2D surfaces – HT1080 and MDA-MB-231	55
3.3.2. Cell migration in a 3D collagen matrix.....	60
3.3.3. Does fibronectin affect cell migration when added to a 3D collagen matrix?	63
3.3.4. Fibrillar structure of the 3D collagen matrix.....	68
3.3.5. Compressing collagen to increase matrix stiffness and elasticity	69
3.3.6. Cell migration from 2D to 3D – can the context be simplified?	74
3.3.7. Cell invasion at border zones	76

3.4. Discussion.....	77
4. Modelling Metastasis <i>In Vivo</i>	85
4.1. Introduction.....	85
4.2. Materials and methods	90
4.2.2. CAM fixing and staining	92
4.2.3. Embedding and sectioning.....	93
4.2.4. CAM microscopy	93
4.2.5. Confocal spectral unmixing microscopy	94
4.3. Results.....	95
4.3.1. Developing CAM assay for ECM interaction	95
4.3.2. Are lentiviral GFP+ cells easier to identify in CAM?.....	106
4.3.3. Immuno-staining of human cancer cells in CAM.....	117
4.3.4. Determining a timeline of invasion.....	125
4.3.5. Migration or colonisation?.....	131
4.4. Discussion.....	134
5. Development of Decellularized Tissue as a 3D Context for the Exploration of Meta stasis	
.....	143
5.1. Introduction.....	143
5.2. Materials and methods	148
5.2.1. Decellularization of chick chorioallantoic membrane	148

5.2.2. Decellularization of rat lung.....	148
5.2.3. Decellularization of rat pup skin.....	148
5.2.4. Culture of cells on dCAM	149
5.2.5. Culture of cells on dSkin.....	150
5.2.6. Culture of cells on dLung	150
5.2.7. Fixing and staining cells and decellularized tissue.....	150
5.2.8. Embedding and sectioning decellularized tissue samples.....	151
5.2.9. Scanning Electron Microscopy (SEM)	151
5.2.10. Confocal microscopy.....	151
5.3. Results.....	152
5.3.1. Decellularized rat lung as a 3D biological scaffold for cell culture	152
5.3.2. Optimization of decellularization of chick chorioallantoic membrane	160
5.3.3. dCAM as a 3D Growth Matrix	166
5.3.4. Decellularization of rat pup skin (dSkin)	170
5.4. Discussion.....	174
6. An Integrated Approach to the Study of Metastatic Mechanisms.....	181
6.1. Introduction.....	181
6.2. Materials and methods	184
6.2.1. Inverted invasion assay.....	184
6.2.2. SRC and FAK inhibited 2D/3D colonisation assay.....	185

6.2.3. Cell colonization on compressed collagen.....	185
6.2.4. HT1080 colonization of dCAM	186
6.2.5. Statistics	186
6.3. Results.....	187
6.3.1. Cell colonisation and migration in the presence of FAK and SRC kinase 1 inhibitors	187
6.3.2. Inverting the 2D/3D assay to quantify invasion – inverted invasion assay.....	190
6.3.3. Using the compressed collagen 3D environment to investigate vimentin expression in the absence and presence of FAK and SRC kinase 1 inhibitors	195
6.3.4. Vimentin expression using dCAM as a 3D matrix	199
6.3.5. Keratin expression in cells seeded on dCAM	206
6.4. Discussion.....	208
7. Discussion.....	216
7.1. Background.....	216
7.2. Comparable and compatible models of metastasis.....	216
7.3. Technical issues and mitigation	222
7.3.1. Mycoplasma	222
7.3.2. Microscopy	223
7.3.3. Quantification of 3D assays using 2D analytical methods	225
7.4. Further work and potential application of methods	227

References.....	229
Appendix A.....	249
A1. DMEM constituents (DMEM, low glucose with pyruvate – 31885 Thermo Fisher).....	249
A2. Qiagen mini-prep and giga-prep kits.....	252
Qiagen mini-prep kit used: QIAprep Spin Miniprep Kit.....	252
Plasmid Giga Kit (12191).....	253
Appendix B.....	255
B1. 2D coatings.....	255
B2. 3D collagen.....	256
B3. Collagen/fibronectin (MDA-MB-231).....	257
B4. 2D/3D assay.....	258
B5. 2D coatings: fibronectin/collagen/Matrigel.....	259
MDA-MB-231 Cells – Distance to Start.....	259
MDA-MB-231 cells - speed.....	260
MDA-MB-231 cells – aspect ratio.....	261
HT1080 cells - distance to start.....	262
HT1080 cells - speed.....	263
HT1080 cells - aspect ratio.....	263
HT1080 v MDA-MB-231 speed comparison.....	265
B6. 3D collagen assay for HT1080, MDA-MB-231 and MCF7 cells.....	266

Cell length	266
Aspect ratio	267
Speed.....	270
Distance to start.....	271
B7. 3D collagen with fibronectin.....	274
Distance to start.....	274
Speed.....	275
Track length.....	276
Aspect ratio	276
Cell length	277
HT1080 aspect ratio.....	279
HT1080 cell length	280
HT1080 distance to start.....	280
HT1080 speed	282
Distance from start comparison between HT1080 and MDA-MB-231	283
HT1080 and MDA-MB-231 cells: control group v n1-3 cells on collagen.....	284
B8. 2D/3D assay.....	285
MDA-MB-231 n1-3 - speed	285
HT1080 2D/3D assay - speed	286
Appendix C	287

MCF7 and GFP clones comparison.....	287
MDA-MB-231 v GFP+ clones	289
HT1080 cells v lentiviral GFP+ clones.....	291
Appendix D.....	294
HT1080 on dCAM – vimentin expression.....	294
Appendix E	295
Inverted invasion assay.....	295
Appendix F.....	299

Abbreviations

1D	One Dimension	
2D	Two Dimensions	
3D	Three Dimensions	
ANOVA	Analysis of Variance	
ATCC	American Tissue Culture Collection	
BMDCs	Bone Marrow Derived Cells	
Ca ²⁺	Calcium ion(s)	
CAM	Chorioallantoic Membrane (of chick)	
CC	Compressed Collagen	
CI	Confidence Interval	CO ₂
dioxide		Carbon
COX2	Cyclooxygenase-2	
D2S	Distance to Start	
DAPI	4,6-Diamidino-2-phenylindole	
dCAM	decellularized Chorioallantoic Membrane (chick)	
ddH ₂ O	double distilled water	
dLung	decellularized Lung (from rat)	
DMEM	Dulbeco's Modified Eagles Medium	
DNA	Deoxyribonucleic Acid	
dSkin	decellularized Skin (from rat)	
ECM	Extracellular Matrix	
EDTA	Ethylenediaminetetraacetic acid	
eGFP	enhanced Green Fluorescent Protein	
EMT	Epithelial-Mesenchymal transition	
EndMT	Endothelial-Mesenchymal transition	
FAK	Focal Adhesion Kinase	
FBS	Fetal Bovine Serum	
GDP	Guanosine Diphosphate	
GFP	Green Fluorescence Protein	
GTP	Guanine Triphosphate	
HDFC	High Density Fibrillar Collagen	
ICAM	Intercellular Adhesion Molecule	

iNOS	inducible Nitric Oxide Synthase
IL-6	Interleukin 6
LOX	Lysyl Oxidase
LV	Lentiviral
LV HT1080 GFP+	Lentiviral HT1080 cells expressing green fluorescent protein
LV MDA-MB-231 GFP+	Lentiviral MDA-MB-231 cells expressing green fluorescent protein
LV MCF-7 GFP+	Lentiviral MCF-7 cells expressing green fluorescent protein
MET	Mesenchymal-Epithelial Transition
MMP	Matrix Metalloprotease
MOI	Multiplicity Of Infection
Myr	Myristoylated
NaOH	Sodium hydroxide
PAK	p21 activated protein kinase
PBS	Phosphate-buffered Saline
PEI	Polyethylenimine
Pen/Strep	Penicillin/Streptomycin
PFA	Paraformaldehyde
RNA	Ribonucleic Acid
ROCK	Rho-associated protein kinase
ROS	Reactive Oxygen Species
SD	Standard Deviation
SEM	Scanning Electron Microscopy
Src	Src Kinase 1
TGF β	Transforming Growth Factor Beta
TME	Tumour Microenvironment
UV	Ultra Violet light
VASP	Vasodilator-stimulated Phosphoprotein
VCAM	Vascular Cell Adhesion Molecule
WHO	World Health Organization

Publications and Presentations

Papers

'Compressed Collagen and Decellularized Tissue – Novel Components in a Pipeline Approach to the Study of Metastasis', Keeton, S.J., Cranfield, M., Delalande, J.M., Burns, A., Dash, P.R.

In Preparation, 2016

'Experimental Models of Metastasis' Review, Keeton, S.J. and Dash, P.R., In Preparation,

2016

Posters presented

'Plasticity of Cell Migration at Transition Zones Between Different Dimensions and Substrates', Shirley J Keeton, Steve Ray, Philip R Dash, October 2013, at Invadosome Conference, Nijmegen, The Netherlands.

'Modelling Metastasis – *in vivo* and *in vitro*', Shirley Keeton, Jean-Marie Delalande, Steve Ray, Alan Burns, Philip Dash. July 2014, at University of Reading Postgraduate Conference, University of Reading.

Table of Figures

Chapter 1

	Page
Figure 1.1, The hallmarks of cancer	1
Figure 1.2, The metastatic process	5
Figure 1.3, Cell signalling pathways in cell migration on 2D	15
Figure 1.4, Changes in the tumour microenvironment leading to tumour progression, invasion and metastasis.	17

Chapter 2

Figure 2.1. Vector maps for plasmids used to create GFP positive stably transfected cell lines	32
Figure 2.2, Restriction maps and cutting sites for lentiviral plasmids	34
Figure 2.3, Images for agarose gels run for plasmid selection from the mini-prep	35
Figure 2.4, Flow cytometry controls for determining the best cell transduction of lentivirus in HeLa cells.	37
Figure 2.5, Flow cytometry graphs for optimisation of GFP+ lentivirus transduction quantities	38
Figure 2.6. Cells tracked using MtrackJ ImageJ plugin	42

Chapter 3

	Page
Figure 3.1, Compressed collagen layering	52
Figure 3.2, 2D/3D invasion assay	54
Figure 3.3, MDA-MB-231 and HT1080 cells migrating in two dimensions (2D)	56
Figure 3.4, Cell migration on 2D coated surfaces for MDA-MB-231	59
Figure 3.5, Cell migration in collagen	62
Figure 3.6, MDA-MB-231 cell migration in collagen and collagen with fibronectin	65
Figure 3.7, HT1080 cell migration in collagen and collagen with fibronectin	66
Figure 3.8, Cell Migration tracked in collagen and collagen with fibronectin	68
Figure 3.9, Collagen matrix structure determined by reflectance microscopy	65
Figure 3.10, Compressed collagen populated with MDA-MB-231 cells	71
Figure 3.11, MDA-MB-231 cells leaving Compressed Collagen are rounded	72
Figure 3.12, Cell morphology and structure of compressed collagen	73
Figure 3.13, MDA-MD-231 and HT1080 cells move faster at collagen borders	75
Figure 3.14, Cell invasion at collagen borders	76

Chapter 4

	Page
Figure 4.1, <i>In ovo</i> development of chick embryo and extra-membranous tissues	86
Figure 4.2, Eggs windowed at Day 2-3	90
Figure 4.3 Timeline for CAM <i>in vivo</i> experiments	91
Figure 4.4, Development of CAM metastasis assay	97
Figure 4.5, Development of CAM Metastasis Assay: MDA-MB-231 myristoylated GFP Cells / Cells in Collagen seeded onto the CAM surface	98
Figure 4.6, Development of CAM metastasis assay – cells in collagen on CAM surface	100
Figure 4.7, MDA-MB-231 myristoylated GFP cells on harvested CAM	101
Figure 4.8, Confocal images of MDA-MB-231 myristoylated GFP cells on CAM	102
Figure 4.9, HT1080 myristoylated GFP+ cells on CAM membrane, 6 days after seeding	103
Figure 4.10, MDA-MB-231 Myristoylated GFP+ cells migrating on 2mg/ml collagen	104
Figure 4.11, Comparison of MDA-MB-231 cells with MDA-MB-231 myristoylated GFP+ cells	105
Figure 4.12, Comparison of MCF7 and MCF7 lentiviral clones	108
Figure 4.13, Comparison of MDA-MB-231 with lentiviral clones	109
Figure 4.14, Comparison of HT1080 cells with lentiviral clones	110

	Page
Figure 4.15, Lentiviral cells seeded at CAM surface	111
Figure 4.16, Ink injection to show CAM vasculature	112
Figure 4.17 Chick erythrocytes fluoresce in the green spectrum	113
Figure 4.18, Nucleated red blood cells in chick	114
Figure 4.19, Determining GFP+ cells in CAM	115
Figure 4.20, Spectral unmixing confocal imaging to differentiate GFP+ cells from erythrocytes	119
Figure 4.21, LV MDA-MB-231 GFP+ cells, ZB2 clone invading CAM	120
Figure 4.22, LV MDA-MB-231 GFP+ ZB2 cells on whole CAM	121
Figure 4.23, LV HT1080 GFP+ (A1D9) cells invading CAM	122
Figure 4.24, LV HT1080 GFP+ (A1D9) cells invading CAM	123
Figure 4.25, LV MCF7 GFP+ (DPF5) cells on/in whole CAM	124
Figure 4.26, CAM sections showing layered structure	126
Figure 4.27, Timeline for invasion of scratched CAM for LV MCF7 GFP+ cells	127
Figure 4.28, Timeline for invasion of scratched CAM for LV MDA GFP+ cells	128
Figure 4.29, MCF7 and MDA-MB-231 cells were invasive on unscratched CAM	129
Figure 4.30, LV HT1080 GFP+ cells invaded without scratching CAM	130
Figure 4.31, Cell division on CAM	132
Figure 4.32, CAM with no cells seeded stained for Ki67	133

Chapter 5

	Page
Figure 5.1, Decellularized rat lung	154
Figure 5.2, MDA-MB-231 GFP+ cells colonizing decellularized rat lung (dLung)	155
Figure 5.3, Rat dLung co-culture	156
Figure 5.4, Decellularized rat lung co-culture shows cluster formation comprising both cell types	157
Figure 5.5, Decellularized rat lung colonized with MDA-MB-231 and LV HT1080 GFP+ (A1D9) cells stained for vimentin expression	159
Figure 5.6, Decellularizing CAM	161
Figure 5.7, Scanning Electron Microscopy for dCAM before protocol optimisation	162
Figure 5.8, Decellularization of CAM – was decellularization complete?	163
Figure 5.9, Optimization of peracetic acid clearance of CAM tissue during decellularization	164
Figure 5.10, Scanning Electron Microscopy images for peracetic acid step optimization	165
Figure 5.11, Cells seeded on dCAM proliferate over the surface	166
Figure 5.12, MDA-MB-231 cells colonize dCAM	167
Figure 5.13, dCAM co-culture colonized with MDA-MB-231 and LV MCF7 GFP+ cells	168
Figure 5.14, HT1080 cells proliferate over dCAM	169

	Page
Figure 5.15, Rat skin and decellularized rat skin compared via Scanning Electron Microscopy	170
Figure 5.16, Sectioned whole rat pup skin compared to decellularized rat skin	171
Figure 5.17, Rat skin decellularization with rat pup hair removed first	172
 Chapter 6	
Figure 6.1, Cell colonization of a 2D/3D assay	189
Figure 6.2, MCF7 cell invasion into collagen using an inverted invasion assay	191
Figure 6.3, MDA-MB-231 cell invasion into collagen measured using an inverted invasion assay	192
Figure 6.4, HT1080 cell invasion into collagen measured using an inverted invasion assay	194
Figure 6.5, Vimentin expression of MDA-MB-231 cells on compressed collagen with/without inhibitors for FAK or SRC Kinase 1	197
Figure 6.6, HT1080 cell colonization of compressed collagen with/without SRC kinase 1 inhibitor	198
Figure 6.7, Comparison of HT1080 vimentin expression on 2D plastic (2D), compressed collagen (CC) and decellularised chick chorioallantoic membrane (dCAM)	200
Figure 6.8, HT1080 expression of vimentin on dCAM in the absence and presence of SRC kinase 1 inhibitor	201
Figure 6.9, Comparison of HT1080 vimentin expression between 2D and 3D environments with and without SRC kinase 1 inhibitor	202
Figure 6.10, Timeline of vimentin expression for HT1080 cells seeded onto dCAM	203

	Page
Figure 6.11, Is vimentin expression related to cell morphology	205
Figure 6.12, Keratin expression in HT1080 cells seeded on dCAM at 1 and 7 days	207
Chapter 7	
Figure 7.1, A pipeline approach to the experimental modelling of metastasis	217
Appendix C	
Figure C1. Immuno-staining controls for GFP antibody on CAM	294
Appendix F	
Figure A.7, Comparison of HT1080 (HT) and MDA-MB-231 (MDA)	295

Table of Tables

	Page
Table 1.1, Hallmarks and characteristics of cancer	2-3
Table 1.2, Models of metastasis	6
Table 1.3, Epithelial-Mesenchymal Transition (EMT) in cancer progression	8-9
Table 1.4, Modes of cell migration and associated characteristics	11
Table 1.5, Cell protrusions and migration mode	12
Table 3.1, Average cell length of cells migrating on different coatings	58
Table 4.1, The advantages and disadvantages in using the CAM as an <i>in vivo</i> model to study cancer metastasis	141
Table 5.1, Benefits and disadvantages of decellularized tissue for the exploration of cell behaviour	180

1. Introduction

1.1. Cancer

Cancer is one of the leading causes of death worldwide, with 14 million new cases and 8.2 million cancer related deaths reported in 2012 (IARC 2014). In the same year it was estimated that 2.5 million people in the UK were living with cancer and that this was projected to rise to around 4 million by 2030 (Maddams et al. 2012).

Cancer is in fact a set of diseases, each cancer being unique to the person, arising as it does from changes within individual cells leading to aberrant cell behaviour, unregulated tissue function and ultimately to organ failure. Hanahan and Weinberg have defined a framework for the development and spread of cancers based on common characteristics and mechanisms found through research in the field (Hanahan and Weinberg 2011). Six hallmarks and a further two emerging hallmarks have been described along with two enabling characteristics and these are illustrated in Figure 1.1 and summarised in Table 1.1.

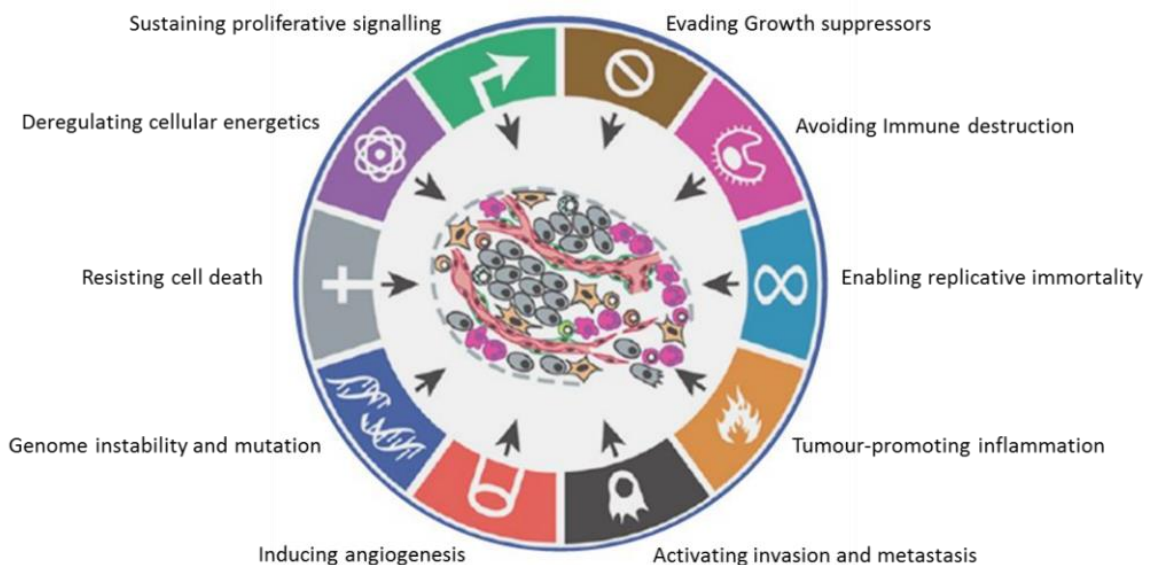


Figure 1.1, The hallmarks of cancer (Hanahan and Weinberg 2011).

Table 1. 1 Hallmarks and characteristics of cancer, based on Hanahan and Weinberg, 2000 and 2011.

Hallmark	Description	Evidence
Sustained proliferative signalling	Cell cycle progression is tightly controlled in normal cells to maintain tissue homeostasis. Deregulated signalling sustained over time leads to uncontrolled growth and tissue destabilization. These are key features of tumorigenesis.	(Keller et al. 2014, Kerkhoff and Rapp 1998, Medema and Macúrek 2011, Nik-Zainal et al. 2012, Pylayeva-Gupta et al. 2011, Youssef et al. 2012)
Resisting cell death	Programmed cell death as a means of eliminating damaged or malfunctioning cells is important in tissue homeostasis. Aberrant cells avoiding apoptosis can contribute to increasing tumour mass.	(Kim et al. 2012, Mehlen and Puisieux 2006, Ouyang et al. 2012, Stewart and Abrams 2008)
Evading growth suppressors	To develop successfully a tumour must also avoid negative regulators which suppress aberrant growth during normal tissue homeostasis. RB and TP53 are key tumour suppressor proteins which act as gatekeepers at cell cycle checkpoints which are frequently defective in cancers.	(Kim Mi Ra et al. 2012, Song et al. 2012, Stewart and Abrams 2008)
Activation of invasion and metastasis	Metastasis has been described as a complex multi-step process involving: invasion, intravasation, transit and escape, culminating in colonization of suitable niches where micrometastases, may develop into secondary tumours.	(Bravo-Cordero et al. 2012, Canel et al. 2013, Nguyen et al. 2009, Sanz-Moreno et al. 2008, Scheel et al. 2007)
Enabling replicative immortality	Cells are normally limited in the number of divisions they make via mechanisms such as fixed length telomeres. Cells able to divide indefinitely run the risk of incorporating and perpetuating errors which combined with genomic instability and apoptosis resistance lead to continuous replication of aberrant cells.	(Shay and Wright 2011, Stewart et al. 2002)
Angiogenesis induction	Tumour mass is limited without a method of transport of nutrients and waste products. Angiogenesis is triggered in many cancers allowing further development. Hypoxia is a key contributor to the up-regulation of growth factor secretion, along with other changes in cell signalling.	(Ghosh et al. 2008, Lorusso and Rugg 2008, Lu 2006, Orimo and Weinberg 2006, Wang Zongwei et al. 2015, Weis and Cheresh 2011)
Deregulation of cell energetics	Altered metabolism in cancer lesions may further enable growth and cell proliferation by utilizing aerobic glycolysis and up-regulating associated receptors to provide the necessary glucose required. Links between oncogene expression, mutations in tumour suppressor genes and glycolytic switching have been observed.	(Cairns et al. 2011, Martinez-Outschoorn et al. 2011, Räsänen and Vaheri 2010, Sebastián et al. 2012)

Hallmark	Description	Evidence
Avoidance of immune destruction	Immune surveillance usually provides a mechanism to eliminate unwanted bodies. Immunocompromised patients suffer greater cancer incidence which suggests the importance of a healthy immune system in cancer development.	(Dadi et al., Malladi et al. 2016, Stewart and Abrams 2008)
Enabling characteristic		
Genomic mutation/instability	A genotype allowing aberrant cell behaviour is believed to be important in the development of cancer at the cellular level.	(Medema and Macćurek 2011, Nguyen Don X. and Massaguć 2007)
Tumour-promoting inflammation	The presence of immune cells and the similarity between cancerous lesions and wound healing have led to the belief that chronic inflammation is important in some cancers.	(Candido and Hagemann 2012, Mantovani et al. 2008, Räsänen and Vaheri 2010, Spaeth et al. 2008)

Regardless of the initial trigger, it is generally the accumulation of a number of errant traits at a cellular level which render normal tissue homeostasis and error correction mechanisms ineffective, allowing the outward spread of cancer via invasion and metastasis to occur.

1.2. Metastasis

Metastasis is the main cause of cancer related death (WHO 2015). It is a complex multi-step process in which cells move away from a primary tumour, establishing themselves elsewhere in the body where they may form new tumorous growths known as metastases. One of the eight hallmarks of cancer, metastasis is enabled by: changes in character of the escaping cell, compliance and flexibility of the surrounding environment and the assistance of non-tumour cells that reside within (Hanahan and Weinberg 2011, Lorusso and Ruegg 2008).

Non-cancerous tumour related cells may be recruited by and associate with the tumour itself or be part of the environment through which the escaping cell passes (Hanahan and Coussens 2012, Joyce and Pollard 2008, Karnoub et al. 2007, Wyckoff et al. 2007). The initial steps of invasion and metastasis are therefore dependent on changes which allow tumour cells to escape, these changes arising within the tumour cells themselves or as a result of the properties of the surrounding tumour microenvironment (Alexander and Friedl 2012, Radisky et al. 2005). A number of different models of metastasis have been proposed which are summarised in Table 1.2. Each of these models suggests a complex pathway in which cancer progression is dependent on cellular change over time. For metastasis to occur, cells must escape from the primary tumour, invade into the surrounding tissue and migrate or transit away to take up residence at a new site, successful colonization at the distant site being the final stage of the metastatic process as a secondary growth or metastasis forms (Figure 1.2). Metastasis is therefore a progressive and complex process involving multiple stages (Valastyan and Weinberg 2011). Most cancers occur in epithelial or endothelial tissue in which cells are bound together via cell-cell junctions in either single or multiple layers (McCaffrey and Macara 2011, Radisky 2005, Radisky et al. 2005). A number of different types of junction connect the cells: tight junctions, channel-forming gap junctions and signal

relay junctions (Balda and Matter 2008, Bissell and Radisky 2001, Lecuit and Yap 2015). In addition, cells are anchored to the basement membrane, a specialized extra-cellular layer comprising a combination of proteins secreted by the epithelial or endothelial cells which attach to one side and the stromal fibroblasts of the extra cellular matrix (ECM) on the other side (McCaffrey and Macara 2011, Rowe and Weiss 2008). Cells must detach from the basement membrane as well as each other if they are to migrate (Kelley et al. 2014, Rowe and Weiss 2008). An unanchored cell would normally undergo anoikis, that is cell death due to loss of anchorage, but a key feature of cellular transformation in cancer is the gaining of anchorage-independence allowing a tumour cell to commence its journey to a new site (Hanahan and Weinberg 2011, Hernandez-Caballero 2013, Mehlen and Puisieux 2006). This type of cell transition is similar to the tightly regulated epithelial-mesenchymal transition (EMT) which takes place during embryogenesis (Thiery et al. 2009, Zoltan-Jones et al. 2003) a process believed to originate from early in the evolution of multicellular organisms (Larue and Bellacosa 2005).

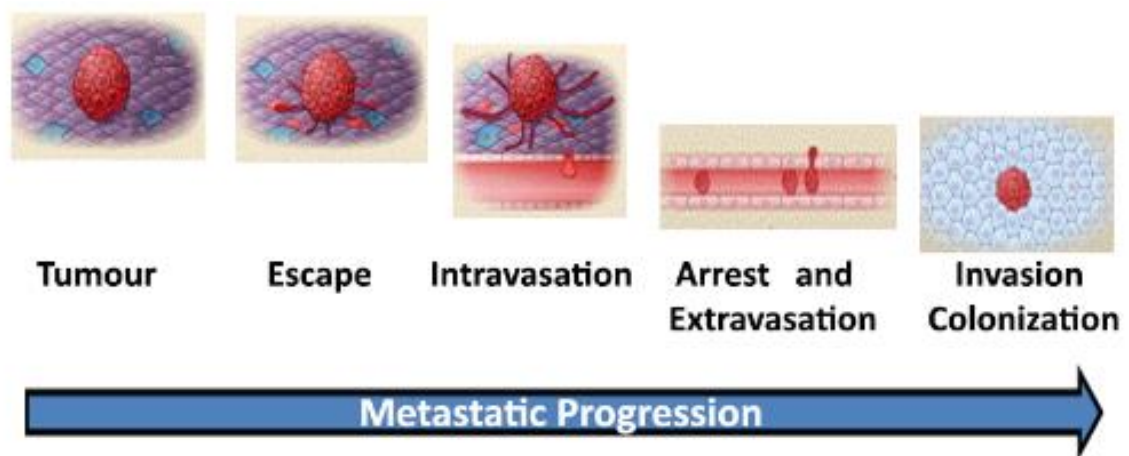


Figure 1.2, The metastatic process. Metastasis is a staged process, cells interacting with and transiting through a number of different environments before reaching and colonizing at a new site. Based on Valastyan and Weinberg 2011.

Table 1.2, Models of metastasis

Model	Description	Proponents	Reference
Linear Progression	Step-wise progression of cancer. Primary tumour matures before metastasis commences.	Leslie Foulds	(Foulds 1958)
Parallel Progression	Metastatic cells disseminate early in primary tumour development and development of tumorous tissue occurs in parallel. Proposed due to size and occurrence of secondary growths which could not be explained by time course of linear progression model.	Collins, Loeffler and Tivey	(Collins et al. 1956)
Dissemination to first pass organ	Metastasizing cells move and develop into secondary growths at new sites dependent on the circulatory pathways of the body, e.g. breast cancer metastasizing to the lungs.	James Ewing	(Ewing 1928)
Metastatic Cascade Theory	The step-wise progression of metastasis: escape, invasion into surrounding tissue, intravasation of the circulatory system, extravasation, invasion, colonization at a distal site and development of secondary growths.	Bross, Viadana and Pickren	(Bross et al. 1975)
Seed and Soil Hypothesis	Successful metastasis is based on both the dissemination of malignant cells and the ability of a cell to grow in the secondary tumour microenvironment, the 'pre-metastatic niche'.	Stephen Paget	(Paget 1989)
Cancer Stem Cell Hypothesis	A small pool of multipotent cells with self-renewing capability provide a pool of cells available for the production of tumour cells with metastatic capability.	Reya, Morrison, Clarke and Weissman	(Reya et al. 2001)
Clonal Selection and Expansion	Genetic and epigenetic changes cause a series of mutations to arise in cells resulting in the development of cancer, either via the loss of tumour suppressor function or by a gene gaining 'oncogenic' capacity.	Fidler and Kripke, expanded by Vogelstein, Fearon and Hamilton	(Fidler and Kripke 1977, Vogelstein et al. 1988)
Epithelial-Mesenchymal-Transition (EMT) Metastatic progression Model	Cells escaping from a primary tumour in solid cancers undergo a phenotypic change allowing them to adopt mesenchymal cell characteristics involving the down-regulation of proteins including those binding the cell within its tissue.	Boyer and Thiery	(Boyer and Thiery 1993)

1.3. Epithelial-Mesenchymal Transition (EMT)

EMT is a highly regulated process in healthy tissue and involves several steps summarised in Table 1.3 below. In EMT, epithelial cells detach from a tissue mass and take on the cell characteristics of a de-differentiated mesenchymal cell, allowing their migration to a new location (Radisky 2005, Rowe and Weiss 2008). Mesenchymal cells are anchorage-independent stromal cells able to migrate, synthesize and organize ECM components and secrete proteases (including matrix metalloproteases - MMPs) and growth factors (Larue and Bellacosa 2005, Radisky 2005). EMT is induced by a range of both genetic and environmental factors including hyaluronan expression, MMP exposure, Reactive Oxygen Species (ROS), TGF β /SMAD signalling pathway (Radisky 2005, Radisky et al. 2005, Zoltan-Jones et al. 2003).

An EMT like process has been observed during cancer progression, triggered by the tumour and its surrounding environment, but in contrast to the highly organised and programmed step-wise EMT, this takes place in an un-regulated fashion (Kalluri and Weinberg 2009, Tsai and Yang 2013). E-cadherin expression is an important characteristic of epithelial cells organised into layered tissue, the cadherin-adheren tight junction assembly allowing cells to maintain polarity and cell position within tissue and thus acting as a tumour suppressor (Larue and Bellacosa 2005, McCaffrey and Macara 2011). The breaking of tight junctions is therefore a vital step in the EMT process (Bissell and Radisky 2001, Onder et al. 2008).

Table 1.3, Epithelial-Mesenchymal Transition (EMT) in cancer progression

Mechanism	Processes involved	Result	Evidence
Loss of cell-cell adhesion at tight junctions. Loss of cell polarity	<ul style="list-style-type: none"> • E-cadherin down-regulated (sequestered into vesicles) and replaced by N-cadherin • Up-regulation of vimentin (AKT1 target) and fibronectin may occur • Beta-catenin released and may activate canonical Wnt pathway leading to transcription factor activation • Delta-catenin released which may activate GTPases. • Increased cellular hyaluronan 	Cell morphology changes to elongated mesenchymal type and individual cells are free to migrate	(Larue and Bellacosa 2005, Schafer et al. 2014) (Evanko et al. 2007, Mani et al. 2008, Onder et al. 2008, Zhu et al. 2011)
Loss of cell-ECM adhesion	<ul style="list-style-type: none"> • Integrins giving a cell polarity and binding it to basement membrane are lost 		
Induction of pro-invasive cell signalling pathways	<ul style="list-style-type: none"> • TGFβ activates RhoA GTPase • PI3K/AKT • Increased hyaluronan in many cancers believed to influence key cell signalling pathways 	Activation of cell migration associated signalling pathways	(Madsen et al. 2015, Sahai and Marshall 2003, Sanz-Moreno et al. 2008, Zoltan-Jones et al. 2003)
Matrix degradation	<ul style="list-style-type: none"> • Secretion of Matrix Metalloproteases (MMPs), serine proteases, cathepsins • Membrane bound matrix metalloproteases may also degrade pericellular tissue • MMP3 and MMP9 linked to Rac1b induction 	Degraded tissue gives cells space to move into. Rac1b signalling known to drive cell migration in some cancers	(Radisky et al. 2005, Rolli et al. 2003, Zijlstra et al. 2004)
Transcription factors induced: SNAIL, SLUG, TWIST	<ul style="list-style-type: none"> • ROS triggers SNAIL which triggers EMT • TWIST linked to early EMT steps 	Inhibition of apoptosis and block cell differentiation favouring cell migration	(Onder et al. 2008, Scheel et al. 2011, Sleeman and Thiery 2011)

Mechanism	Processes involved	Result	Evidence
Acquisition of stem cell type characteristics: <ul style="list-style-type: none"> • Self-renewal capability • Phenotypic plasticity 	<ul style="list-style-type: none"> • Possible that cells undergoing de-differentiation during EMT like process also gain other properties of stem cells such as self-renewal allowing them to persist until a suitable environment for growth is available. • Ability to remain de-differentiated or to differentiate according conditions encountered in a new environment. 	Cancer Stem Cells which can seed themselves at distant sites and initiate the growth of a new tumour.	(Hanahan and Weinberg 2011, Mani et al. 2008, Schwitalla et al. 2013)

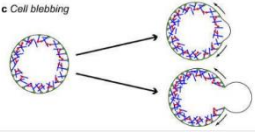

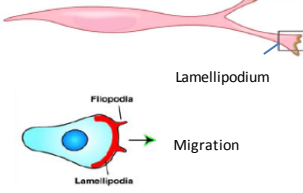

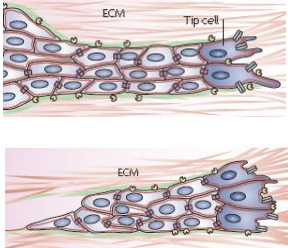
In mesenchymal cells, N-cadherin expression is up-regulated allowing cells to function independently and facilitating migration (Larue and Bellacosa 2005, Onder et al. 2008). The PI3K/AKT signalling pathway is also known to be involved in EMT, driving the process and interacting with other important cell signalling pathways (Larue and Bellacosa 2005). When the PI3K/AKT pathway is triggered, phosphorylated activated AKT leads to the expression of transcription factors Slug and Snail which act to repress E-cadherin expression at cell-cell junctions, enabling a cell to detach from its host tissue. Vimentin and fibronectin expression are also increased as is the expression of matrix metalloproteases allowing basement matrix degradation to take place (Xu et al. 2015). Mesenchymal-epithelial transition (MET), the reverse process of EMT, is believed to facilitate the seeding of tumour cells at distant sites where with the right environmental conditions they may develop into metastases (Scheel et al. 2007, Tsai and Yang 2013). Once cells have detached from tissue either individually or as a group, they may adopt a variety of mechanisms to enable movement either over or through tissue (Friedl and Gilmour 2009, Friedl and Wolf 2003).

1.4. Cell migration

Cell migration is a process driven by the biophysical properties of the cell substrate as well as by the characteristics of the moving cell itself (Discher et al. 2005, Friedl Peter and Wolf 2003a, Lämmermann and Sixt 2009). A number of different modes of migration have been observed with cells adopting a range of morphologies when moving across or through tissue (Fackler and Grosse 2008, Friedl Peter and Wolf 2003a, Wolf et al. 2003). Cells have been seen to move either individually or as a group under different experimental conditions both *in vivo* and *in vitro* (Doyle et al. 2012, Friedl and Alexander 2011, Hegerfeldt et al. 2002, Petrie et al. 2009). Plasticity in both morphology and mechanism have also been observed. Friedl and Wolf describe this in their ‘tuning model’ suggesting that plasticity lies on a continuum in which cells may change their strategy from one form and mechanism to another based on environmental cues (Arciero et al. 2011, Friedl and Gilmour 2009, Friedl and Wolf 2009a). The modes of cell migration and associated characteristics are summarised in Table 1.4.

In order to move forward, a cell must translocate itself mechanically using either a pushing or pulling mechanism (Petrie and Yamada 2012). In a two dimensional environment (2D) cells have been observed to crawl across a surface employing the mechanisms of protrusion, attachment, contraction, and detachment (Bergert et al. 2012, Ridley 2011).

Table 1.4, Modes of cell migration and associated characteristics

Migration mode	Characteristics	Morphology	Evidence
Amoeboid - blebbing	Expansion and retraction of rounded membrane protrusions at the plasma membrane. Low or no adhesion; no visible polarity		(Charras et al. 2008, Paluch et al. 2006, Sahai and Marshall 2003)
Mixed amoeboid/ mesenchymal	Cells rounded or elongated cells with blunt ended tube like extensions – lobopodia. Cells may have lateral blebs. Weak adhesion. Cell polarity may be present.		(Friedl and Wolf 2009b, Petrie et al. 2012)
Mesenchymal	Elongated individual cells with extensions: filopodia / lamellipodia. Leading and trailing edge; polarized and directed migration.		(Lämmermann and Sixt 2009, Mannherz et al. 2007, Petrie et al. 2012, Yamaguchi and Condeelis 2007)
Cell streaming – multiple cells	Cells may form a chain with loose contacts. Cells move in a stream along tracks or tunnels which may be forged by the leading cell or pre-exist.		(Alexander and Friedl 2012, Friedl and Wolf 2008, Gaggioli et al. 2007, Wolf et al. 2003)
Collective movement	Sheet like invasive movement. Cells may move as a group or sheet with some adhesive connections broken on the outside of the group to allow this. (Primordial cells move collectively in response to chemical gradients.)		(Arciero et al. 2011, Friedl and Gilmour 2009, Hidalgo-Carcedo et al. 2011, Weijer 2009)

In 3D a cell has the opportunity to interact with its environment on all of its surfaces (Doyle et al. 2013). A variety of propulsive mechanisms has been identified including: filopodia, lobopodia, invadopodia and membrane blebs (Le Clairche and Carlier 2008a, Petrie et al. 2012, Ridley 2011, Sahai and Marshall 2003).

Table 1.5, Cell protrusions and migration mode

Type of Cell Protrusion	Dimension (D)	Cell Morphology	Mechanism of Motility Adhesion Type	Evidence
Membrane Ruffling	2D	Flattened and spread	Actin polymerization at the leading edge, retrograde transport and depolymerisation at the trailing edge.	(Le Clainche and Carlier 2008, Wehrle-Haller and Imhof 2003)
Lamellipodia	2D	Flattened and spread	Aggregated focal adhesions provide adhesion comprising proteins including: Vinculin, paxillin, talin, alpha-actinin, zyxin, VASP, FAK p130Cas. At the leading edge, cofilin severs actin filaments and free barbed ends act as sites for actin polymerization, Arp2/3 providing nucleation sites where WAVE acts in conjunction with Rac1 and formins to enable extension of actin filaments.	(Fraleley et al. 2010, Ridley 2011, Sanz-Moreno et al. 2008, Wehrle-Haller 2012)
Filopodia	3D	Various	IRSp53 bends the membrane and recruits Cdc42 and mDia2 WASP/N-WASP which stimulate actin polymerization at the leading edge to form narrow finger-like protrusions. Profilin provides actin monomers for polymerization.	(Le Clainche and Carlier 2008, Ridley 2011)
Lobopodia	3D	<ul style="list-style-type: none"> • Collagen • Matrigel 	In fibroblasts similar signalling process to lamellipodia but with high RhoA at leading edge in a 3D matrix with linear elasticity lobopodia form instead.	(Petrie et al. 2012, Petrie and Yamada 2012, Sixt 2012)
Blebs – rounded and elongated	1D 2D 3D	<ul style="list-style-type: none"> • Rounded • Spread with blebs at leading edges • Elbowing and chimneying 	Initiation, development and retraction of a bleb are driven by internal pressure and acto-myosin cortex contractility – occurs when Rho/ROCK levels are high but Rac signalling is absent.	(Lorentzen et al. 2011, Otto et al. 2011, Sahai and Marshall 2003, Wolf et al. 2003)
Invadopodia	2D, 3D	Various	Protrusive extensions: lamellipodia and filopodia combine with proteolysis of the surroundings allowing cells to invade and move through tissue.	(Magalhaes et al. 2011, Oser et al. 2009, Ridley 2011)

Whether motility is facilitated by pushing or pulling, it is vital for a cell to anchor itself to its substrate so that it can proceed. Anchorage via adhesion proteins is one option and this is employed extensively in lamellipodia and filopodia in a 2D environment where small focal adhesions comprising groups of proteins linked to the cytoskeletal stress fibres anchor the cell to the 2D surface. On a two dimensional surface, cells adopt a flattened morphology advancing via broad veil-like lamellipodia or finger-like filopodia with focal adhesion complexes providing a means of substrate attachment (Ridley 2011, Yamaguchi and Condeelis 2007). Whilst the character of focal adhesions in 3D has yet to be fully characterized, Fraley and colleagues have found that where present, adhesion proteins are diversely spread across the cell surface rather than forming focussed focal adhesions (Fraley et al. 2010). It seems too that focal adhesion composition varies with the deformability of the substrate of attachment (Plotnikov et al. 2012) and that the matrix constituents play a role in the types and sizes of adhesions (Doyle et al. 2015). Cell migration speed has also been linked to the shape and size of focal adhesions (Kim and Wirtz 2013).

As an alternative to adhesion, membrane blebbing in 3D migration may involve the cell levering itself forward as it inserts blebs into pores and gaps in the surrounding matrix or uses a chimneying action where actomyosin contractility is the main force responsible for forwards movement (Charras et al. 2008, Doyle et al. 2012, Doyle et al. 2009, Lämmermann and Sixt 2009, Lorentzen et al. 2011)

At the molecular level, cell migration is co-ordinated by Rho GTPases a group of small cell signalling molecules which act as molecular switches as they cycle between the active bound GTP state and inactive non-bound GDP (Sahai and Marshall 2003a). In mesenchymal movement, actin polymerization at the leading edge must be co-ordinated with

depolymerisation at the rear as well as attachment/detachment of focal adhesion complexes and the release of proteases for matrix degradation in invasive migration (Friedl and Wolf 2009; Wolf et al. 2006). Cell signalling pathways control and regulate this process. Specifically, activated Rac, RhoA and Cdc42 GTPases control the formation of protrusions at the leading edge and RhoA, ERK, phosphatase and proteins for proteolysis of adhesion components are involved in cell retraction (Ridley 2011, Vicente-Manzanares et al. 2005). A simplified schematic of these pathways is shown at Figure 1.3 and specific details for different modes of migration are summarised in Table 1.5. Rho, Rock and Rac have been identified as important factors in the ability of cells to switch between mesenchymal and amoeboid migration modes (Sanz-Moreno et al. 2008). Proteins NEDD9 and DOCK3 complex to drive WAVE2 complex via RAC1 to reduce actomyosin contractility resulting in mesenchymal morphology, whereas Rho via Rock increase actomyosin contractility blocking Rac1 via ARHGAP22 resulting in amoeboid morphology (Sanz-Moreno et al. 2008). Invasive cell migration may also involve proteolysis of the surrounding matrix where cells adopting mesenchymal style migration either secrete or use membrane-anchored proteins to degrade the surrounding matrix as they move through (Bravo-Cordero et al. 2012, Ridley 2011, Sahai and Marshall 2003a).

It seems that cell migration in 3D varies according to a number of different properties of the surrounding matrix such as elasticity, density, porosity, pH, matrix composition and the bundling of collagen fibres within it (Doyle et al. 2015, Fraley et al. 2010, Sapudom et al. 2015, Zaman et al. 2006). The context for a migrating cell is clearly an important consideration when investigating metastasis, a metastasizing cell moving through a range of different contexts and environments during its escape, transit and arrival at a new site.

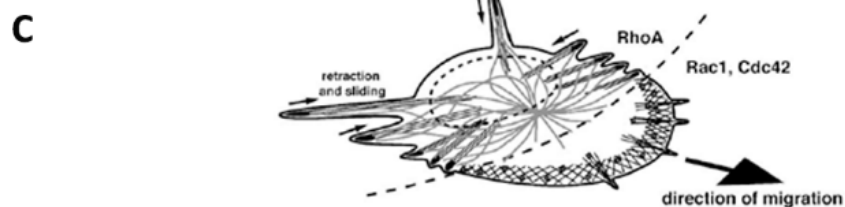
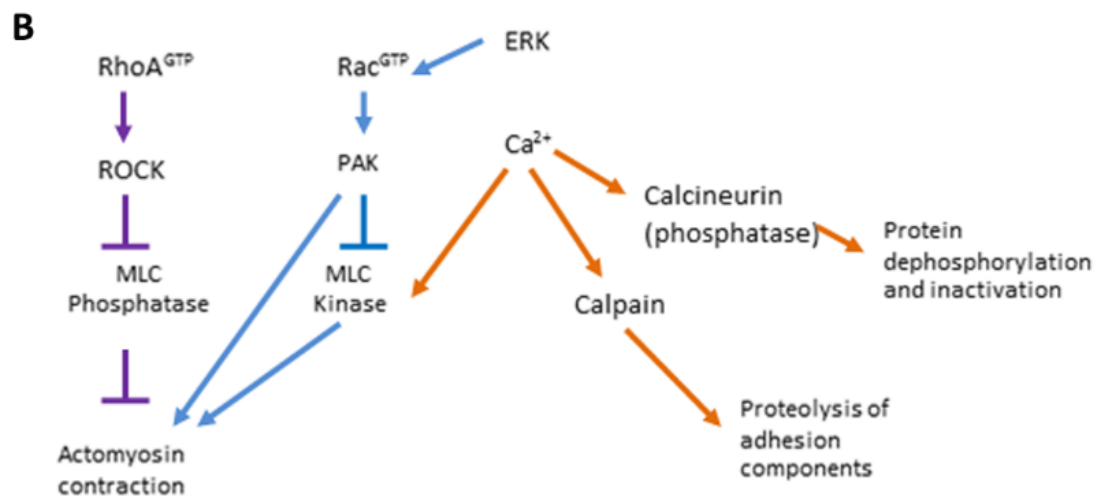
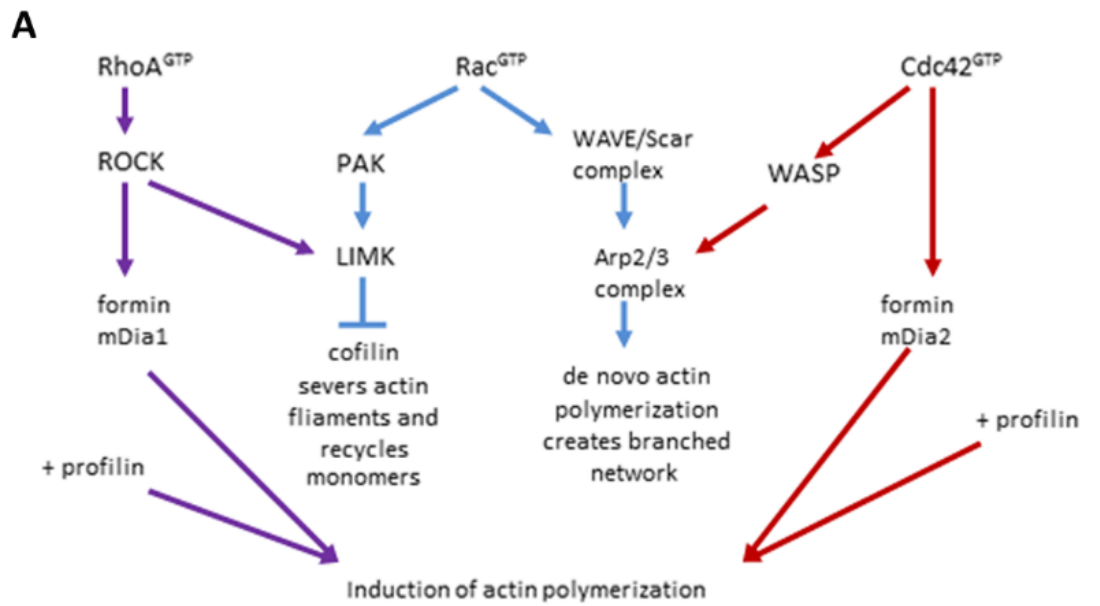


Figure 1.3, Cell signalling pathways in cell migration in 2D: A leading edge, **B** retracting edge, **C** diagram showing signalling in cell migrating in 2D using lamellipodia (Schweitzer et al. 2011, Vicente-Manzanares et al. 2005, Wehrle-Haller and Inhof 2003).

1.5. Metastasis in context

A tumour grows and develops in a tissue context. Metastasizing tumour cells migrating away, move through and interact with the surrounding tissue environment and eventually arrive at and interact in a new tissue context where, if successful, a secondary growth may develop.

1.5.1. The Tumour Microenvironment (TME)

The similarities between the activated tissue surrounding a tumour and those of a healing wound were identified by Dvorak when he likened the tumour microenvironment (TME) to 'a wound that does not heal' (Dvorak 1986). Since then the active role of tissue resident stromal cells has been identified in both facilitating invasion through the creation of a permissive environment and via the paracrine activation of the tumour cells themselves (Bremnes et al. 2011, Rønnev-Jessen and Bissell 2009). Signalling between cancer associated fibroblasts (CAF) and tumour cells has been shown to activate cell migration and the role of macrophages in activation, invasion, migration and intravasation has also been described (Condeelis and Pollard 2006, Gaggioli et al. 2007, Madar et al. 2013, Räsänen and Vaheri 2010). The TME therefore is not only a permissive environment but its composition and stromal interactions can actually drive tumour invasion and metastasis (Bravo-Cordero et al. 2012). Figure 1.4 shows a simplified diagram of the major components and interactions of the TME based on some of the recent research findings. The main elements of the TME are: structural components such as collagen and fibronectin; resident stromal cells including fibroblasts and macrophages; circulating factors including growth factors, cytokines, exosomes and microvesicles; recruited cells such as immune cells and bone marrow derived

cells (Bremnes et al. 2011, McAllister and Weinberg 2014, Quail and Joyce 2013, Räsänen and Vaehri 2010).

Growth factors and cytokines released within the TME and by the tumour cells themselves serve to activate the remodelling as well as to recruit cells outside the environment. The cytokine Interleukin 6, (IL-6) has been found to play a role at the leading edge of tumour cell invasion within the tumour environment as well as in preparing the premetastatic niche (Chang et al. 2013). TGF β has also been identified as an important regulator within the TME, suppressing immune cell function and promoting invasion, however it can also have an anti-tumorigenic role and so more research is needed to understand the targets and mechanisms of this important cytokine in the progression or containment of cancer (Massagué 2008, Padua and Massagué 2009).

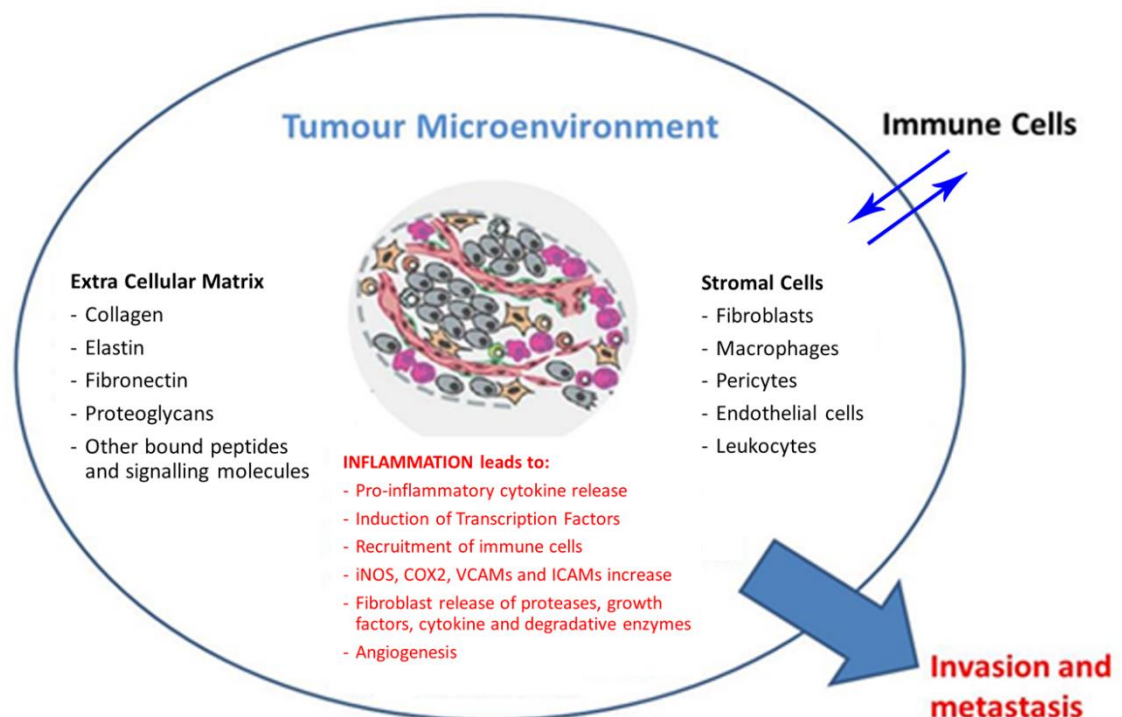


Figure 1.4, Changes in the tumour microenvironment leading to tumour progression, invasion and metastasis. (Based on (Hanahan and Weinberg 2011, Lorusso and Ruegg 2008, Lu H. 2006, Räsänen and Vaehri 2010)).

Inflammation has been identified as an important part of the activation state within the TME, with the associated cell signalling driving the recruitment of external resources in an effort to return correct function to the tissue as part of a wound healing like process (McAllister and Weinberg 2014). This is a similar state to the permanent activation of a chronic wound in which the persistently inflamed and activated state leads to a shift in dynamics with different stromal cell phenotypes emerging (Martin and Nunan 2015). Changes in gene expression have been identified for all cell types within the TME and an over representation of genes associated with TME remodelling (Allinen et al. 2004, Bremnes et al. 2011, Casey et al. 2009). Remodelling of the environment surrounding the tumour has been identified in providing escape routes for tumour cells via matrix stiffening and the alignment of collagen fibres of the extracellular matrix (Bravo-Cordero et al. 2012, Gligorijevic et al. 2012). The structure of the extracellular matrix plays an important role in the normal regulation and homeostasis of tissue and therefore disruption and remodelling of this dynamic element surrounding tissue can assist cancer progression (Joyce and Pollard 2009).

1.5.2. The Extracellular Matrix (ECM)

Extracellular matrix surrounds, supports and provides homeostasis for all tissues in the body, providing a biomechanical and biochemical scaffold for tissues and the cells within, comprising fibrous proteins, proteoglycans and water (Frantz et al. 2010). The ECM for each tissue differs in structure and its specific components. It is a dynamic environment which is constantly modelled and remodelled around the tissue it serves, according to the tissue needs and cues generated via interactive signalling between the tissue and stromal cells that reside within. Fibroblasts are responsible for both secreting and remodelled the structural

components, mainly collagen and elastin which provide tensile strength to the matrix. Cells within the tissue are able to bind to ECM via adhesion proteins and the state of the ECM can dictate whether cell adhesion is migratory. Cells respond to elasticity and rigidity within tissue so the correct contextual properties are important if tissue homeostasis is to be maintained (Discher et al. 2005, Engler et al. 2006). Interaction with the ECM via a number of different binding sites provided by the matrix can also determine patterns of gene expression, driving phenotypic changes in TME cells (Frantz et al. 2010, Hynes 2009, Nelson and Bissell 2006). The ECM is normally a highly controlled and tightly regulated environment, however its dynamic nature means it can become dysregulated in response to disease cues such as in the presence of a tumour (Brizzi et al. 2012, Lu et al. 2012). As part of both the tumour microenvironment and also as a potential site of metastatic colonization, the ECM can be programmed and reprogrammed to provide support and structure to meet the specific requirements of the neoplastic cells.

1.5.3. The premetastatic niche

The seeding and colonization of metastatic cells at a distant site may be assisted by invasive mechanisms within the metastasizing cell and by the preparation of the distant site in advance (Sleeman 2012). There is evidence that both of these may occur. Circulating tumour cells may aggregate with platelets, hijacking the clot formation process and then be assisted in leaving blood vessels and entering a premetastatic niche at an area of endothelial damage. Endothelial exposure of collagen to trigger thrombus formation and platelet accumulation may be caused deliberately so that tumour cells can enter at such a site (Kaplan et al. 2005, Quail and Joyce 2013). The preparation of a premetastatic niche has been observed where factors expressed and disseminated from the tumour and surrounding

microenvironment have been found to home to particular sites at which cells are then able to seed. Bone Marrow derived cells (BMDCs) expressing VEGFR1 are known to be recruited and contribute to the vascularization of the tumour microenvironment, were also found to home to and play a role in the upregulation of fibronectin at premetastatic sites via the VLA4 integrin they express (Kaplan et al. 2005). There is also evidence that tumour hypoxia driven expression of lysyl oxidase (LOX) may play a role in the recruitment of cells for premetastatic niche preparation (Cox et al. 2016, Ertler et al. 2006). Here again is evidence that the extracellular matrix structure plays an important role in the context of metastasis.

When attempting to investigate and model metastasis, the context for study is therefore important, however much of the initial work into invasion and migration has been conducted on 2D surfaces or in overly simplistic environments which do not represent the complexity of the niche environment of a cell in tissue. The aim for modelling metastasis is therefore to create a biologically relevant environment for investigation.

1.6. Modelling cell migration and metastasis

Studying metastasis in the live environment is not possible mainly because by the time a patient is diagnosed with metastatic cancer, the events to be studied have already taken place. In addition, the accumulation of the necessary traits and enabling factors typically takes place over a number of years going unnoticed and if they were to be discovered intervention would be the priority for ethical reasons. Observation and histological examination of tumour samples is possible retrospectively where samples are provided and live imaging and monitoring of tumorous growths in patients undergoing treatments can provide some insight. However, in order to understand the metastatic process at a molecular level, modelling metastasis using research tools allows detailed research to take place in a controlled environment. A range of models from mammalian *in vivo*, *ex vivo*, *in vitro* and *in silico* models has and is being used to elucidate the multiple stages of metastasis with the aim of providing further insight as a basis for the development of better treatments.

Whilst mammalian models may seem the most representative, their inherent complexity means that they are difficult to work with. Invasion and metastasis are spontaneous and therefore unpredictable so even where tumour explants are introduced into a mammalian host such as a mouse or rat, creating a suitable and biologically relevant tumour microenvironment in which to observe metastatic invasion is a challenge. Animal models are usually immunocompromised in order to accept exogenous tumour cells and therefore lack some of the component cells which play a critical role within the tumour microenvironment. Where tumours are grown orthotopically, the environment is less than ideal because most primary tumours develop within a host tissue, surrounded by the stroma rather than sitting on top of it. Cells have been injected into the circulation within *in vivo*

models such as mouse, rat and chick embryo so that extravasation and seeding at metastatic sites can be studied, however the cells introduced are typically a suspension of cells from a cancer cell line, these having been cultured outside the live environment and so their protein expression profiles, mechanisms and behaviours may be quite different to cells that have metastasized and invaded spontaneously within their natural host. Despite these issues, much has been learnt about the steps and mechanisms of metastasis from animal models in recent years, especially with the concurrent development in technology allowing visualization of events in deep tissue to be recorded and analysed. The escape and invasion of metastasizing cells has been modelled in immunocompromised mice with detailed mechanisms being determined for the invasion of tumour cells with partner macrophages (Condeelis and Pollard 2006). The mechanisms of invasion during the spread of mammary tumours to the lungs has also been elucidated in the mouse model using the specialized microscopy techniques of intravital multiphoton imaging, in combination with either the skin flap technique which provides a window into a tumour for several hours at a time or by placing the animal in a stereotactic box which allows images to be taken regularly over a period of 7 days (Gligorijevic and Condeelis 2009, Gligorijevic et al. 2012, Kedrin et al. 2008). In order to specifically identify introduced cells, activated fluorophores have been used so that their mechanisms and interactions with host tissue can be observed and recorded. Spinning disc confocal microscopy has also been used to visualise cell behaviour *in vivo* but is limited in the depth of field and therefore tissue depth it can penetrate and the resolution and therefore clarity with which it can capture events in context (Jonkman and Brown 2015). Second and third harmonic generation imaging have been employed in combination with intravital multiphoton microscopy to provide images of the matrix structure without the

need for fluorophores to define it (Friedl et al. 2007, Gligorijevic and Condeelis 2009, Wang et al. 2005).

The chick embryo model has also been used for the investigation of angiogenesis and metastasis and is a useful model due to its fast development time, easy manipulation and highly vascularized extracellular matrix layer which develops just beneath the shell. Cells or tumours have been grafted onto the chorioallantoic membrane surface, a window having been made in the egg to allow access to this ECM like tissue. Alternatively cancer cells have been injected into the vasculature of the CAM and tracking of cells within both CAM and chick have been carried out to determine the extent of spread to distant sites (Deryugina and Quigley 2008b, Shioda et al. 1997, Zijlstra et al 2002).

Other notable models include the zebra fish, which whilst not mammalian, has several advantages as a genetic model including: fast development, ease of genetic manipulation, transparency and good access for experimental observation due to its small size and low tissue depth (Woodhouse and Kelly 2011). Recently, the initial events in metastasis have been observed and recorded using this model along with reporter cell lines expressing fluorescent proteins to track both tumour cell and macrophage behaviour, allowing the capture of a precipitous chance event to be recorded (Tulotta et al. 2016). The drosophila model has also been used to model the genetic mechanisms involved in metastasis for example to explore the loss of cell polarity during metastasis and the mechanism of action of tumour suppressors in cancer progression (Woodhouse and Kelly 2011).

Following *in vivo* work, the opportunity for the analysis of live events in excised tissue is an option, providing the right support systems can be set up, for example the excision of

tumour and associated stroma from a euthanized mammalian model and further monitoring of live events within the tissue (Gligorijevic et al. 2012).

Much of the work to discover mechanisms in early metastasis such as migration and invasion has initially been conducted on 2D surfaces. Frequently coated with ECM components, these flat surfaces have provided access to visualize cells moving over and interacting with each other and the surface beneath. High resolution microscopy and techniques such as total internal reflectance imaging (TIRF) have enabled the elucidation of mechanisms such as focal adhesion turnover as cells have traversed a coated 2D plate (Berginski et al. 2011, Pasapera et al. 2015). However as the 2D models lacked the complexity and biological relevance, simple 3D models emerged in which soft gels such as agarose were used to encapsulate cells. ECM components such as collagen, fibronectin and laminin have also provided soft gel like contexts for the encapsulation of cells or for cells to be seeded onto and allowed to invade. However as the elasticity and tension of a tissue has been found to affect cellular responses such as adhesion and migration, more relevant biological matrices have been sought for the investigation of metastasis. Artificial matrices have been used along with tissue culture plastic, such as the Boyden chamber, in which cells are encouraged to translocate through a hanging 3D filter towards an attractant such as a growth factor of interest (Boyden 1962, Chen 2005). Imaging the extent of invasion could then be conducted via confocal microscopy once cells had been fixed and stained with appropriate fluorophores. Recently more complex artificial matrices have been designed for the use of 3D cell culture, such as Alvetex (Reinervate), a polystyrene based porous cell scaffold which can be sterilized and used as a biocompatible tissue culture scaffold, either cut to a specific shape and size or as a tissue culture well insert (Davies et al. 2015, Smith et al. 2015).

One of the advantages of a 3D culture environment is that it can be set up and manipulated according to a specific experimental design and cells cultured over a longer period than cells on 2D surfaces. Recording and observation of events can therefore be conducted over longer periods than in 2D or *in vivo* experiments and therefore 3D culture is potentially more useful in establishing a timeline of events. However, as with *in vivo* models, where 3D matrices are used for the study of metastatic mechanisms, accessing and visualizing cell behaviours and interactions is impeded by properties of the matrix and the density of cells contained within, especially where matrices are opaque, autofluorescent or have high reflectance.

The construction of a biologically relevant 3D matrix which is sufficiently representative of the tissue to be studied, but one that can be manipulated and controlled for experimental purposes, is the ideal for studying metastasis. Tissue engineering techniques offer useful tools with which to create relevant biological niche environments in which to study processes such as metastasis. A number of these techniques are beginning to emerge as possibilities including the use of decellularized tissue as a scaffold for cell population and 3D bio-printing as a means to recreate a specific organ shape and structure (Guyette et al. 2016, Lu et al. 2014, Murphy and Atala 2014).

1.7. Project aims

Given that context is important, the ability to model cancer metastasis in a biologically relevant environment is crucial. It is also important to be able to create, manipulate and then observe and record the emerging behaviours within any model used. As any experimental model used will have both advantages and limitations, the use of a number of models with different attributes permits investigation from different perspectives.

The overall aim of this PhD Project was to develop a set of *in vitro* assays which would allow an integrated approach to the investigation of the metastatic mechanisms involved in escape and invasion and colonization at a metastatic site. The requirement for models developed was that they could be created and assembled using easily available and every day laboratory items so that they would be cheap and easy to replicate. Capturing and quantification of events should be carried out with standard technologies which are widely available. Innovation would be sought from tissue engineering practices in creating a range of environments which were biologically relevant and could be used to create a suitably representative model of the metastatic niche for metastatic escape and invasion from a primary tumour and for the metastatic niche at which colonization could then be studied.

Using the suite of assays it should be possible to select the appropriate experimental models in order to compare and contrast cell behaviours under different conditions. It should be possible to move between the models to enable the manipulation and further investigation of specific behaviours observed.

Hypothesis: Cell behaviour will vary according to the structural and biophysical properties of the experimental model into which they are introduced.

2. Materials and Methods

This chapter includes general materials and methods. Specific details relating to materials and methods employed are located within each results chapter.

Materials were obtained from Sigma Aldrich unless otherwise stated.

2.1. Cell culture

Three cell lines were selected for culture and testing of the models developed: HT1080 fibrosarcoma cells, MDA-MB-231 adenocarcinoma cells and MCF-7 adenocarcinoma cells.

Both HT1080 and MDA-MB-231 cells are highly migratory and cells are able to display morphologies ranging from rounded/amoeboid to mesenchymal in different contexts.

HT1080 cells originate from a primary site and selecting this cell line provided cells which had not yet adapted to a distant metastatic site. In contrast, MDA-MB-231 cells originate from a metastatic site and will have adapted to inhabit the new niche from which they were collected. MCF-7 cells are also metastatic in origin but characteristically invade as a sheet and do not typically migrate individually as do the HT1080 and MDA-MB-231 cells. MCF-7 cells were used as a control cell-line for cell migration characteristics. The individual details for each cell line are given in the following sections.

2.1.1. HT1080 human fibrosarcoma cells

HT1080 human fibrosarcoma cells were obtained from The Health Protection Agency (HPA), European Collection of Cell Cultures. The original source for the cell line was the American Type Culture Collection (ATCC), USA, the cell sample having been taken from a fibrosarcoma located close to the acetabulum of the hip joint in connective tissue of a 35year old male Caucasian in 1972. The HT1080 cells were cultured and routinely passaged in either 25cm² or 75cm² culture flasks (Greiner bio-one) in Dulbecco's Modified Eagles Media (DMEM)

(containing 1mM Sodium Pyruvate, 3.97mM Glutamine, 5.56mM D-Glucose, full list of contents at Appendix A1) supplemented with 1% Penicillin/Streptomycin and 10% Fetal Bovine Serum (FBS) (Gibco, Thermo Fisher Scientific). Cells were placed in a humidified incubator at 37°C, 5% CO₂ where they were allowed to settle, adhere and grow. Cells were passaged whilst in the log growth phase typically at around 60-80% confluence. Overlying growth medium was aspirated and cells washed with 5ml sterile Phosphate-buffered Saline solution (PBS, Gibco). Washed cells were trypsinized using 0.05% Trypsin-EDTA (Gibco) to detach them from the surface of the flask. Cells were re-suspended in pre-warmed supplemented DMEM and transferred to either culture flasks or plates with additional pre-warmed medium used to make up the appropriate volume according to the flask or well size. The cell dilution used was adjusted according to the cell density required and time available for growth.

2.1.2. MDA-MB-231 human adenocarcinoma cells

MDA-MB-231 adenocarcinoma cells were also obtained from the HPA European Cell Collection of Cell Cultures. The source for the cell line was the American Type Culture Collection, USA, the original sample having been obtained from an adenocarcinoma, pleural effusion metastatic site in a 51 year old female Caucasian suffering from breast cancer.

MDA-MB-231 cells were cultured in a similar way to that described for HT1080 cells using DMEM containing the same supplements in the same proportions. Cells were passaged during the log growth phase and plated at a density sufficient to allow good adherence and growth, typically a 1:4 – 1:6 split from cells growing at 60-80% confluence.

2.1.3. MCF7 human adenocarcinoma cells

MCF7 adenocarcinoma cells were obtained from the HPA European Cell Collection. These cells were categorized as epithelial and originated from a metastatic invasion of the lung in a 69 year old Caucasian female and were collected via a pleural effusion.

The cells were cultured and passaged in a similar way to MDA-MB-231 cells using DMEM supplemented with 10% FBS and Penicillin/Streptomycin. Cells were passaged during the log growth phase and plated at a density sufficient to allow good adherence and growth, typically a 1:4 – 1:8 split from cells growing at 60-80% confluence.

2.2. Cell culture materials

2.2.1. Matrigel preparation

Matrigel (BD Biosciences) defrosted and kept on ice, was diluted with DMEM (no Pen/Strep or FBS added) or cells re-suspended in DMEM (no additives). Diluted Matrigel was added to wells of 6 or 12-well tissue culture plates (Cellstar, Greiner Bio-one) or 35mm microscope dishes (Ibitreat-Ibidi, Thistle Scientific Ltd.) using a chilled 200µl pipette tip and left to polymerise for 20-30 minutes in an incubator at 37°C, 5% CO₂. Supplemented growth medium was then added gently.

2.2.2. Collagen preparation

Rat Tail Type 1 Collagen was obtained from either BD Biosciences or Merck Millipore at 2.3-5mg/ml (concentration varied by batch). This was stored at 4°C and kept on ice during preparation. To obtain the desired collagen concentration, collagen was added to 10X DMEM (Gibco, Thermo Fisher Scientific) and the pH adjusted with 0.5 M sodium hydroxide solution to give pH 7-8. The required volume was made up with cells re-suspended in DMEM or with DMEM only for a cell-free matrix. Collagen solution with or without cells was added to tissue culture plates (6-well or 12-well - Cellstar, Greiner Bio-one) or 35mm microscopy dish (Ibitreat-Ibidi, Thistle Scientific Ltd.).

2.2.3. Fibronectin preparation

Human fibronectin was obtained (R&D Systems) and a stock solution of 150µg/ml made in sterile PBS which was aliquoted and stored at -20°C. Aliquots were defrosted as required and used either as a collagen additive or added to PBS to make a coating.

2.3. Development of permanently expressing Green Fluorescent Protein (GFP+) cell lines

2.3.1. Myristoylated GFP+ cell lines

MDA-MB-231 and HT1080 cells were permanently transfected to overexpress a membrane tagged Green Fluorescent Protein (GFP) using a PB CAG myr GFP transposon (Figure 2.1 A) and PB HYPBASE transposase (Figure 2.1 B) - kindly gifted by Dr Mike McGrew of The Roslin Institute.

The transfection protocol was first optimized using three different ratios of transposon to transposase: 1:1, 1:3 and 2:3. The optimal ratio of 1:1 was then used to transfect cells which had been grown to 60% confluence in a 12-well plate (Greiner Bio-one) using 4µg each of transposon and transposase, 12µl Fugene 6 (Promega) and 372µl DMEM (no additives). Cells were left for 48 hours then GFP+/puromycin resistant cells were selected (Puromycin from Fisher Scientific). Media containing puromycin was changed every 2-3 days and cells monitored until only fluorescent cells remained. These were then expanded for experimental use. Initially, selective pressure with puromycin was in the range of 0.5 - 1µg/ml and ongoing selective pressure was 0.3µg/ml for MDA-MB-231 CAG Myr GFP+ cells and 0.5µg/ml for HT1080 CAG Myr GFP+ cells (although MDA-MB-231 GFP+ cells were also stable without puromycin). Transfection success was verified using epifluorescence microscopy.

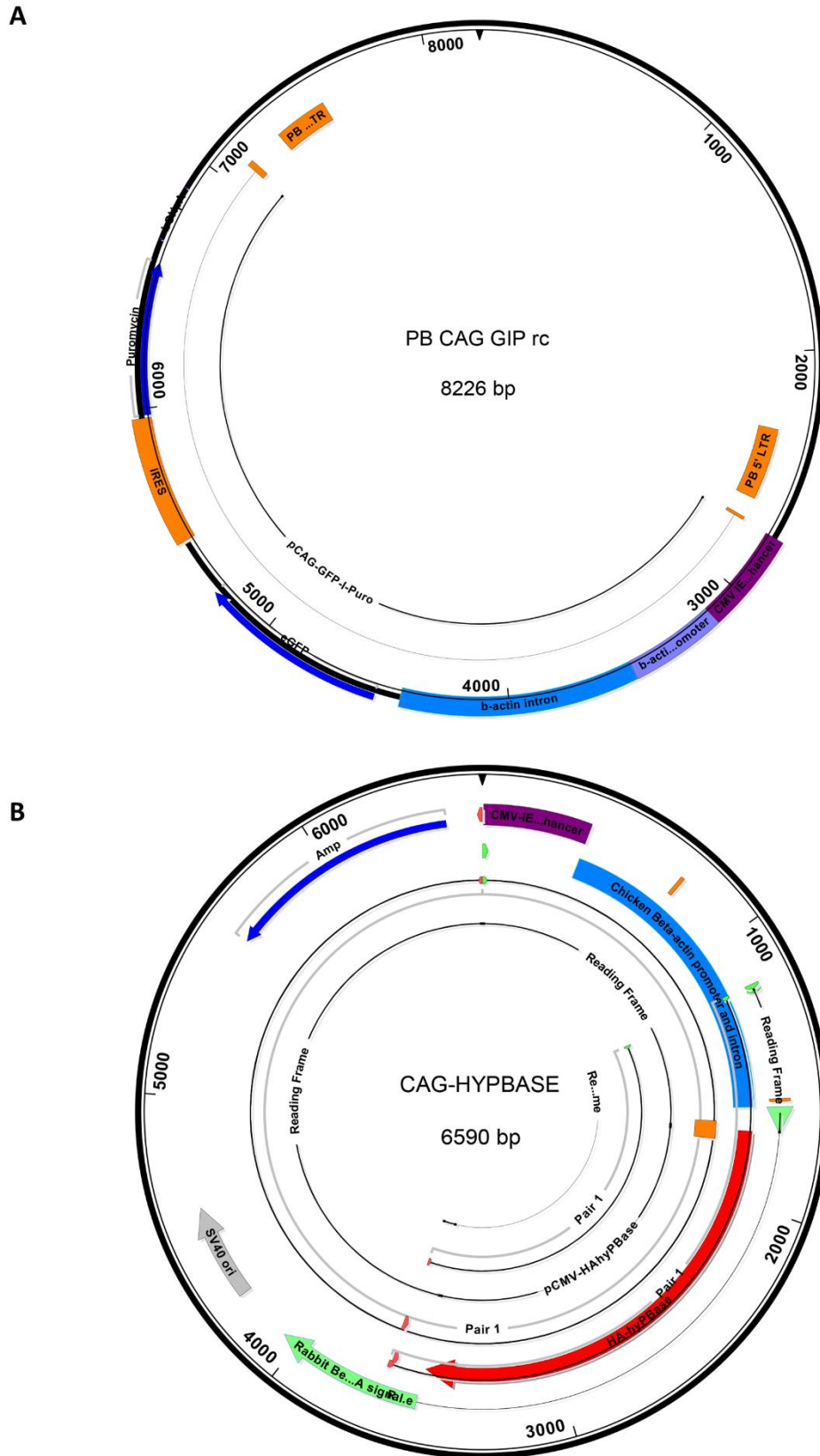


Figure 2.1. Vector maps for plasmids used to create GFP positive stably transfected cell lines: A PB CAG Myr GFP plasmid with puromycin resistance gene; B PB HYPBASE transposase plasmid.

2.3.2. Lentiviral GFP+ cell lines

2.3.2.1. Plasmid preparation

A lentiviral vector for enhanced Green Fluorescent Protein was assembled from three plasmids:

- pMD2.G **envelope plasmid;**
- pCMV-dR8.74 **packaging plasmid;**
- pHR.sin.cPPT.SFFV.eGFP.WPRE **plasmid containing eGFP gene to be expressed.**

Plasmid stocks were expanded as follows: Excell Gold 10 *Escherichia coli* cells (Agilent) were transformed with each of the three plasmids and grown on LB agar/ampicillin 100µg/ml overnight. A colony was selected for each plasmid, transferred and cultured overnight in LB broth/ampicillin (100µg/ml). A mini-prep kit (Qiagen – details at Appendix A2) was used to extract and purify the plasmids and glycerol stocks were made. A restriction digest was conducted (restriction maps shown at Figure 2.2) to check the size of each plasmid and the resultant linearized fragments were run out on a 1% agarose gel with ethidium bromide (1µl/ml) used to enable visualisation (Figure 2.3).

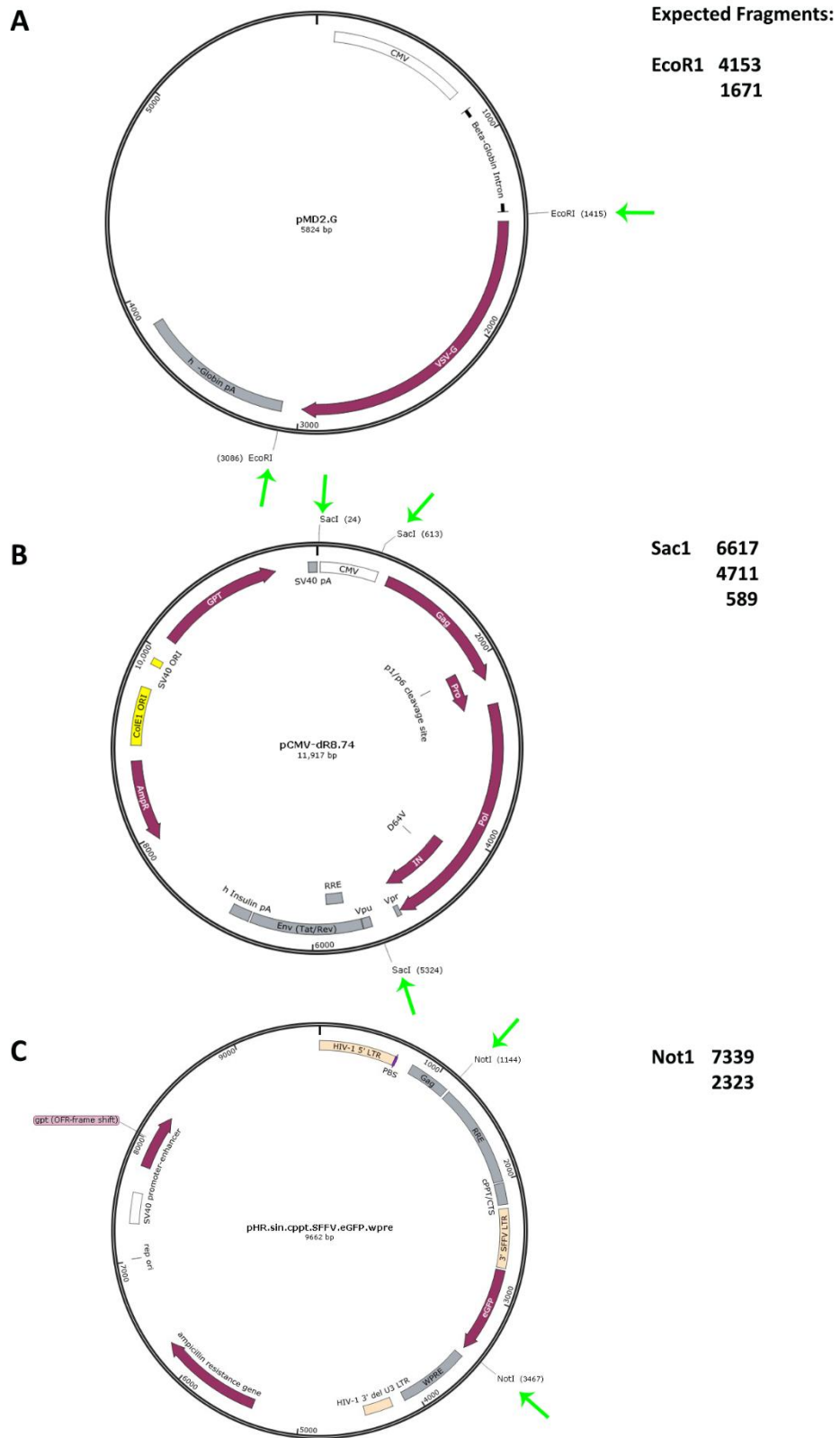


Figure 2.2, Restriction maps and cutting sites for lentiviral plasmids. Cutting sites selected for each enzyme are indicated with green arrows for each plasmid and fragment sizes in bases are listed to the right. **A**, pMD2.G; **B**, pCMV-dR8.74; **C**, HR.sin.cPPT.SFFV.eGFP.WPRE. Plasmid maps were generated using SnapGene Viewer 3.1.4.

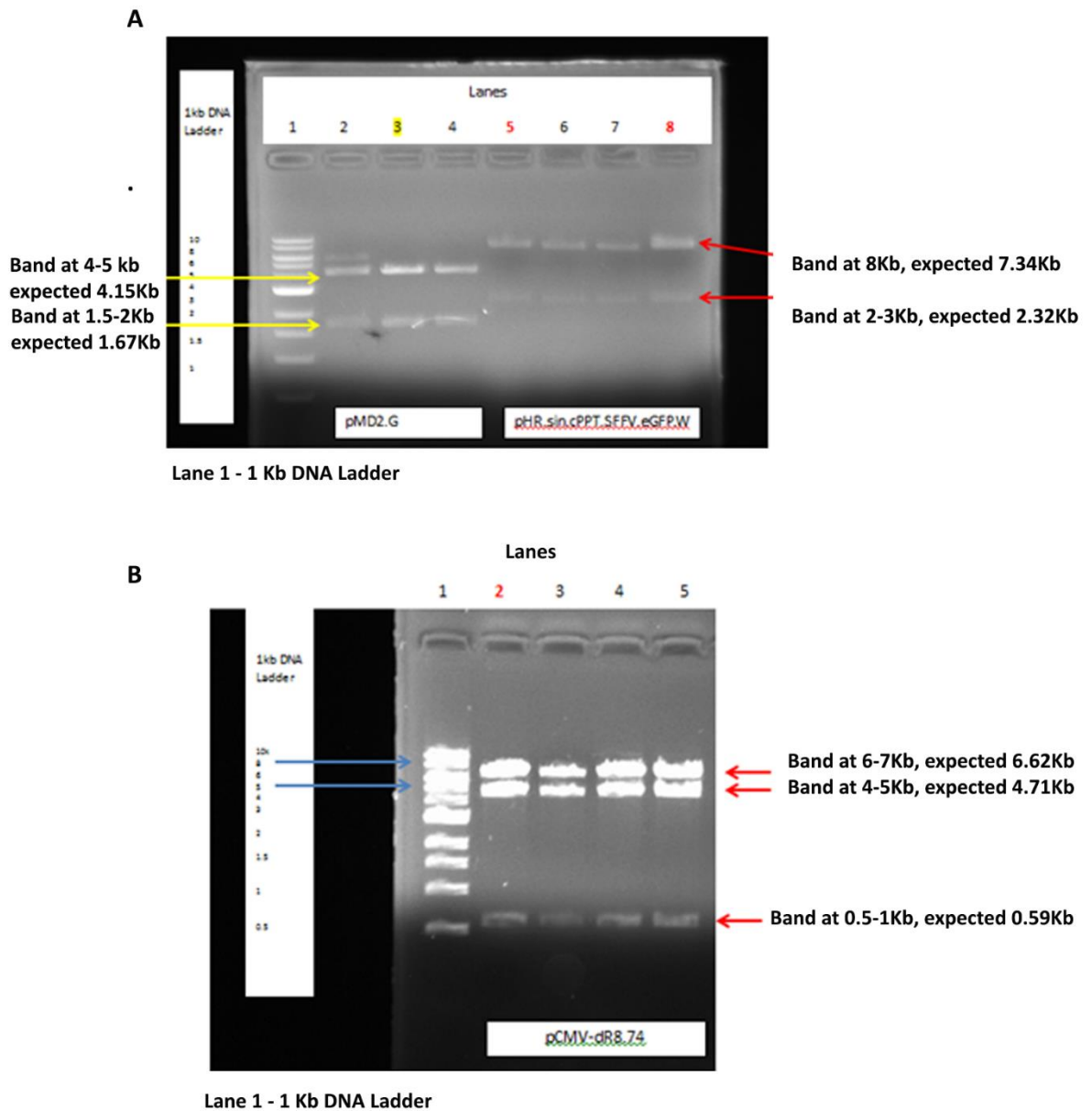


Figure 2.3, Images for agarose gels run for plasmid selection from the mini-prep.

A plasmids pMD2.G (Sample H2/2 in Lane 3 was selected) and pHR.sin.cPPT.SFFV.eGFP.WPRE (sample P1 shown in Lanes 5 and 8 was selected);
B Plasmid pCMV-dR8.74 (sample H1/1 in Lane 2 was selected). Units = Kb (Kilobases).

2.3.2.2. Lentivirus production

HEK 293T cells were obtained and cultured in 175cm² flasks (T175) in DMEM with 10% FBS and 1% Penicillin/Streptomycin. Cells were transduced using a protocol based on Salmon

and Trono, (Salmon and Trono, 2007): 2 hours before transduction, the growth medium was aspirated and replaced with DMEM / 2% FBS.

The plasmid mix was prepared in a tube containing the following: Packaging plasmid pCMV.R8.7.4, 18.96µg, Envelope plasmid pMD2.VSV.G, 8.17µg, Transfer plasmid (with eGFP gene) 29.17µg. Serum free DMEM was added to plasmid mix to make 1/3 of final volume.

Polyethylenimine (PEI – Sigma) was added to make up the final volume, mixed well and incubated for 15 minutes. Transduction mix was added to 20ml of reduced serum medium over cells in each T175 flask at 75µl/cm² flask surface area. After 16 hours the medium was replaced with DMEM/ 2% FBS.

Lentivirus was harvested from cells both two and three days after transduction. Growth medium was first aspirated and replaced with DMEM/ 2% FBS. The aspirated medium was centrifuged at 1230g for 10 minutes at room temperature and the supernatant was then passed through a 0.22µm Nalgene filter (Fisher Scientific). The filtered supernatant was transferred to ultracentrifuge tubes and centrifuged at 50,000g for 2 hours at 4°C to retrieve the lentivirus. The supernatant was discarded and the pellet air dried by inverting the spin tube. The lentivirus was recovered by re-suspending the pellet in PBS which was then left on ice for an hour. Lentivirus/PBS was mixed then transferred to 1.5ml eppendorf tubes for centrifugation at 1500g at room temperature for 10 minutes to remove any debris. The supernatant was transferred to a new tube where the suspension was adjusted to 10mM magnesium chloride and 5 units/ml DNASE added, followed by 30 minutes incubation at 37°C. The Lentivirus product was aliquoted, frozen and stored at -80°C.

2.3.2.3. Titration of lentivirus using HeLa cells

HeLa cells were cultured in DMEM (High glucose @ 4.5g/L, L-glutamine, Pyruvate) + 10% FBS, 1% PenStrep, then seeded at 50,000 per well in a 6 well plate (Greiner Bio-one). After 24 hours, GFP+ lentivirus was added in 3 dilutions: 7 μ l, 14 μ l and 21 μ l per well. The lentivirus was added in the presence of polybrene (Sigma) at a final concentration of 16 μ g/ml to assist transduction. After 16-24 hours the growth medium was replaced. Cells were harvested after a further 2 days and re-suspended in 1% PFA/PBS for analysis via flow cytometry. Control cells were also prepared: negative control, HeLa cells with no virus added (GFP-) and for a positive control: MDA-MB-231 Myr GFP+ cells (GFP+). Flow cytometry samples were run on a BD Accuri C6 Flow Cytometer, two samples for each condition. FlowJo software was used to format and analyse data and then an MOI (multiplicity of infection ratio) was calculated. Figure 2.4 shows the flow cytometry run for control cells to define the parameters for selection.

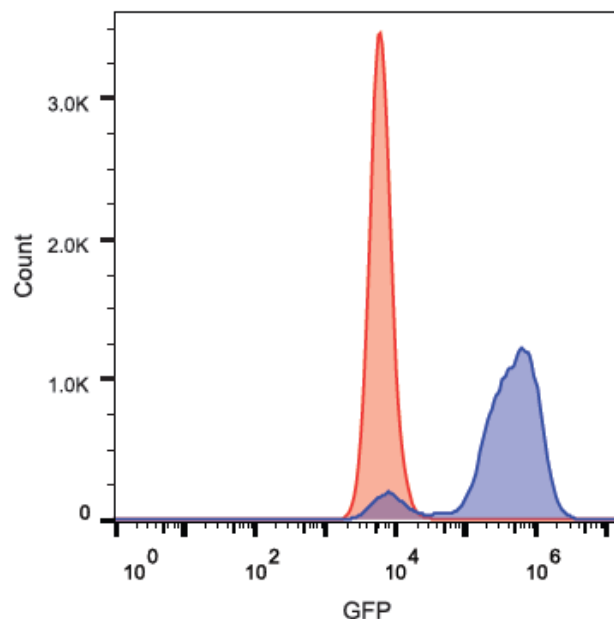


Figure 2.4, Flow cytometry controls for determining the best cell transduction of lentivirus in HeLa cells. Red peak shows the unstained HeLa cell population. Blue peaks show MDA-MB-231 GFP+ cells used as a positive control. The blue peak is mainly shifted to the right compared to the red peak for unstained cells. This signature location for the blue peak is used to locate GFP+ cells on experimental runs.

Y axis shows cell count, X axis shows fluorescence.

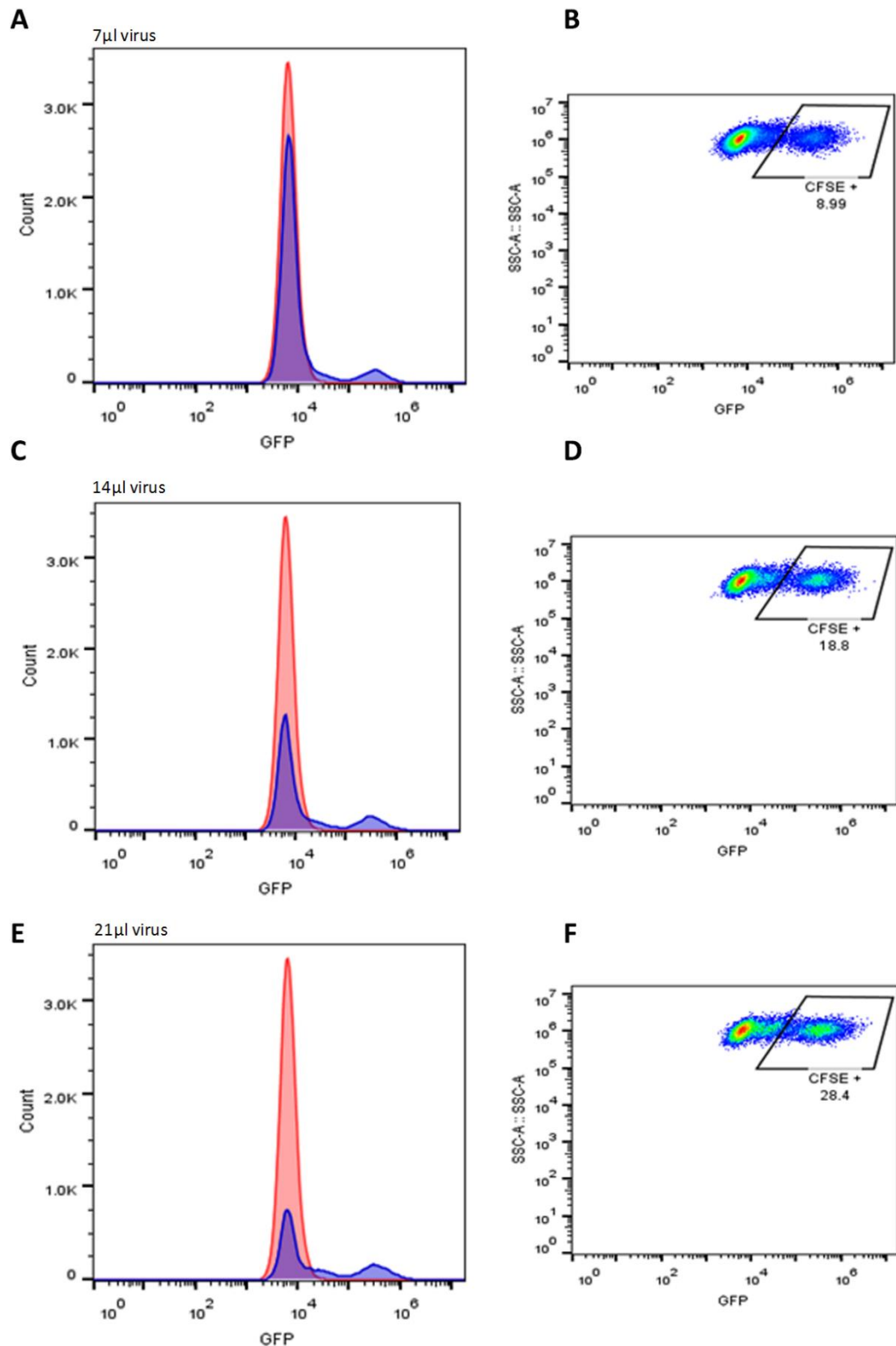


Figure 2.5, Flow cytometry graphs for optimisation of GFP+ lentivirus transduction quantities. The shifted blue peak in **A, C, E** shows the number of GFP+ cells after lentivirus transduction and the red peak shows non GFP+ cells (unsuccessful transduction). The GFP+ population is quantified as a % (CFSE+ value shown in the polygon) for each sample: **B, D, F**. Thus the addition of 21 μ l (**E**) of lentivirus results in 28.4% transduction in a 6 well plate for HeLa cells (**F**).

2.4. Fixing and staining cells

Cells and or tissues were fixed in pre-warmed 4% paraformaldehyde/PBS then washed three times with PBS. Where cells were contained in or seeded onto collagen they were then washed for ten minutes three times in PBS. Cells were permeabilized with 0.2% Triton X-100/PBS (TritonX-100 from Sigma) for ten minutes then washed a further three times with PBS. Blocking was carried out for 4-6 hours or overnight at 4°C using either 10% goat serum/PBS (Fisher Scientific) in 0.1% TritonX100/PBS or the specific block solution specified for an antibody. Primary antibodies diluted into the appropriate block solution were added to the cells which were then incubated overnight at 4°C (12-16 hours). Cells were washed with 0.1% TritonX100/PBS three times then blocked for ½ -1 hour at room temperature using 2% Goat Serum diluted into 0.1% Triton X-100/PBS. The secondary antibody was added to blocking solution at the appropriate concentration then added to cells for at least 1 hour in the dark at room temperature or for at least 2 hours at 4°C. Cells were washed three times with 0.1% TritonX100/PBS then three times with PBS and mounted using Vectashield containing DAPI (4',6-Diamidino-2-phenylindole dihydrochloride, Vector Laboratories) alternatively DAPI was added at 10µg/ml to the penultimate PBS wash (Sigma) and Vectashield H-1000 fluorescence mounting medium (Vectorlabs) was used. All washes were conducted for 10 minutes each at room temperature. Where phalloidin stain was used alone, this was added after cell permeabilization in 0.1% TritonX100/PBS and left overnight at 4°C or for 2 hours at room temperature. Where phalloidin was part of immuno-staining it was added with the secondary antibody. Samples were mounted onto Superfrost slides (Thermo Scientific – Menzel Gläser) unless otherwise stated. Menzel Gläser No 1 coverslips (Thermo Scientific), 22 x 22mm for small samples. Samples were mounted using Vectashield mounting medium either with or without DAPI unless otherwise stated.

Details of antibodies and stains used are as follows:

Stains:

4',6-Diamidino-2-phenylindole (DAPI) was used at 10µg/ml.

Phalloidin - either Invitrogen (546) or phalloidin-atto 565 (Sigma), both used 1:250.

Primary antibodies:

GFP – anti-rabbit Sigma A11122, 1:100, 0.1% TritonX-100/PBS 10% goat serum (Fisher Scientific);

Keratin – anti-mouse, Abcam ab118817, 1:200, 0.1% TritonX-100, 0.1% BSA (Fisher Scientific), 10% goat serum;

Ki67 – anti-rabbit, abcam16667, 1:500, blocking solution 1% BSA in 0.1% TritonX-100/PBS

Vimentin – anti-mouse, abcam ab8978, 1:250, blocking solution 1% BSA in 0.1% TritonX-100/PBS

Secondary antibodies:

Anti-rabbit 488, AlexaFluor from Fisher Scientific

Anti-mouse 488, AlexaFluor from Fisher Scientific

Anti-rabbit 647, AlexaFluor from Fisher Scientific

Anti-mouse 647, AlexaFluor from Fisher Scientific

These were all used at either 1:100 for 1 hour at room temperature or 1:200 for 2 hours at room temperature for better binding and a cleaner result and diluted into 2% goat serum / 0.1% TritonX-100/PBS. (Samples were blocked first in the same solution for at least half an hour before adding the secondary antibody.)

2.4.1. Embedding and sectioning samples

Some dense collagen or tissue based samples were embedded and sectioned to enable further and more detailed microscopic analysis. Samples were fixed using 4% PFA/PBS as required then washed three times in PBS to remove the PFA. Staining was carried out if required although some samples were stained after sectioning.

Samples to be embedded were subjected to a sucrose gradient: 5% sucrose/PBS overnight on rollers at 4°C followed by 15% sucrose/PBS at room temperature for 2 hours, rocking and then a further two hours in 30% sucrose/PBS, rocking. Samples were embedded in OCT (Cell Path) and frozen in an isopentane liquid (Fisher Scientific) bath on dry ice then transferred to -80°C freezer for at least 2 hours. Samples were labelled and mounted on circular cork bases (Fisher Scientific) and stored at -80°C until they were sectioned. Sections were made using a Kryostat (Model OTF, Bright 5040) using an MB35 Premier blade (Thermo Scientific) with sections mounted onto polylysine coated slides (Polysine, Thermo Fisher).

2.5. Microscopy

2.5.1. Phase contrast time-Lapse

Time-lapse sequences were taken using either a Nikon Eclipse TE200 with a Jencons PLS Nikon lamp, UV box, moveable stage and environmental chamber, running NIS Elements AR3 using Nikon lenses: Plan Fluor 10X/0.30 PH1 DL, Plan Fluor 20X/0.45 PH1 DM and Plan Fluor 40X/0.60 PH2 DM or a Nikon Eclipse TiE with moveable stage and environmental chamber running NIS Elements software and PlanApo 10x DIC L lens with intermediate magnification changer (to give either x1 or x1.5 magnification). The environmental chamber for each microscope was set at 37°C with a continuous flow of CO₂ through the plate.

Post-hoc image processing was conducted using NIS Elements and IImageJ software (Figure 2.6) and Photoshop CS6 Extended.

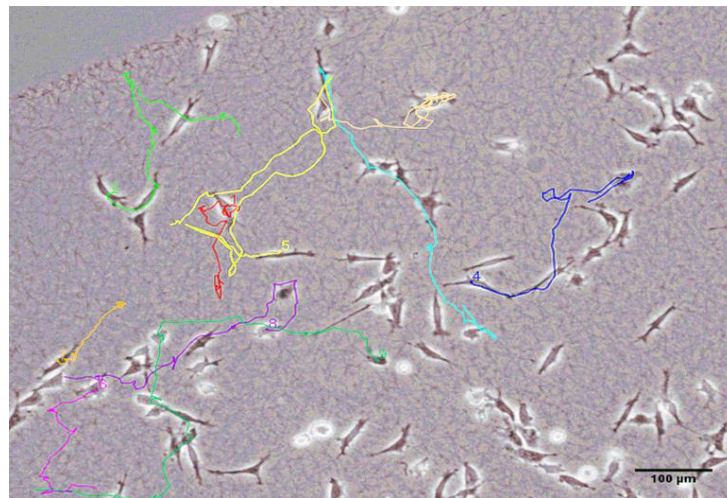


Figure 2.6. Cells tracked using MtrackJ ImageJ plugin. Each cell was tracked in a stepwise manner, each track appearing in a different colour. If a cell divided one of the daughter cells was tracked from that point onwards. Track measurements were generated and saved in Excel format. Track data for each cells was then extracted and cell speed calculated. Scale bar= 100μm.

2.5.2. Epifluorescence microscopy

A Zeiss Axioimager was used for epifluorescence microscopy of slides in combination with Zeiss Software version 4 and lenses (x5, x10, x20, x40).

A Zeiss Axio Vert.A1 epifluorescence microscope with an inverted lens and moveable platform was used to take individual images of live cells to monitor experiment progress and check for fluorescent protein expression. Lenses used were: x5 Planar Plan Neofl Ph1 0,15 ∞ /0,17, x10 Zeiss A Plan 0,25 Ph1 lens and x20 Zeiss LDA Plan 20x/0,35 Ph1 ∞ /1,0 (PS), x40 Zeiss LDA Plan 40x 0.55 Ph1 ∞ /1,0 (PS).

2.5.3. Confocal microscopy

Live and fixed cell imaging was conducted using inverted confocal microscopes:

Leica TCS SP2 (HCX PlanApo lbd.BL 63x oil immersion lens) running Leica Application Software version 2.61 or Nikon A1-R and A1 Plus microscopes running NIS Elements AR with environmental chamber and Nikon Intensilight CHGFI lamp were used with the following optics: x4 Plan Fluor 4x 0.13 ∞ /1.2 WD 16.5; x10 0.30 Plan Fluor OFN 25 Ph1 D2; x20 0.75 Plan Apo DIC N2 OFN 25 WD 1.0; x60 1.40 Plan Apo ∞ /0.17 WD 0.13; x100 APO TIRF1.49 ∞ /0.13 0.20 DIC. On the A1 Plus system a Visible Fiber Laser WFL P Series laser source was also used. Images were processed and analysed using NIS elements AR (Nikon), ImageJ (FIJI, 64bit) software and prepared for presentation using Photoshop CS6 Extended.

2.6. Statistical analysis

2.6.1. Quantification of sample size

The appropriate sample size required for statistical analysis for experiments was determined using power calculation software G*Power 3.1.9.2. (Franz Faul, Germany). For each experiment, an initial data set was gathered, mean value and standard deviation calculated for each experimental condition and these values entered using the F test/ ANOVA option. The required power ($1-\beta$ error of probability) and significance (α error of probability) were selected and sample size calculated. Ideally significance=0.05 and Power=0.95 were selected to give a highly probable outcome of difference but where this gave a sample size which was not possible within the time and resources available, the power and significance were reduced. Microsoft Excel Office 365 was used for data preparation of data for statistical evaluation and to calculate mean and standard deviation for each experimental condition.

2.6.2. Statistical analysis of experimental results

GraphPad Prism version 6 for Microsoft Windows was used for statistical analysis and graphical presentation of results. For each cell population, the distribution of data was investigated by conducting a normality test (Shapiro Wilk test). Where a Gaussian or normal distribution of data was found for all cell populations to be compared, a parametric test was selected. If one or more cell populations did not meet the conditions of the Shapiro Wilk test for normality, a non-parametric test was selected. Where three or more groups of data were to be analysed for more than one comparative factor and these were normally distributed, a two-way Analysis Of Variance (ANOVA) was conducted. If the data for one or more of the groups to be compared was not normally distributed a non-parametric statistical test was conducted, the Kruskal Wallis test. Where multiple comparisons were made as part of the statistical analysis a multiple comparisons correction test was also run:

Tukey's Test for ANOVA and Dunn's test for the Kruskal Wallis test, this reducing the likelihood of a significant difference emerging due to the chance arising through making a number of comparisons within the same analysis.

3. Modelling Metastasis *In Vitro*

3.1. Introduction

Given that cancer metastasis is a complex multi-stage process, metastatic behaviour is challenging to model (Bradbury et al. 2012, Geiger and Peeper 2009, Kramer et al. 2013). Indeed the temporal nature of tumour growth, invasion, dissemination and development of metastases is one which takes place over months and years for most cancers and is therefore difficult to capture and study. Understanding the molecular and cellular mechanisms involved is important if metastatic disease is to be contained and prevented (Hanahan and Weinberg 2011). Experimental models provide a controlled environment in which to investigate metastasis and to test associated drugs during their development (Fischbach et al. 2007, Onion et al. 2016, Pampaloni et al. 2007).

In vivo models are few, expensive, challenging to set up and are not necessarily representative of human metastatic disease (Khanna and Hunter 2005). For example, where tumour explants are carried out into mammals such as mice, the tumour microenvironment is either absent, lost or maybe quickly overtaken by the development of murine ECM (Holliday and Speirs 2011, Khanna and Hunter 2005, Saxena and Christofori 2013).

Furthermore capturing the steps of metastasis in a dense tissue environment in real-time is fortuitous due to the spontaneity and unpredictable timing of events and requires expensive equipment for observation and capture (Decaestecker et al. 2007, Kaufman et al. 2016).

The biological complexity of tissue means that modelling metastasis *in vitro* requires materials and structural components which together give a biological context sufficiently relevant to yield meaningful results (Yamada and Cukierman 2007). Successful models must

be tractable, reproducible and quantifiable, ideally requiring materials which are easily available and relatively inexpensive (Pampaloni et al. 2007).

Early research in this field was conducted in a two dimensional context using cell lines derived from histological samples grown as monocultures and passaged numerous times on 2D surfaces (Freshney 2010), for example the early subculture of fibroblasts, (Carrel and Ebeling 1923) and of HeLa cells (Lucey et al. 2009) . Cell culture for research still largely follows this approach, with cells grown in monolayers on tissue culture plastic. Cells typically adhere and proliferate but they lack the normal and necessary environmental cues provided by a natural biological context. Furthermore, cells are continuously bathed in culture medium and provided with plentiful oxygen and carbon dioxide, a very different and alien context to a tissue environment (Yamada and Cukierman 2007). Without the extra cellular matrix which surrounds most tissues, cells seeded in 2D lack structural support, the physical cues and the signals provided within their environment allowing differentiation and tissue polarity to be established (Doyle et al. 2013, Friedl et al. 2012, Yamaguchi et al. 2005). The heterogeneous mix of cells within normal tissue was also absent in this context (Bissell and Radisky 2001). Replicating essential environmental conditions *in vitro* with sufficient complexity to produce meaningful data is thus a challenge for the researcher.

A successful *in vitro* model requires a tissue architecture and context with natural borders and boundaries which provide the important structural cues instructing co-operative cell behaviour (Haeger et al. 2015, Rørth 2012). A basement layer for example is an important feature of most tissue types which contains cells and retains context (Kalluri 2003).

Recent models have sought to provide a better contextual environment for the study of cell behaviour and the metastatic process. ECM components such as collagen type 1, fibronectin

and laminin have been used to create gel like layers as a simple tissue based model (Bissell et al. 2003, Pampaloni et al. 2007, Schor 1980, Wolf et al. 2009). Matrigel has also been used as a representative basement membrane layer with cells embedded and observed within it (Novaro et al. 2003, Zaman et al. 2006).

Observation and quantification of behaviour and events requires an environment in which cell behaviours can be clearly identified (Driscoll and Danuser 2015). Matrix density and opacity as well as suitable access to samples for microscopy are therefore important features. The optics associated with time-lapse and laser scanning microscopy require that cells within their modelled context be within the working distance of the lens (Vasaturo et al. 2012). Back scatter of light and autofluorescence of matrix components may also interfere with observation techniques, especially when collagen is used within a matrix (Artym and Matsumoto 2010, Wu et al. 2003). The development of a three dimensional model therefore needs to provide sufficient depth and context for cell interaction yet be sufficiently thin to be penetrable allowing observation and tracking of cell events. The full range of cell behaviours observed *in vivo* should also be demonstrated.

Starting with the simplest approach of 2D coating on tissue culture plastic, this project explored the opportunities for *in vitro* modelling.

Hypothesis: A simple *in vitro* model could be created using extracellular matrix components which would provide sufficient context for cells to display the range of morphologies and behaviours observed *in vivo* and would allow these behaviours to be observed and recorded.

3.2. Materials and methods

3.2.1. 2D cell migration assays

6-well tissue culture plates were coated with collagen (Rat Tail Collagen Type 1 at 0.5mg/ml), fibronectin (10µg/ml) and Matrigel (3mg/ml, from BDBioscience). Fibronectin, collagen and Matrigel coatings were prepared as described in Section 2.2 at the above concentrations. Coatings were added to the wells and left to set in a tissue culture incubator at 37°C/5% CO₂ for 1 hour. Fibronectin wells were then washed gently with PBS twice before use. HT1080 and MDA-MB-231 cells were trypsinized, re-suspended in medium and added to the coated culture wells to give a confluence of around 15% once cells were settled. Cells were left to settle and adhere for two hours then transferred to and equilibrated in the environmental chamber of the time-lapse and multipoint time-lapse imaging set up. Ideally a control cell line such as MCF-7 which is invasive with cells migrating as a sheet rather than individually (Gest et al. 2013, Holliday and Speirs 2011), would also have been used as a negative control as it has elsewhere in this project, however, as time and resources were limited, the work was not carried out as part of this project. Images were taken at 10 minute intervals and analysis carried out for the first 8 hour period using ImageJ MtrackJ tool. Thirty MDA-MB-231 cells were tracked for each coating type initially (90 cells in total) and mean and standard deviation values calculated for each coating type for 'distance from start' cell migration. These values were entered into G*Power to determine the appropriate sample size for a meaningful statistical analysis to be performed. A sample size of at least 75 was determined to give a power of 0.95 and a significance of 0.05 (Appendix B.1). A further 30 cells were measured and tracked for each cell and coating type for each of three experiments in total n1-3 (with the exception of MDA-MB-231 cells in experiment n2 where only 15 cells were available to be tracked on collagen). A two-way ANOVA was selected as

multiple populations of cells which were normally distributed, were to be conducted for multiple 2D coating types. Tukey's test for multiple comparisons test was also used to reduce the likelihood that a significant result arose due to multiple comparisons being made within one analysis.

3.2.2. 3D collagen cell migration assay

MCF7, MDA-MB-231 and HT1080 cells were trypsinized and re-suspended in growth medium. Collagen was prepared as described in section 2.2, and cells suspended in medium were added to give a final concentration of 1mg/ml and 2mg/ml collagen. Cells in matrix for each cell line were added to the centre of a 6 or 12 well tissue culture plate and left to set as described previously. Further medium was added as required to give a total volume of 2mls per well. Time-lapse microscopy was used to record migration characteristics over a 21 hour period with images taken at 10 minute intervals. ImageJ software was used to measure cell length and width and the aspect ratio of length:width calculated for 50 cells of each type in each matrix concentration. Cell tracking was carried out (section 2.5.1) and initial mean and standard deviation values entered into G*Power to determine the required sample size needed based on 'distance from start' for 1mg/ml for all three cell lines. At least 45 cells per experiment were required to give a power of 0.95 and significance of 0.05 (Appendix B.2). A further 100 cells per matrix per experiment were tracked (n1-3). Graphpad prism 6 was used for statistical analysis with a two-way ANOVA followed by Tukey's test for multiple comparisons, to analyse and interpret the significance of differences in behaviour between different cell lines in each environment and between the same cells in different collagen concentrations. A two-way ANOVA was chosen as data were normally distributed and the behaviour of multiple populations of cells was to be compared for multiple matrix types.

Tukey's test for multiple comparisons was used to reduce the likelihood of a significant result arising due to multiple comparisons being made within the same statistical analysis.

3.2.3. 3D collagen and fibronectin cell migration assay

MDA-MB-231 or HT1080 cells were added to collagen at 1mg/ml and 2mg/ml with or without fibronectin at 5µg/ml and 10µg/ml, prepared as described in Section 2.2. The cells in matrix were set for 20-30 minutes at 37°C/5% CO₂ and growth medium added. Cells were left to settle for 2 hours then time-lapse microscopy was used to capture cell migration behaviour for 21 hours with images taken at 10 minute intervals. ImageJ software was used for quantification, cell length and width being measured for cells in each matrix type and cell tracking carried out using the MTrackJ tool. G*Power was used to calculate an appropriate sample size based on the analysis of MDA-MB-231 cells for one experiment. A sample size of 90 cells was selected to give a power of 0.9 and significance of 0.1 (Appendix B.3) due to the fact that over 200 cells would be required per experiment to allow a power of 0.95 and significance of 0.05 which was outside the time and resources available. Graphpad prism 6 was used for statistical analysis, with a two-way ANOVA conducted followed by Tukey's multiple comparison test to test for differences between matrix conditions for multiple cell populations. A two-way ANOVA was selected as cell population data was normally distributed and multiple cell populations were to be compared for multiple matrix conditions. Tukey's multiple comparisons test was used to reduce the likelihood of a significant result arising due to multiple comparisons being made within the same analysis.

3.2.4. Compressed Collagen (CC) assay

Rat tail collagen type I was used to make compressed collagen gels with cells seeded either into or onto the gel. 2mg/ml collagen solution was made as described in section 2.2 2ml

quantities of collagen solution were added to wells of a 12-well plate which was used as a mold and allowed to set in an incubator at 37°C, 5% CO₂ (20-40 minutes). Set gels were turned out onto a sterile fine nylon mesh (average hole size of 0.37 mm) located above a stack of dry filter papers as shown in Figure 3.1. A glass plate and weights totalling 126g were used to compress the gel for either 2 ½ or 5 minutes (Chen B. et al. 2012, Jones et al. 2012). Where cells were encapsulated within the collagen gel, a copper wire mesh (1.7 mm hole size) was also used to prevent too much cell compression resulting in cell death. Compressed gels were then placed onto a thin layer of liquid 1mg/ml collagen in a 6-well plate and left to set for 20-30 minutes in the incubator until set after which supplemented DMEM was added. Time-lapse microscopy was used to observe and record population of the compressed collagen disc and the surrounding lower concentration collagen over a period of days following experimental set-up.

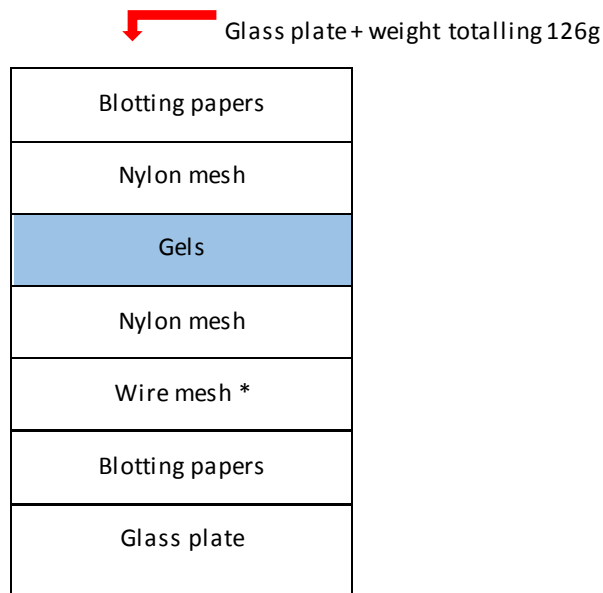


Figure 3.1. Compressed collagen layering. A wire mesh was used *when cells were seeded into the gel to avoid cells being crushed.

3.2.5. 2D/3D invasion assay

Cell-free collagen was prepared at a 2mg/ml pH 7.0 - 7.5 was prepared (section 2.2) and added to the centre of each well of a 6 well plate and left to set. Cells were re-suspended in normal growth medium (supplemented DMEM) and these added around the outside of the set collagen, Figure 3.2. The cells were left to settle and adhere for 30-40 minutes and supplemented DMEM then added carefully to avoid washing cells onto the collagen. Cell behaviour was recorded using time-lapse microscopy (images every 10 minutes for 12 hours) and cell migration analysed using ImageJ based on cell location: plastic/2D, collagen border zones or 3D/collagen. Initially ten HT1080 cells for each region were tracked, average and mean values calculated and entered into G*Power used to determine the appropriate sample size for statistical evaluation. A sample size of thirty cells was determined to give a power of 0.95 and significance of 0.05 (Appendix B.4). Tracking and analysis was repeated for three experiments for MDA-MB-231 cells. A two-way ANOVA was carried out followed by Tukey's test for multiple comparisons. The two-way ANOVA was selected as cell population data was normally distributed and multiple cell populations were to be compared for multiple contexts. Tukey's multiple comparisons test was used to reduce the likelihood of a significant result arising due to multiple comparisons being made within the same analysis.

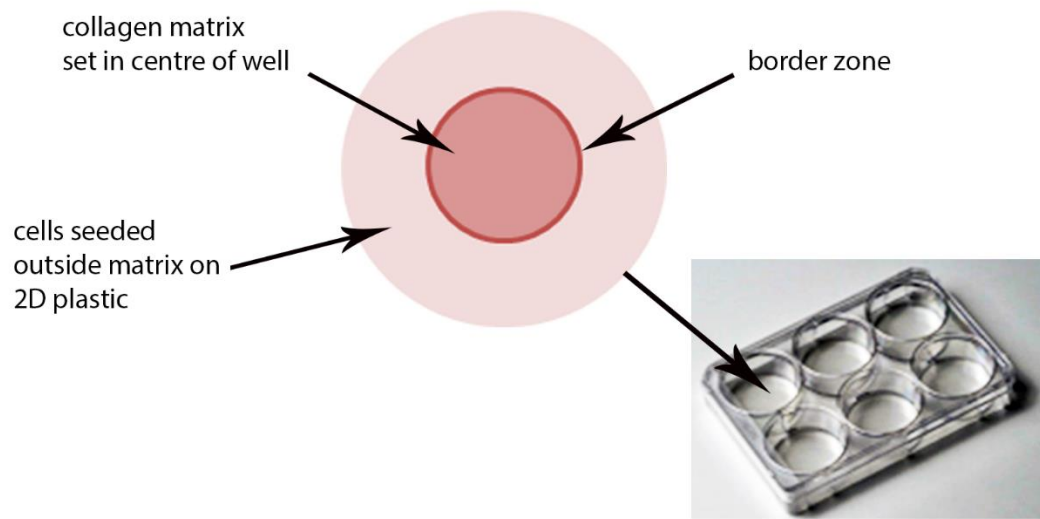


Figure 3.2, 2D/3D invasion assay. Collagen matrix solution was pipetted into the centre of a 6-well (or 12-well) plate and left to set in an incubator at 37°C/5% CO₂. Cells suspended in medium were added around the outside of the matrix and left to adhere. Additional cell growth medium was added.

3.3. Results

3.3.1. Cell migration on coated 2D surfaces – HT1080 and MDA-MB-231

Until recently, cell migration research has been conducted mainly in a two dimensional environment (2D) so a baseline 2D cell migration experiment was carried out for two cancer cell lines: MDA-MB-231 breast cancer cells and HT1080 fibrosarcoma cells. These cell lines were chosen as they are known to migrate well having been used extensively in *in vitro* and *in vivo* research in this field (Artym et al. 2015, Taubenberger et al. 2013, Wolf et al. 2003). In this initial experiment set, cell migration was characterised for cells moving on 2D surfaces coated with collagen type 1 and fibronectin, both extracellular matrix constituents and for Matrigel, a basement membrane extract from a mouse tumour environment. As the morphology of migrating cells can vary (Friedl and Wolf 2009a) cells were observed and quantified by measuring length and width so that aspect ratio (length : width) could be calculated, mesenchymal/elongated cells having a high aspect ratio and rounded or spread cells a low aspect ratio (Konen et al. 2016). Images showing the typical morphology for both cell lines in each environment are shown in Figure 3.3 A-G. Both HT1080 and MDA-MB-231 cells adopted a flat, spread morphology on fibronectin (Figure 3.3 A, E) with a low aspect ratio (Figure 3.3 H, I). On Matrigel, cells from both cell lines were rounded and compact (Figure 3.3 C, G) with a low aspect ratio (Figure 3.3 H, I) and tended to group together, frequently forming chains (Figure 3.3 C, D, G). On collagen however, cells from both cell lines were elongated showing long thin protrusions (Figure 3.3 B, F) and had a significantly higher aspect ratio (HT1080 mean=3.55, MDA-MB-231 mean=4.19) than when migrating on either fibronectin (HT1080 mean=1.66, MDA-MB-231 mean=1.95) or Matrigel (HT1080 mean= 1.86, MDA-MB-231 mean=1.20) (Figure 3.3 H, I). For MDA-MB-231 cells the aspect ratio was significantly different between all three coating types (fibronectin and collagen at

$p \leq 0.001$, fibronectin and Matrigel at $p \leq 0.0001$, collagen and Matrigel $p \leq 0.0001$) and for HT1080 cells there was a significant difference between collagen and Matrigel ($p \leq 0.0001$) and collagen and fibronectin ($p \leq 0.0001$).

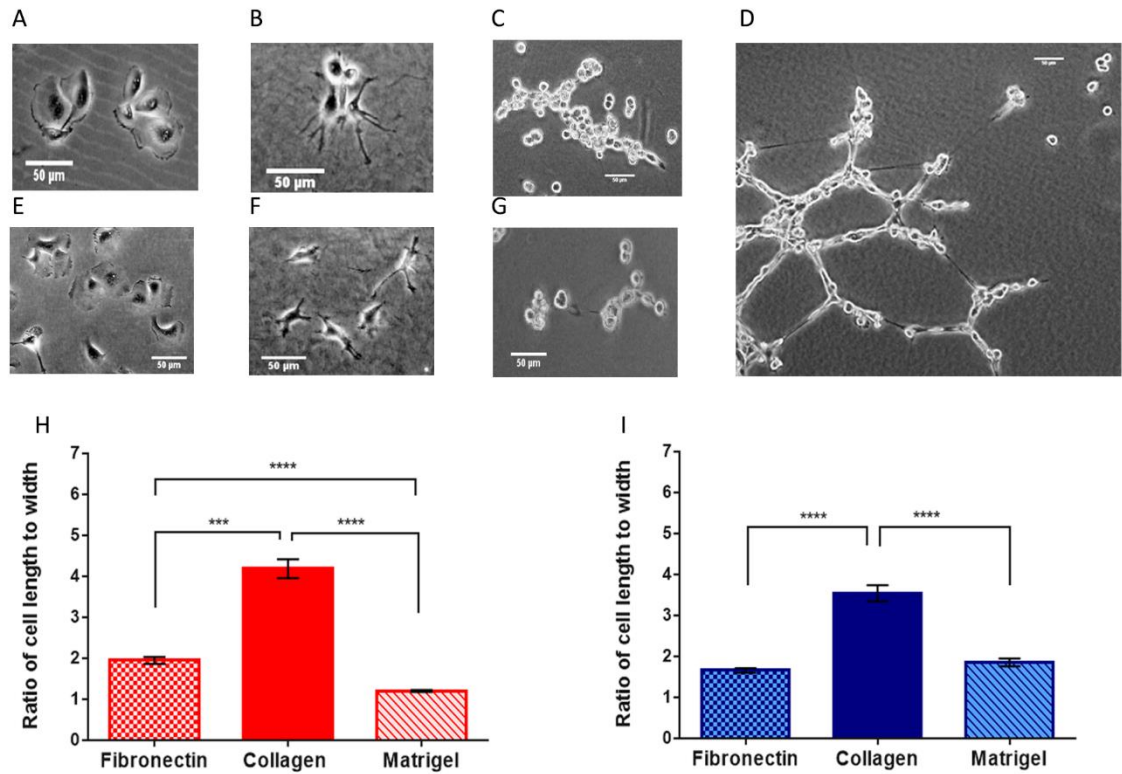


Figure 3.3, MDA-MB-231 and HT1080 cells migrating in two dimensions (2D) on tissue culture plastic with different coatings: fibronectin (10 μ g/ml), collagen (2mg/ml) and Matrigel (3mg/ml). **A-C** MDA-MB-231 on fibronectin, collagen, Matrigel, **E-G** HT-1080 on fibronectin, collagen, Matrigel. **D** HT1080 chain formation on Matrigel (also visible for MDA-MB-231 in **C**). Graphs **H** (MDA-MB-231) and **I** (HT1080) show cell aspect ratio which indicates their overall cell morphology on each coating (a high aspect ratio equating to a long narrow cell morphology). Three experiments (n1-3) with 30 cells per experiment were measured (with the exception of MDA-MB-231 n2 which contained 15 cells). Statistics were generated using Graphpad 6 via a two-way ANOVA with Tukey's test for multiple comparisons. Error bars show standard error of the mean. Significance is shown: *** $p \leq 0.001$, **** $p \leq 0.0001$ (Full statistical details for each test are shown in Appendix B.5). Scale bars on all images = 50 μ m.

Migration characteristics were compared for each cell line for the three coating types in terms of distance migrated and speed of migration. Tracking data for the total track length: 'track length' and for the distance a cell had travelled from its start point: 'distance from start' was used to quantify the extent of cell migration on each surface type. A comparison of 'track length' and 'distance from start' is shown for each cell line in Figure 3.4 A, B. The mean cell length for cells on each coating was also calculated to allow interpretation of cell migration in terms of cell lengths for both 'track length' and 'distance from start' (Table 3.1). Whilst cells from both cell lines had on average migrated at least one cell length from their starting point, the decrease and significant difference between 'track length' and 'distance from start' for each coating for MDA-MB-231 (fibronectin $p \leq 0.0001$, collagen $p \leq 0.0001$ and Matrigel $p \leq 0.001$) and for HT1080 ($p \leq 0.0001$ fibronectin, collagen and Matrigel) showed that the cell migration route was indirect (Figure 3.4 A,B). However as the trend in 'track length' was similar to that for 'distance from start' for each cell line and as 'distance from start' gave the final cell position after eight hours, this was taken as the measure for cell migration.

When comparing 'distance from start' for each cell line (Figure 3.4 C, D; Table 3.1), a significant difference was evident between migration on fibronectin and collagen (MDA-MB-231 $p \leq 0.001$, HT1080 $p \leq 0.01$) and between fibronectin and Matrigel (MDA-MB-231 $p \leq 0.001$, HT1080 $p \leq 0.0001$) with cells migrating further on fibronectin. Cell migration between collagen and Matrigel for both cell lines was similar with no significant difference detected (Figure 3.4 C, D). In terms of speed of cell migration ('track length'/time), MDA-MB-231 cells moved at a significantly different speed for each coating type (Fibronectin and collagen $p \leq 0.0001$, Collagen and Matrigel $p \leq 0.01$ and Fibronectin and Matrigel $p \leq 0.0001$, Figure 3.4 E). Speed of migration for HT1080 cells was significantly different between fibronectin and

collagen ($p \leq 0.0001$) and fibronectin and Matrigel ($p \leq 0.0001$) but not between collagen and Matrigel (Figure 3.4, F).

Overall, these results indicated that varying the 2D coating on tissue culture plastic lead to different cell migration characteristics in two migratory cell lines, MDA-MB-231 and HT1080 when cells from the same original population of each cell line were seeded and observed on fibronectin, collagen and Matrigel.

Table 3.1 Average cell length of cells migrating on different coatings

	MDA-MB-231					HT1080				
2D Coating	Av. cell length μm (n1-3)	Av. Total track length μm	No. Cell Lengths	Av. Distance from Start μm	No. Cell Lengths	Av. cell length μm (n1-3)	Av. Total track length μm	No. Cell Lengths	Av. Distance from Start μm	No. Cell Lengths
Fibronectin	46	218	4.7	80	1.7	46	183	4.0	65	1.4
Collagen	46	123	2.7	51	1.7	53	121	2.3	47	1.1
Matrigel	16	89	5.6	50	3.1	31	102	3.3	40	1.4

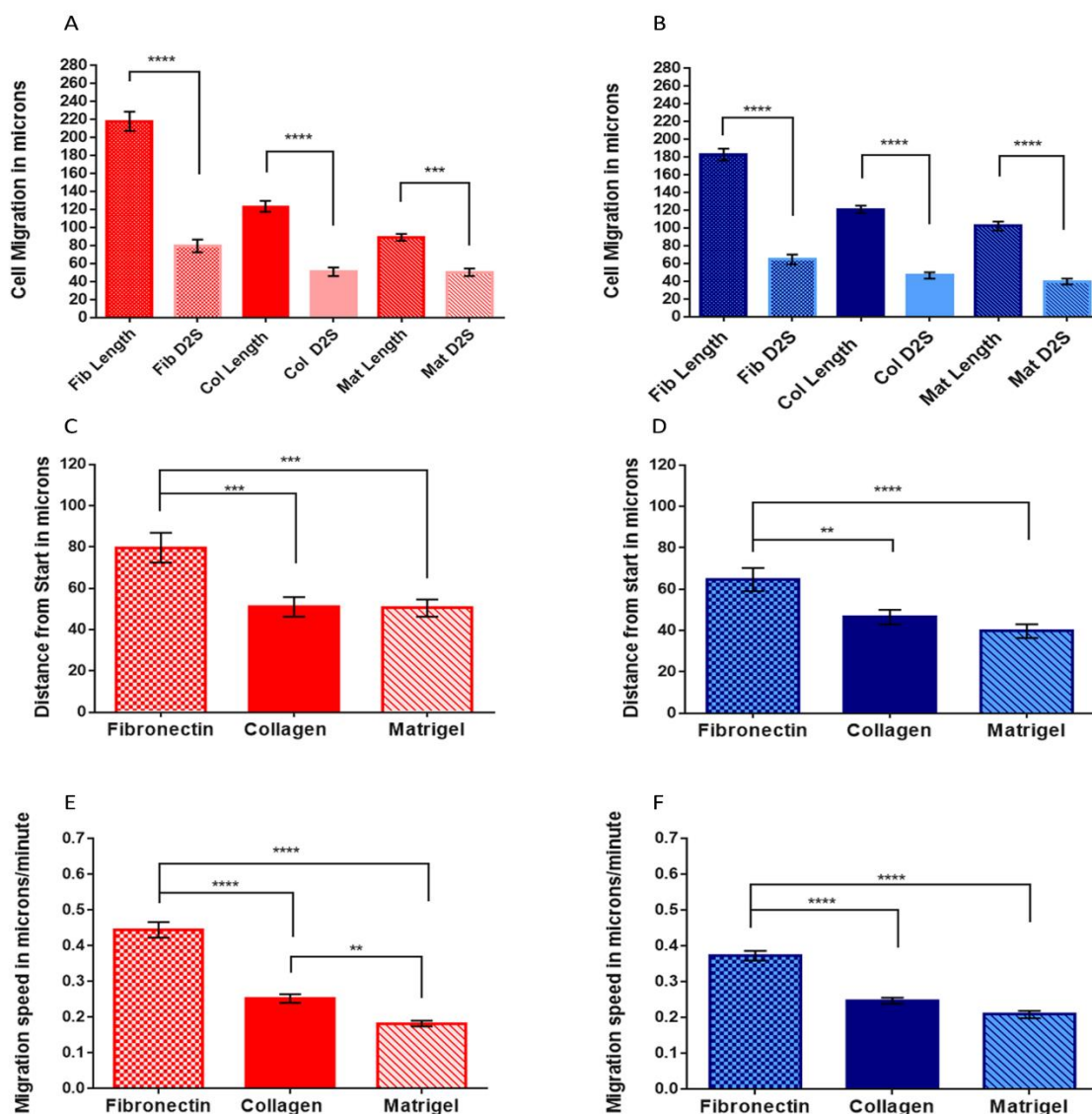


Figure 3.4, Cell migration on 2D coated surfaces for MDA-MB-231(A,C,E) and HT1080 (B,D,F). Graphs A and B show cell migration for cells tracked every ten minutes from an 8 hour time-lapse movie. Track length 'Length' for each coating is compared to distance from start (D2S). Graphs C and D compare distance from start of cells migrating on different coated surfaces (Collagen (Col), Fibronectin (Fib), Matrigel (Mat)). Graphs E and F show the speed of cells migrating on each surface. Three experiments with 30 cells per experiment were tracked (with the exception of MDA-MB-231 n2 which contained 15 cells). Statistics were generated using Graphpad6 via a two-way ANOVA with Tukey's test for multiple comparisons. Error bars show standard error of the mean. Significance is shown: ** $p \leq 0.01$, *** $p \leq 0.001$, **** $p \leq 0.0001$ (Full statistical details for each test are shown in Appendix B.5).

3.3.2. Cell migration in a 3D collagen matrix

During metastasis, a migrating cancer cell is unlikely to move in two dimensions only. Cells escaping a developing tumour are likely to migrate in the context of the extracellular matrix surrounding it. As the major constituent of the extracellular matrix is collagen type 1, collagen type 1 (from rat tail) was used at two different concentrations (1mg/ml and 2mg/ml) to create a simple *in vitro* 3D environment for the observation and quantification of cell migration. MDA-MB-231 and HT1080 cells were selected due to their invasive and migratory phenotype (Barry et al. 2015, Kraning-Rush et al. 2011, Wolf et al. 2003) and MCF7 breast cancer cells were selected as a control cell line known for its low migration characteristics (Peela et al. 2016).

Cell morphology for each cell line at each collagen concentration (Figure 3.5 A-F) was quantified using aspect ratio (Figure 3.5, I). The mean aspect ratio for MCF7 cells was low (2.01 in 1mg/ml collagen and 1.84 in 2mg/ml collagen) suggesting an oval/spread morphology (Figure 3.5 A, D, I). For MDA-MB-231 cells the aspect ratio had a higher mean value (3.10 in 1mg/ml and 3.78 in 2mg/ml collagen) indicating a longer, narrower cell morphology, more mesenchymal in appearance (Figure 3.4 I). Figure 3.4 B, E show several typical cells which are either elongated or rounded with elongated protrusions, which support this finding. HT1080 cells in 1mg/ml collagen had a mean aspect ratio of 5.35 whereas in 2mg/ml they had a lower mean aspect ratio of 4.57, a difference that was found to be significantly different at $p \leq 0.01$ level (Figure 3.5, C,F,I and Appendix B.6). There was no significant difference between either MCF7 in the two collagen concentrations nor MDA-MB-231 in the two contexts but again HT1080 cells were more elongated in 1mg/ml collagen (mean=77.16 μ m compared to 70.77 μ m) which was significantly different at $p \leq 0.05$ level in

line with that identified in the aspect ratio for the same cells (Figure 3.5 I,J). Cell migration was quantified in the collagen matrices, using 'distance from start' and speed of migration based on cell tracking data. A significant difference at the $p \leq 0.0001$ level was found for cells of both MDA-MB-231 and HT1080 for 'distance from start' between the two collagen concentrations, with cells of each type moving further from their start point in the less dense collagen during the 21 hour tracking period (Figure 3.5 G,J). As expected, MCF7 cells moved less than one cell length (mean lengths: 31.3 in 1mg/ml and 27.3 in 2mg/ml) from their starting point, remaining in groups which expanded gradually as cells divided. Migration speed was also quantified and a significant difference was found for all three cell lines between the different collagen concentrations (Figure 3.5 H). MCF7 cells moved mainly on the spot (Figure 3.5 G) at 0.11 microns/minute in 1mg/ml collagen and 0.08 microns/minute in 2mg/ml collagen and so although the difference between these two values was significant at the $p \leq 0.01$ level, it is clear from the 'distance from start' values (Figure 3.5 G) that these cells didn't migrate within this timeframe. MDA-MB-231 and HT1080 cells moved faster in the 1mg/ml collagen matrix than in the 2mg/ml matrix (MDA-MB-231 mean values: 0.27 microns/minute and 0.20 microns/minute and for HT1080 0.38 and 0.32 microns/minute respectively). When compared with MCF7 cells, HT1080 and MDA-MB-231 cells moved significantly faster and further in both collagen concentrations (significant at $p \leq 0.0001$ for all comparisons, Figure 3.5 and Appendix B.6).

In summary, cells from three different cancer cell lines showed different cell morphology and migration characteristics when each was compared in two different 3D collagen matrix concentrations. Cells typically moved further and faster in the lower density collagen matrix and HT1080 cells were significantly more elongated in the lower density matrix.

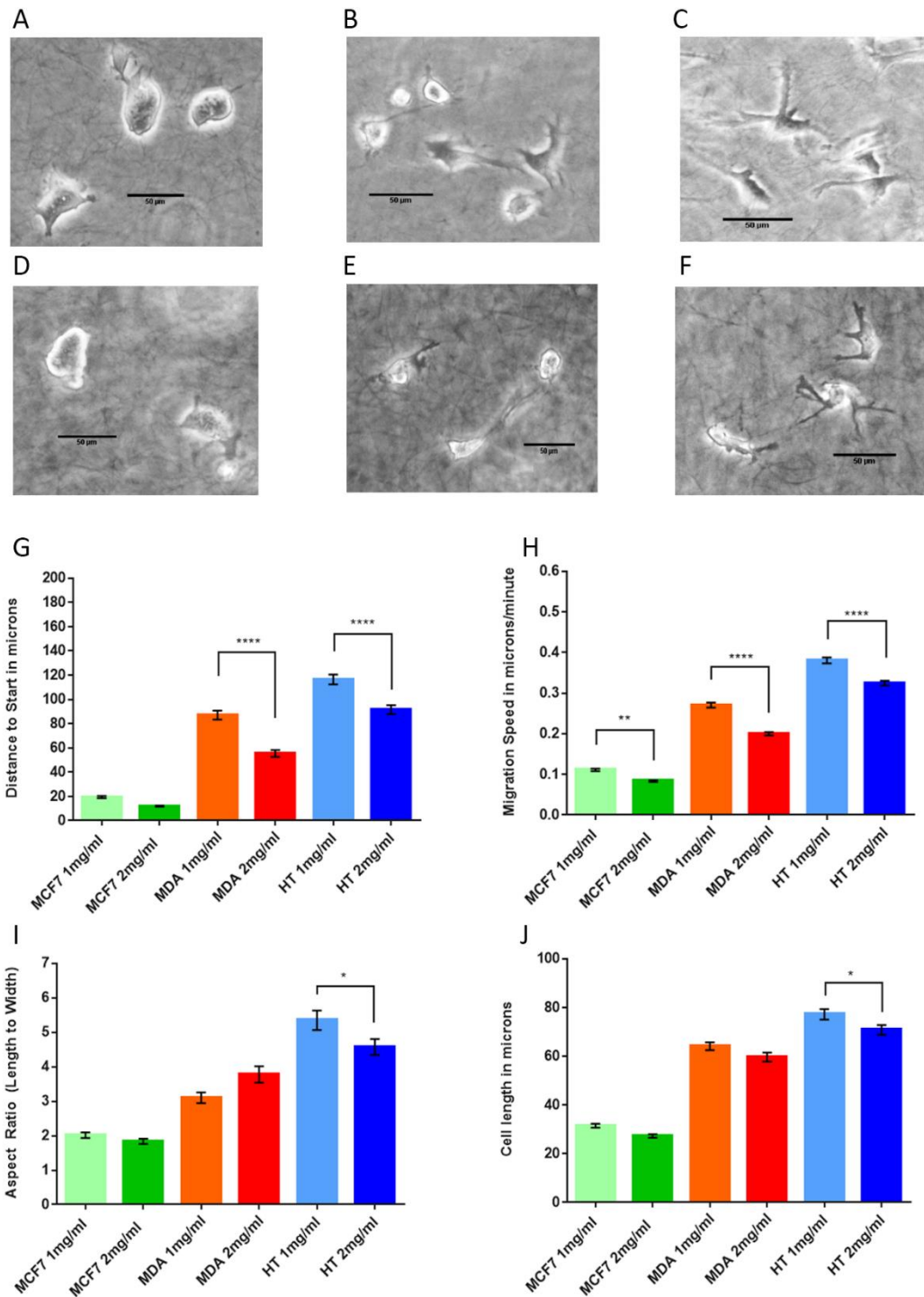


Figure 3.5, Cell migration in collagen. Cell migration in 1 and 2mg/ml collagen for MCF7, MDA-MB-231 and HT1080 cells was tracked over a 21 hour period (images taken at 10 minute intervals). **A-C** shows cell morphology in 1mg/ml collagen and **D-G** in 2mg/ml collagen MCF7 (**A, D**), MDA-MB-231 (**B, F**) and HT1080 (**C, G**). Graphs: **G** shows the 'distance from start' for each cell line and **H** shows the speed of migration in 1 and 2mg/ml collagen. Cell morphology was quantified using aspect ratio: **I**, and this is compared with the cell length for each cell type **J**. 100 cells were measured for each cell line and this repeated 3 times. A two-way ANOVA with Tukey's test for multiple comparisons was used to investigate whether differences were significant. Error bars show standard error of the mean. Significance is shown: ** $p \leq 0.01$, *** $p \leq 0.001$, **** $p \leq 0.0001$ (Full statistical details for each test are shown in Appendix B.6). Scale bars on all images = 50 μ m.

3.3.3. Does fibronectin affect cell migration when added to a 3D collagen matrix?

On a 2D coated surface, MDA-MB-231 and HT1080 cell migration was significantly faster and further on fibronectin compared with collagen. As fibronectin is an important and frequent constituent of the extra cellular matrix, type 1 collagen was augmented with fibronectin to provide cells with a more complex and biologically relevant matrix. However, when MDA-MB-231 cells were set in collagen at 1mg/ml and 2mg/ml with/without fibronectin at 5 or 10 $\mu\text{g/ml}$, their morphology appeared similar (Figure 3.6 A-F for n1-3) and when cell length and aspect ratio were quantified, there was no significant difference (two-way ANOVA and Tukey's test) in the measurements across the different matrix environments (Figure 3.6 G, H). Indicative results for HT1080 cells taken from one experiment using the same six environmental contexts (30 cells measured for each context), also showed similar morphology in each context (Figure 3.7 A-F) and no significant difference was found for aspect ratio between contexts (Figure 3.7 G). However, there was a significant difference in cell length, cells being longer on average at the lower collagen concentration (mean values: 1mg/ml =90.67 μm , 2mg/ml=61.47 μm , Figure 3.7 H). In 2mg/ml collagen with 10 $\mu\text{g/ml}$ fibronectin, HT1080 cells were also significantly longer (mean length= 61.47 μm) than when in the 2mg/ml collagen only matrix (mean length= 77.63 μm). The difference in cell length but not in aspect ratio suggests that some cells were also wider or more spread thus reducing the aspect ratio so that it was similar in all contexts.

Cell migration distance, both for 'track length' and 'distance from start' suggested that there was no difference when fibronectin was added to either collagen concentration, the only significant differences being between the 1mg/ml and 2mg/ml contexts with or without fibronectin (Figure 3.8 A,B). A similar trend for both 'track length' and 'distance from start'

was also evident, with cells moving $\frac{1}{3}$ to $\frac{1}{4}$ of their track length from their starting position during the 21 hour period. A similar pattern was seen for HT1080 cells for collagen only and collagen with 5 $\mu\text{g}/\text{ml}$ fibronectin. There was great variation in the 1mg/ml collagen with 10 $\mu\text{g}/\text{ml}$ fibronectin so the difference was not significant (Figure 3.8 C). A comparison of cell migration between cell lines in each context suggested that MDA-MB-231 cells moved further in the lower concentration collagen without or with 5 $\mu\text{g}/\text{ml}$ fibronectin (Figure 3.8 E). Migration speed for both cell lines varied significantly between collagen matrix densities but not between collagen and fibronectin settings (Figure 3.8 D-F).

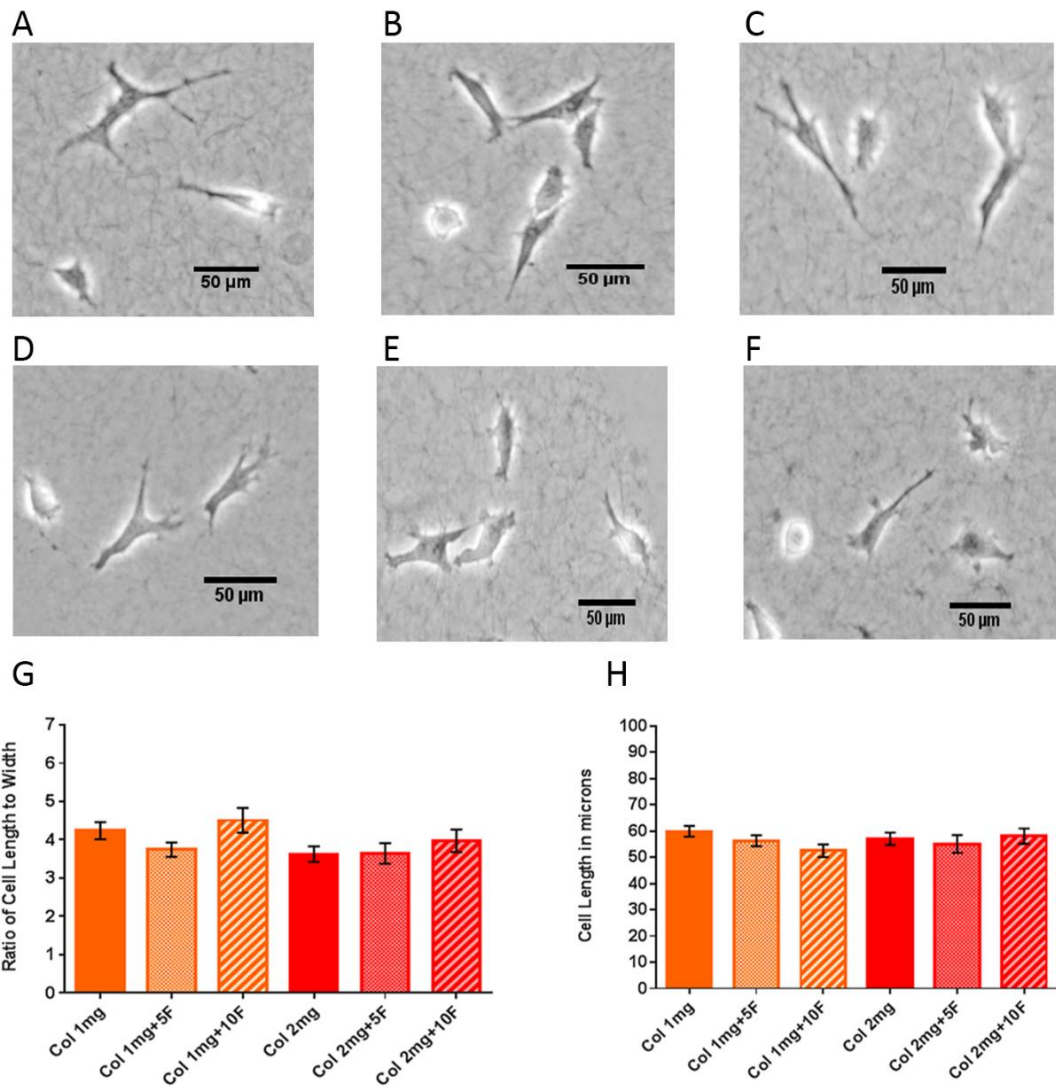


Figure 3.6, MDA-MB-231 cell migration in collagen and collagen with fibronectin. Cells were set in 1mg/ml collagen (Col 1mg) or 2 mg/ml collagen (Col 2mg) or collagen at 1 or 2mg/ml with either 5 or 10µg/ml fibronectin (Col 1mg+5F, Col 1mg+10F and Col 2mg+5F, Col 2mg+10F). **A-C** show cell morphology in 1mg/ml collagen (**A**), Col 1mg+5F (**B**) and Col 1mg+10F (**C**) and in 2mg/ml collagen (**D**), Col 2mg+5F (**E**), Col 2mg+10F (**F**). Cell morphology was quantified via aspect ratio (**G**) and cell length in (**H**) for 30 cells in each matrix type, repeated three times (n1-3). A two-way ANOVA with Tukey's test for multiple comparisons suggested that there is no significant difference in either aspect ratio or cell length between any of the matrices. Error bars show standard error of the mean. (Full details at Appendix B.7.) Scale bars on all images = 50µm.

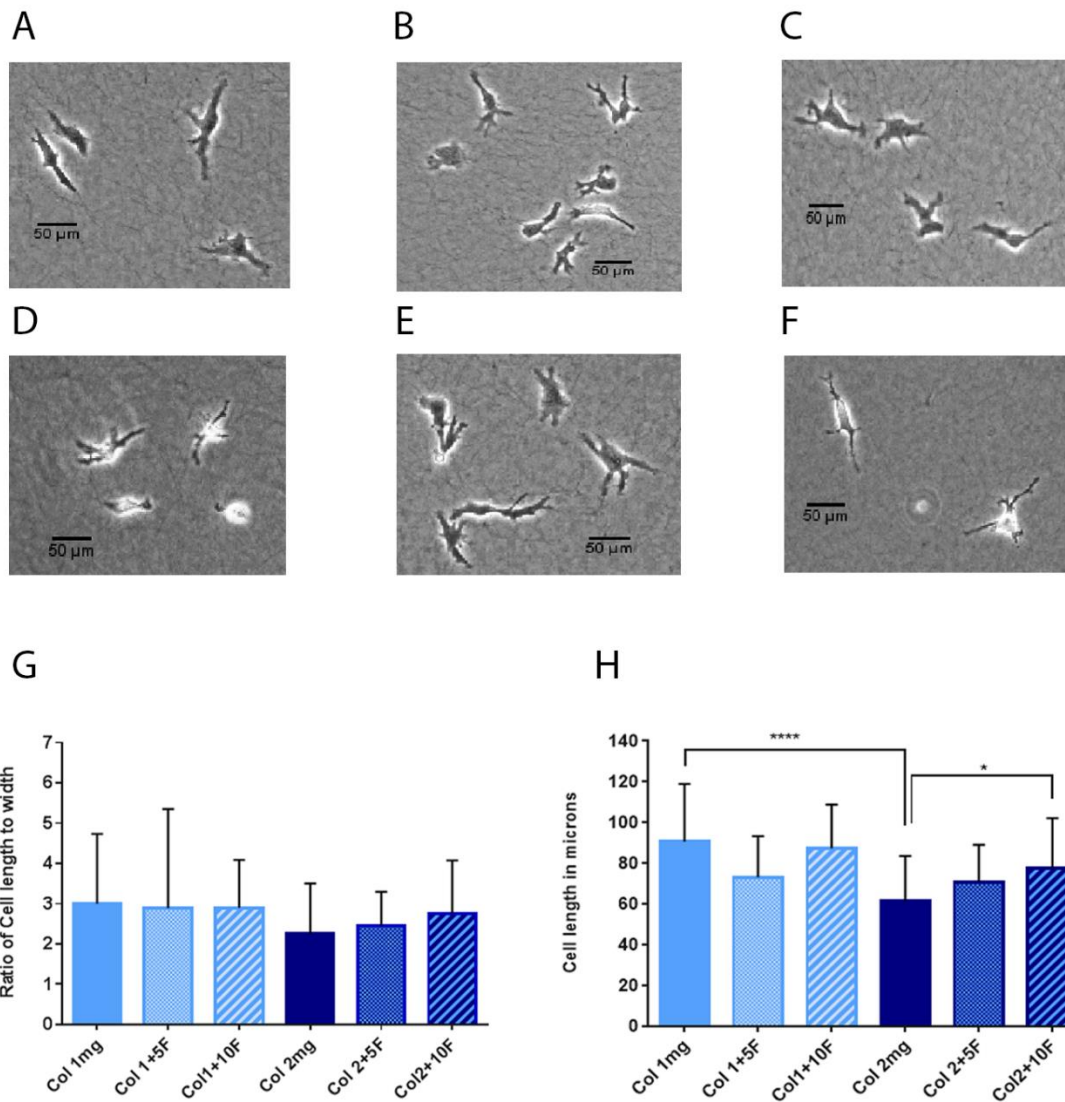


Figure 3.7, HT1080 cell migration in collagen and collagen with fibronectin. Cells were set in 1mg/ml collagen (Col 1mg) or 2 mg/ml collagen (Col 2mg) or collagen at 1 or 2mg/ml with either 5 or 10 μ g/ml fibronectin (Col 1mg+5F, Col 1mg+10F and Col 2mg+5F, Col 2mg+10F). **A-C** show cell morphology in 1mg/ml collagen (**A**), Col 1mg+5F (**B**) and Col 1mg+10F (**C**) and in 2mg/ml collagen (**D**), Col 2mg+5F (**E**), Col 2mg+10F (**F**). Cell morphology was quantified via aspect ratio (**G**) and cell length in (**H**) for 30 cells in each matrix type in one experiment set up for comparison with MDA-MB-231 cells. A two-way ANOVA with Tukey's test for multiple comparisons suggested that there was no significant difference in aspect ratio but that cell length did vary significantly between collagen concentrations. Error bars show standard deviation. (Full details at Appendix B.7.) Scale bars on all images = 50 μ m.

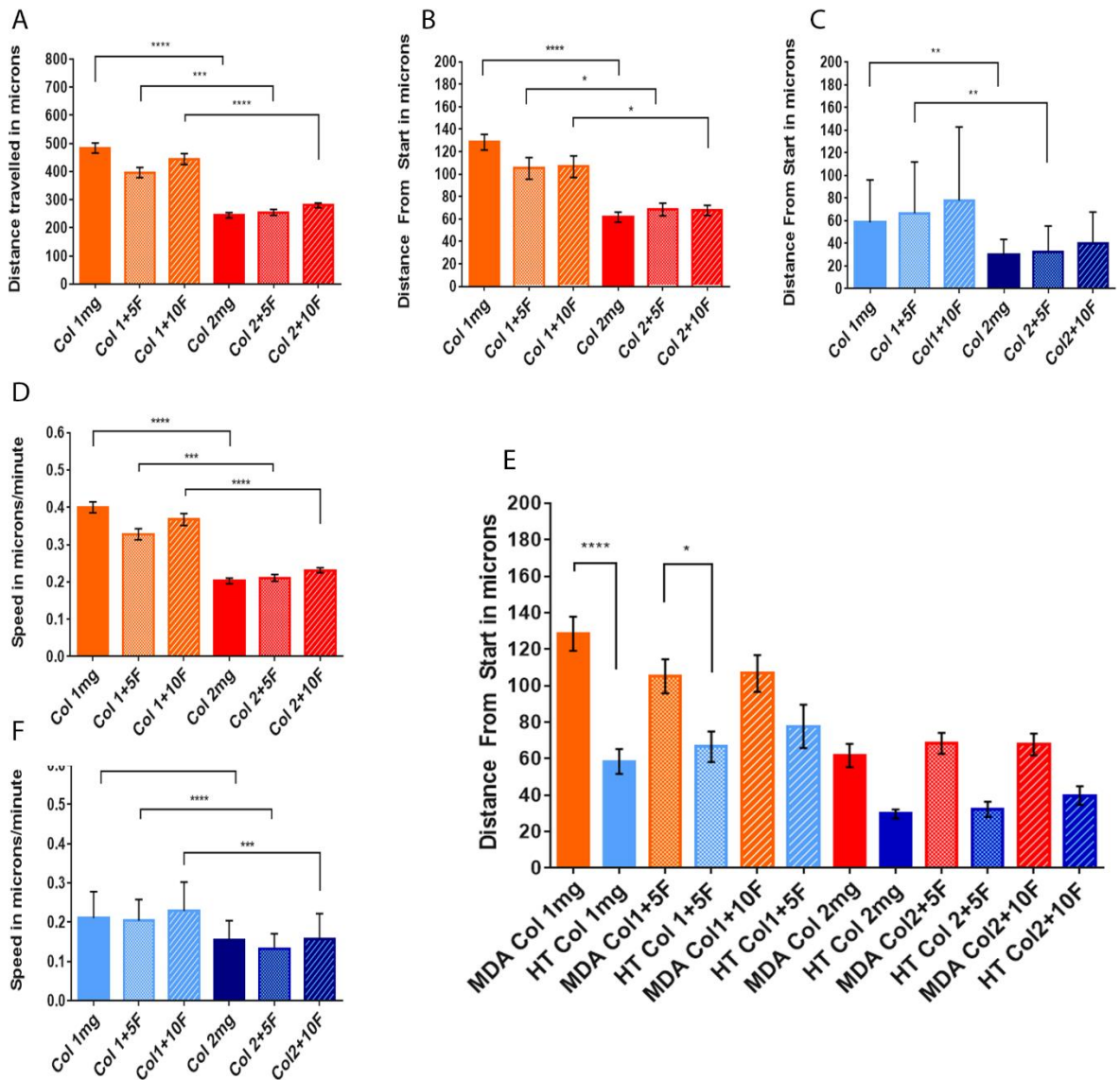


Figure 3.8, Cell migration tracked in collagen and collagen with fibronectin. Cells were set in 1mg/ml collagen (Col 1mg) or 2 mg/ml collagen (Col 2mg) or collagen at 1 or 2mg/ml with either 5 or 10µg/ml fibronectin (Col 1mg+5F, Col 1mg+10F and Col 2mg+5F, Col 2mg+10F). 30 cells were tracked for each condition/ cell type over a 21 hour period with images at 10 minute intervals. The experiment was replicated three times for MDA-MB-231 cells (MDA) and once for HT-1080 cells (HT). Graph **A** shows ‘track length’ for MDA-MB-231 cells migrating in each matrix type and **B** the distance from start (error bars show standard error of the mean for n1-3, 30 cells for each replicate). A two-way ANOVA with Tukey’s test was used to test significance of differences for MDA-MB-231 cells. Graph **C** shows cell migration for HT1080 cells for 30 cells in one experiment (error bars show standard deviation) A Kruskal-Wallis ANOVA with Dunn’s test for multiple comparisons was used. For both cell lines a significant difference for cells migrating between different collagen concentrations was evident. In **E** cell migration distance from start is compared for each cell line by matrix type using a Kruskal-Wallis ANOVA with Dunn’s test for multiple comparisons. Graphs **D** and **F** show cell migration speed for MDA-MB-231 and HT1080 cells respectively (Full details at Appendix B.7.).

3.3.4. Fibrillar structure of the 3D collagen matrix

To examine further the properties of the 3D environments being used, the matrix contexts were visualised using reflectance microscopy. Figure 3.9 A shows collagen at 2mg/ml which appears disorganised with many short fibres at different orientations. Figure 3.9 B shows 2mg/ml collagen with 10µg/ml fibronectin which appears to be denser, with shorter fibres. Despite these visual differences in the matrix, it seems that adding fibronectin to collagen did not impede cell migration nor significantly change the cell morphology for MDA-MB-231 cells and indicative results for HT1080 cells suggested a similar pattern of behaviour may be evident for this cell line.

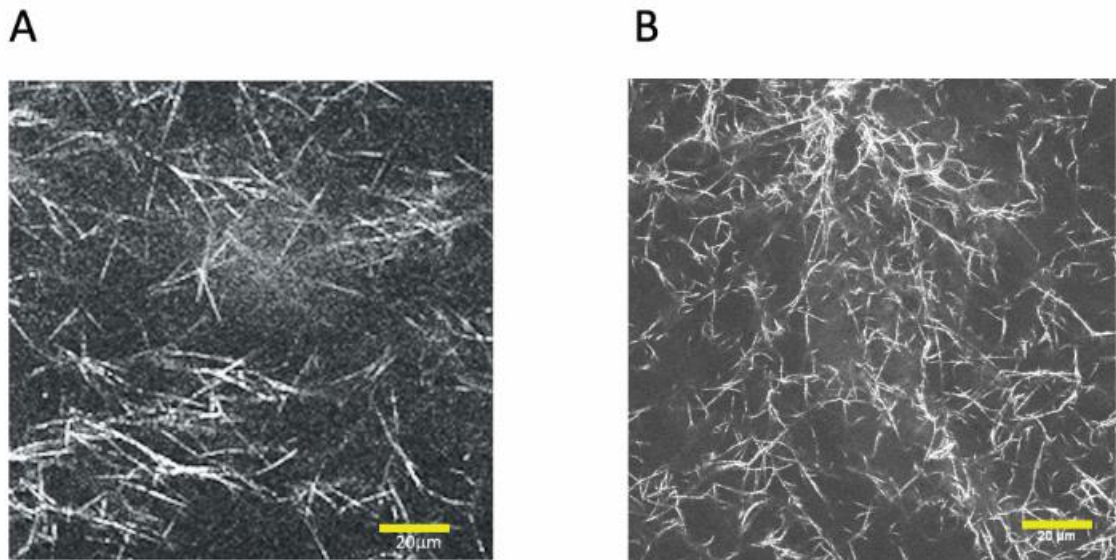


Figure 3.9 Collagen matrix structure determined by reflectance microscopy. A 2mg/ml collagen, **B** 2mg/ml collagen with 10µg/ml fibronectin. Images taken using Leica TCS SP2 using 488 argon laser and Aplanachromat 60x oil immersion lens. Scale bars = 20µm.

3.3.5. Compressing collagen to increase matrix stiffness and elasticity

To provide a stiffer more biologically relevant environment a compressed collagen assay was used (Jones et al, 2012). MDA-MB-231 cells set into compressed collagen (CC) moved and divided, gradually populating the compressed collagen over a number of days (Figure 3.10). Whilst a few cells emerged into the lower concentration collagen base (L) at CC borders, the majority of cells remained within the higher density collagen until it was highly populated (Figure 3.10 C-F). When cells did emerge, they moved individually and many moved along borders and returned to the denser CC (Figure 3.10 A, E, F). Cells were both elongated/mesenchymal and rounded in the CC environment (Figure 3.10 A, B). Once the CC was well populated, some cells at border zones were seen to emerge in a rounded morphology, budding out and moving into the lower density collagen (Figure 3.11 A-C and E). Some cells however, seemed to move away in a collective manner, following each other along tracks (Figure 3.11 D). To further investigate and visualise cell behaviour at compressed collagen borders, lentiviral GFP+ transduced HT1080 cells (preparation: section 2.3.2; testing: section 4.32 and figure 4.14) were seeded onto compressed collagen and set into 1mg/ml collagen. Many cells with rounded morphology could be seen at the CC borders as well as mesenchymal/ elongated cells (Figure 3.12 A-C). Reflectance microscopy indicated a denser structure for CC with collagen fibres more aligned (Figure 3.12 D, compared with Figure 3.9 A).

This assay showed that colonisation of a stiffer matrix appeared to be more important than migration away from it. Cells on and in the stiffer compressed collagen adopted both elongated and spherical morphologies and cell morphology. Cell behaviour at border zones

showed distinctive features different to that seen in either the higher or lower density collagen matrix and warranted further investigation.

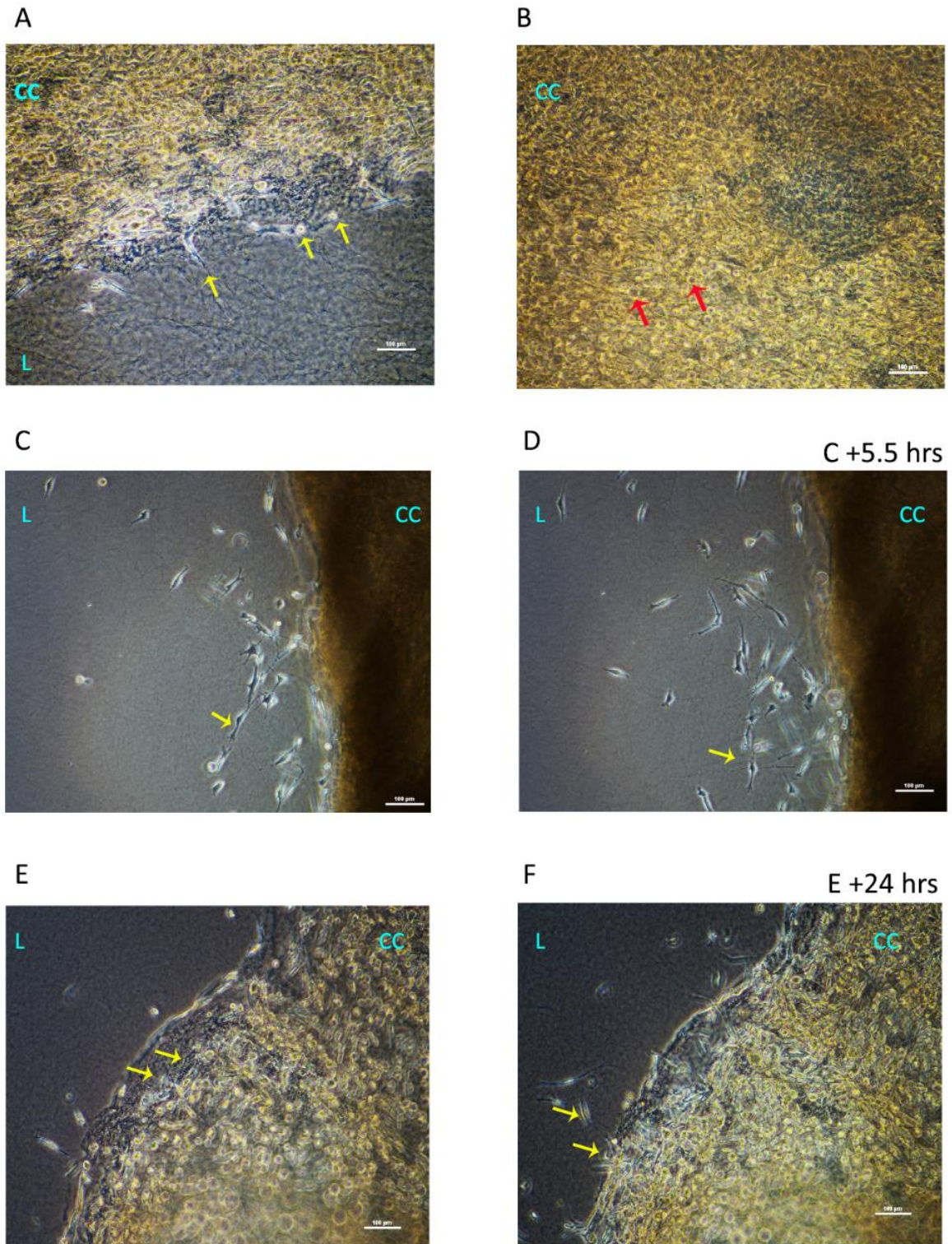


Figure 3.10, Compressed collagen populated with MDA-MB-231 cells. **A** Cells starting to move out (yellow arrows) into 1mg/ml collagen (L) from compressed collagen environment (CC). **B** Cells populate and constantly move within the compressed collagen and many are rounded (red arrows). **C, D** cell migration away from the compressed collagen – cells form chains but move individually indicated by yellow arrows (D= C+ 5 ½ hours). **E, F** cells populate the compressed collagen but few move out into 1mg/ml collagen indicated by yellow arrows (E=+24 hours after set-up and F=48 hours after set-up at same location). Scale bars = 100µm.

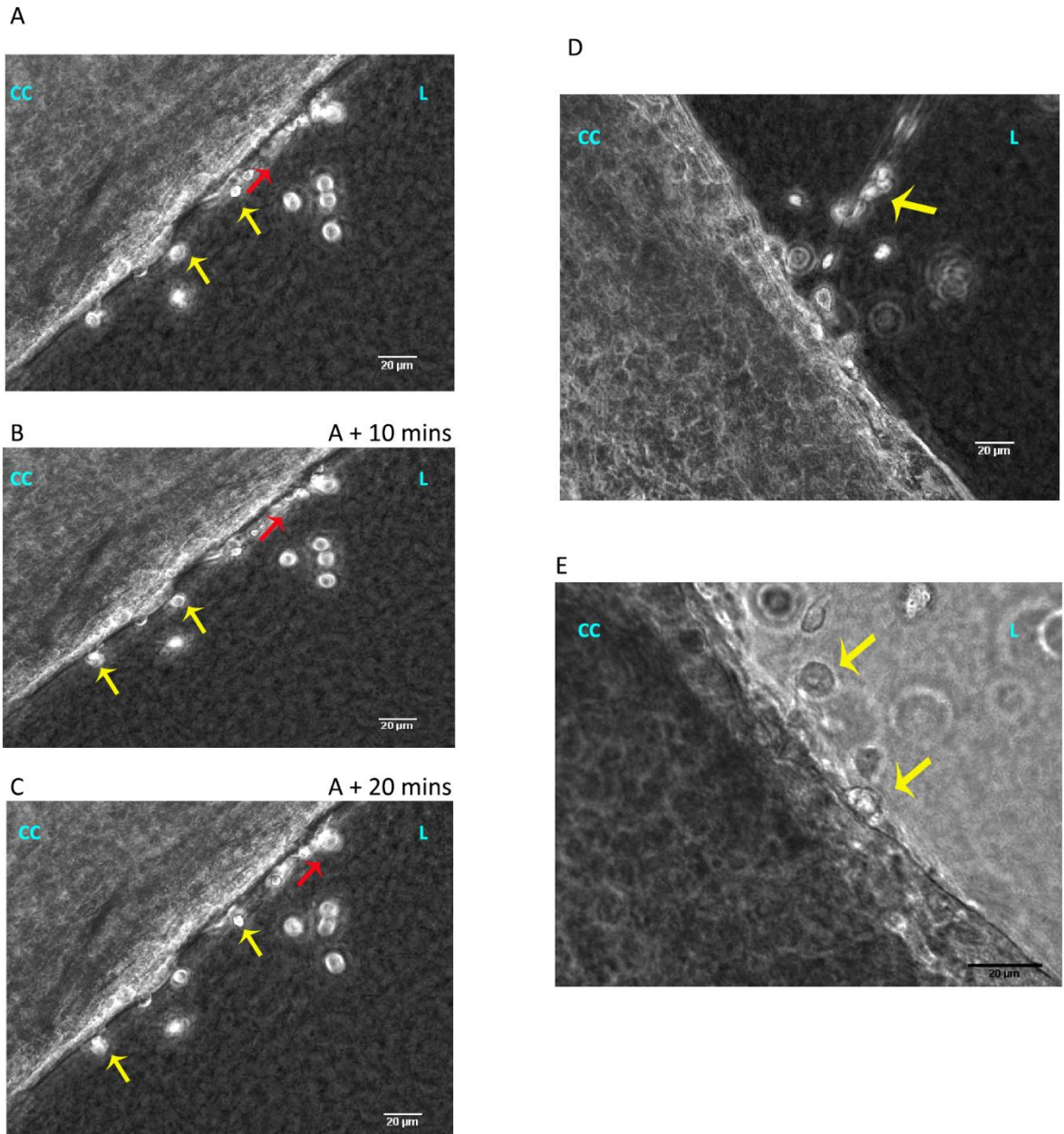


Figure 3.11, MDA-MB-231 cells leaving compressed collagen are rounded. Cells appeared to bud out from the compressed collagen (CC) into the surrounding 1mg/ml collagen (L). **A-C** shows a sequence in which rounded cells move out into 1mg/ml collagen (yellow arrows) or along the compressed collagen border (red arrows). **D** shows rounded cells moving out in a group along a track like pathway (yellow arrows). **E** shows rounded cells leaving compressed collagen close up (yellow arrows). Scale bars = 20μm.

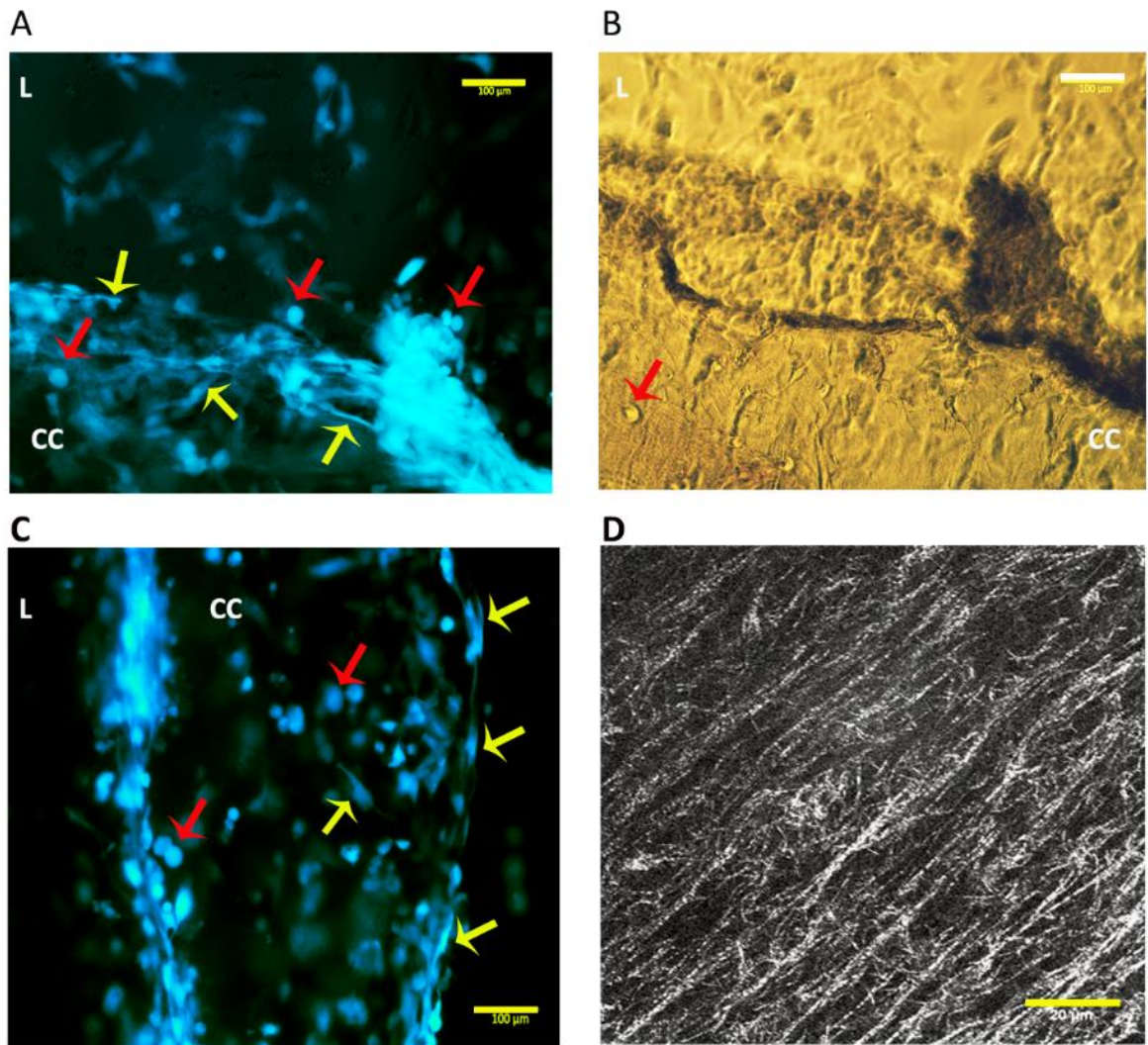


Figure 3.12 Cell morphology and structure of compressed collagen. HT1080 GFP+ cells seeded onto compressed collagen (CC) showed mixed morphology as they colonised the matrix. **A, C** Fluorescent HT1080 cells adopted a rounded morphology (red arrows) and elongated/mesenchymal morphology (yellow arrows) when colonising the compressed collagen. **B** shows a bright field image for the same view as **A**. **D** shows a reflectance image of the compressed collagen structure in which fibres appear to be more aligned and densely packed than in uncompressed collagen. A-C were imaged using Zeiss Axio Vert.A1 epifluorescence microscope. D was imaged using Leica TCS SP2. Lower density collagen base (L). For A-C, scale bars = 100 μ m. For D, scale bar = 20 μ m.

3.3.6. Cell migration from 2D to 3D – can the context be simplified?

It was clear from observation of cells moving between CC and the 1mg/ml collagen base, that cell behaviour at borders may be different from that within either a 3D matrix or on a 2D coating. To investigate this further, the novel CC was adapted to provide a 2D/3D assay (Figure 3.2) using an uncompressed collagen matrix which provided border zones for cells to exploit or invade (Figure 3.13 A,B). This allowed cell behaviour and morphology to be observed and quantified in three distinct regions: 2D, 3D and border zones, as well as their transition between them. Both MDA-MB-231 and HT1080 cells were observed in this assay and when quantified over a period of twelve hours (n1-3, 10 cells for each region per experiment), significant differences in cell speed were observed for cells migrating in 2D and 3D and between border zones and 3D collagen for both cell lines (Figure 3.13 C, D). MDA-MB-231 cells had mean values of 0.53µm/minute in 2D, 0.65 µm/minute at border zones and 0.29 µm/minute on the 3D collagen matrix. HT1080 cells were slower moving and had mean values: of 0.25µm/minute in 2D, 0.39 µm/minute at border zones and 0.13 µm/minute on the 3D collagen matrix. For HT1080 cells there was also a significant difference in migration speed between border zones and 3D, with cells moving three times as fast at border zones (means: border = 0.39 µm/minute, 3D= 0.13 µm/minute, difference significant at the $p \leq 0.0001$ level.) MDA-MB-231 cells moved more quickly on 2D/plastic and at border zones than they did on 3D collagen.

These data not only demonstrated cell migration differences between 2D and 3D environments but also that environmental features such as border zones are important for cell migration, with cells using border zones as migration tracks to achieve effectively 1D migration at significantly faster speeds. Cells were also observed transitioning between the

2D and 3D environments but the speed and dynamics for this needed more careful quantification and were not analysed and included as part of this experiment.

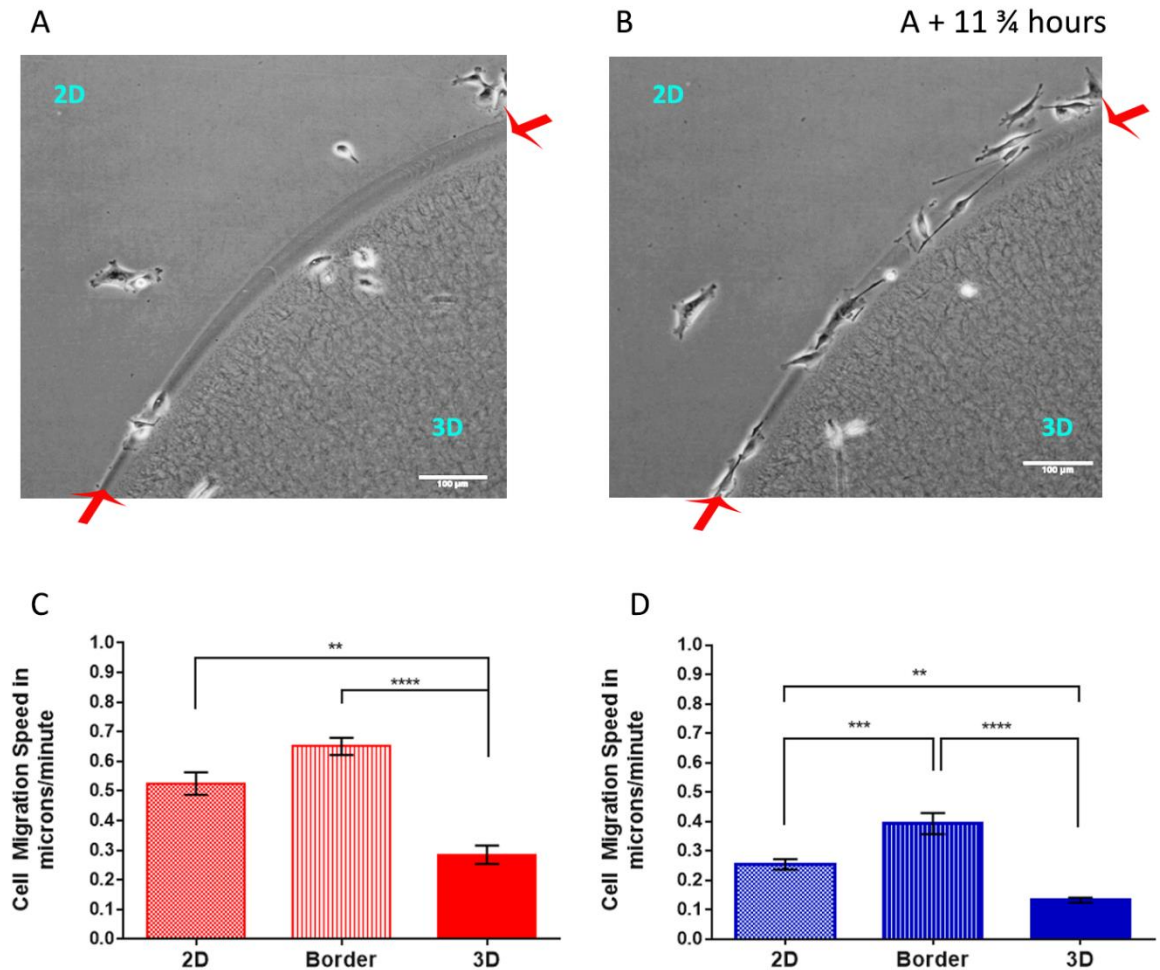


Figure 3.13, MDA-MD-231 and HT1080 cells move faster at collagen borders. MDA-MB-231 cells colonized and used border zones as tracks for cell migration **A, B**. Cells moving on plastic (2D), at borders (red arrows) and on collagen (3D) were tracked for a 12 hour period and migration speed compared for each region. 10 cells migrating in each region were tracked for three separate experiments (n1-3) for MDA-MB-231 cells **C** and HT1080 cells **D**. A two-way ANOVA was conducted with Tukey's test for multiple comparisons. Error bars show standard error of the mean. (Full details at Appendix B.8.) Scale bars = 100µm.

3.3.7. Cell invasion at border zones

Cell invasion could be observed closely at border zones (Figure 3.14) either in the live environment (Figure 3.14 A) or fixed and stained for protein expression (Figure 3.14 B, C). This simple assay allowed cells to be observed simultaneously interacting with different surfaces of both two and three dimensional matrices as well as giving the opportunity to observe behaviour at border zones such as invasion.

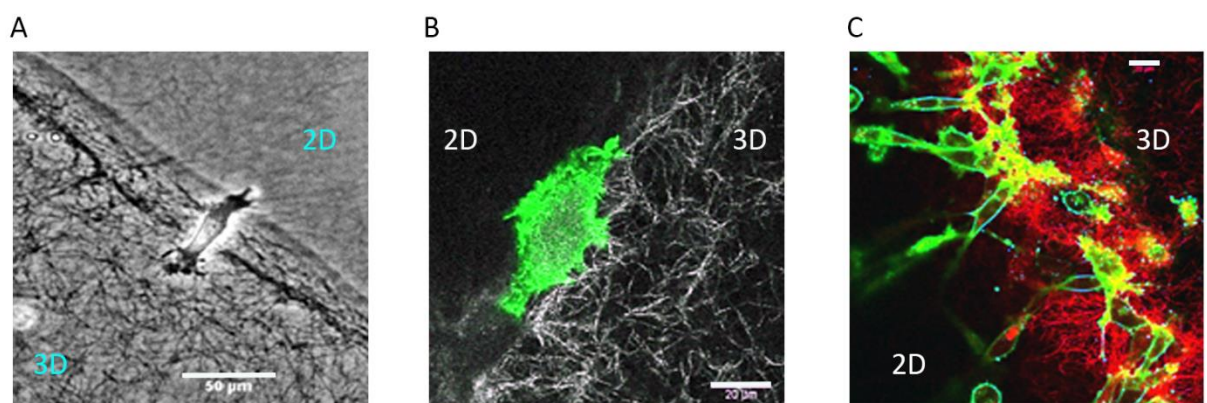


Figure 3.14, Cell invasion at collagen borders. An HT1080 cell migrating from 2D to 3D collagen matrix pushes its way into the gaps between collagen fibres, time-lapse phase contrast image taken from a sequence, Nikon TiE, **A**. An HT1080 GFP+ cell invading a 2mg/ml collagen matrix – confocal imaging, Leica SP2. Fluorescence and reflectance images are overlaid, **B**. MDA-MB-231 myristoylated GFP+ cells invading at a 2mg/ml collagen border, **C**. Confocal imaging using Leica TCS SP2. A, scale bar = 50μm; B and C, scale bars = 20μm.

3.4. Discussion

Tissues are complex, comprising multiple cell types in a highly structured dynamic matrix environment (Nelson and Bissell 2006). A successful *in vitro* model must provide a context in which cells show the range of morphologies and behaviours observed *in vivo*. Simple approaches to modelling such as coating tissue culture surfaces with ECM components have provided a basis for the investigation of metastasis *in vitro* but cells adhering to and moving over these surfaces are known to behave atypically compared to their 3D tissue context (Doyle et al. 2013).

Extracellular matrix components used to create 2D and 3D contexts have resulted in interesting observations relating to cell behaviour and matrix interactions but understanding the relevance compared to the live context is critical if results are to be interpreted and extrapolated in a meaningful way (Hickman et al. 2014, Pampaloni et al. 2007). Collagen type 1 and fibronectin are both important constituents of the ECM and have been found in high proportions in the matrix surrounding some tumours (Lu et al. 2012, Provenzano et al. 2006, Provenzano et al. 2008). Matrigel, a basement membrane extract produced from a murine tumour microenvironment containing collagen IV, laminin, heparin sulfate proteoglycans, nidogen and growth factors, (Hughes et al. 2010) has been used to model basement membrane as both a 2D and 3D model. There is also evidence that basement membrane is remodelled within the tumour microenvironment (Cox and Epler 2011). These three components were used as a starting point to coat 2D surfaces in this project. Whilst experiments reported here showed differences in cell behaviour on 2D coated surfaces between surface type for two different cancer cell lines, cell morphology on collagen and fibronectin was elongated/mesenchymal when compared to *in vivo* findings (Wang et al. 2002). Cell migration over fibronectin was faster than for collagen. There is evidence that

although focal adhesions are expressed by cells adhering on both surface types, that focal adhesions on fibronectin are non-fibrillar and therefore facilitate a faster migration with lower adhesion (Cukierman et al. 2001). Whereas cells on fibronectin and collagen moved individually over the matrix, cells seeded onto Matrigel in these experiments moved towards each other forming groups and chains and appeared to contract the matrix. This behaviour on Matrigel has been reported by other researchers (Gest et al. 2013, Yu and Machesky 2012) and cells are known to pull on matrix fibres causing contraction (Doyle et al. 2015, Foster et al. 2015). Matrigel is a basal lamina derived matrix comprising a number of components including growth factors which will have influenced cell behaviour on this coating type (Hughes et al. 2010). Cell proliferation and differentiation in response to the collagen type IV, growth factors and other constituents of the Matrigel may well have contributed to the behaviours observed with cells forming groups and potentially starting to interact and form tissue structures (Uemura et al. 2010). These results clearly showed that each cell type responded differentially according to the 2D tissue component coating and that these behaviours were similar when comparing the two different cell lines used. MDA-MB-231 cells were sourced from a metastatic lesion in the lung but are epithelial in origin so could be classed as metastatic and adapted to invade a new niche environment. HT1080 cells however were taken from a primary tumour and although fibroblastic in morphology and behaviour have not necessarily gained the range of behaviours that a metastasizing cell might display. The fact that cells from both cell lines displayed similar behaviours on all three coatings suggests that it was the 2D ECM context that drove the cell behaviour. Whilst differences in cell behaviour were observed, the 2D coating context lacked the structure, support and complexity provided by ECM and therefore how relevant to the *in vivo* environment could these cell behaviours be deemed to be? On fibronectin and collagen,

cells were elongated with no amoeboid morphology or migration mode observed (Friedl and Wolf 2003). On Matrigel however, cells adopted a largely ovoid or amoeboid morphology. Adhesive strength on softer matrices has been associated with low adhesion modes of migration such as amoeboid migration, yet matrix contraction has been associated with stronger matrix adhesion (Discher et al. 2005). This begs the question: what behaviours were elicited in these cells by the matrix conditions? Were cells migrating, colonising or adapting to enable their survival in an alien environment? In the case of adaptation, was this behaviour closer to niche colonisation than solely about cell transition over a surface? To investigate these questions, the properties of this environment were enhanced in an incremental way, with cells encapsulated into a simple 3D collagen or collagen/fibronectin matrix.

In three dimensions, collagen density has been shown to affect cell migration, with different migration strategies adopted according to fibrillar structure and matrix porosity (Wolf et al. 2009, Wolf et al. 2013). ECM components collagen type 1 and fibronectin were used here to construct a simple 3D matrix in which to study cell behaviour. MCF7 breast cancer cells were used as a comparison to MDA-MB-231 and HT1080 cells as they tend to divide and remain in groups, rather than to migrate. Results from these experiments showed a clear difference in both migration speed and distance for the migratory cell lines (HT1080 and MDA-MB-231) with cells moving more slowly within the denser collagen. Both HT1080 and MDA-MB-231 cells adopted an elongated/mesenchymal morphology. MCF7 cells however had a more ovoid morphology when encapsulated and as expected remained in groups rather than migrating through the collagen matrix. The addition of fibronectin (for MDA-MB-231 and HT1080 cells) however did not make a significant difference for either speed or distance, despite the fact that the matrix appeared to be denser. If cells were able to use the

same migration mode in 3D as on the 2D fibronectin coating then perhaps this isn't surprising, as matrix impedance could have been countered by the ability of cells to bind to fibres and move through the matrix (Cukierman et al. 2001). Slower migration in 3D collagen matrices could also have been related to the need for cells to adapt to their new environment (Friedl et al. 2012). Encapsulated cells had been cultured in 2D flasks so could be expected to be adapted to their 2D growth environment. The enzymatic cleavage of adhesive proteins during cell detachment prior to encapsulation would also affect the initial ability of cells to adhere and migrate.

The introduction of an intrinsically amoeboid cell line to the models developed, such as melanoma cells A375M2, would have allowed the interaction of cells within the different contexts to have been characterized still further. The plasticity of these highly metastatic cells has been demonstrated *in vivo*, cells switching from amoeboid to mesenchymal morphology within tumours, A375M2 cells using the mesenchymal mode to infiltrate densely packed tumour tissue or fast amoeboid movement at tumour borders (Pinner and Sahai 2008, Sanz-Moreno et al. 2008). In the models presented here, it would be expected that A375M2 cells would adopt an amoeboid morphology at the interfaces and border zones presented in the 2D/3D assay and compressed collagen assay at the border zones or when seeded onto a thick layer of collagen (Calvo et al. 2011). Within a 3D matrix environment, the A375M2 cells have been shown to secrete matrix metalloproteases (MMP-9 and MMP-13) which would allow them to migrate within the 3D collagen and compressed collagen matrix environment (Orgaz et al. 2014). Where cells became densely populated, A375M2 might be expected to switch to a mesenchymal morphology to move between gaps and into new spaces, for example in the compressed collagen assay once the matrix was well colonized.

The 3D matrix as a model facilitated a longer experimental run-time, the depth and context providing cells with the opportunity to colonise and interact with each other and with the matrix in multiple orientations, the added dimension providing a much greater surface area for this interaction. In comparison, cells in a 2D environment typically grow as a monolayer and when fully confluent become quiescent or die. It takes time for cells to colonise a 3D matrix and even in these simple experiments, cells could be left for 2-3 days whilst observation of events took place. This temporal issue is an important one, with metastatic initiation difficult to capture due to its spontaneity. Some cell behaviours may take time to develop, for example the collective invasion of MCF7 cells would require seeded cells to form cell-cell junctions and tissue to become polarised before invasion commenced (Cheung et al. 2013, Gest et al. 2013).

The 3D collagen with/without fibronectin provided a simple ECM based environment but for each cell line, cell behaviour was restricted to one cell morphology and migration mode. Under the experimental conditions described, the full range of *in vivo* behaviours from amoeboid to mesenchymal and collective cell migration (Table 1.4), to be modelled was not evident. Reflectance images of the 3D matrix indicated that collagen fibres were short and randomly oriented in a loosely packed matrix. As ECM surrounding many tumours is known to become denser and tissue more rigid (Cox and Ertler 2011, Wang et al. 2002), a stiffer more structured ECM model would seem a more relevant environment.

Tissue engineering techniques have been used for some time in an attempt to create biologically relevant contexts for appropriate cell culture and tissue growth for transplant (Edmondson et al. 2014, O'Brien 2011). Stem cells have been seen to differentiate in response to the elasticity of their microenvironment (Engler et al. 2006, Wen et al. 2014).

Indeed when mesenchymal cells were seeded onto 2D gel substrates with varying elasticity values (E, kPa) spindly neuronal phenotypes emerged on a soft matrix (0.1 – 1kPa elasticity), mesenchymal phenotypes on medium matrices (8-17kPa) and spread phenotypes on firm, more rigid matrices of 25-40 kPa (Engler et al. 2006). A more highly organised cytoskeleton has been evident on more rigid 2D surfaces coupled with the upregulation of focal adhesions for cell-substrate adhesion (Wyckoff et al. 2006). Furthermore the traction forces of cells on or in a matrix contribute to the matrix structure and assembly (Kraning-Rush et al. 2011, Lemmon et al. 2008). In recent corneal tissue engineering research, a compressed collagen matrix was constructed and used as a model of the cornea for the differentiation of stem cells into limbal epithelial cells (Jones et al. 2012). When characterised, Jones et al, showed the compressed collagen matrix to be denser and stiffer, with an elastic modulus 100 times greater than the equivalent uncompressed matrix. This tissue engineering approach was adapted and used here as a novel assay in which to observe cell behaviour in relation to metastasis with HT1080 and MDA-MB-231 cells seeded either onto or encapsulated within the compressed collagen (CC). A range of cell morphologies was observed from rounded and amoeboid to elongated/mesenchymal, that is, spanning the range described in the cell migration tuning model (Friedl and Wolf 2009a) and those associated with *in vivo* cell migration (Bravo-Cordero et al. 2012, Condeelis et al. 2001, Gligorijevic et al. 2012, Sahai and Marshall 2003, Wang et al. 2002). Matrix features were observed to play an important role, with cells colonising some areas of the matrix first. Cells also remained within the compressed collagen matrix in preference to migration out into the lower density uncompressed collagen in which the CC was seated. Indeed, cells seen escaping at boundaries frequently moved along the CC edge and re-joined it further along the border rather than move out and away from it. Cells also formed layers at border zones perhaps

using the more rigid edges as a scaffold along which to layer and commence the formation of a basic tissue structure (Berzat and Hall 2010). This engineering approach adapted here, has some similarities to that recently developed in the Condeelis lab, a thin high density fibrillary collagen layer (HDFC) prepared via centrifugation which has been reported to stimulate the production of invadopodia (Artym et al. 2015). The stiffer style matrix (HDFC) was found to stimulate invasive behaviour in a range of cells and so is suitable for the study of metastatic invasion on a 2D surface. The CC used in this work however, has the additional advantage of cell encapsulation so that metastatic events such as niche colonisation can be visualised within a full 3D ECM based environment.

Cell migration in 1D, for example along muscle fibres (Otto et al. 2011) and in tumour invasion (Wang W. et al. 2002) has been seen both *in vivo* and *ex vivo*. Guidance cues have been reported as important both within living tissue and have been observed *in vitro* (Berzat and Hall 2010, Sapudom et al. 2015). Border zones in the results for both the CC and the 2D/3D assay seemed to provide guidance cues, similar to the discrete cell migration paths along which cells orient themselves *in vivo* and as such could be used for the study of cell properties associated with 1D migration and invasion or emergence across border zones (Katz and Lasek 1980, Tsai et al. 2012). Recent research in biomaterials engineering has indeed sought to mimic the properties of tissue boundaries as an important tool for cell research in this field (Sapudom Jiranuwat et al. 2016). Whilst cells in/on CC showed a range of cell migration strategies including rounded cells budding out from CC into lower density collagen, cells in the 2D/3D assay were elongated/mesenchymal and did not show either the range of morphology or migration strategies. Discher et al. (2005) have stressed the importance of the need for variation within a 3D model, natural variation in ECM being a feature of the tissue environment (Bissell and Radisky 2001, Bissell et al. 2002, Lu et al.

2012). There are many additional factors likely to make CC more complex other than its stiffness/elasticity, including nutrient and oxygen availability and the associated gradients which are known to affect cell migration *in vivo* and may be represented in this denser ECM environment (Cox and Eler 2011, Yamada and Cukierman 2007).

In summary, this chapter has demonstrated that whilst simple 2D and 3D models using ECM components are able to support some of the cell behaviours associated with metastasis, only the denser more structured compressed collagen based on tissue engineering techniques came close to representing a suitable 3D structure useful for modelling living ECM. An ECM based *in vivo* model which could be used to observe metastatic cell behaviour would potentially provide a more complex and biologically relevant environment, with the benefits of blood flow for nutrient and gas exchange. Techniques from the *in vitro* work described in this chapter were used and applied to such a model: the chick embryo model, described in the next chapter.

4. Modelling Metastasis *In Vivo*

4.1. Introduction

The developing chick embryo has been used in the study of developmental biology for hundreds of years with early studies using it as a model to understand blood circulation, heart development and heart function (Kain et al. 2014). More recently it has been used as a vertebrate model to study specific processes relating to abnormal development and disease (Deryugina and Quigley 2008b, Ribatti 2014, Ribatti et al. 1996). As a vertebrate model it has the benefit of a short developmental timeline of just 21 days between the start of incubation and the chick hatching.

In the very early stages of development during gastrulation, three germ layers form from which the chick embryo and associated tissues develop, these being: ectoderm, the outer layer; mesoderm, the middle layer and endoderm, the inner layer (Lillie 1919, Romanoff 1967). There is a division in developing tissues between embryonic and extraembryonic layers, the extraembryonic layers functioning to provide nutrition, respiration and excretion of waste products (Romanoff 1967). Membrane folds develop at the interface between the embryo and extraembryonic layers and four distinct extraembryonic membranes are formed: the amnion, chorion, allantois and yolk. The ectoderm and mesodermal layers grow to form the amnion and chorion and the allantois and yolk sac are formed from the endoderm and mesodermal layers. The chorion develops from the blastoderm at the same time as the amnion (the fluid filled sac surrounding and cushioning the embryo) but the chorion lies outside. The allantois, starts to develop on the second day of incubation, gradually spreading over the developing embryo and forming a flattened sac. The mesodermal layer of the allantois which is presented on the outer surface, merges with the

mesodermal layer of the chorion between days 4 and 5 to form the chorioallantoic membrane (CAM) (Romanoff 1960). By day 6 the combined chorioallantoic membrane fuses with the shell membrane to form a mechanism for gas exchange and a portal through which calcium can be imported this being needed for bone growth and development in the chick embryo (Gilbert 2010), Figure 4.1. Vascularisation of the allantois begins within the mesodermal layer around day 4 (Gabrielli and Accili 2010). Between days 5 and 10, a capillary plexus forms within the mesodermal layer. This initially lies just beneath the thin ectodermal layer but then pushes outwards towards the shell so that by day 12 it lies above the ectodermal layer close to the shell membrane to enable efficient gas and nutrient exchange (Gabrielli and Accili 2010, Romanoff 1960). The arterioles and veins however remain within the mesodermal layer. Two arteries and a single vein serve to move blood to and from the CAM to the embryo beneath (Ribatti 2010).

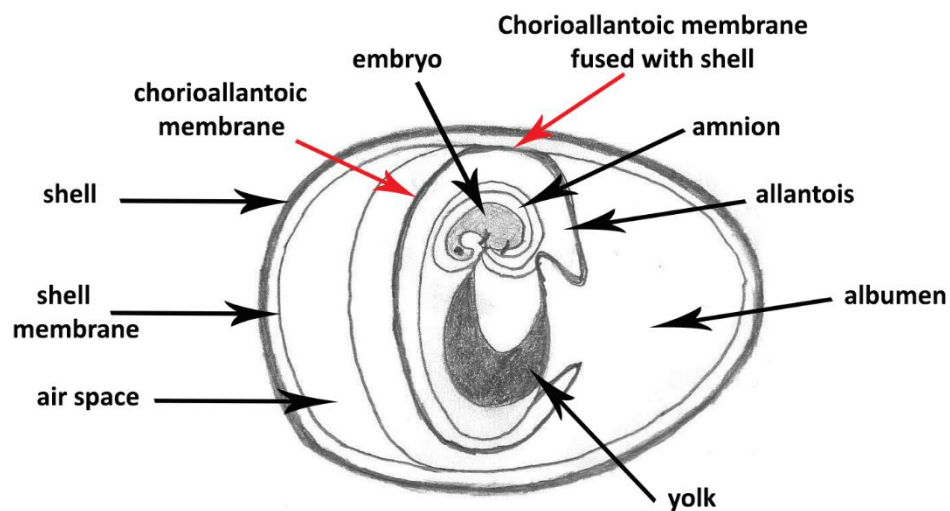


Figure 4.1, *In ovo* development of chick embryo and extra-membranous tissues. The allantois and chorion fuse to form the chorioallantoic layer which spreads over the developing embryo to cover it completely by day 6. (Diagram based on schematic (Valdes et al. 2002)).

A lymphatic network also develops from around day 6 alongside the blood vessels (Romanoff 1960). The chorioallantoic membrane thus comprises three layers, the outer layer derived from ectoderm which fuses with the inside of the porous egg shell, the mesoderm a highly vascularised stromal layer and the endoderm located on the inner surface of the membrane at the interface with yolk sac and amnion (Lillie 1919). The epithelial and stromal components of the chorioallantoic membrane (CAM) of the vertebrate chick also bear many similarities to human epithelia and associated extracellular matrix, the CAM providing an epidermal layer with a stromal compartment beneath comprising: collagen type I, fibronectin and laminin of similar composition to that found in human stroma beneath the epidermal layer (Alberts et al. 2002, Gabrielli and Accili 2010, Lokman et al. 2012). The CAM therefore provides a suitable model which can and has been exploited for the investigation of angiogenesis and metastatic processes (Kain et al. 2014, Ribatti 2010). In particular the main components of ECM: collagen type I, laminin and fibronectin are all major constituents found within the tumour microenvironment (Lokman et al. 2012, Provenzano et al. 2006).

The CAM not only provides a tissue of suitable composition for experimental purposes, but as cell mediated immunity within the chick does not start to develop until the second week of incubation (Jankovic et al. 1977). The immature immune system can thus be exploited for experimentation purposes allowing exogenous cells and tissues to be introduced without rejection (Kain et al. 2014, Ribatti 2010). Cell based immunity within the developing chick develops first within the thymus and bursa and by day eight lymphocytes are evident. By the eleventh day lymphocytes and granulocytes are present in the spleen and granulocytes in the bone marrow of the developing embryo (Jankovic et al. 1977).

Xenografts and explants have been placed on CAM in experiments dating back to the early 20th century, in which mammalian tissues and cells were found to be accepted by the developing CAM (Kain et al. 2014). Early experiments in which rat tumour explants placed on CAM grew successfully until day 18 of incubation (but not in chicks) conducted by Murphy in 1914 (Ribatti 2014) provided evidence that mammalian cells and tissue could be supported in the developing chick model. Cells have also been injected into the CAM vasculature to enable the investigation of the steps of metastasis, in particular, intravasation and extravasation of cancer cells and transit to distal sites (Deryugina and Quigley 2008b, Ribatti 2014).

It has been suggested that the CAM assay provides an easy and inexpensive model for the investigation of all the steps of metastasis (Kain et al. 2014, Ribatti 2014). Whilst the CAM has been used for the study of tumour growth, cellular escape, intravasation and extravasation, it also has great potential for its use in the detailed study of the interactions of cells within the tumour microenvironment. The potential to investigate cell-cell and cell-ECM interactions in detail within CAM using emerging tools and technologies provided the basis for a novel application of the CAM assay in relation to metastasis.

The aim of this part of the project therefore, was to use the CAM assay as a model to explore the interaction of cancer cells with CAM tissue using it as a model for both the tumour microenvironment as cells invaded down through the ECM layers and for colonization of the metastatic niche. The introduction to the CAM of cancer cells originating from both a primary tumour (HT1080 cells) and from metastatic sites (MDA-MB-231 and MCF7 metastatic breast cancer cells) enabled the comparison and contrast of cell morphology and mechanisms employed during invasion, migration and colonization. Using specifically

developed GFP expressing cells of each cell type, different methods of fluorescence microscopy were explored for tracking cancer cells and probing mechanisms of interaction during: cell invasion and migration, tissue interaction and ECM colonization.

4.2. Materials and methods

Fertilized chicken eggs obtained from Henry Stewart and Co. Ltd. were allowed to settle overnight at 19°C following transportation, then placed in a humidified incubator at 37°C (Day 0). Eggs were windowed on Day 2-3 (Figure 4.3 shows timeline) by removing 2-3 ml of the albumen with a syringe through a small hole made at the blunt end of the egg with sharp pointed scissors, then cutting an oval window longitudinally, approximately 3 x 2 cm, using curved scissors. The window was then covered with clear adhesive tape (Figure 4.2 A). Windowed eggs were racked and returned to the humidified incubator until Day 8 (Figure 4.2 B).

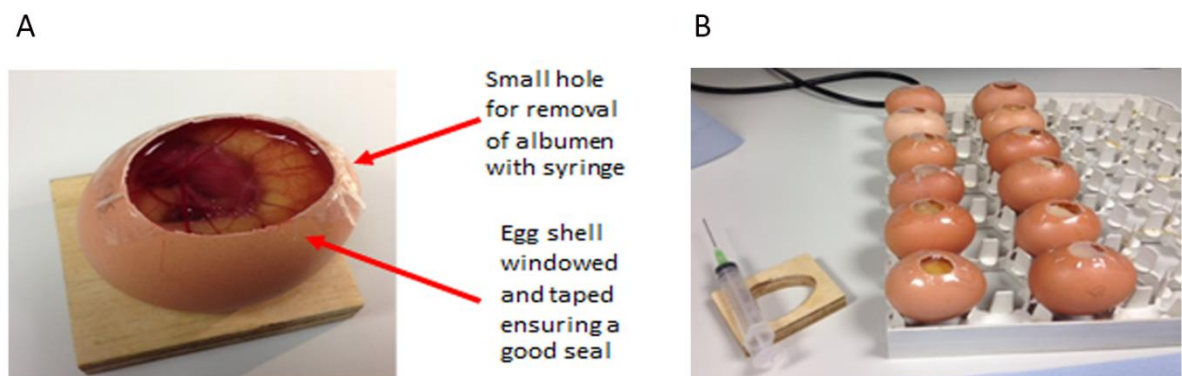


Figure 4.2, Eggs windowed at day 2-3: **A**, a windowed brown egg showing syringe access and window with adhesive tape covering; **B**, windowed brown eggs racked for return to incubator.

Cells from human cancer cell lines were counted using a haemocytometer, suspended in growth medium or in liquid collagen and added to the CAM beneath the windowed area either directly to the CAM surface or to an area which was first injured by scratching the CAM surface with a 0.12mm diameter tungsten dissecting probe (World Precision Instruments). Once on the CAM, cells were kept moist by adding a drop of un-supplemented DMEM (Appendix A) containing 1% Penicillin/Streptomycin (Gibco, Invitrogen).

Human cancer cells were observed *in situ* on the CAM using a stereoscopic dissection microscope (either Leica DC500 or Zeiss Steri SV6). CAMs with seeded cells were harvested for either *ex vivo* microscopy or for fixation on or by Day 14 (Figure 4.3).

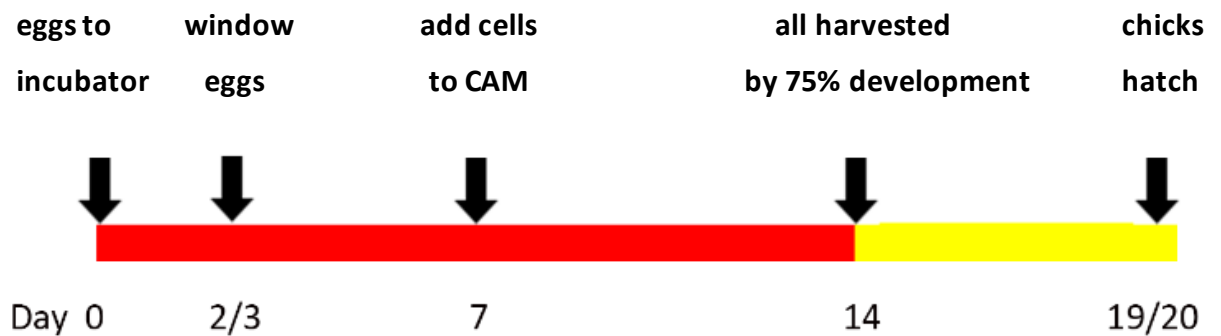


Figure 4.3 Timeline for CAM *in vivo* experiments. Eggs transferred from holding incubator at 19°C to a humidified incubation incubator at 37°C on Day 0. Eggs incubated and chicks harvested within 75% of *in ovo* development.

4.2.1.1. Ink staining of CAM vasculature

Indian ink (Daler Rowney) was mixed at 1:5 concentration in a small dish. Three to four days after cell seeding (10-11 days incubation) the shell was removed from the developing chick, keeping the membranes intact. The chick sternum was opened up and an incision made into the chick embryo's heart. Using a fine glass needle (1.3mm diameter, hand-made) ink was blown gently into the pumping heart through a mouthpiece at the top of fine rubber tube attached to the glass needle. The chick heart pumped the ink through the vasculature of the embryo and the CAM for around twenty minutes. The CAM was harvested and fixed with 4% Paraformaldehyde/PBS.

4.2.2. CAM fixing and staining

Whole CAM was first fixed in 4% paraformaldehyde/PBS for 2 hours then washed in PBS twice and stored in PBS at 4°C until required.

The primary antibodies used were: anti-GFP antibody: GFP Rabbit IgG antibody (A11122 Invitrogen) used at a 1:250 dilution and anti-Ki67 antibody: anti-rabbit (abcam16667) used at a 1:500 dilution. The secondary antibodies used were: anti-rabbit Alexafluor 488 and anti-rabbit Alexafluor 647 (Fisher Scientific) both used at a 1:500 dilution.

Cell stains used were: Phalloidin Atto 565 stain at a 1:250 dilution, added with secondary antibody and DAPI (Sigma) stain added to give a 10µg/ml final concentration.

4.2.2.1. Immuno-staining

CAM was permeabilized and blocked using 10% goat serum in 1% Triton-X 100/PBS overnight at 4°C then washed twice with 0.1% Triton X-100/PBS. Primary antibodies were diluted into blocking solution and samples were incubated for 2-3 days at 4°C. Samples were washed twice for 30 minutes in 0.1% Triton/PBS then secondary antibodies and phalloidin stain were added in block solution and incubated for 2-4 hours in the dark at room temperature. Samples were washed again twice for 30 minutes in 0.1% Triton/PBS and mounted. DAPI was added to a final 30 minute PBS wash. All wash and incubation steps took place on rocker/rollers so that samples were kept in constant motion. A quick PBS wash was carried out before mounting for microscopy or embedding for sectioning.

4.2.2.2. Staining only

Where phalloidin/DAPI only staining was carried out, samples were removed from PBS. Phalloidin was added to 1% Triton-X 100 solution at 1:250 and samples left overnight at 4°C on rollers. CAM tissue samples were washed twice with 0.1% Triton-X 100/PBS for 30

minutes then DAPI added to PBS for a further 30 minute wash. A quick PBS wash was carried out before mounting for microscopy or embedding for sectioning.

4.2.2.3. Mounting tissue

Whole CAM was mounted from PBS onto Superfrost microscope slides using either Vectashield H-1000 (Vectorlabs) or Hydromount (Agar Scientific) as mounting media.

4.2.3. Embedding and sectioning

Whole CAM tissue was rolled up (like a layered tube) before placing it into OCT so that multiple layers could be seen within the same section to maximise the chance of finding GFP+ cells within the section. Fourteen micron sections were made using a Kryostat (section 2.4.1) and mounted onto polylysine coated slides (Polysine slides, Thermo Scientific), allowed to dry and stored at -80°C until required. Further staining was carried out for specific proteins. An anti-rabbit anti-GFP antibody (Sigma) was also used to enhance GFP fluorescence. Details of the primary and secondary antibodies used are given above and in section 2.4.

4.2.4. CAM microscopy

Live imaging was conducted using a Leica DC500 fluorescence dissection microscope and images acquired with Adobe Photoshop software (Version 6). Fixed and stained samples mounted on slides were analysed using Zeiss Axioimager (x5, x10, x20, x40 lens details) running Axioimager 4 software. Confocal images were taken using the equipment described in section 2.

4.2.5. Confocal spectral unmixing microscopy

A series of baseline samples was imaged on the Nikon A1 Plus Confocal Microscope using the spectral unmixing acquisition software. Each sample had either no stain or just one stain.

Samples were as follows:

1. CAM only (no stain)
2. CAM with phalloidin atto 565
3. CAM with DAPI
4. Lentiviral transduced GFP+ HT1080 cells on plastic

Images were acquired for CAM tissue samples with and without GFP+ cells using all four lasers and then the predetermined spectral profiles were extracted from the spectral image via a spectral unmixing algorithm. Unmixed images showed only those cells and areas of the CAM fluorescing within the ranges determined by the baseline profiles. These images could be compared to regular confocal images for control purposes.

4.3. Results

The chick embryo model is well characterized and has been extensively used to study both development and disease. Exploiting the ability to drop the albumen level and use the highly vascularised ECM-like chorioallantoic membrane, this work explored the extent to which the chick embryo model could be used to visualise and probe cell-cell and cell-ECM mechanisms using fluorescence microscopy.

4.3.1. Developing CAM assay for ECM interaction

Development of the CAM metastasis assay took place over a series of experiments based at the Institute of Child Health, University College London. The aim of the initial experiments conducted was to find the best way of seeding cells onto the CAM beneath a window made on day 2/3 of incubation (Figure 4.4 A, A1) so that their spread and dissemination over and through CAM tissue could be observed and quantified.

Three approaches were explored:

1. Cells re-suspended in medium, seeded directly onto CAM;
2. Cells re-suspended in medium seeded into small rings onto CAM;
3. Cells re-suspended in collagen and seeded onto CAM.

In the initial set of experiments myristoylated GFP+ cells which expressed GFP at the cell membrane were used. A heterogeneous mix of either HT1080 myristoylated GFP+ cells or MDA-MB-231 myristoylated GFP+ cells (section 2.3.1) was seeded at a density of 8.5×10^5 cells/ml either directly onto scratched CAM (Figure 4.4 B) or into small rings which had been made by cutting lengths of a sterile 1ml pipette tip and glued with surgical glue onto the CAM surface (Figure 4.4 C). Alternatively, cells in 1mg/ml collagen were seeded onto the scratched CAM surface beneath the windowed area (Figure 4.6). The scratch made to the

CAM surface was fine and around 0.25-0.5cm in length, made in an area distant to the major CAM blood vessels. The aim of the scratch was to cause minor damage and allow the human cancer cells a point of access into CAM ECM. In all cases only one application of cells/ cells in collagen was applied to each CAM /egg to enable spread of cells to be investigated from the initial seeding point. Figure 4.4 shows images of cells seeded either directly onto scratched CAM or into rings, these acting as wells to hold cells in medium. The three experiments were observed and images taken one day, three days and seven days after the addition of cells or cells in collagen. Figure 4.5 shows images of cells in medium added at day one (Figure 4.5 A, B, C) and after three days (Figure 4.5 D). It was difficult to find cells using the Leica DC500 microscope beyond this stage on the CAM. HT1080 myristoylated GFP cells were particularly difficult to see as they did not fluoresce very brightly over the background auto-fluorescence of the chick tissues, CAM being collagen rich and fluorescing in the green emission range in particular, as can be seen in the images presented here (Figure 4.5 B-D). Whilst some of the introduced GFP+ cells may not have survived at the CAM surface, others may have moved down into the CAM quickly and so their fluorescence may have been masked by the background auto-fluorescence of the CAM. The variation within the heterogeneous mix of transposed cells would also have resulted in a variation in levels of GFP expression between cells, some being brighter and more easily detected than others. Seeding of cells into rings appeared to be successful initially but vasculature failed to develop beneath these rings, perhaps due to the effects of the surgical glue. Also bacterial infection was seen in a number of the experiments where cells were applied in this way. Seeding cells in 1mg/ml collagen allowed the cells to remain in a specific location / patch at the CAM surface which could be found successfully on subsequent days (Figure 4.6). 1mg/ml collagen was chosen for suspension due to its successful use in *in vitro* assays for cell

migration. Cells have also been observed to sink within collagen at low concentrations during experiments conducted within this project and this has also been observed and reported by other researchers (Artym and Matsumoto 2010). This *in vitro* behaviour was exploited to allow cells to gain close proximity to the CAM surface whilst still providing encapsulation to give an identifiable seeded patch.

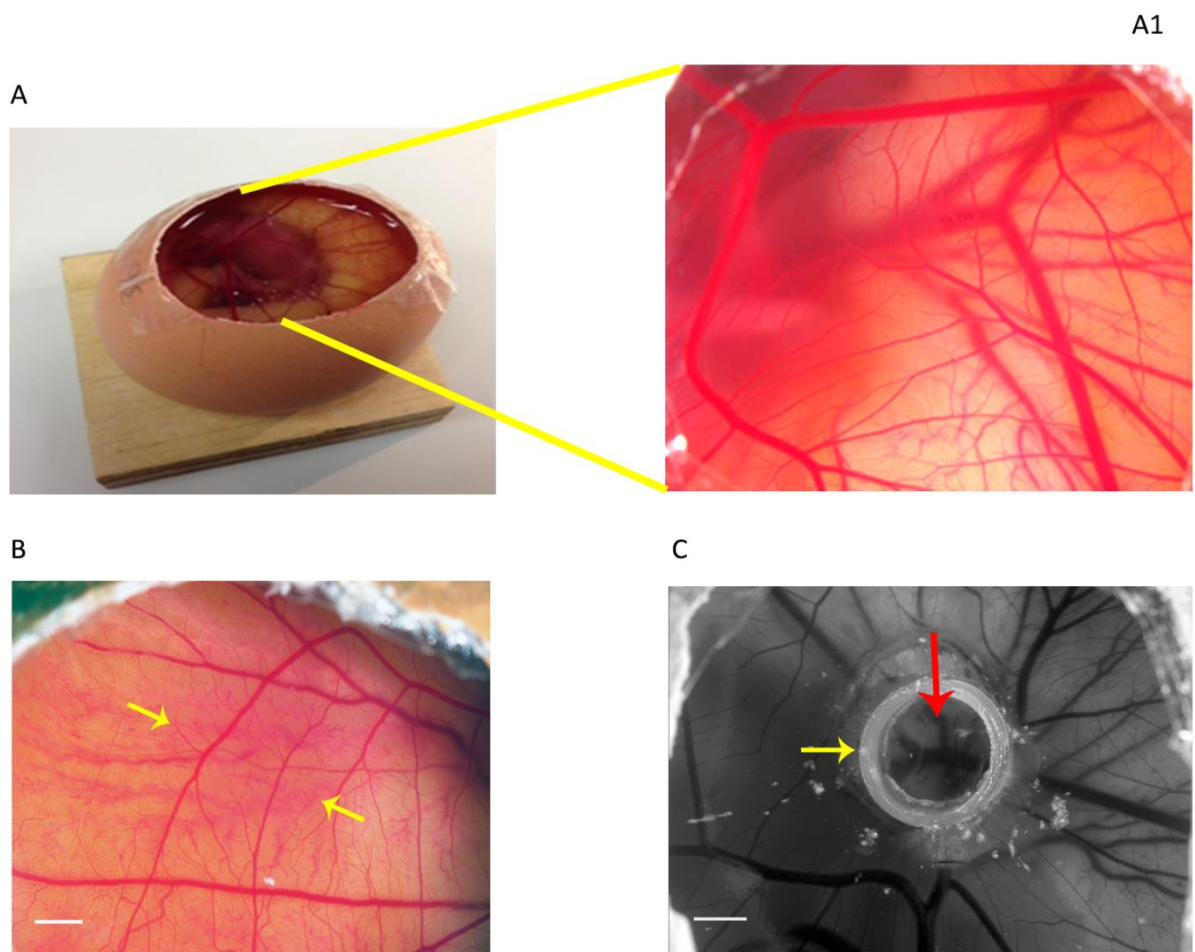


Figure 4.4, Development of CAM metastasis assay. **A** Shows a windowed egg with CAM exposed and vasculature evident (note that the window in this image has been expanded for the purposes of demonstration so is larger than the 3 x 2cm window made at Day 2 or 3). **A1** shows an expanded image of the CAM surface and vasculature in the windowed egg (not to scale). **B** MDA-MB-231 myristoylated GFP+ cells have been added in medium to the CAM surface which looks slightly pink due to the DMEM medium they were suspended in (between yellow arrows). **C** a ring (yellow arrow) glued to the CAM surface provides a well for cells to be added (red arrow). Brightfield images A1-C taken with a Leica DC500 microscope. B, C Scale bars = 2mm.

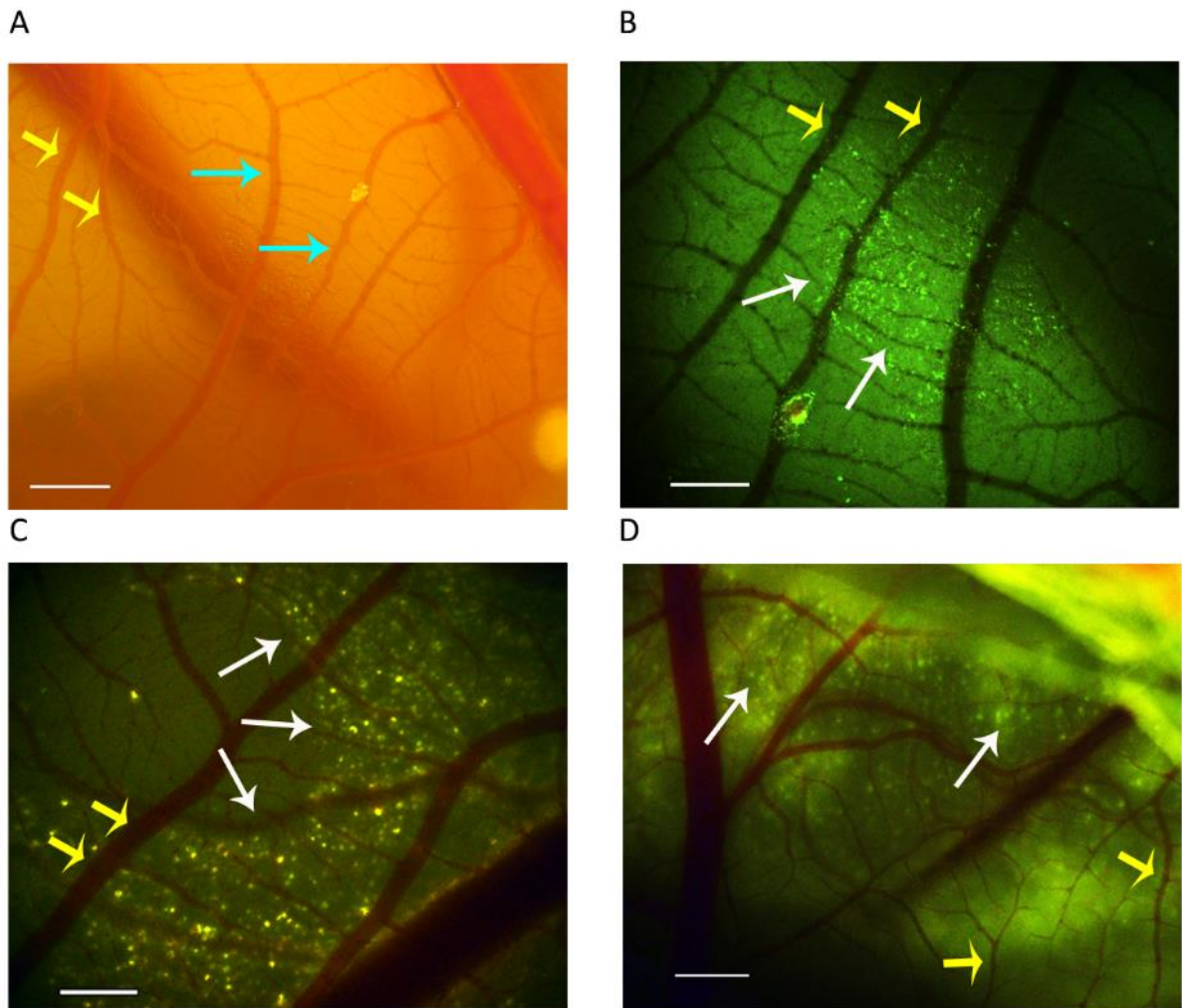


Figure 4.5, Development of CAM metastasis assay: MDA-MB-231 myristoylated GFP Cells / cells in collagen seeded onto the CAM surface. **A** Brightfield image of cells seeded in medium onto scratched CAM (in area of blue arrows). **B** Epifluorescence image showing cells seeded and spread over surface of CAM (white arrows). **C** Cells on CAM at higher magnification – individual cells can be seen (white arrows). **A-C** Images taken 1 day after seeding cells. **D** shows cells in media spread over the CAM surface, 3 days after seeding. Yellow arrows indicate vasculature in all images. Images taken with a Leica DC500 microscope. A,B Scale bars = 1mm, Scale bar in C = 0.5mm, Scale bar in D = 2mm.

Brightfield and fluorescence images taken one day after seeding showed that for some experiments cells and collagen remained in a small patch (Figure 4.6, A, B). For other experiments the cells in collagen seemed to spread out well and individual cells could be seen within the collagen on the surface of the CAM one day after addition to the CAM surface (Figure 4.6 C, D). There was evidence however that over subsequent days the collagen tended to dry out (Figure 4.7 A, B). Samples from the initial experiment were

harvested after six days, fixed, stained and investigated further using fluorescence and confocal microscopy to determine the extent of spread of cells into CAM tissue.

Two methods of harvesting CAM were explored, firstly harvesting of the whole CAM from the *ex ovo* chick and secondly, enlarging the window and excising the CAM from beneath the windowed area. This second approach was more successful as the original seeding area could be determined under a dissection microscope for harvesting and cell dissemination could be investigated within a sample of at least 6 cm². Initial samples were fixed, stained and mounted and images taken with a Zeiss Axioimager (Figure 4.7). Cells could be seen spread out in collagen on the CAM surface and many were rounded and flat. Several cells seemed to be aligned or in chain formation. Further images were taken using confocal microscopy to explore the extent and depth of spread of myristoylated GFP+ MDA-MB-231 cells (Figure 4.8) and HT1080 cells (Figure 4.9) on the CAM.

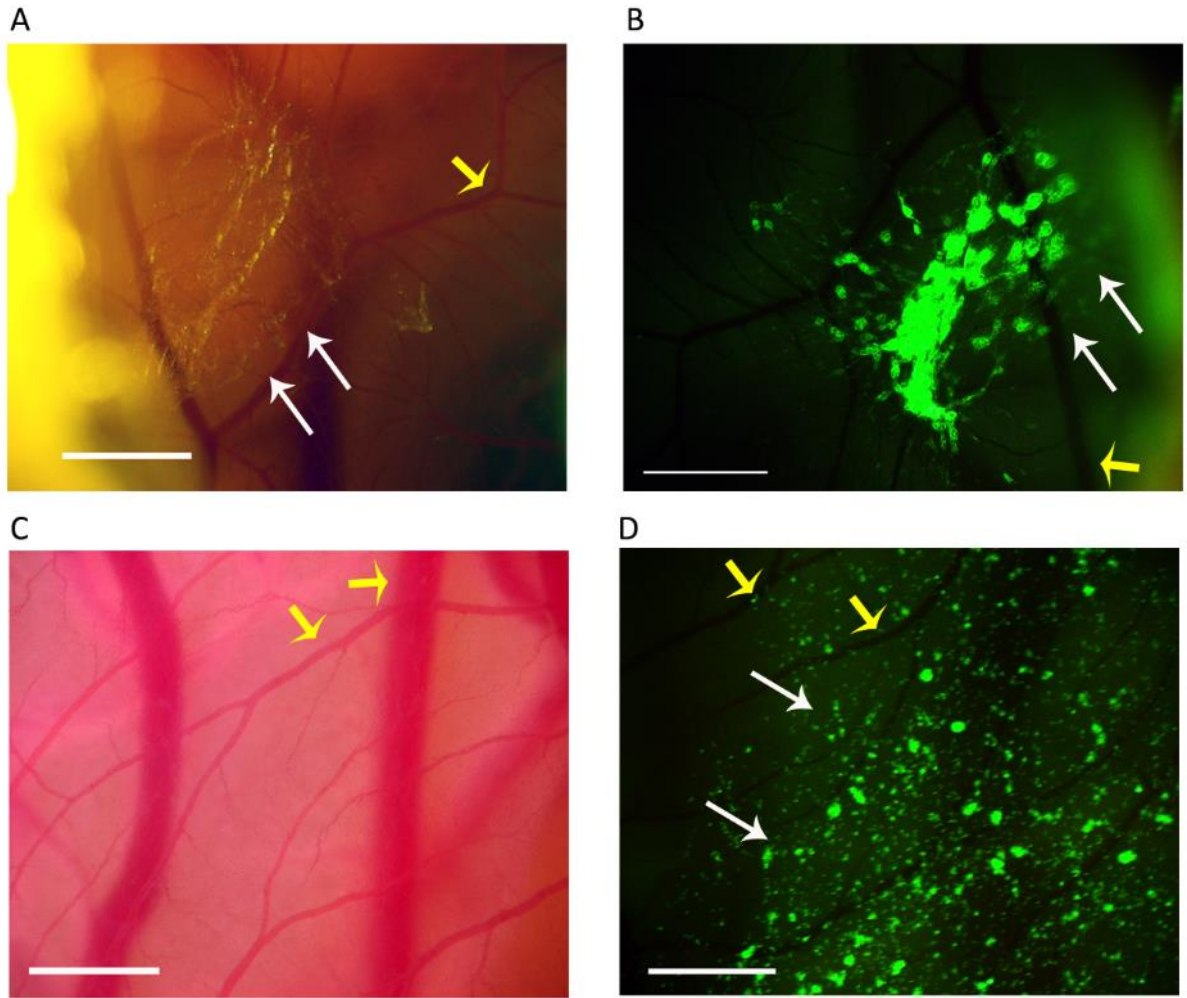


Figure 4.6, Development of CAM metastasis assay – cells in collagen on CAM surface.
A, Brightfield image of cells in collagen on CAM (white arrows). **B** MDA-MB-231 myristoylated GFP (MDA GFP+) cells in collagen on CAM surface indicated by white arrows.
C Brightfield image of CAM with cells in medium (cells not individually visible) and **D** epifluorescence image showing the same area and patch of cells in collagen (white arrows in figure D) these appearing more dispersed than cells in A, B. In all images vasculature is indicated with yellow arrows. Images were taken with a Leica DC500 microscope. Scale bars = 1mm.

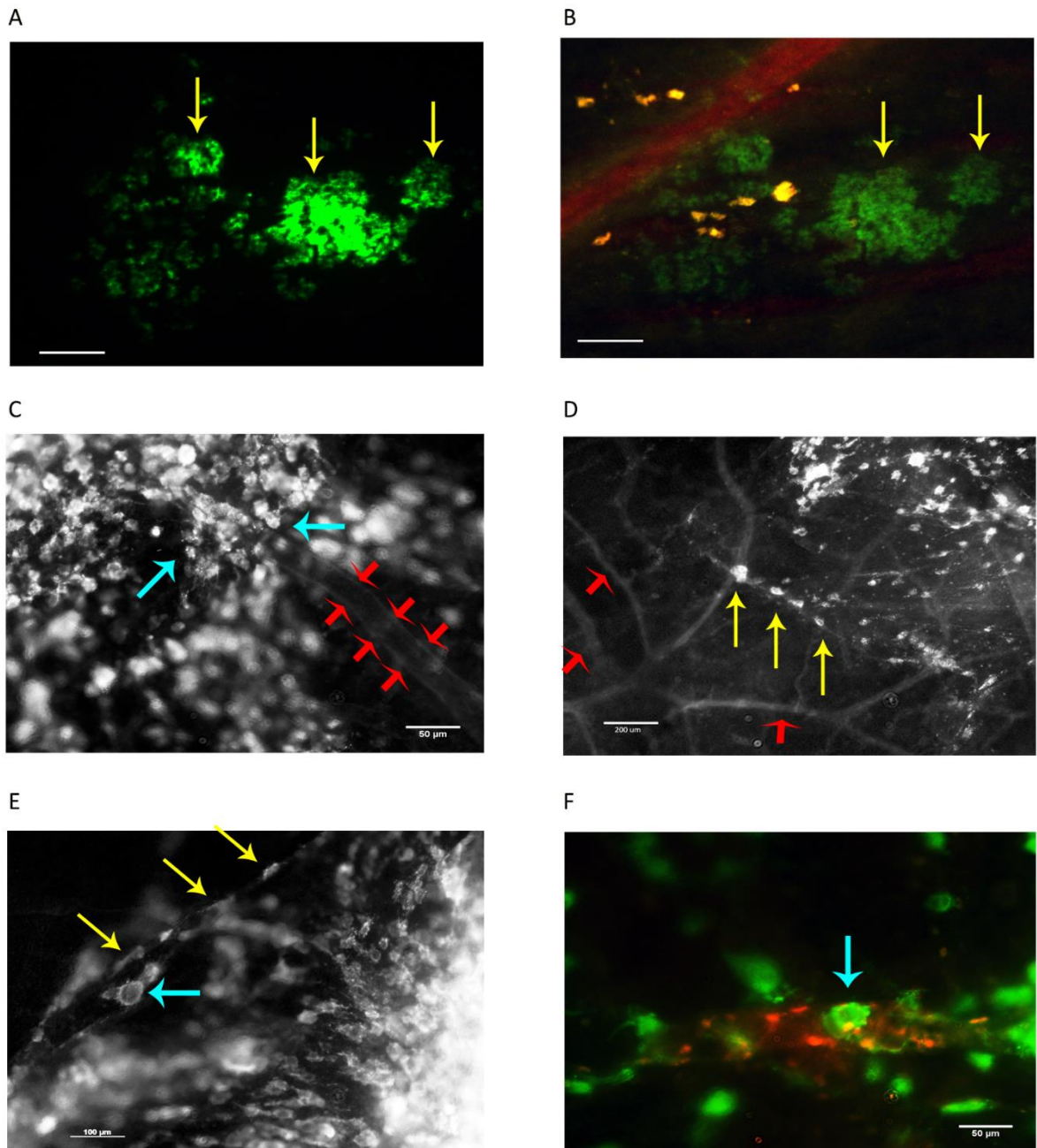


Figure 4.7, MDA-MB-231 myristoylated GFP cells on harvested CAM. **A, B** After 2-3 days, collagen appeared to be clumped and dried out in places on the CAM (yellow arrows). Red channel shows CAM tissue, green shows collagen/cells. Scale bars = 500µm. Images taken with Leica DC500 microscope. **C-F** Fixed and stained CAM mounted and imaged using a Zeiss Axioimager. **C** GFP+ cells (blue arrows) appeared to sit on and around a blood vessel (red arrows). Cells appeared rounded and flat. **D** Cells appeared to be well spread in collagen over the CAM surface (red arrows indicate vasculature) and appeared to line up along edges of the collagen (yellow arrows) **D, E.** **E, F** Rounded flattened cells can be seen on the CAM (blue arrows). **D** Scale bar= 200µm, **C, F** scale bars= 50µm, **E** scale bar = 100µm.

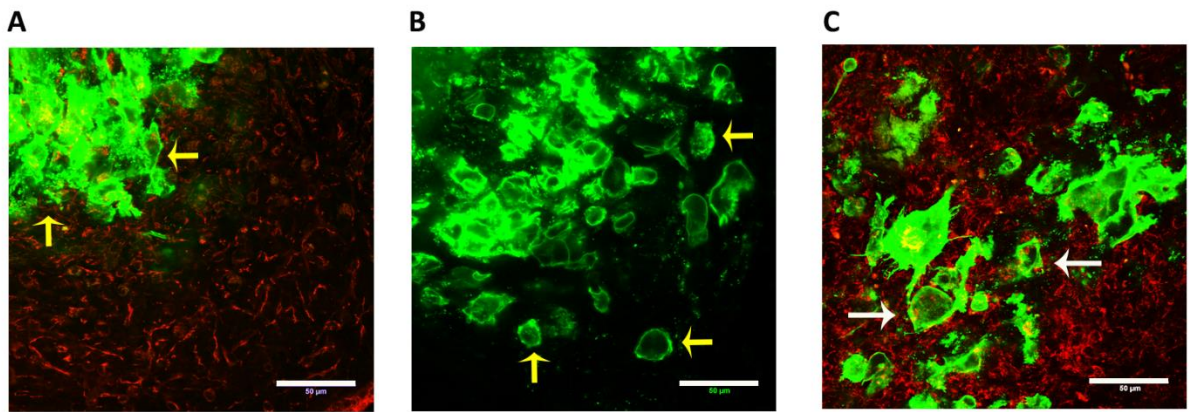


Figure 4.8, Confocal images of MDA-MB-231 myristoylated GFP cells on CAM. A GFP+ cells indicated by yellow arrows grouped on CAM surface (green) with CAM phalloidin shown in red channel. **B** Cells adopted compact shapes (yellow arrows). Myristoylated GFP is clearly seen outlining the cell membrane. **C** Cells are grouped and spread over the CAM (white arrows indicate cells). Confocal images were taken with a Leica TCS SP2 confocal microscope. Scale bars = 50µm.

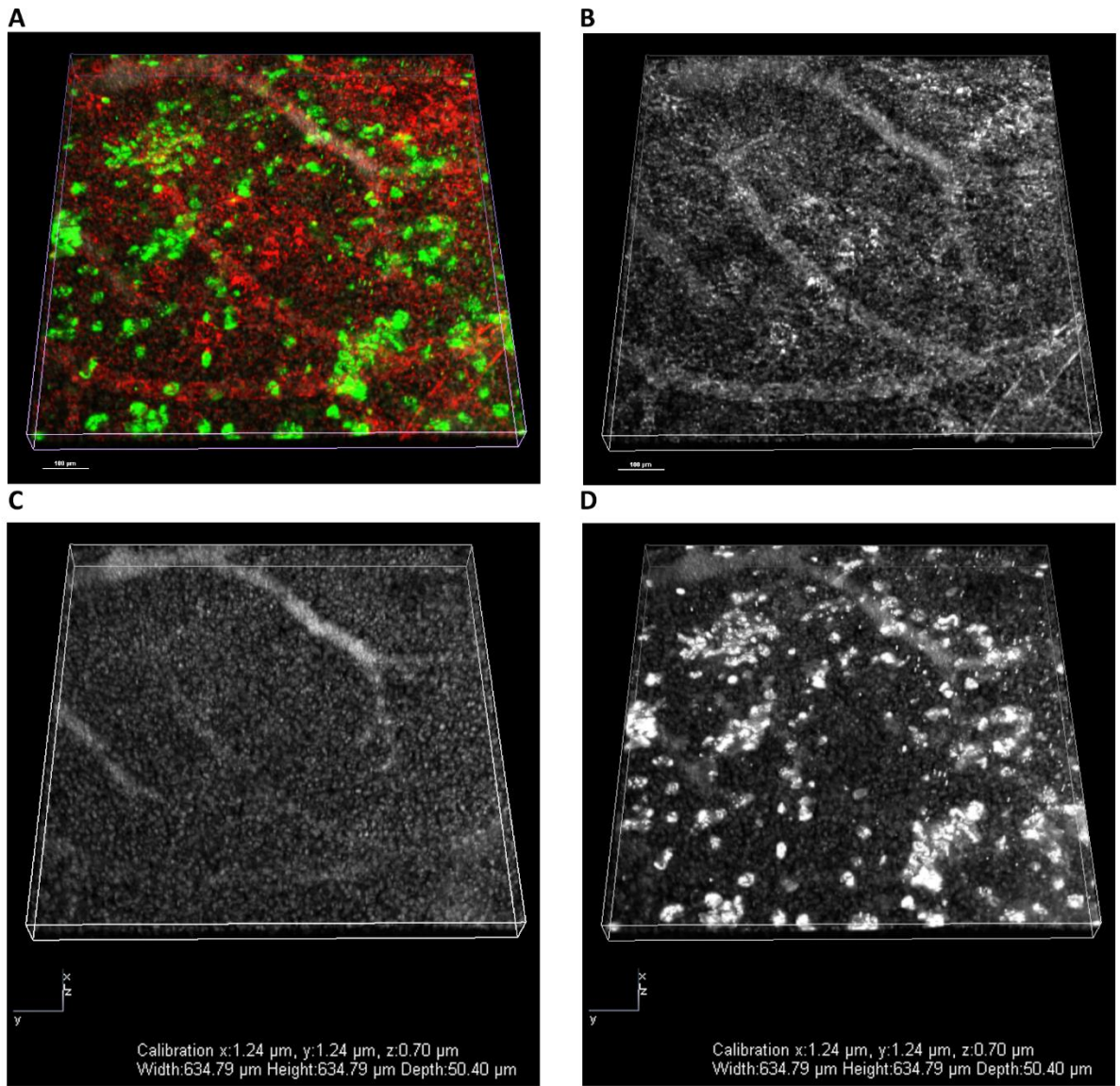


Figure 4.9, HT1080 myristoylated GFP cells on CAM membrane, 6 days after seeding. Cells are seen in small groups or individually, some still within the collagen. **A** Combined image, **B** Phalloidin in red channel, **C** DAPI in blue channel. **D** GFP+ in green channel. Images were taken using Nikon A1 confocal system. Scale bars = 100µm and as shown in 3D scale at the base of images C and D.

Following the initial cell seeding trials onto the CAM, suspending and seeding cells in collagen proved to be the most successful method. To improve the chances of cell survival for invasion, the cell seeding density was increased to give 35-40,000 in 20µl instead of the initial 15-20,000 cells per application. Following seeding on CAM, a drop of growth medium was added on the following 1-2 days to keep collagen moist on the CAM surface.

Although the membrane-tagged myristoylated GFP+ cells had proved successful on the surface of the CAM, it was difficult to see them within the CAM tissue. Further work to characterize myristoylated GFP+ cells was carried out to assess their suitability as a tool within this assay. MDA-MB-231 myristoylated GFP+ cells were added to a 2D/3D assay (section 3.2.5) and observed over a 24 hour period to check cell migration and morphology characteristics. They were placed in a humidified tissue culture incubator at 37°C and monitored using an Etaluma LED microscope with x40 lens. Figure 4.10 A-C show cells migrating on collagen. Cells can be seen to move in and out of the highlighted area (red ellipse) and to change their morphology from rounded to elongated or vice versa.

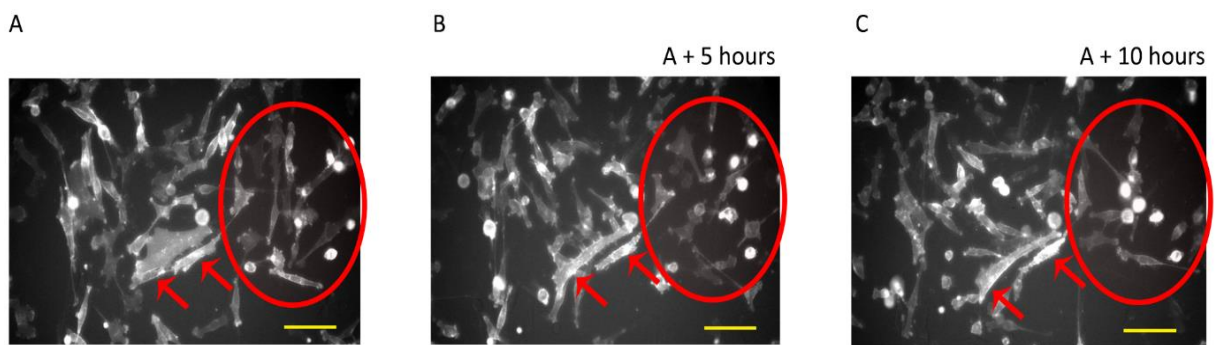


Figure 4.10, MDA-MB-231 myristoylated GFP cells migrating on 2mg/ml collagen.

Images (A-C) were taken over a 24 hour period every 10 minutes using an in incubator Etaluma LED microscope. Red arrows indicate the same two cells on each image and show that over the 10 hour period these cells changed morphology and moved on the collagen. The red ellipse depicts an area of collagen in which a number of elongated cells can be seen in image A. In B and C changes in cell morphology and location can be seen within the red ellipse, compared with A, over the 10 hour period. Scale bars = 100µm.

Cell migration speed and total track length for a 24 hour period were compared for MDA-MB-231 and the modified myristoylated GFP cells using time-lapse microscopy (Figure 4.11 A,B). The results suggested that both cell migration speed and total distance migrated over 24 hours differed between the two cell populations, with the modified GFP+ cells moving less distance and more slowly. Whilst the aspect ratio of the GFP+ cells compared with the parent cell line migrating on collagen (Figure 4.11 C) appeared to be similar, many of the

GFP+ cells appeared to have a more crinkled membrane (red arrows in Figure 4.11 D,E). The characteristics of these cells meant that they were not ideally representative of the parent cell line. Immuno-staining using an anti-GFP antibody to enhance the fluorescence and aid identification of myristoylated cells against the autofluorescent CAM was an option considered but this would have increased the time and resources employed for each experiment and would only be of use in harvested fixed tissue.

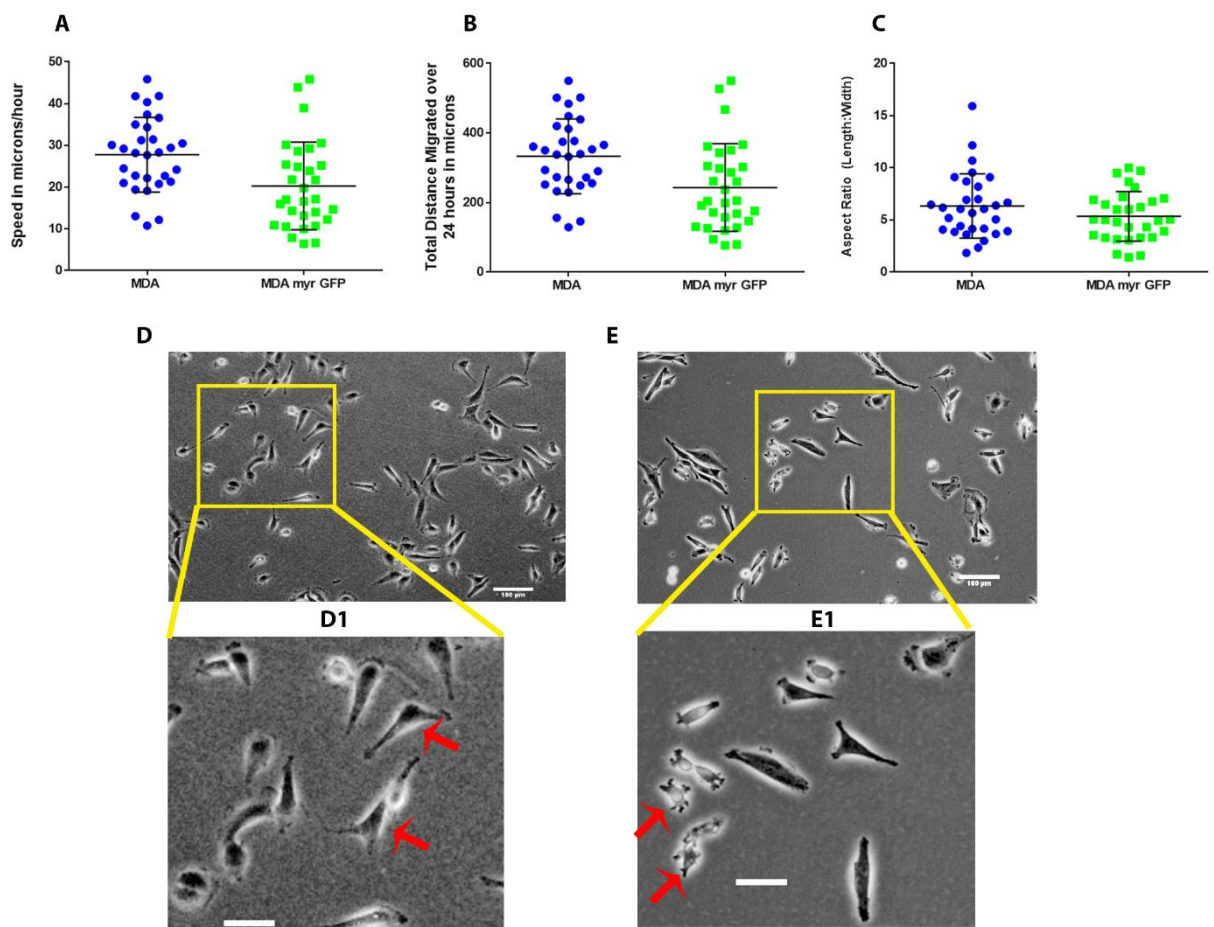


Figure 4.11, Comparison of MDA-MB-231 Cells (MDA) with MDA-MB-231 myristoylated GFP cells (MDA myr GFP). A, Speed of migration; B Total track length for a 24 hour period; C Aspect ratio. Each spot represents a cell. Error bars show standard deviation. D shows MDA-MB-231 cells migrating in 1mg/ml collagen with D1 an expanded view. E shows myristoylated GFP+ cells with E1 an expanded view of the area in the yellow rectangle. Cells indicated with red arrows have unusual crinkly looking membranes when compared to MDA-MB-231 cells (red arrows). Scale bars = 100 μ m.

4.3.2. Are lentiviral GFP+ cells easier to identify in CAM?

As the morphology and invasive capacity of the cells observed in CAM was important as well the ability to identify them, lentiviral green fluorescent protein (GFP) expressing cell-lines were developed for MDA-MB-231, HT1080 and MCF7. These cell lines were developed to express GFP in the cell cytoplasm and were expected to be brighter and easier to identify in CAM. The assembly of the virus and transduction of each cell line is described in section 2.3.2. Following clonal expansion for each cell line, clones were screened for fluorescence, cell morphology and proliferation rate, selection made based on those most resembling the parent cells. Three clones for each cell line were chosen and these were cultured following the cell culture procedures described in section 2.1. for the relevant parent cells. For each parent cell line and clone, an *in vitro* comparison was carried out and repeated three times (n=3), in which cells were encapsulated in 1mg/ml collagen, left to settle then tracked following the procedure outlined in section 2.5.1. Cell morphology was quantified using length and width measurements to give aspect ratio and 'distance from start' was determined from cell tracking data extracted from the ImageJ MTrackJ measurements file. A combination of descriptive statistics and statistical difference was used to establish similarity in this context based on a group of 30 cells for each independent experiment observed in the 3D collagen context *in vitro*.

Results were summarised and quantified and are presented for MCF7 (Figure 4.12), MDA-MB-231 (Figure 4.13) and HT1080 (Figure 4.14). There was no significant difference found between MCF7 parent cells and clones for either distance from start or for aspect ratio (Figure 4.12, C, F). Cells for all three clones were fluorescent in the green emission spectral range (\approx 500-600nm) and grew in group formation in a similar way to parent cells (Figure

4.12 A-B, D-E). MDA-MB-231 clones were also similar to parent cells in their cell migration characteristics (Figure 4.13, F) and aspect ratio, with no significant difference for clones YA1 and ZB2 but a slightly more elongated/mesenchymal cell morphology evident for clone XB5 (significantly different at $p \leq 0.05$, MDA mean=2.293, XB5 mean=3.758). All three clones fluoresced green as expected and could be seen within the 1mg/ml collagen under epifluorescence light with a green filter (Figure 4.13 B, D, E). In order to establish similarity rather than difference using statistics, a larger data set would ideally be used, however in this case the approach of identifying difference in combination with cell fluorescence has been employed as a reasonable method of clone selection.

When HT1080 lentiviral GFP+ clones were compared with parent cells (Figure 4.14) the aspect ratio for each clone was similar to that of the parent cells, with a mean aspect ratio close to 4 for each cell type (Figure 4.14 C). All clones showed good fluorescence (Figure 4.14 A-B and D-E). However, GFP+ clones migrated less distance when compared to parent cells, this being significantly different in each case (Figure 4.14 F). However, cells of each clone were still able to migrate so were used in subsequent experiments.

Clones selected for each cell line were used and seeded at least three times each onto CAM both with and without first scratching the CAM surface. Lentiviral cell-lines were clearly visible at the CAM surface (Figure 4.15). When visualising cells in CAM, identifying the shape and form of the vasculature was an important consideration. In order to visualise this in relation to invading cells, ink injection was explored (Figure 4.16). This allowed cells seeded onto CAM to be seen in relation to the vasculature and could be used as a technique which did not require fluorophores, these then being available for staining CAM and cancer cells.

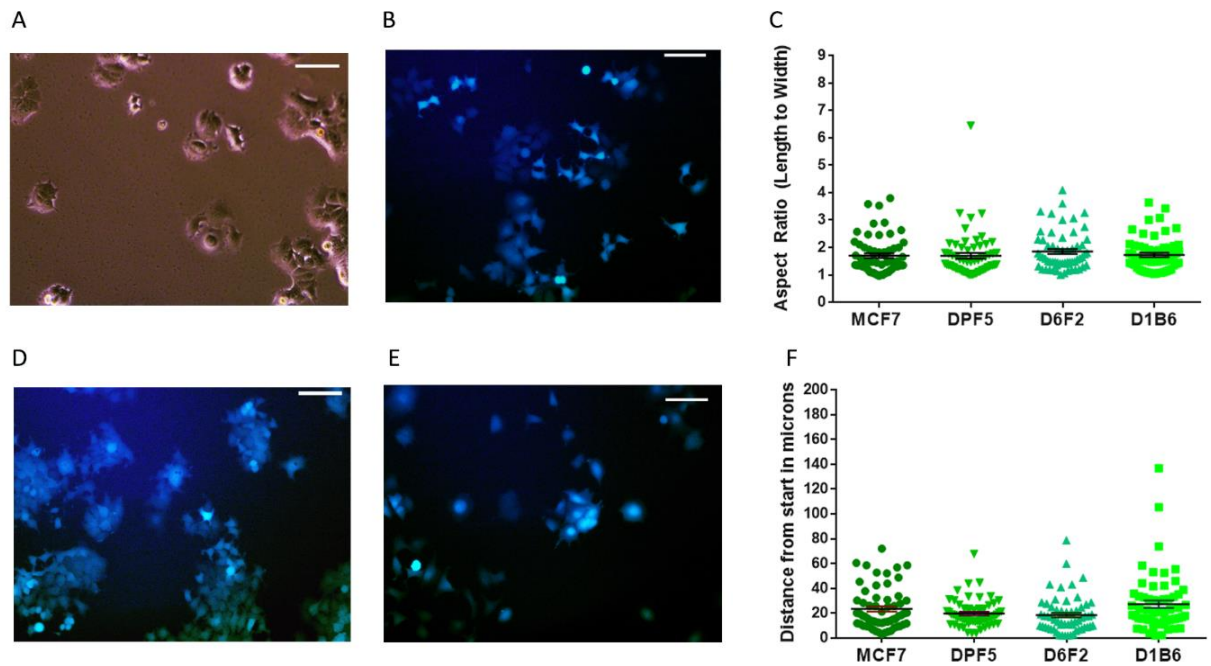


Figure 4.12, Comparison of MCF7 and MCF7 lentiviral clones. MCF7 cells and lentiviral GFP+ transduced clones were encapsulated in 1mg/ml collagen and cell migration tracked over a 21 hour period with images taken at 10 minute intervals using a Nikon TiE microscope. The length and width of 10 cells from each of 3 experiments was measured and 10 cells tracked for each experiment and cell type using ImageJ MTrackJ tool. **A** shows MCF7 using bright field microscopy, and clones are shown: **B** D6F2, **D** D1B6 and **E** DPF5, all imaged using a Zeiss Axio Vert.A1 epifluorescence microscope. Scale bars on all images are 100 μ m. Graph **C** shows aspect ratio and graph **F** distance from start for tracked cells. A two-way ANOVA followed by Tukey's multiple comparisons test indicated no significant difference for either aspect ratio or distance from start between parent cells and clones. Error bars show SEM. (Statistics shown in detail in Appendix C.)

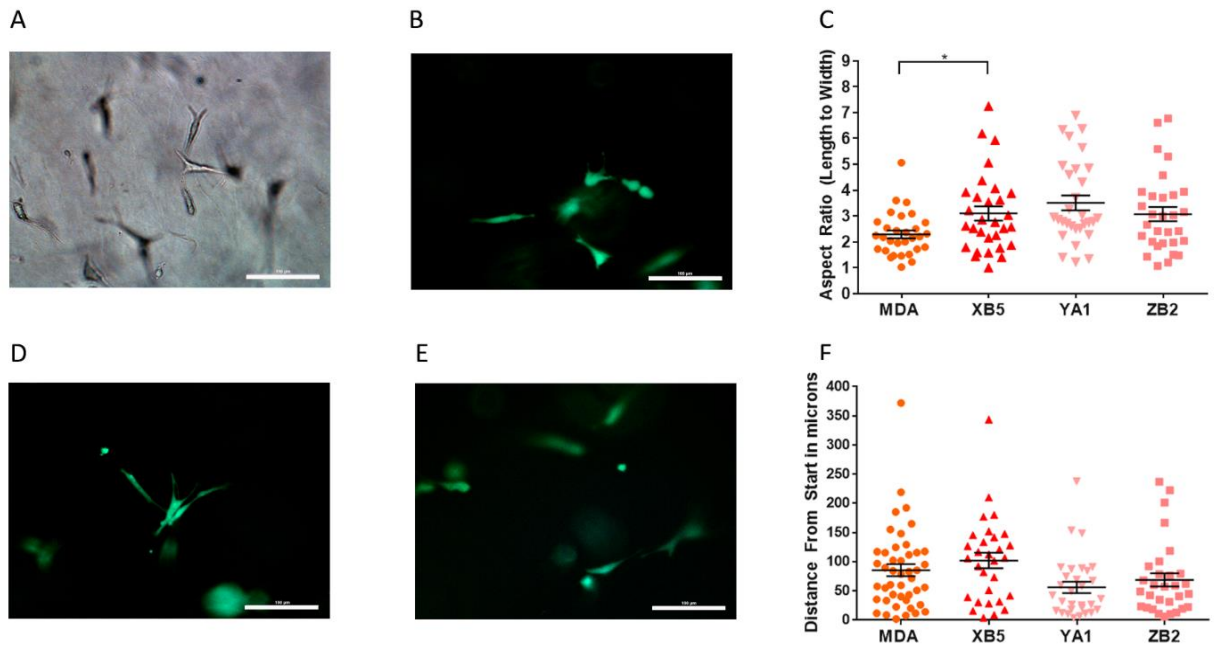


Figure 4.13, Comparison of MDA-MB-231 with lentiviral clones. MDA-MB-231 (MDA) cells and lentiviral GFP+ transduced clones (XB5, YA1, ZB2) were encapsulated in 1mg/ml collagen and cell migration tracked over a 21 hour period with images taken at 10 minute intervals using a Nikon TiE microscope. The length and width of 10 cells from each of 3 experiments was measured and 10 cells tracked for each experiment and cell type using ImageJ MTrackJ tool. **A** shows MDA cells in collagen using bright field microscopy and clones are shown: **B** XB5, **D** YA1, **E** ZB2, all imaged using a Zeiss Axio Vert.A1 epifluorescence microscope. Scale bars on all images are 100μm. Graph **C** shows aspect ratio and graph **F** distance from start for tracked cells. A two-way ANOVA followed by Tukey's multiple comparisons test indicated no significant difference for distance from start between parent cells and clones. A difference at $p \leq 0.05$ was detected for aspect ratio between MDA and XB5 clone cells. Error bars show SEM. (Statistics shown in detail in Appendix C.)

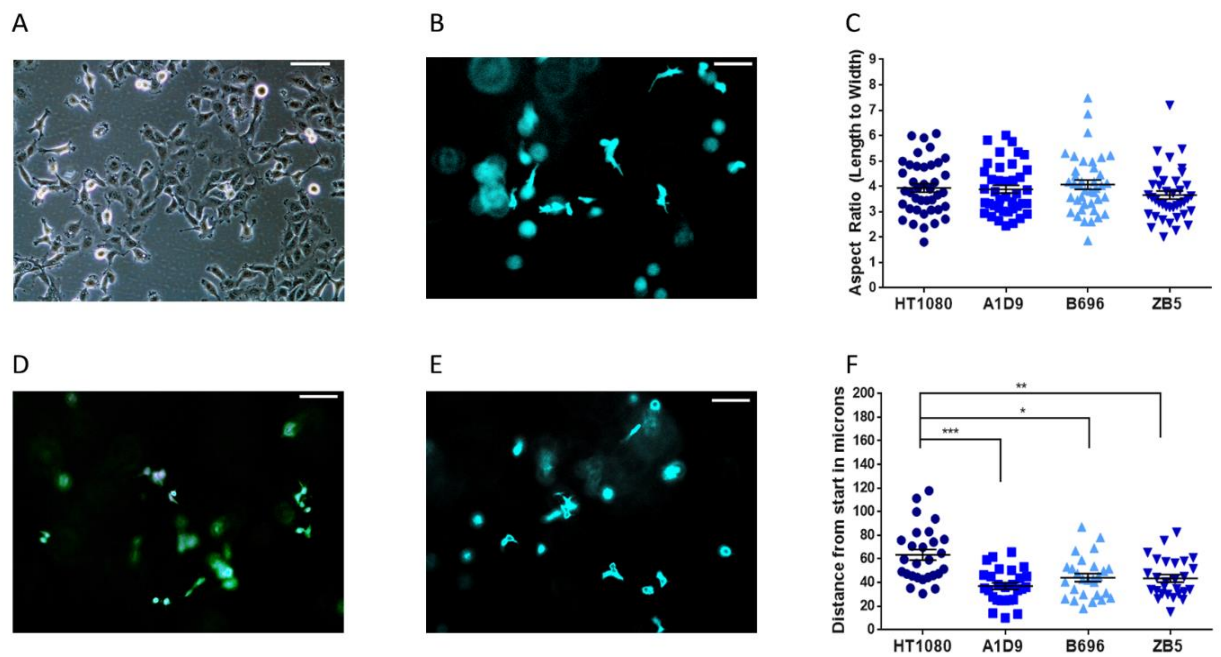


Figure 4.14, Comparison of HT1080 cells with lentiviral clones. HT1080 cells (HT) and lentiviral GFP+ transduced clones (A1D9, B696, ZB5) were encapsulated in 1mg/ml collagen and cell migration tracked over a 21 hour period with images taken at 10 minute intervals using a Nikon TiE microscope. The length and width of 40 cells from each of 3 experiments was measured and 27 cells tracked for each experiment and cell type using ImageJ MTrackJ tool. **A** shows HT cells in collagen using bright field microscopy, **B** shows clone A1D9, **D** B696, **E** ZB5, all imaged using a Zeiss Axio Vert.A1 epifluorescence microscope. Scale bars on all images are 100 μ m. Graph **C** shows aspect ratio and graph **F** distance from start for tracked cells. A two-way ANOVA followed by Tukey's multiple comparisons test indicated no significant difference for aspect ratio between parent and clones. For distance from start, differences were seen between parent and clones * $p \leq 0.05$, ** $p \leq 0.01$, *** $p \leq 0.001$. Error bars show SEM. (Statistics shown in detail in Appendix C.)

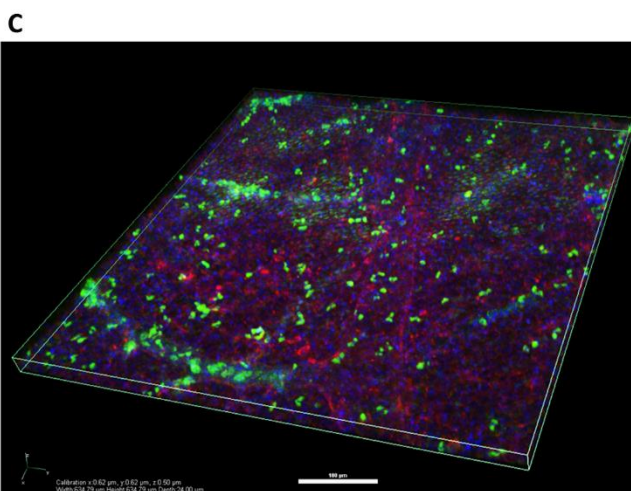
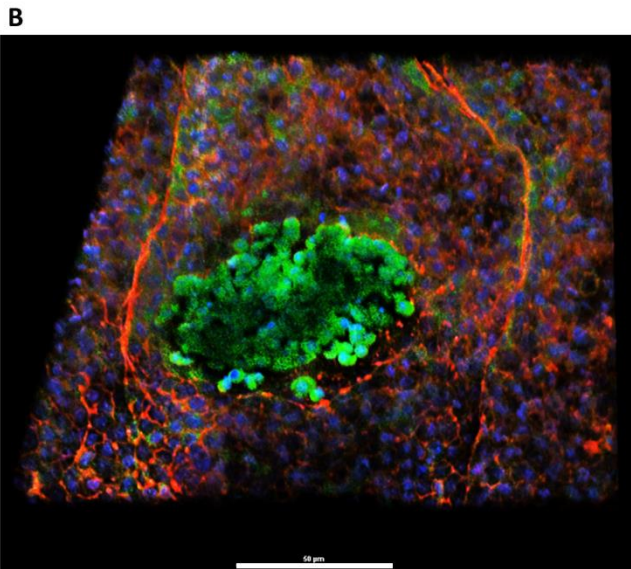
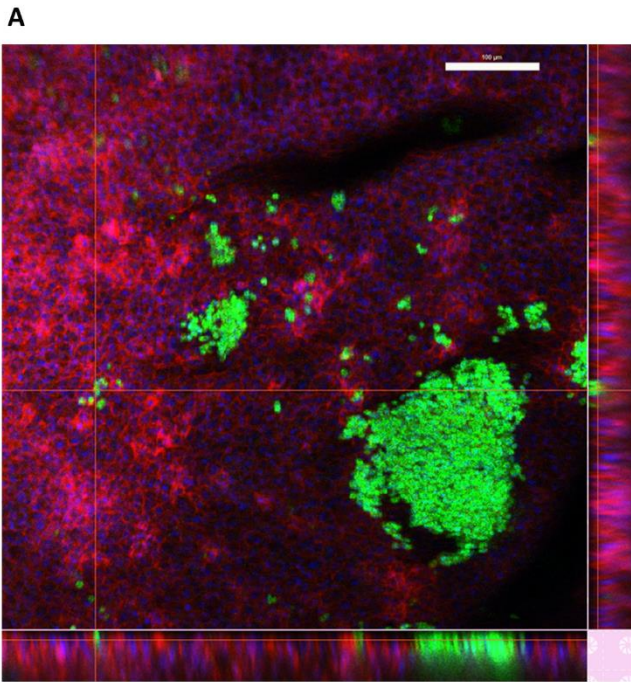


Figure 4.15, Lentiviral cells seeded at CAM surface.

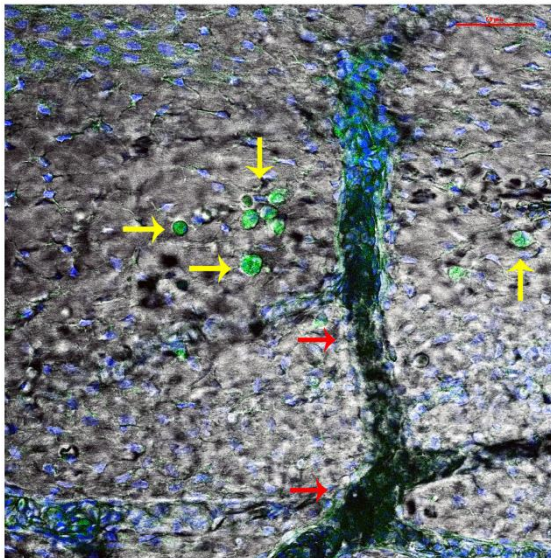
A LV MCF7 GFP+ (D6F2) cells are clearly seen in two large groups on CAM surface. **B** shows a patch of LV MDA-MB-231 GFP+ (ZB2) cells in collagen on CAM surface. **C** LV HT1080 GFP+ (ZB5) cells are dispersed over CAM. All images were taken using a Nikon Confocal A1 microscope.

Scale bars A, C = 100 μ m and B = 50 μ m.

A



B



C

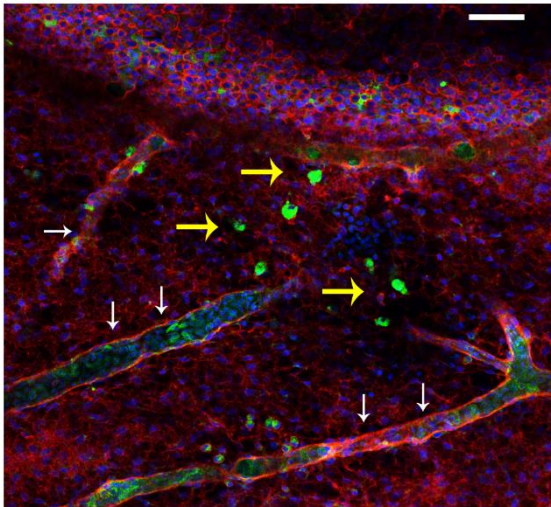


Figure 4.16, Ink injection to show CAM vasculature.

Indian ink was injected into the chick embryo heart 3 days after cells were seeded onto the CAM surface. Ink was pumped into the CAM and vasculature by the beating heart. CAM was fixed and stained with phalloidin and DAPI. Ink in blood vessels can be seen using bright field imaging **A** (red arrows). **B** shows merged brightfield and fluorescence images – GFP fluorescing cells can be seen in CAM tissue (yellow arrows). **C** Confocal image showing phalloidin in the red channel, GFP+ cells in the green channel and DAPI in the blue channel for the same CAM sample shown in A, B. GFP+ cells are visible in CAM tissue (yellow arrows) and close to blood vessels (white arrows). Images were taken using Nikon A1-R confocal microscope.

Scale bars = 100µm for A and 50µm for B and C.

When imaging fixed and stained whole CAM seeded with lentiviral cell lines, the auto-fluorescence from nucleated chick erythrocytes was a confounding issue (Figure 4.17, 4.18) as the erythrocytes were nucleated and fluoresced in the green spectral range. The chick erythrocytes appeared as disc shaped with a central nucleus and in some samples were seen in vasculature and within CAM tissue (Figure 4.18). Comparison of CAM both with and without lentiviral cell lines seeded was conducted using identical confocal settings across samples (Figure 4.19). Whilst a clear difference could be seen between samples with GFP+ cells at the surface of Figure 4.19 B and D, compared with A and C respectively, when looking at individual cells within the CAM, it was difficult to determine whether cells were definitely human cancer cells. Individual cells in Figure 4.18 C, appeared to vary in shape and be morphologically different to those marked with white arrows in Figure 4.18 D, which were almost certainly chick erythrocytes due to their symmetrical morphology.

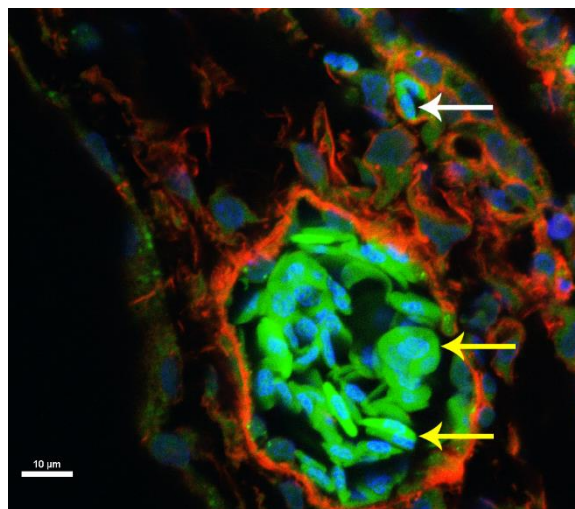


Figure 4.17 Chick erythrocytes fluoresce in the green spectrum. Nucleated erythrocytes within a large blood vessel (yellow arrows) and the CAM, white arrow. They are round and flat with a centralised nucleus (DAPI stained – blue). Image taken using Nikon A1 Plus confocal microscope. Scale bar = 10μm.

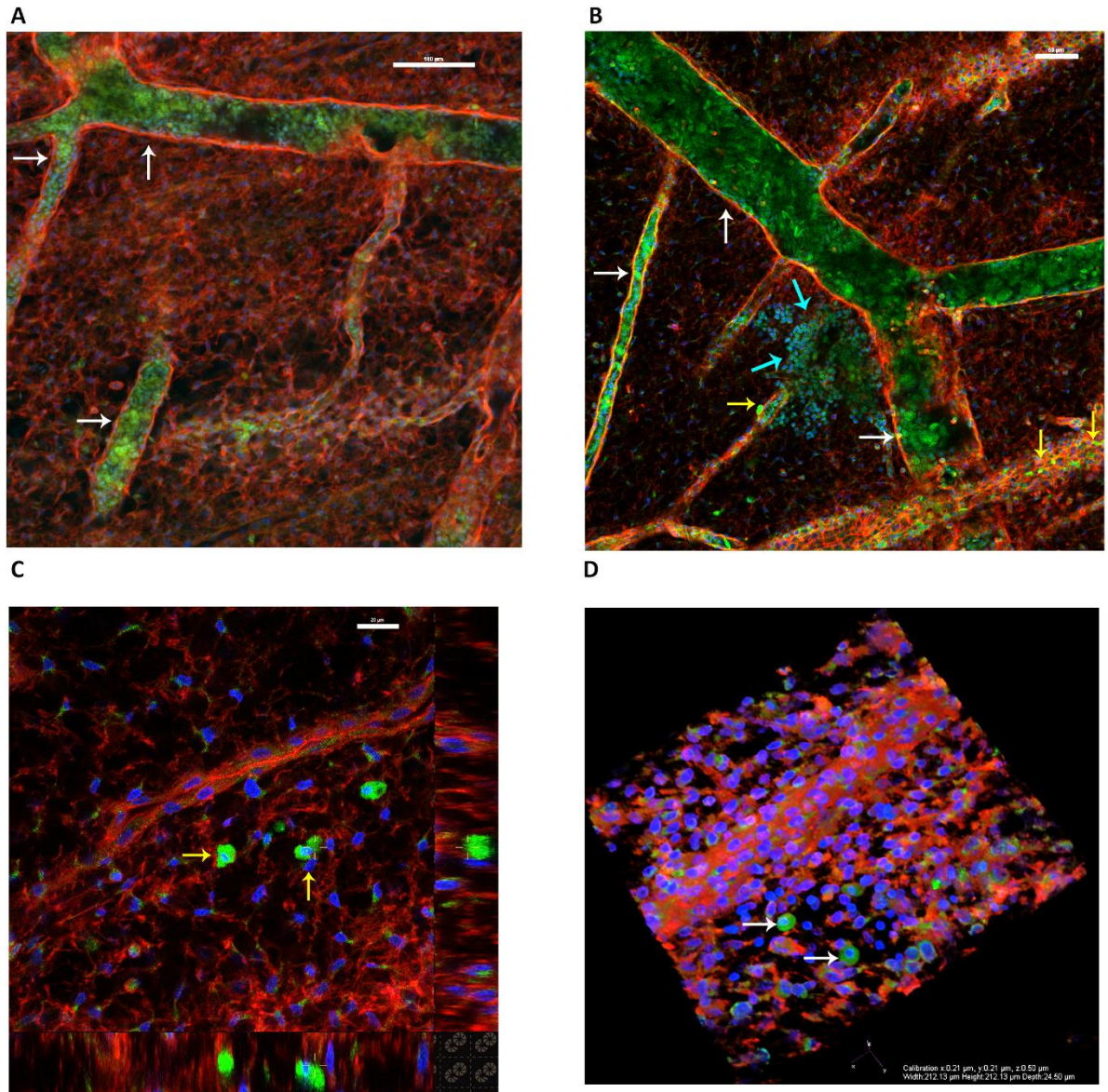


Figure 4.18, Nucleated red blood cells in chick. Chick erythrocytes are autofluorescent in the green and far red light emission spectral ranges. As erythrocytes leave capillaries and perfuse the CAM this means that they could potentially be misidentified as GFP+ cancer cells. **A** CAM at low magnification with no GFP+ cells seeded. White arrows indicate blood vessels. Green fluorescence in blood vessels is from nucleated erythrocytes. **B** LV MDA-MB-231 GFP+ YA1 cells seeded onto CAM (blue arrows). It is difficult to determine which cells in vasculature (white arrows) are GFP+ and which are erythrocytes using green fluorescence alone. Yellow arrows indicate likely GFP+ cells on/in CAM ECM. **C, D.** Higher magnification images of green fluorescent cells in CAM from LV MDA-MB-231 GFP+ ZB2 cells seeded CAM. Erythrocytes are more regular in shape and those indicated with white arrows in **D** are likely to be erythrocytes. Those indicated in **C** are irregular shaped and appear to be larger and likely to be GFP+ cancer cells. Images taken with a Nikon A1 Plus microscope. A, B Scale bars = 100 μ m. C Scale bar = 20 μ m.

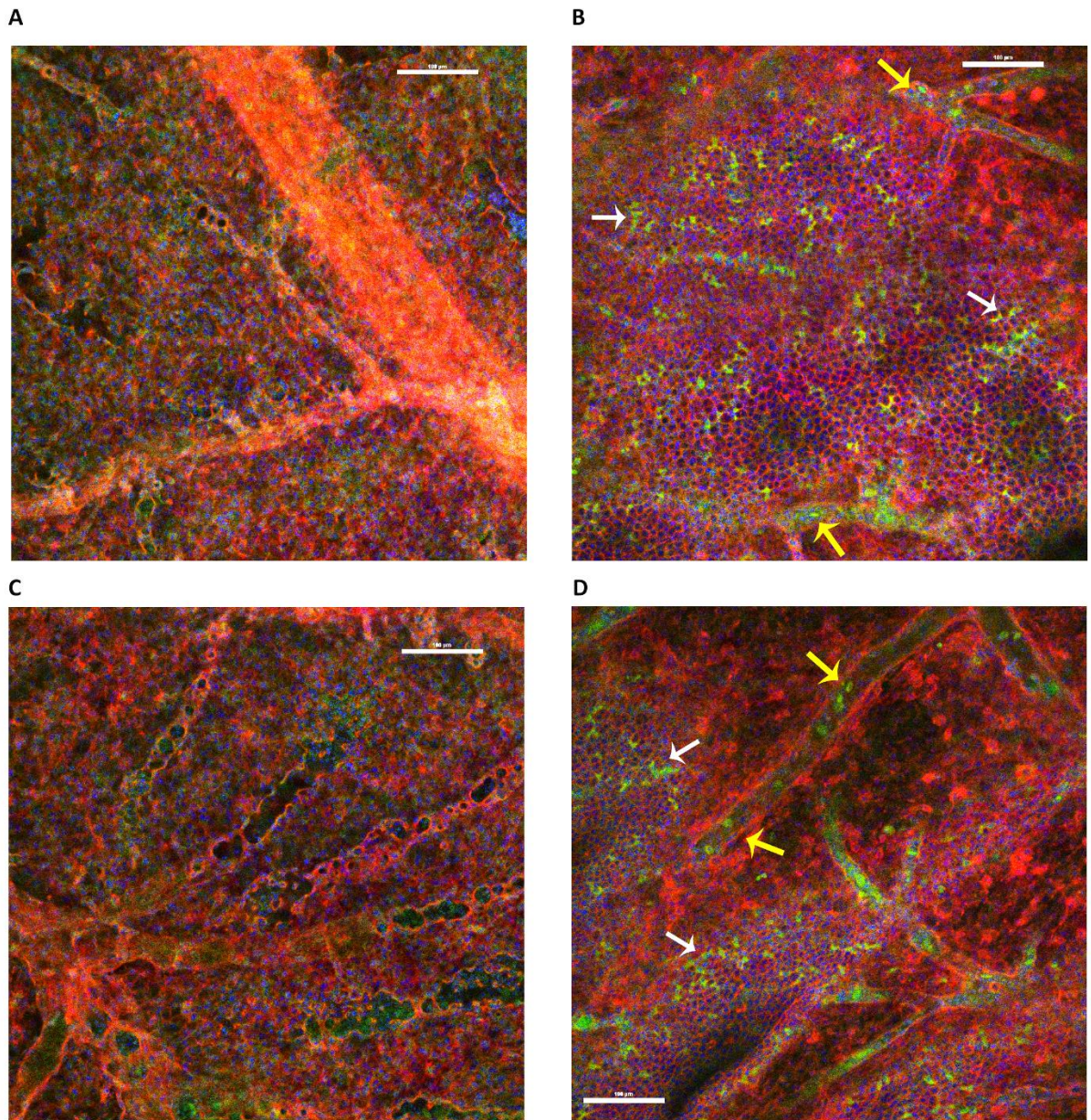


Figure 4.19, Determining GFP+ cells in CAM. CAM with no cells and CAM seeded with LV HT1080 GFP+ ZB5 cells from the same egg batch are compared using the same confocal settings. Spectral unmixing was used to obtain process these images using three filters: blue for DAPI, red for phalloidin and green for GFP from lentiviral cells. **A, C** CAM at low magnification with no GFP+ cells seeded. Some auto-fluorescence seen in the green range but there is no evidence of GFP+ cells at the CAM surface. **B, D** CAM onto which LV HT1080 GFP+ (ZB5) cells have been seeded. White arrows indicate GFP+ cells and yellow arrows indicate GFP+ cells in blood vessels. Images were taken with Nikon A1 Plus confocal microscope. Scale bars = 100µm.

Spectral unmixing confocal microscopy was used as a technique to reduce the auto-fluorescent background of CAM tissue and to help differentiate between GFP+ human

cancer cells and nucleated chick erythrocytes. Figure 4.20 A, shows a regular confocal image in which a large number of cells in collagen can be seen on the CAM surface, these appearing as GFP+ and roughly spherical with blue nuclei (DAPI). The larger rounded green cells indicated by blue arrows had a cell diameter in the range of 13-17 μ m and are likely to be the lentiviral transduced GFP+ cancer cells in this image. Figure 4.20 B shows the phalloidin only channel for image A, in which the actin cytoskeleton (blue arrows) can be seen for many of the GFP+ cells within the collagen. The cell characteristics of cytoskeletal staining, cell morphology and a nucleus all suggest that these can be identified as the GFP+ human cancer cells seeded within the collagen at the CAM surface. However, in Figure 4.20 A, some smaller green fluorescing cells with a round/ ovoid morphology (cell diameter 12-13 μ m) can also be seen at some locations within the collagen. These were fluorescent only in the green channel and were smaller than chick erythrocytes. The breakout panel in Figure 4.20 A, shows these more clearly. In Figure 4.20 B, in the equivalent phalloidin breakout panel, these small green cells are not visible so they do not appear to have an actin cytoskeleton. Using spectral microscopy to probe this mix of green fluorescent cells further, the higher magnification image at Figure 4.20 C, shows an image taken using three extraction filters: blue (DAPI), green (GFP) and red (phalloidin). The erythrocytes appear as bright yellow, rounded discs due to the diffuse actin within them picked up by the red filter in combination with the green auto-fluorescence. Other cells within the collagen however appear to be mainly green in colour, the interaction of the red filter for the actin cytoskeleton being much lower, thus the two cell types are distinct. The morphology of the cells indicated by white arrows, likely to be erythrocytes, is clearly different to the cells indicated with blue arrows as human cancer cells, with the erythrocytes being regular and round but flat when seen side on (cell diameter 12-13 μ m) with a central nucleus around 4 μ m in diameter.

Figure 4.20 D, shows a mix of green fluorescing cells within collagen on CAM in further detail and here again a clear distinction can be drawn based on the interaction of fluorescence filters and cell morphology.

Thus despite developing lentiviral GFP+ cell lines to allow better identification of metastatic invasion and colonisation of CAM, human cancer cells could not always be identified by their GFP expression alone and therefore their presence needed further qualification.

4.3.3. Immuno-staining of human cancer cells in CAM

Although morphological features of human cancer cells in CAM compared to those of chick cells could aid identification and differentiation, a clear and unequivocal method for the identification of human cancer cells was needed. To this end an anti-GFP antibody was used to detect the GFP within the cytoplasm of the lentiviral GFP+ cancer cells when staining. Images of stained whole CAM are shown for each cell line (Figures 4.21-25). LV MDA-MB-231 GFP+ (ZB2) cells were clearly labelled by the anti-GFP antibody (Figure 4.21) and cells could be identified within the mesodermal layer of the CAM in all three channels based on their fluorescence and additional labelling in the green channel, their morphology and by the phalloidin labelled cytoskeleton seen in the red channel. A negative control for primary and secondary antibodies was run on CAM with no GFP+ cells seeded and a control for the primary antibody was run with secondary antibody only for each condition (Figure C1 at Appendix C). Individual cell morphology for the ZB2 cells is shown in Figure 4.21 with most cells appearing compact and rounded or ovoid. Cells were also captured during cell division in these images (indicated by yellow arrows). In Figure 4.21 A, the indicated cells seem to form a group or chain, with two cells attached, one of which is dividing. LV HT1080 GFP+ (A1D9) cells were also clearly identified in CAM and in CAM vasculature when anti-GFP

staining was carried out (Figure 4.22-23). In Figure 4.23 the 3D rendered images show cells adopting a variety of morphologies as they move between CAM cells and through gaps in the ECM structure. In Figure 4.25 LV MCF7 GFP+ DPF5 cells are shown counter-stained with the anti-GFP antibody in whole CAM images. These cells are seen spread across the CAM surface (Figure 4.25 A) and within CAM vasculature (Figure 4.25 B). At higher magnification, the cells can be seen squeezing through gaps in the CAM tissue (Figure 4.25 C) with nuclei distorted as they move through it (Figure 4.25 D). Two pairs of cells can also be seen invading CAM tissue together (Figure 4.25 C-D).

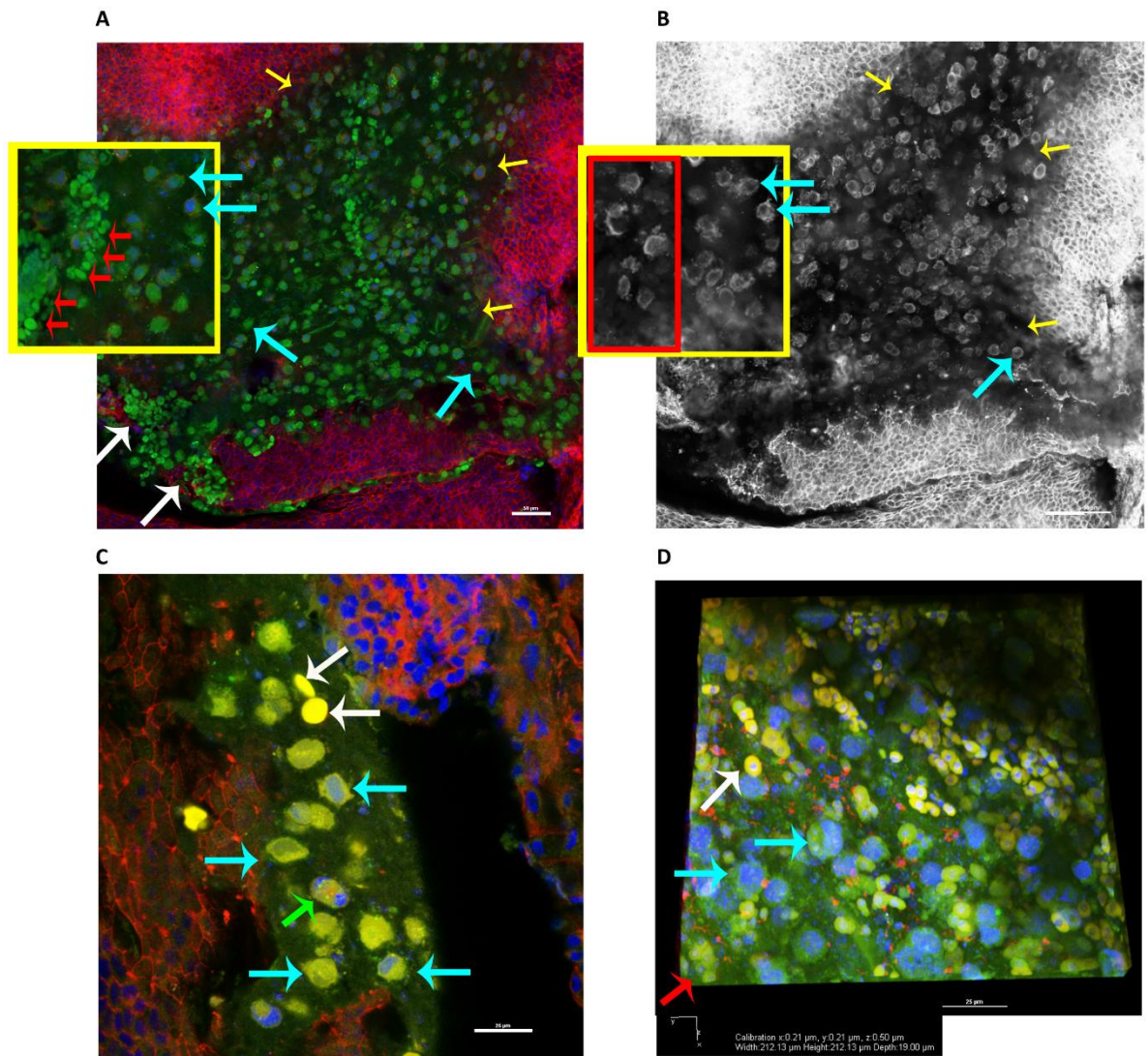


Figure 4.20 Spectral unmixing confocal imaging to differentiate GFP+ cells from erythrocytes. **A, B** Confocal images showing LV HT1080 GFP+ cells (ZB5 + 3 days after seeding) in collagen seeded at CAM surface. **A** GFP+ cells seeded at CAM surface in collagen. Expanded section shows both human cancer cells (blue arrows) and erythrocytes (red arrows in box and white arrows in larger image) which fluoresce green. **B** phalloidin only channel for A shows that GFP+ cells have actin cytoskeleton (blue arrows) which is not seen in erythrocytes (red box). Baseline samples for CAM, DAPI, phalloidin and GFP were imaged using spectral confocal settings. Seeded CAM samples were imaged and the specific emission spectra for phalloidin, GFP+ and DAPI were extracted. **C** erythrocytes show as bright yellow discs (white arrows) whereas GFP+ cells (ZB5 + 3 days) are more green and irregular in shape (blue arrows) with larger nuclei. The green arrow indicates a dividing GFP+ cancer cell. **D** shows a mix of LV MCF7 GFP+ (D6F2 4 days after seeding) and other chick cells in collagen on CAM using spectral filters. Cancer cells are larger and indicated with blue arrows. Erythrocytes appear yellow/green and are smaller than cancer cells, and there are a number of other small green cells within the collagen, for example those indicated with a red arrow. Scale bars for large images: A, B = 50µm and scale bars for C = 25µm.

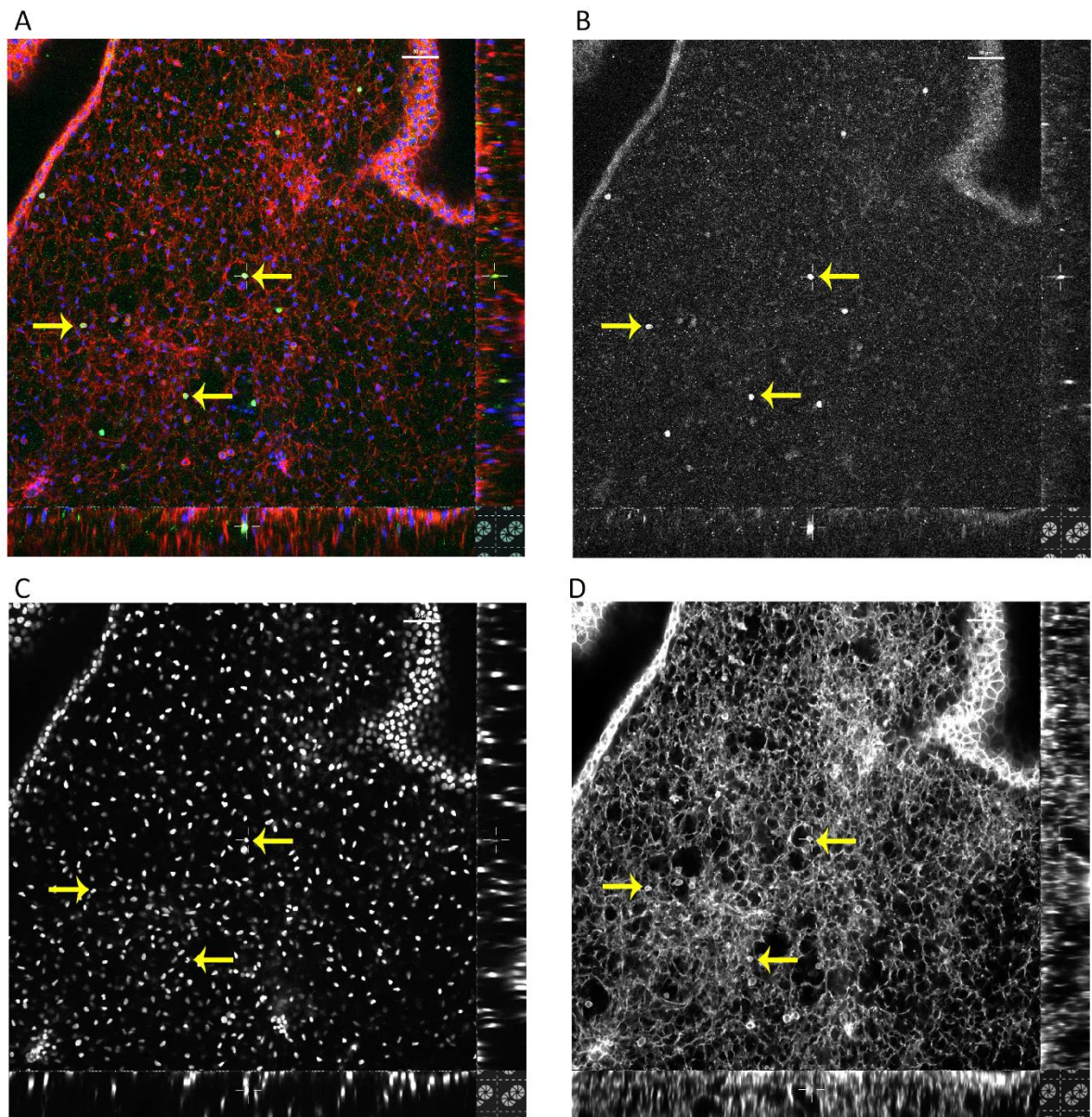


Figure 4.21, LV MDA-MB-231 GFP+ cells, ZB2 clone invading CAM. Whole CAM imaged at low resolution, 4 days after cells were seeded onto scratched CAM. Staining of whole CAM was conducted using phalloidin (red channel) DAPI (blue channel) and an anti-GFP antibody to enhance fluorescence of GFP+ cells in the green channel. Cells can be seen to have invaded CAM and are compact/rounded in morphology. **A** three channels merged, **B** green channel shows GFP cells only, **C** DAPI, blue channel, **D** red channel. Yellow arrows indicate the same cells in each image. Scale bar is 50μm. Images were acquired using a Nikon A1 Plus confocal microscope.

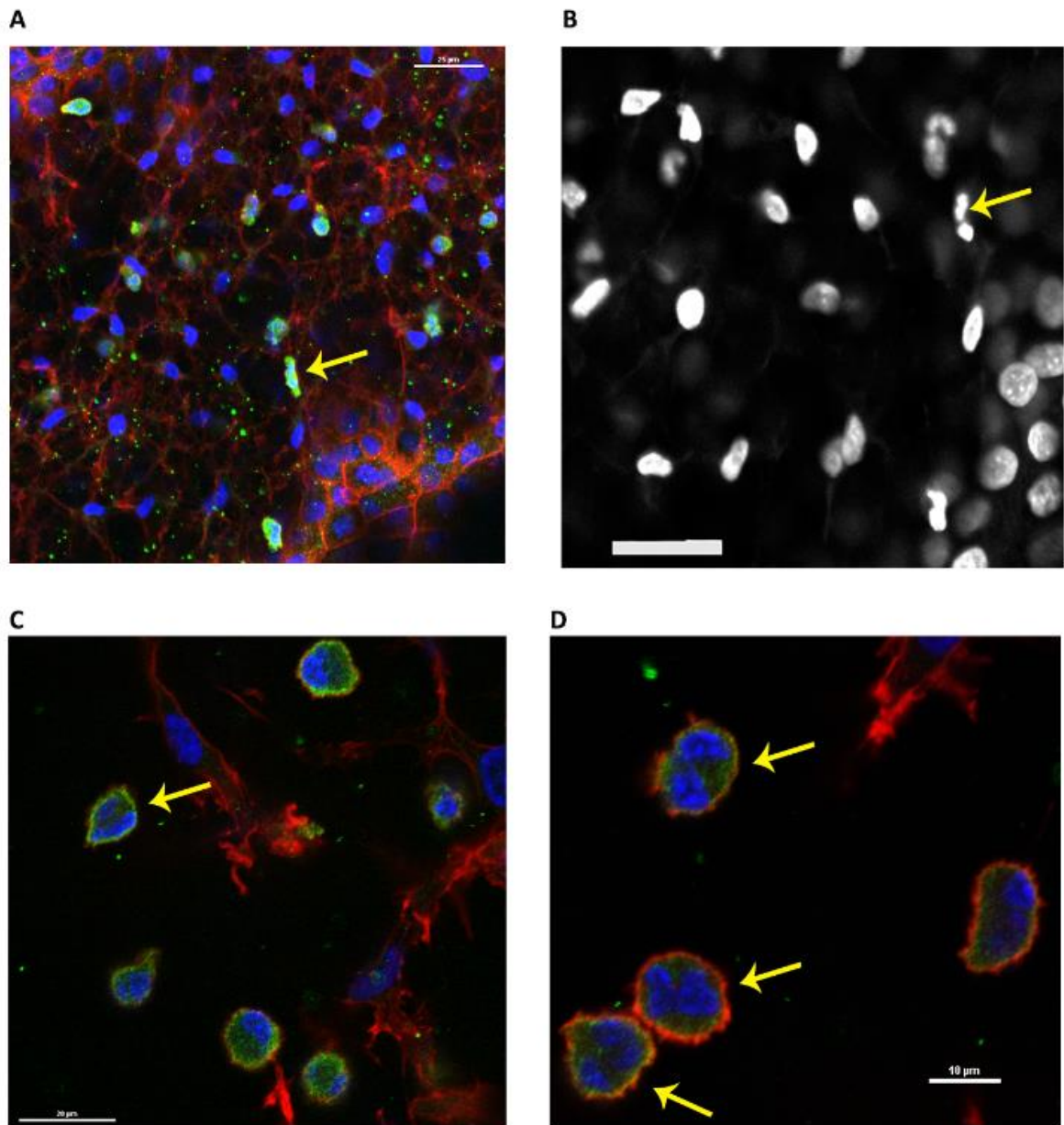


Figure 4.22, LV MDA-MB-231 GFP+ ZB2 cells on whole CAM. Cells can be seen within CAM, rounded up and dividing. Yellow arrows indicate cells in which two nuclei are visible. **A** Yellow arrow indicates two GFP+ cells, one which is dividing and the other seems to be attached. **B** Blue channel for A enlarged to show the nuclei for the same two cells in A indicated by the yellow arrow. **C** and **D** show rounded cells in CAM at high magnification. Images were taken using Nikon A1 Plus confocal microscope. A, B scale bars= 25µm, C scale bar= 20 µm and D scale bar = 10 µm.

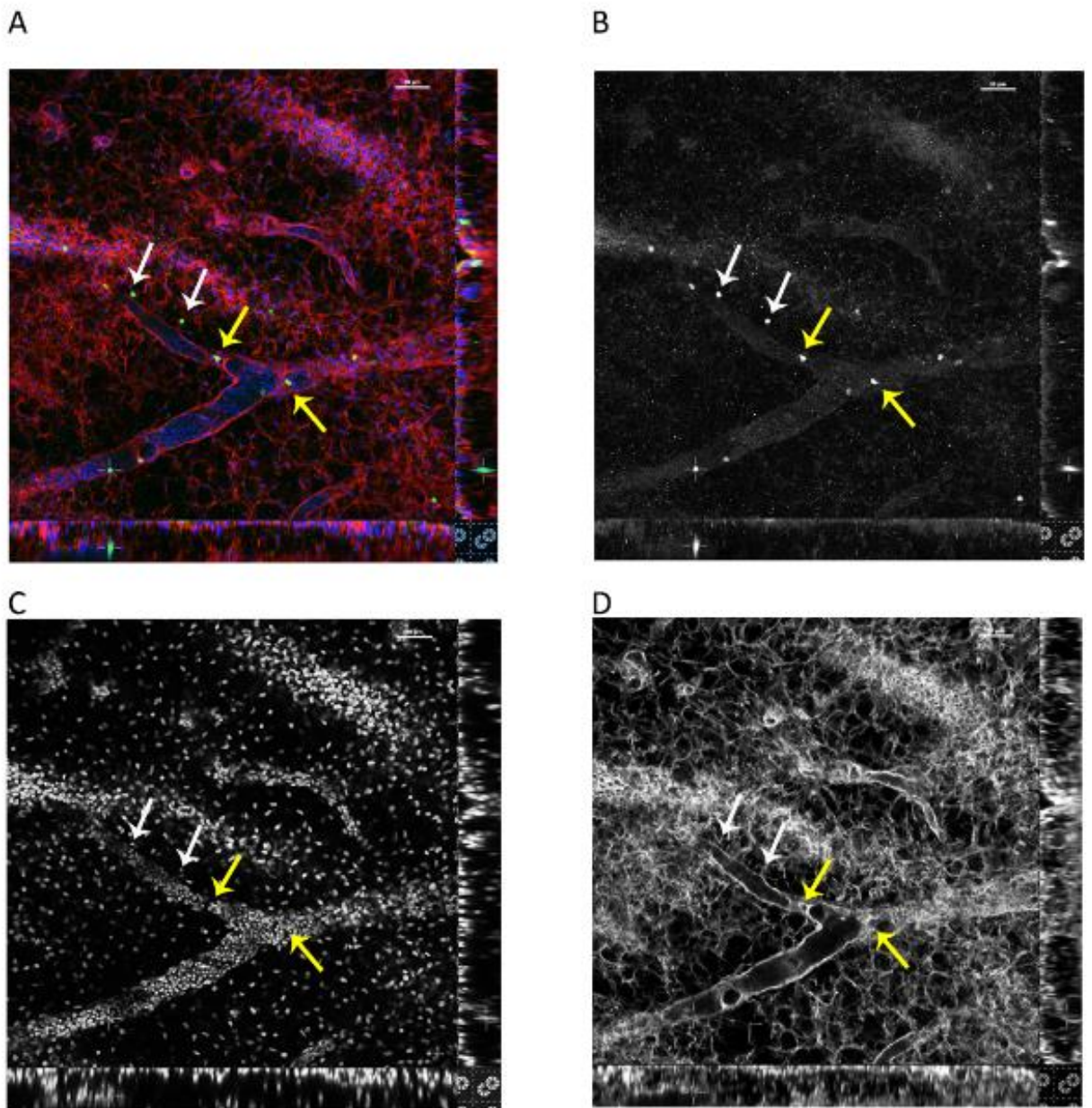


Figure 4.23, LV HT1080 GFP+ (A1D9) cells invading CAM. Whole CAM images with anti-GFP antibody to enhance GFP of cells against background auto-fluorescence of CAM. Cells can be seen within CAM tissue (white arrows) and blood vessels (yellow arrows). **A** three channel merged image, **B** GFP+ cells in green channel, **C** DAPI staining in blue channel, **D** phalloidin staining in red channel. Scale bars = 50µm. Images taken using Nikon A1 Plus confocal microscope.

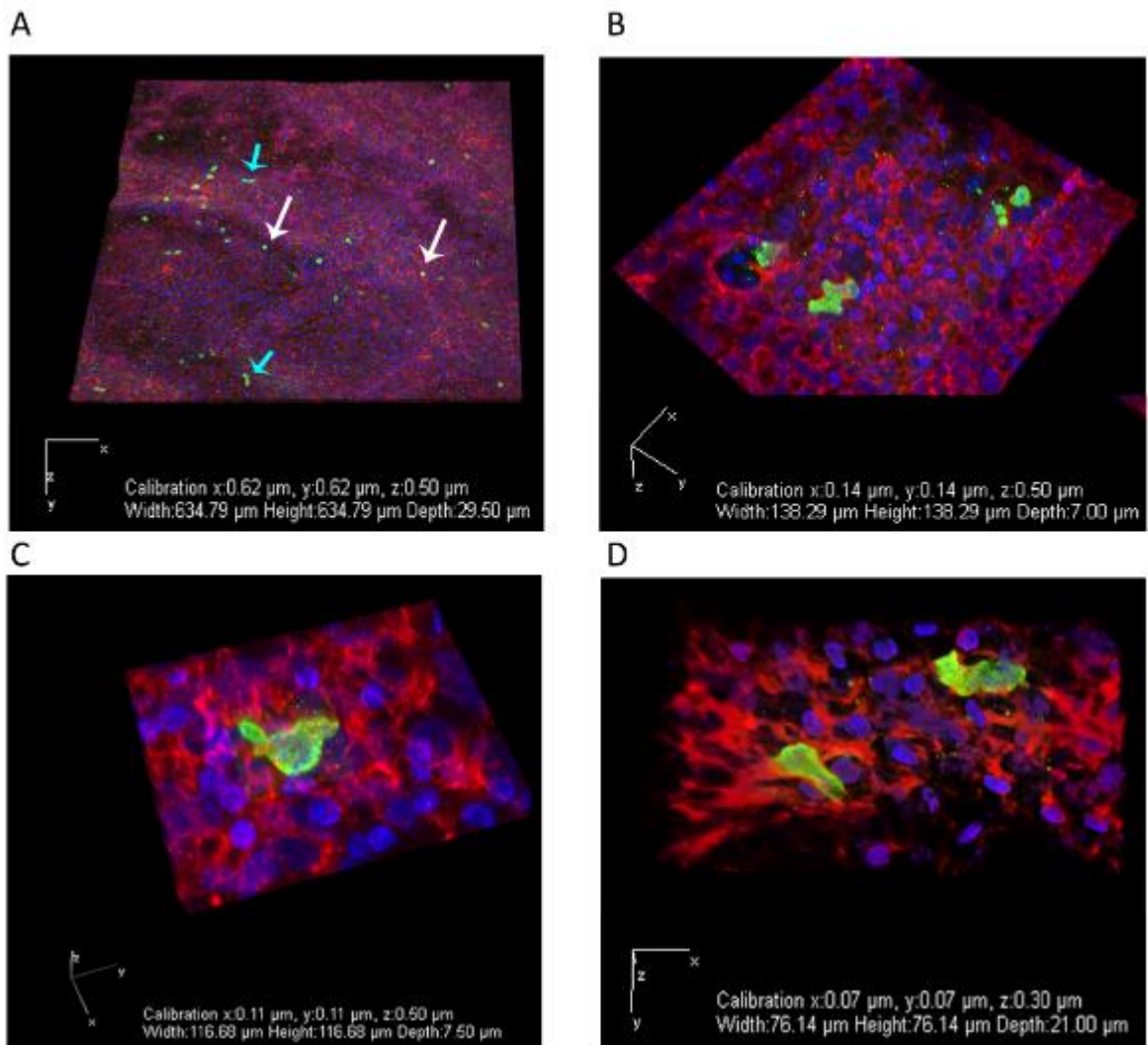


Figure 4.24, LV HT1080 GFP+ (A1D9) cells invading CAM. Whole CAM images were taken with anti-GFP antibody used to enhance the visibility of GFP cells against background auto-fluorescence of CAM. 3D reconstructions generated using NIS Elements software with dimensions as labelled. White arrows show rounded cells on CAM. Blue arrows show elongated/ ovoid cells on CAM. **A** shows GFP+ cells on/in CAM at lower magnification and cells appear to be well spread. Cells invading CAM are shown at higher magnification in **B-D**. Images were taken using Nikon A1 Plus confocal microscope.

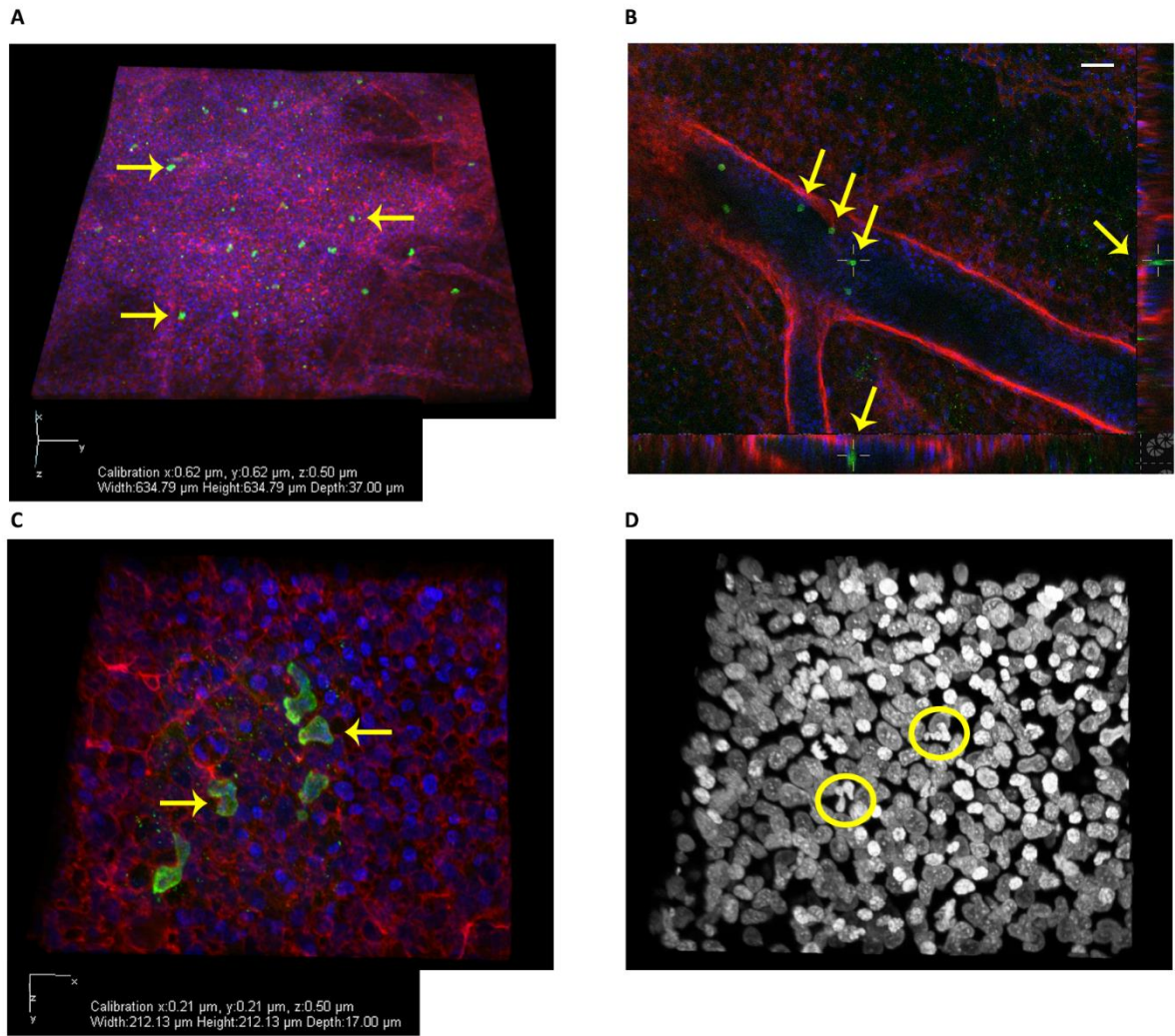


Figure 4.25, LV MCF7 GFP+ (DPF5) cells on/in whole CAM. **A** Whole CAM 3D image showing rounded and ovoid shaped GFP+ cells at CAM surface. **B** GFP+ cells can be seen located in blood vessels – yellow arrows. **C** GFP+ cells moving through CAM – two pairs of cells are indicated by yellow arrows and in **D** their nuclei (DAPI) are shown squeezing through CAM within the yellow circles. Channels: GFP+ in green, DAPI in blue and phalloidin stain for actin in red. Images taken using Nikon A1 Plus confocal microscope. Scale in B=50 μm . 3D scale for C and D is shown below C.

4.3.4. Determining a timeline of invasion

Whilst whole CAM imaging was informative, to be able to observe and investigate the timescales of invasion and cell interaction within the CAM in more detail, CAM sections were made and then probed using immuno-staining. An example CAM section is shown at Figure 4.26, labelled to show the different CAM layers and to give some orientation for the figures that follow. LV MCF7 GFP+ cells are shown within all layers of the CAM ECM and are compact in shape.

A timeline for CAM invasion was constructed for LV MCF7 and LV MDA-MB-231 GFP+ cells (Figures 4.27-8). In Figure 4.27 LV MCF7 GFP+ D1B6 cells can be seen invading scratched CAM with samples spanning a 5 day period shown. By the third day cells can be seen within CAM vasculature and have pervaded the CAM ECM well by day 5. In Figure 4.28 LV MDA-MB-231 GFP+ XB5 cells are shown at day1-3 and a 5 day sample for ZB2 is also shown. These sections show that cells have invaded CAM within the first 24 hours and are found both in CAM ECM and vasculature by day 3. Figure 4.29 shows sections for CAM that was not scratched prior to seeding in which both LV MCF7 GFP+ and LV MDA GFP+ cells were still invasive. Figure 4.30 shows that LV HT1080 GFP+ cells were also invasive on non-scratched CAM and could be found both in CAM ECM and in the vasculature amongst the chick erythrocytes.

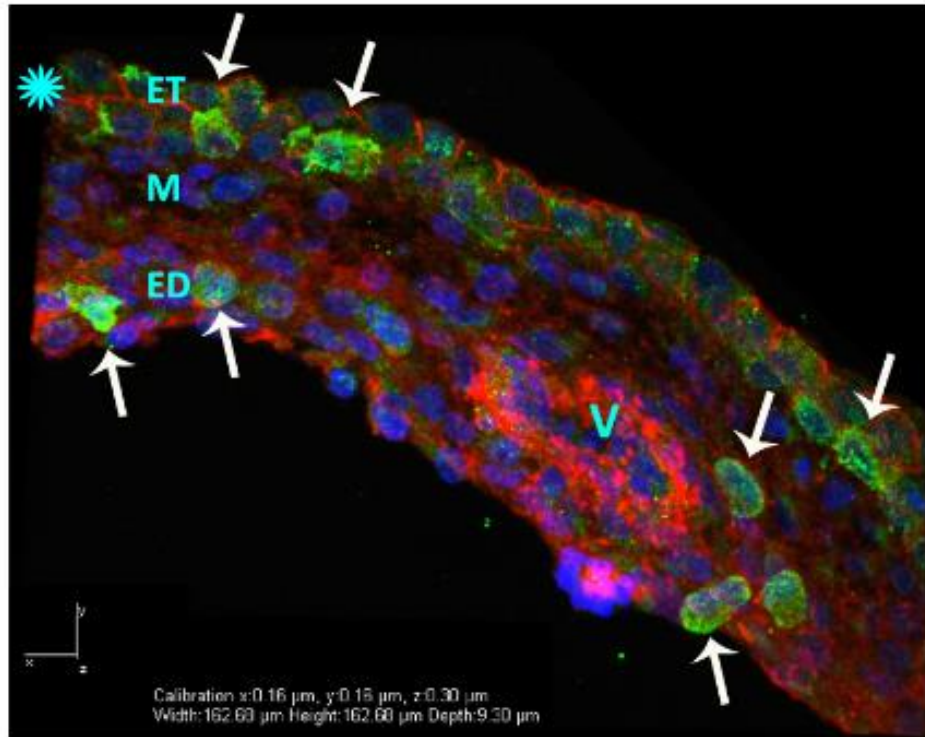


Figure 4.26, CAM sections showing the layered structure. The three layered structure of CAM is labelled in this section, according to the origin of the layer. ET (blue star) is derived from ectoderm, M from mesoderm and ED from the endoderm. The mesoderm is highly vascularised – a blood vessel is labelled V in this section. Image taken using Nikon A1 Plus confocal microscope and shows LV MCF7 GFP+ cells invading CAM (white arrows).

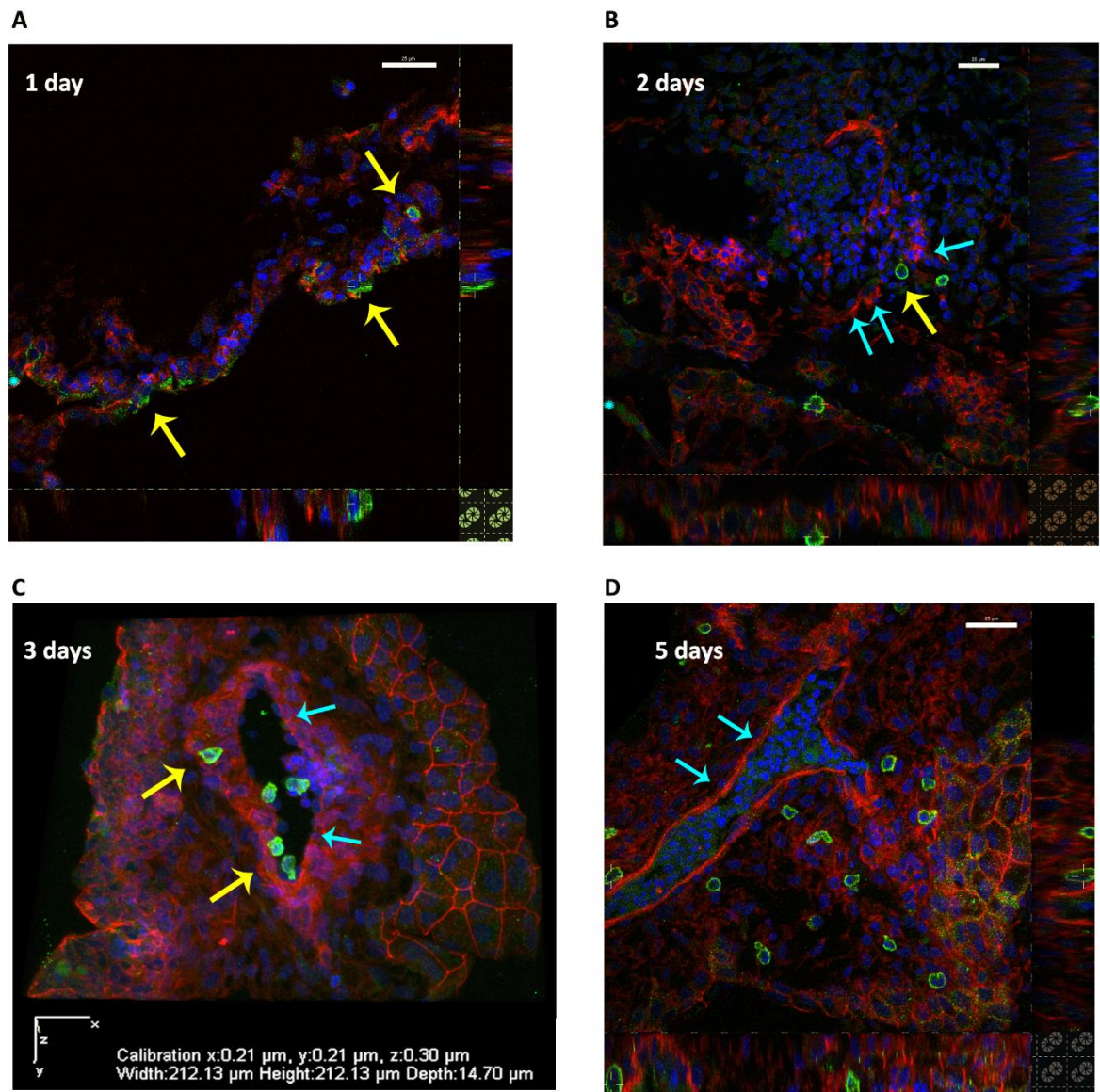


Figure 4.27, Timeline for invasion of scratched CAM for LV MCF7 GFP+ cells (D1B6). CAM was harvested from eggs at daily intervals, fixed, stained with phalloidin, DAPI and anti-GFP antibody to enhance GFP+ cell fluorescence. Sections were made, mounted and images made with Nikon A1 Plus confocal microscope. Samples range from 1 to 5 days after seeding. **A** +1 day sample. GFP+ cells at surface and beginning to invade CAM (yellow arrows). **B** +2 day sample, GFP+ cells can be seen in CAM tissue (yellow arrow) and close to CAM vasculature (blue arrows). **C** +3 day sample. GFP+ cells (yellow arrows) can be seen in CAM blood vessel (blue arrows). **D** +5 day sample. Many GFP+ cells can be seen throughout ECM tissue. Blue star at lower left on A, B, denotes top surface of CAM (See Figure 4.26). Scale bars: A, D 25 μ m and B 20 μ m.

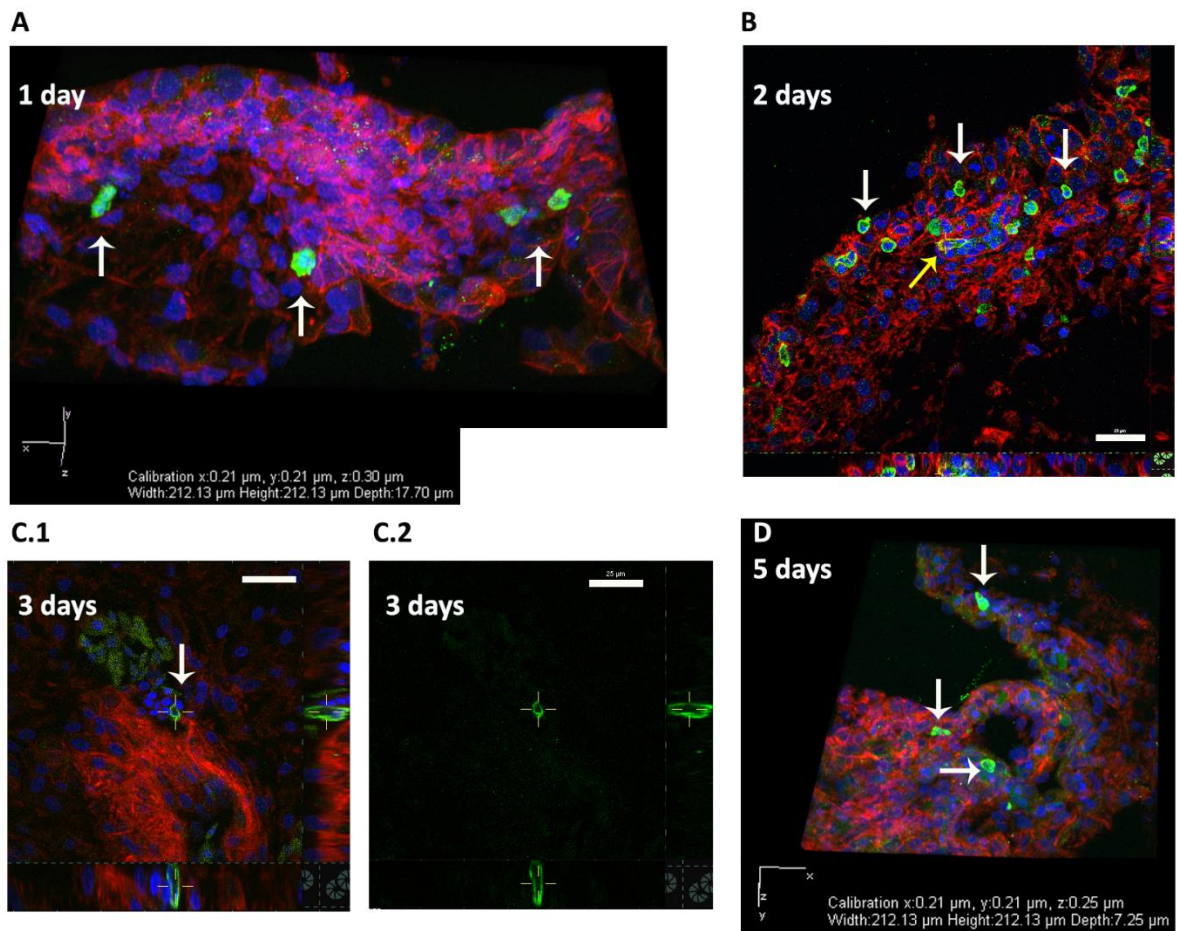


Figure 4.28, Timeline for invasion of scratched CAM for LV MDA GFP+ cells. CAM was harvested from eggs at daily intervals, fixed, stained with phalloidin, DAPI and anti-GFP antibody to enhance GFP+ cell fluorescence. Sections were made, mounted and images made with Nikon A1 Plus confocal microscope. Samples for 1-3 days are from XB5 and 5 day sample is ZB2 clone. **A** +1 day sample. GFP+ cells can be seen within mesenchymal layer of CAM (white arrows). **B** +2 day sample, GFP+ cells can be seen throughout CAM tissue (white arrow) and within CAM vasculature (yellow arrow). **C.1** + 3 day sample. One GFP+ cell shown close to blood vessel (white arrow) and **C.2** Green channel only shows the cell morphology in CAM more clearly. **D** +5 day sample for ZB2 clone. GFP+ cells can be seen located throughout ECM tissue (white arrows). Scale bars: B, C 25µm.

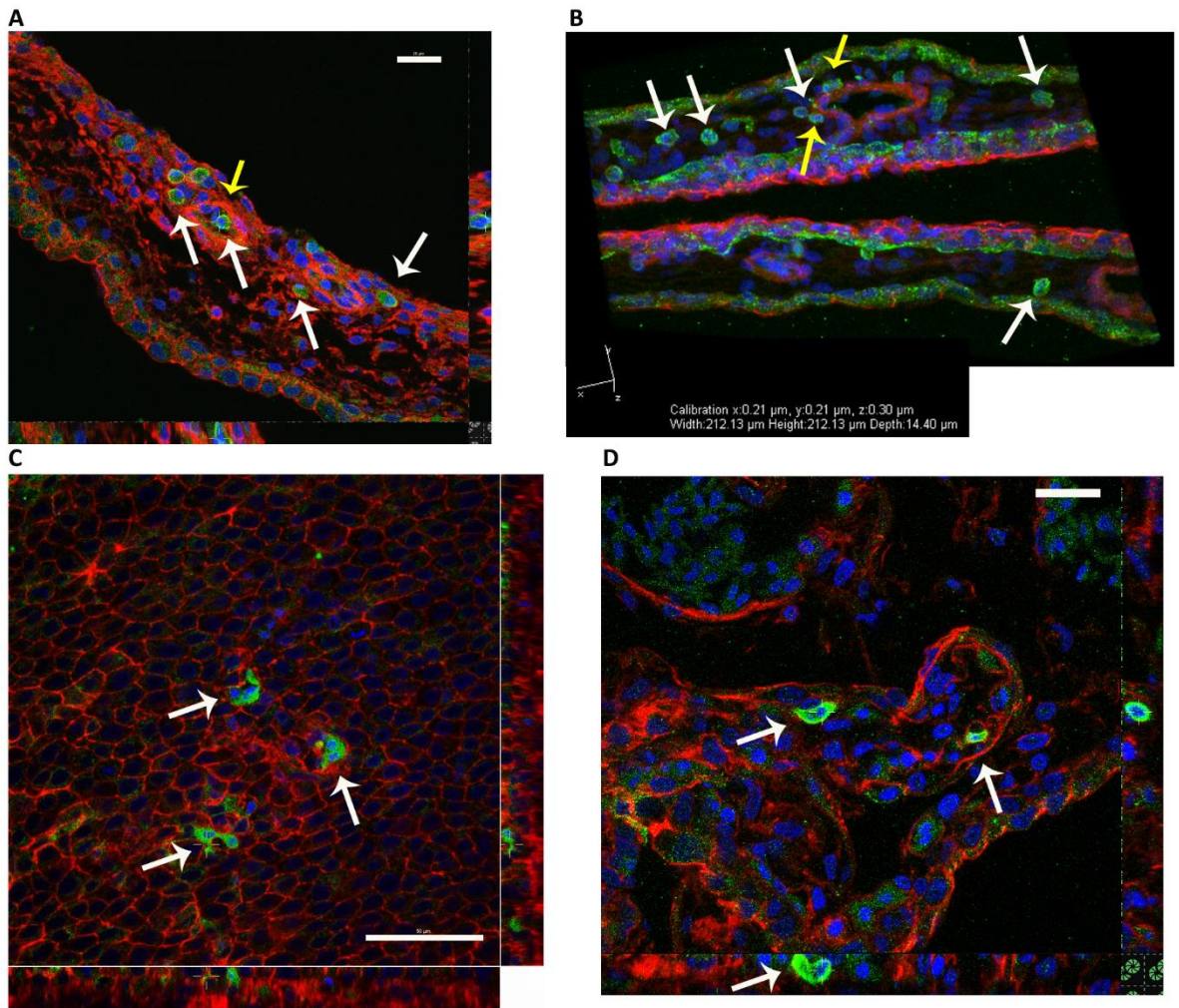


Figure 4.29, MCF7 and MDA-MB-231 cells were invasive on unscratched CAM. LV MCF7 GFP+ cells (DPF5) are shown within CAM **A** 3 days and D1B6 **B** 5 days after seeding at CAM surface. LV MDA-MB-231 GFP+ cell are seen 3 days after seeding for YA1 **C** and ZB2 at **D**, cells indicated with white arrows in CAM tissue and on/in blood vessels with yellow arrows. Images were taken with Nikon A1 Plus confocal microscope. Scale bars A= 20μm, C = 50μm and D = 25μm.

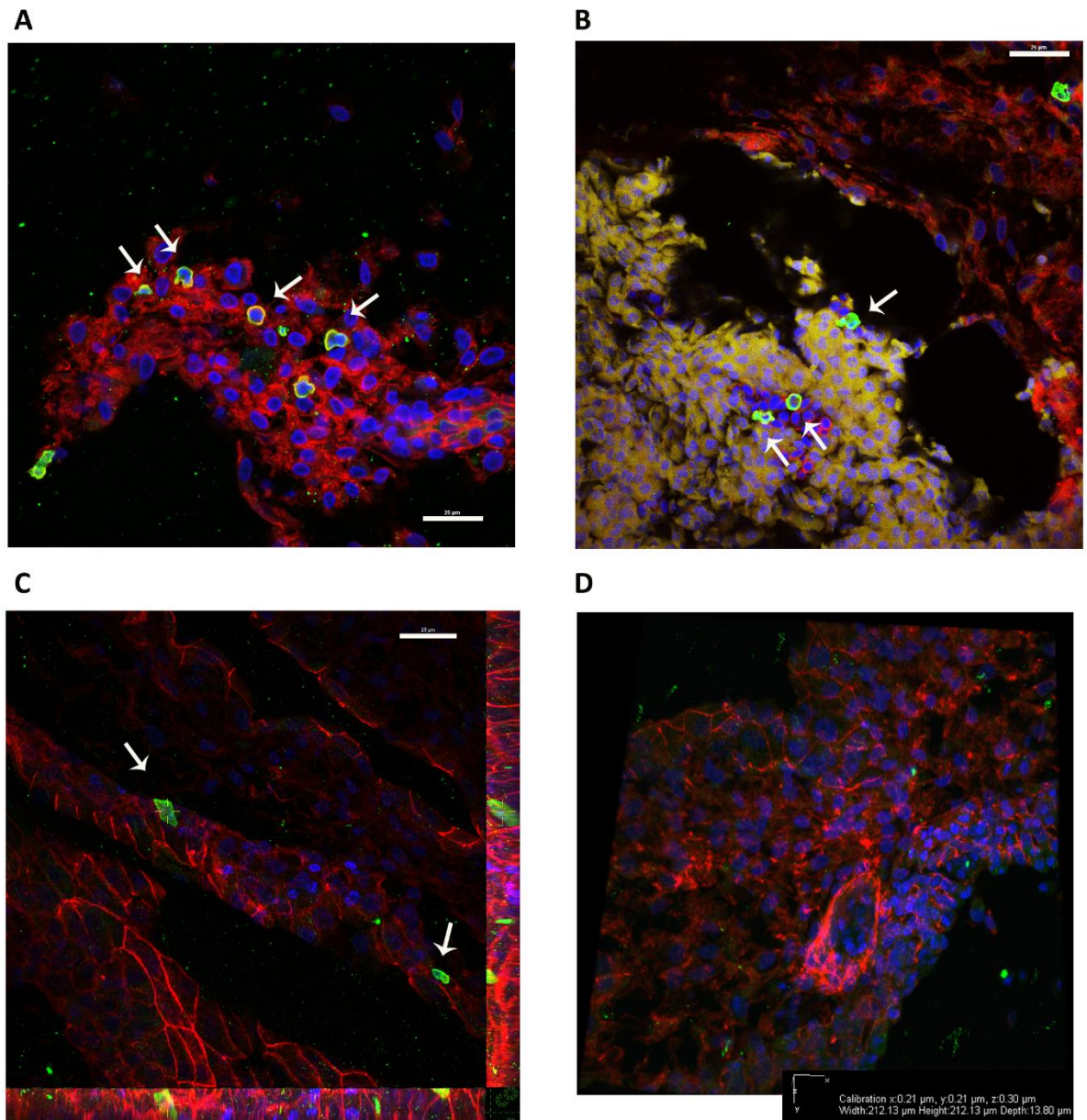


Figure 4.30, LV HT1080 GFP+ cells invaded without scratching CAM. **A** A1D9 cells 3 days after seeding are seen within mesodermal layer of CAM tissue (white arrows). **B** ZB5 after 3 days with GFP+ cells in blood vessel (white arrows) seen amongst erythrocytes (imaged in far red channel and appear yellow here), **C** B696 after 3 days seen within CAM tissue. Scale bars = 25µm. **D** 3D reconstruction of CAM with no cells stained with anti-GFP antibody. Images taken with Nikon A1 Plus confocal microscope.

4.3.5. Migration or colonisation?

A number of CAM images have shown evidence of cell division of GFP+ cells on or in CAM tissue and so to examine proliferation of these cells further, counter staining for the protein marker for proliferation, Ki67, was conducted using a far-red secondary antibody and the fourth available laser on the Nikon A1 Plus confocal microscope to image CAM tissue containing GFP+ cells. Figure 4.31 A and B show images of GFP+ cells which seem to be dividing within CAM, these having been counter stained with anti-GFP antibody to check their provenance. Figure 4.31 C and D show CAM stained for Ki67 (far red laser shown in white) which indicates a number of proliferating (human) cells within the CAM tissue. Control images for CAM with no cells seeded for the far red channel are shown at Figure 4.32. These two pieces of evidence together suggest that human cancer cells were proliferating within the CAM tissue.

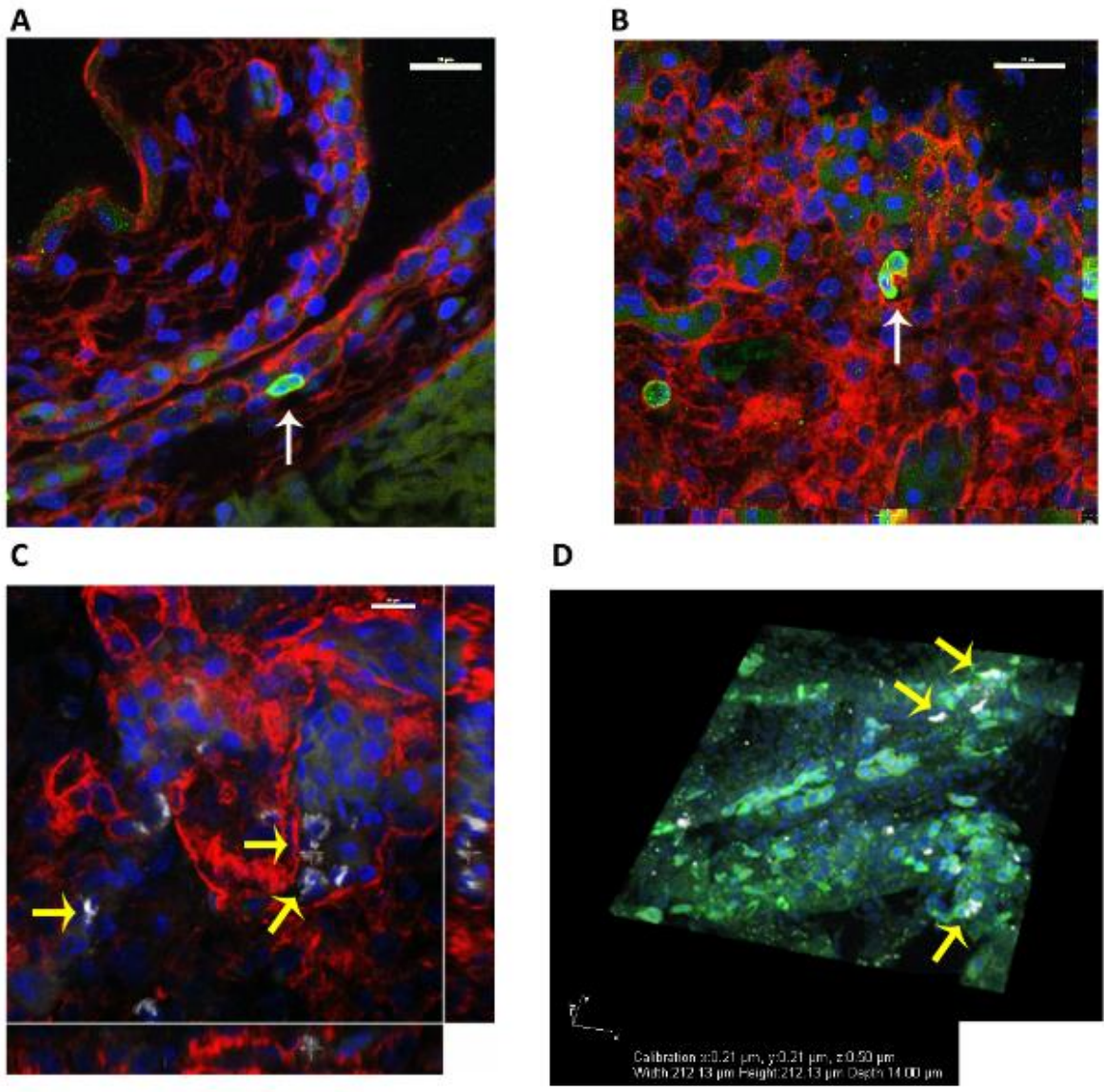


Figure 4.31, Cell division on CAM. **A, B** Images of LV HT1080 GFP+ B696 cells immuno-stained with anti-GFP antibody were captured showing two nuclei within one cell (white arrows) which suggested that cells were dividing within CAM. Further immuno-staining for Ki67 for LV MDA-MB-231 cells showed that the Ki67 marker for cell division was expressed in cells within CAM (yellow arrows), **C and D.** Images taken with Nikon A1 Plus confocal microscope. Scale bars = A, B 20 μ m and C 10 μ m.

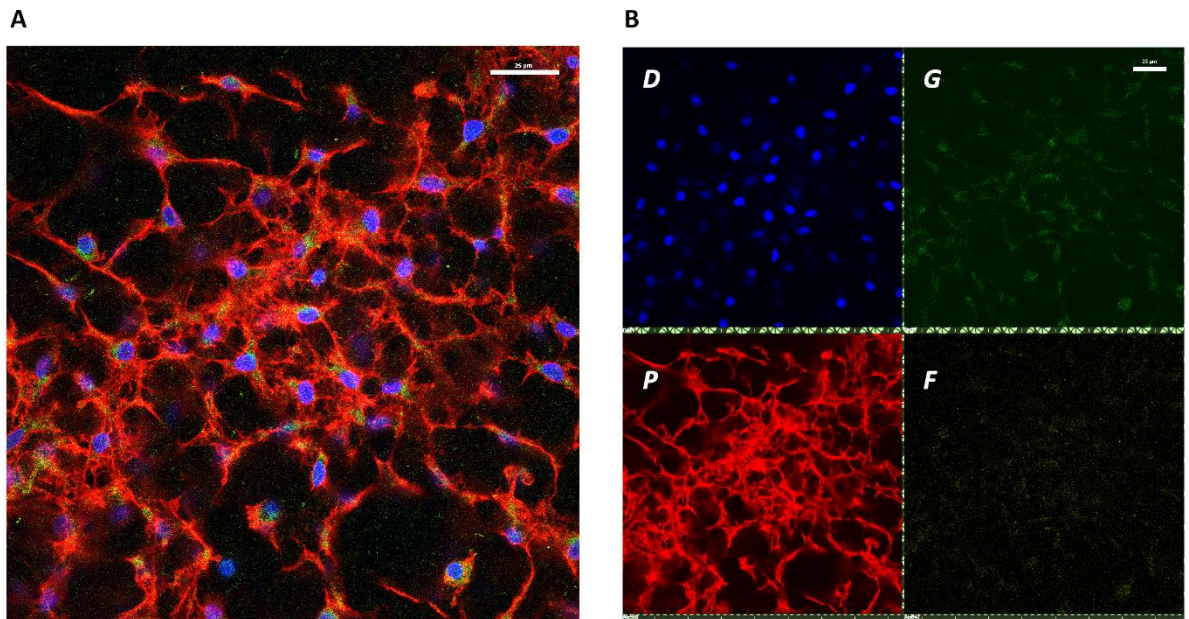


Figure 4.32, CAM with no cells seeded stained for Ki67. **A** shows the merged image for all four channels. **B** shows *D* DAPI in the blue channel, *G* green channel (no GFP+ cells seen here so green is auto-fluorescence only), *P* phalloidin in the red channel shows CAM structure and *F* is the Far Red channel which shows a small amount of background noise (yellow). Confocal images were taken using a Nikon A1 plus microscope. Scale bars = 25μm.

4.4. Discussion

The chorioallantoic membrane (CAM) of the developing chicken provides a highly vascularised extracellular matrix environment with many similarities to human tissue. This living model quickly develops a useful and relevant tissue structure for the study of cell interactions within ECM and to visualise and monitor progress of intravasation and extravasation of cancer cells added topically. Used and developed initially for the investigation of developmental processes, in more recent years it has been used to explore the cell biology relating to disease processes. The metastatic process has been explored in the developing chick embryo model in a number of ways at different times (Kain et al. 2014, Ribatti 2010). In this project, the chick embryo and in particular the CAM, was investigated as a potential *in vivo* model for the exploration of cell-cell and cell-ECM interactions which take place as part of the metastatic process. Ideally the full range of cell morphologies and behaviours seen within human cancer metastasis should be represented within the model. Using staining techniques and microscopy, cell interactions between seeded human cells and human cells and chick cells could be explored with reference to cell morphology and cell position on or in the CAM.

Initial work was carried out in partnership with Dr Alan Burns' laboratory at University College London, in which the chick model is used to study diseases associated with abnormal childhood development. The skills transfer and ideas generated as a result of working with both Dr Alan Burns and Dr Jean-Marie Delalande enabled the development of a working assay which could be transferred, set up and further explored at the University of Reading. The initial results were gained using green fluorescent cells which expressed a myristoylated GFP membrane insertion protein, the plasmid for their development having been kindly gifted by Dr Mike McGrew of The Roslin Institute, Edinburgh. However, when these cells

were observed on CAM and characterised *in vitro*, the low levels of GFP expression meant that the cells were difficult to identify once within the CAM tissue. The cell membranes of myristoylated GFP+ cells also appeared to be deformed and so they were not a suitable representative cell line for the original parent cells. It was determined that the ideal tool for further work would be an invasive/migratory metastatic cell line which could be clearly identified above the auto-fluorescence of the CAM. Based on recent work within other laboratories, lentiviral transduced permanently expressing fluorescent cells were likely to provide a good GFP+ signal without affecting the cell membrane and so were proposed as a good tool to develop for the purpose. A set of three plasmids which could be assembled to make a lentiviral vector for the expression of GFP in the cell cytoplasm was provided for the purpose by the Foster laboratory at University of Reading. The expansion of plasmid stocks, creation, infection and production of the GFP lentiviral vector was carried out as part of this project, ultimately leading to the transduction of three stock cell lines which could be used to investigate invasion and metastasis in CAM these being: MCF7 and MDA-MB-231 breast cancer cells and HT1080 fibrosarcoma cells. Clones from these cell lines were clearly visible at the CAM surface when seeded however, once within the CAM tissue and vasculature they were more difficult to identify.

Whilst GFP+ cancer cells could be identified for some samples, the natural auto-fluorescence of chick tissue and cells was problematic when imaging using fluorophores to differentiate between different cells and structures of the assay. With the available light emission spectrum for confocal laser microscopy spanning blue light to far red (400-700nm), four laser lines / channels were available to detect fluorophores used for staining and detection. In order to stain the CAM, DAPI and phalloidin were used to identify nuclei and tissue structure. Cancer cells were identified using DAPI (nuclei), phalloidin (actin cytoskeleton)

and GFP (cell cytoplasm). The peak emission and detection channel for each stain used was: DAPI: 461nm – blue channel, (enhanced) GFP: 509nm – green channel and phalloidin atto 565 at 592nm – red channel, leaving the far red channel available for a further stain if required. The extracellular matrix of the CAM auto-fluoresced mainly in the green channel, however erythrocytes auto-fluoresced in both green and far red channels. This meant that fluorophores used whose emissions were detected in these channels had to be much brighter than the background auto-fluorescence of the CAM and CAM cells. Unfortunately the auto-fluorescence of some CAM cells was similar to the GFP fluorophore emission and so it was difficult to differentiate between human and CAM cells. In particular the chick erythrocytes fluoresced brightly in the green channels. As chick erythrocytes are nucleated, they could not be deducted due to lack of nuclei, however as they were also auto-fluorescent in the far red channel, collecting emissions from all four laser channels meant that the erythrocytes could be identified and discounted from images.

The confocal imaging technique, spectral unmixing was employed to reduce the confounding effect of auto-fluorescence, however, CAM cells were still detected within the defined filters and so they could not be exclusively identified or excluded using this technique. Other research published in which GFP+ cancer cells have been employed within the CAM assay, have viewed the cells mainly in the live context. Where research has entailed the growth of a GFP+ tumour at the CAM surface, evidence of the outward migration of cells has clearly shown GFP+ cells moving over CAM. Intravital imaging has been successfully employed to conduct fluorescence time-lapse movies in this way and GFP+ cells have been successful in their application (Klingenberg et al. 2014, Zijlstra et al. 2008). However, the GFP+ cells have an origin in this case and can be tracked from their start point so their provenance is known. When searching for GFP+ cells using a green filter in either whole CAM or in sections, the

researcher is reliant purely on the emission spectra from the fluorophores used plus cell characteristics to determine their provenance. In fact when reviewing the evidence presented by other researchers, specific identification of human cancer cells is always necessary, for example using anti-CD44 for the identification of cells in tissue (Zijlstra et al. 2004). In the case of this research, the GFP expression alone against the background auto-fluorescence was insufficient to identify the human cells and had to be augmented by an anti-GFP antibody for clear identification. When further staining was required to probe for specific mechanisms with cancer cells, the far red channel could be used but care to exclude background auto-fluorescence from CAM and erythrocytes was necessary.

Cancer cells for all three cell lines, were seen within the CAM and CAM vasculature within three days of seeding. Individual MDA-MB-231 GFP+ cells were seen to adopt a rounded compact morphology whether in CAM tissue or vasculature, quite different to the elongated mesenchymal morphology seen when the same cells were encapsulated in 1mg/ml collagen *in vitro*. HT1080 GFP+ cells also adopted a more compact morphology in CAM however they were often more irregular in shape as they appeared to be pushing their way through the CAM tissue layers. HT1080 protrusions into the CAM were smoother and more rounded than the spikey invasive protrusions for the same cells seen in collagen *in vitro*. MCF7 GFP+ cells used as a control cell line in CAM because *in vitro* they do not typically migrate, were seen to have migrated into CAM tissue and were evident either as individual cells or as pairs. This suggests that in CAM, cells were either migrating together or they were dividing, with daughter cells remaining attached to each other following division. Further staining for cell junction proteins such as e-cadherin or keratin would elucidate this behaviour. The MCF7 cells behaviour in CAM was thus different to that seen *in vitro*. When cultured on a 2D surface, MCF7 cells proliferate to form mounds with cells making tight

junctions which can be seen when cells are stained for e-cadherin (Borley et al. 2008), however in a 3D environment these cells are known to be more invasive (Nguyen-Ngoc et al. 2012, Vantangoli et al. 2015). The CAM provides not only a 3D context but also a whole range of growth factors and nutrients which give potential for chemotactic guidance cues for cell migration (Berzat and Hall 2010). Cells from all three lines and clones were seen to have invaded throughout the CAM and were seen within CAM vasculature. From these experiments it was not clear whether cells moved mainly down through the CAM from the surface or whether they moved into vasculature and then escaped to colonise CAM at distant sites. Both of these behaviours have been reported within the literature. In a recently published paper studying the tumour microenvironment of Burkitt lymphoma on CAM, the lymphoma cells were seen to migrate mainly down through the CAM ECM tissue (Klingenberg et al. 2014). In research reported by the Quigley lab, HT1080 cells from engrafted tumours were seen to wrap themselves around blood vessels and when GFP+ HT1080 cells were injected into the CAM vasculature they were seen to cling to blood vessel walls (Deryugina and Quigley 2008b). Extravasating GFP+ cancer cells were also identified in groups in CAM ECM at distant sites, having emerged from blood vessels. Thus steps involved in both intravasation and extravasation have been reported for the CAM assay and it is likely that intravasation and extravasation had occurred in these experiments based on the location of cells seen both within and near vasculature as well as throughout the CAM within just 3-5 days of seeding. Although a specific quantification of cell morphology of cells that had invaded into the CAM was not conducted as part of this project, it is clear from the data shown in this chapter that were a number of sections to be made from CAM seeded with cells from the three different cell lines and these imaged under the same conditions, that the aspect ratio for the cells could be quantified and compared. Indeed this could be carried out

for cells found according to the timeline of invasion as well as for the CAM layer in which cells were found.

In these experiments, cells were found throughout the CAM, regardless of whether the CAM surface had been scratched. This suggests that cells are able to penetrate the CAM ECM and or vasculature using their own mechanisms such as matrix metalloproteases to break down tissue. However, it is possible that just the action of placing cells on the CAM could cause minor damage to the delicate two celled ectodermal layer at the CAM surface and that this is sufficient to aid the cells in their initial invasion. Indeed, previous research suggests that the ectoderm of the CAM is indeed easily susceptible to such injury (Armstrong et al. 1982). However, in the developing microenvironment surrounding a tumour, the action of cell growth and division and pressure on surrounding tissues may not be dissimilar in nature.

Within the CAM, there was evidence of an immune response which occurred following the addition of human cancer cells, with small nucleated leukocytes seen within the collagen at borders around the GFP+ cancer cells. Evidence of an inflammatory response when either wounding the CAM (Ribatti et al. 1996) or when collagen onplants were added has been documented in other research, with the infiltration of leukocytes visible in onplants within 24 hours of their addition on the CAM (Deryugina and Quigley 2008a, Zijlstra et al. 2006).

The developing immunity and ability of the chick embryo to generate an immune response can be seen as a benefit of using the CAM model providing the opportunity to investigate the interactions between immune cells and cancer cells, one that is absent in the immunocompromised mouse model for example. In fact the Burkitt Lymphoma study found that chick leukocytes infiltrated the developing lymphoma on CAM providing useful

information regarding stromal interactions in the tumour microenvironment (Klingenberg et al. 2014).

With the clear mobility and invasion of cells within the CAM and its vasculature, there is potential for the use of the CAM assay as an *in vivo* model as part of a range of assays to investigate metastasis further. There are many advantages to its use but also a number of drawbacks and these are summarised in Table 4.1 below. When using fluorescent staining and probes, careful staining and analysis is important to ensure that the high background auto-fluorescence does not interfere with interpretation of data. For harvested and fixed samples, panel staining is possible to identify specific proteins present in interacting cells. Cross reactivity with chick antibodies must also be considered and carefully controlled for if this approach is taken.

Table 4.1, The advantages and disadvantages in using the CAM as an *in vivo* model to study cancer metastasis

Aspect	Advantages	Disadvantages
Time	Short and fast development time of chick embryo <i>in ovo</i> enables many experiments and replicates.	Metastasis is a process that occurs over time in the real environment and so the establishment and colonisation of a metastatic niche in just 5 days is too short in real terms.
Set Up	Easy and cheap. No licence required if harvesting within 75% of development cycle.	Developing tissue may not respond in the same way as established tissue surrounding a tumour.
Equipment	Readily available and obtainable equipment required - Incubator and dissection microscope.	Ideally need fluorescence microscope for live work with camera and acquisition software and access to confocal microscope for fixed and stained tissue.
Tissue Histology	Living system with all the benefits of blood flow and live tissue accessible for experimentation. CAM is similar to human ECM and highly vascularised. Thin and partially transparent. Developing immune system allows exogenous tissues to be added.	Tissue auto-fluorescence; Inflammatory response when cells are added to CAM.
Application	Well researched as a vertebrate model and can support mammalian cells. Used as an <i>in vivo</i> model for a number of processes and diseases including angiogenesis and metastasis.	For drugs testing: cells / explants ideally need to be treated before addition to CAM and drugs tested could adversely affect CAM and chick so that model is compromised.

The interaction of cells with other cells and with the ECM *in vivo* in this model is challenging due to the tissue auto-fluorescence of developing chick and associated tissues. *Ex ovo* approaches to cell study on/in CAM generally require special equipment such as intravital microscopy equipment. Imaging of GFP+ cells on excised CAM was explored as part of this

work but even though weighted down or stretched out, samples tended to shrink and contract soon after harvesting and so time-lapse imaging was only possible over short periods. Taking the idea of CAM excision further, harvesting and decellularizing CAM was considered as a possible option for the study of cell interactions in a 3D environment which could be compared and contrasted to interactions seen both in *in vivo* CAM assay and with the *in vitro* assays already described.

Decellularization of tissue is a biomaterials approach that has been taken in recent years in the development of allografts and implants for reconstructive surgery, for example in skeletal muscle (Fishman et al. 2013) and heart valve development (Theodoridis et al. 2015). Decellularized tissues have great potential in providing a biologically relevant three dimensional matrix in which to explore cell behaviours and interactions. Decellularization was explored in this project as a method of providing the structure of the CAM in which to study cell-cell and cell-structure interactions, without the complication of the chick/CAM cells. This novel approach to studying cancer metastasis using the CAM could provide useful insight into the cellular mechanisms involved in cancer metastasis yet benefit from the ease, low cost and simplicity of the developing chick embryo environment as a host for the provision of sample tissue. The decellularization of chick chorioallantoic membrane tissue is presented in the next chapter as a novel *ex vivo* approach to link the study of metastasis *in vivo* in the CAM assay to that taken *in vitro* described in the first chapter.

5. Development of Decellularized Tissue as a 3D Context for the Exploration of Metastasis

5.1. Introduction

Cell culture in two dimensions places cells in an atypical environment in which they lack the tissue context and cues of a relevant biological niche. Many attempts at constructing a suitable 3D cell culture environment have been made, frequently using tissue extracts such as collagen, or using non-biological matrix materials such as the proprietary Alvetex polystyrene scaffold (Reinnervate). However, many of these are either overly simplistic, lacking the structure and variable features of a natural matrix or they are unnatural in construction and therefore not representative of the live environment. The ability to image cells interacting in a 3D environment is also an important consideration, with any model ideally providing the ability to image interactions in real-time as well as post harvesting.

Tissue engineers have developed a range of approaches to both study and develop artificial tissue environments. Artificial matrices have formed an important part of this development but in recent work acellular living tissue has been prepared and used for population as a more relevant and host compatible structure. Tissue engineering using decellularized tissue as a framework for tissue reconstruction is being pioneered in a number of surgical specialties including: orthopaedics – cartilage grafting (Schwarz et al. 2012) and musculoskeletal reconstruction (Cheng et al. 2014, Fishman et al. 2013); in ophthalmology for corneal replacement (Gonzalez-Andrades et al. 2011, Shafiq et al. 2012) and in all or partial organ reconstruction such as liver (Mazza et al. 2015), heart valve (Theodoridis et al. 2015) and the myocardium (Guyette et al. 2016). A number of different approaches and protocols for decellularization have been developed and compared, each tissue offering its

own specific features and challenges. One approach has been the decellularization of whole organs such as liver and heart (Crapo et al. 2011, Guyette et al. 2014) and others have sought to decellularize tissue sections (Medberry et al. 2013). Different approaches to the decellularization protocol have included the use of osmotic pressure, variation in pH and use of chemicals or more typically a combination of all three (Crapo et al. 2011, Guyette et al. 2014). Recently decellularization under pressure for whole organs has also been investigated as a means of better retaining tissue integrity (Momtahan et al. 2015, Struecker et al. 2015).

Stem cell differentiation based on the cues provided by a decellularized matrix environment has been important when exploring the repopulation of material and organs (Gilpin et al. 2014, Hoshiba et al. 2016). Where stem cells are able to respond to the matrix and populate it in a natural way the resultant artificially produced tissue is likely to be a more robust and useful product, especially where donor stem cells are provided by the eventual recipient of reconstructed tissue.

There is an opportunity then to decellularize relevant tissues for use in the study of cancer metastasis. Processes involved in the early stages of metastasis such as cell migration and invasion could be studied in this context as well those of metastatic seeding and niche colonization relating to the later stages of the development of metastatic disease.

Surprisingly decellularized tissue has not been used extensively in this field to date, perhaps because protocols and tissue integrity of product material are still being developed.

However, the relevance of work with these materials has been shown in a recent publication in which healthy and diseased human tissues were decellularized, characterized and repopulated with metastatic cells, these adhering more readily to the diseased tissue and

showing differences in morphology and migration characteristics between the two environments (Dunne et al. 2014). Recently published breast cancer research used decellularized lung and liver tissue to explore the speed of invasion and colonization of three breast cancer cell lines: MDA-MB-231, MCF7 and 4T1. The highly mobile lines (MDA and 4T1) migrated deep into decellularized tissue sections and colonized them well, however the MCF7 cells stayed closer to the surface and did not populate the matrix as easily. The researchers also used the matrix to explore the importance of an epithelial-mesenchymal transition related protein, ZEB1, in migration and invasion, finding that its reduction lead to reduced invasion in the decellularized tissue environment (Xiong et al. 2015).

The matrix composition of decellularized tissue has also been investigated and utilized in tissue colonization studies as an *in vivo* implant. Recent research used liquefied decellularized lung and liver tissue as a coating for an artificial matrix to investigate cancer cell response to the decellularized tissue ECM components from diseased (DCM) and healthy tissues (HCM). When implanted, cancer cells colonized the DCM coated artificial matrix more quickly and extensively than the matrix coated with HCM (Aguado et al. 2016).

It is clear from this research that the ECM components of decellularized tissues are important for cells colonizing a matrix as they provide biological cues as well as a dynamic three dimensional structure. The composition and contribution of each component to the ECM within different tissues is known to vary, each tissue having its own unique tissue specific combination (Frantz et al. 2010, Nelson and Bissell 2006). It is, therefore, important to select an appropriate tissue for decellularization and recolonization based on the characteristics and features of the niche environment that is to be represented and to carry out the decellularization in way that maintains the structure and characteristics of the ECM

components of that tissue (Balestrini et al. 2015, Xiong et al. 2015). The main residual components of decellularized lung tissue have been characterized as: collagen IV, fibronectin and laminin. Epithelial ECM typically comprises collagen type 1, fibronectin and laminin and these are the main components known to be present in the chick chorioallantoic membrane structure (Deryugina and Quigley 2008b, Gabrielli and Accili 2010, Romanoff 1967).

The aim of this *ex vivo* section of the project was to assess the potential for the use of decellularized tissue as an approach to 3D cell culture in the study of cancer metastasis both for the study of invasion and for seeding and colonization of the metastatic niche. The overall aims were to develop decellularization and culture techniques using ECM materials relevant to the study of cancer metastasis.

The initial aim was to use decellularized rat lung provided by the CASE partnership company, Natural Biosciences, to establish the best method of preparing decellularized tissue for tissue culture purposes and then to facilitate, monitor and assess the extent of colonization of cells introduced. As the lung is a common site for the metastatic spread of breast cancer, it was a relevant tissue for the initial testing for the seeding and colonization of breast cancer cells. Methods of sample preparation and microscopy to determine the best approach to gather data for interpretation formed an important part of this investigation. Once a successful protocol for preparation, seeding and colonization had been established, the aim was to develop and optimize a protocol for the decellularization of CAM. This novel approach to the preparation of CAM would provide a second stage assay for the *in vivo* CAM work allowing the further exploration of cell-cell and cell-ECM interactions in a more tractable environment and over a longer period of time, *in vivo* assays being limited to just a few days. The final aim was to extend and modify the decellularization approach for a third

tissue type to provide an alternative tissue structure for comparison and contrast with the dLung and dCAM and to enable the further study of cell behaviours in different types of ECM in the study of cancer metastasis.

5.2. Materials and methods

5.2.1. Decellularization of chick chorioallantoic membrane

Decellularization was carried out using an adapted protocol based on that published by Medberry et al, 2013. Chorioallantoic membrane of chick eggs was harvested at day 9 or 10, and immediately flash frozen flat in liquid nitrogen then stored at -80°C until required. For decellularization, frozen CAM tissue was defrosted and placed in double distilled water at 4°C for 30 minutes. Once drained it was added to pre-warmed 0.02% trypsin (Gibco)/0.05% EDTA (Sigma) and stirred at 37°C for five minutes, washed with ddH₂O, then soaked in 3% Triton X100 for 5-10 minutes, washed twice in ddH₂O, soaked in 1M sucrose (Fisher) for 5 minutes, washed with ddH₂O, soaked in 4% deoxycholate (Sigma) for 5 minutes, washed twice in ddH₂O, soaked in 0.1% peracetic acid/4% ethanol (Sigma/ Fisher) for 5-15 minutes, washed twice then soaked in ddH₂O for five minutes. Decellularized CAM (dCAM) was then freeze dried and stored.

5.2.2. Decellularization of rat lung

Decellularized lung was prepared and freeze dried based on the protocol described by Medberry and colleagues for bladder tissue (Medberry et al. 2013) by Dr Mark Cranfield of Natural Biosciences (PhD CASE industrial partner) using lungs from 12 week old Sprague Dawley rats. The decellularized freeze dried rat lung was used as decellularized material (dLung) for seeding cells.

5.2.3. Decellularization of rat pup skin

Rat pup skin was harvested from pups at postnatal day 12-13 and frozen. Defrosted skin was treated with Immac (Veet) for ten minutes and hair/fur gently scraped from the surface, then cut into squares approximately 1cm² using blunt ended scissors. A protocol based on

that described by Medberry and colleagues was used as follows: rat skin pieces were stirred in double distilled water in a flask at 4°C overnight. Once drained it was added to pre-warmed 0.02% trypsin/0.05% EDTA and stirred at 37°C for sixty minutes, washed with ddH₂O, then soaked in 3% Triton X100 for 70 minutes at room temperature (all steps from here were at room temperature), washed twice in ddH₂O, soaked in 1M sucrose for 30 minutes, washed with ddH₂O, soaked in 4% deoxycholate for 60 minutes, washed twice in ddH₂O, soaked in 0.1% peracetic acid/4% ethanol for 120 minutes, washed twice then soaked in ddH₂O for five minutes. Decellularized rat skin (dSkin) was then freeze dried and stored. Prior to use dSkin was placed under a UV lamp for at least 15 minutes for UV sterilisation.

5.2.4. Culture of cells on dCAM

Decellularized CAM tissue was prepared for use as a growth matrix. dCAM was cut to size and placed in tissue culture labware under a UV lamp for at least 15 minutes for UV sterilisation. Sterile PBS was added and dCAM/PBS placed into a tissue culture incubator at 37°C / 5% CO₂ and left for 1-2 days. PBS was carefully aspirated and replaced with supplemented culture medium suitable for the cells that would be seeded. The tissue was returned to the incubator and left for at least 2 days. Medium was aspirated and either new medium (controls) or medium containing cells (experiments) were added to dCAM with just enough to cover the tissue. Plates were returned to the incubator for 2-6 hours until cells were seen to be attached to the matrix, then additional medium was added. The tissue/cells were monitored and medium replaced or tissue was transferred to new dishes as required. Images were taken to track colonisation using an inverted epifluorescence microscope (Zeiss Axio Vert.A1).

5.2.5. Culture of cells on dSkin

Decellularized rat pup skin was prepared in a similar way to dCAM. Pieces were placed in tissue culture labware dishes/plates and placed under a UV lamp for 15-20 minutes for sterilisation. They were soaked in PBS for at least 24 hours and then culture medium for another 2 days. Cells were added and left to adhere and then additional medium was added, ensuring the skin samples were completely covered. These were monitored and medium changed every three days. Samples were harvested, fixed, permeabilized, stained and then embedded for sectioning.

5.2.6. Culture of cells on dLung

Decellularized rat lung was prepared for use as a 3D culture matrix in a similar way to that described for dCAM. Slices were made using a sterile razor blade and these placed in tissue culture labware and sterilized under the UV lamp for 15-20 minutes, or placed in 70% ethanol for 5 minutes. After this PBS was added and plates placed in a tissue culture incubator as previously described. PBS was aspirated after 24 hours and culture medium was added. Samples were left for at least 2 days before cells were added. Cells were re-suspended and added in a minimum amount of media to allow for some cells to adhere to the tissue surface. After 2-6 hours depending on cell adhesion, additional medium was added. Cell growth in the scaffold was monitored using an epifluorescence microscopy and samples were harvested, fixed and embedded for sectioning.

5.2.7. Fixing and staining cells and decellularized tissue

Cells and tissue were fixed with 4% paraformaldehyde/PBS. Colonized decellularized tissue was permeabilized and blocked with 1% TX100/PBS / 10% Goat Serum (Fisher Scientific)

overnight. Colonized tissue was permeabilized and blocked using 0.3%TX100/PBS for at least 2 hours. Immuno-staining was conducted and antibodies were used according to the manufacturers recommendations: Ki67 (abcam 16667, 1:500), vimentin (abcam RV202 ab8978, 1:250), keratin (Abcam ab118817 1:200) ecadherin (#3195 cell signalling, 1:200), anti-GFP (A11122, Molecular Probes). Phalloidin atto 565 (Sigma) and a DAPI (Sigma)/PBS wash were also used.

5.2.8. Embedding and sectioning decellularized tissue samples

Decellularized tissue was soaked in sucrose solution (5% overnight at 4°C, then 15% and 30% for 2 hours each at room temperature) then embedded in OCT (Fisher) before sectioning (14µm sections) using a Cryostat (Bright Model OTF). Sections were then stained as described above.

5.2.9. Scanning Electron Microscopy (SEM)

SEM was conducted for decellularized tissue which was first gold coated using an Edwards S150b gold sputter coater, mounted on 12mm carbon discs (AGG334N, Elektron Technology) and 12.55mm aluminium stubs (SP12, EM Resolutions) and imaged using a Quanta FEI 600F.

5.2.10. Confocal microscopy

A Nikon A1 plus or Nikon A1 confocal microscope was used with either predefined filters (A1 or A1 plus) or using spectral unmixing (A1 plus), as described in Chapter 4.

5.3. Results

Tissue context plays a vital role in cell behaviour *in vivo*, therefore the development of relevant 3D cell culture systems is important for the intelligent exploration of cell behaviour and processes in both healthy and diseased tissue. Recently, tissue engineering approaches have been employed to help develop biologically relevant 3D cell matrix environments. Decellularizing tissue is one approach used initially by surgeons seeking to provide better alternatives for patients needing reconstructive surgery. This native acellular environment provides a useful and relevant environment for cell culture and the study of cell-cell and cell-ECM interactions. The results presented here explore the development and use of three decellularized tissue types for the exploration of cancer metastasis.

5.3.1. Decellularized rat lung as a 3D biological scaffold for cell culture

Decellularized rat lung provided by Natural Biosciences (CASE industrial partners) was used as a 3D growth matrix as a starting point for development of culture protocols and microscopy trials. The structure and surfaces of the dLung were visualized using SEM (Figure 5.1) to determine that the dLung was indeed cell free and also for later comparison with colonized samples. Two samples were gold coated and imaged. The sample shown in Figure 5.1 A and C had surfaces that were smooth and folded, showing the structure of the outer surfaces of the lung. The second sample shown in Figure 5.1 B and D was porous showing an open lattice structure containing the many tunnels and surfaces consistent with gas exchange in the lung tissue.

The approach to cell culture started by optimizing the approach to sterilization and seeding of cells on the dLung. Freeze dried decellularized lung tissue was sliced using a sterile blade. Two approaches to sterilization were trialed: samples were either soaked in 70% ethanol or

exposed to UV light, each followed by soaking in PBS overnight to wash and rehydrate the tissue. On the first round of seeding cells resuspended in medium, the cells (LV MDA-MB-231 GFP+ breast cancer cells) did not appear to adhere to either of the treated tissue samples. The protocol was then amended so that tissue rehydrated in PBS was then soaked in complete medium (which contained 10% FBS) for at least a further 48 hours before cells were seeded. This was more successful and cells were re-suspended at a 1:5 ratio with sufficient volume added to cover and form a bubble around the decellularized lung tissue fragments, around 200µl, giving 1cm² confluence per application equivalent once cells settled and adhered (approximately 1 x 10⁵ cells). Giving cells sufficient time to adhere but keeping cells and tissue covered by the medium, was important to retain cell health and tissue integrity, therefore samples were monitored regularly. Between two and six hours provided a good time window of opportunity for this to occur before additional medium was added. As many cells ended up on the tissue culture dish, whilst samples floated freely in medium, after 3 days samples were transferred to new dishes using sterile pipette tips. This meant that most cells proliferating were on the decellularized tissue and not on the base of the tissue culture plate. Images were taken to determine the extent of colonisation of both the UV and the ethanol treated dLung and the extent of colonization compared. Figure 5.2 shows images taken of colonized dLung. Figure 5.2 A and B show images of ethanol treated lung, four days after seeding. GFP+ cells can be seen to adopt both elongated and rounded morphologies as they colonize the dLung. Comparative images seventeen days after cell seeding are shown in Figure 5.2 C and D, the UV treated sample being well populated compared to the ethanol treated sample which had many un-colonized areas. Whilst both approaches were successful, UV treatment for sterilization was adopted as the standard, given that samples were small and the UV light was likely to gain access to

the tissue well. Further colonization experiments were conducted with MDA-MB-231 cells, LV MDA GFP+ cells and a co-culture of MDA-MB-231 with LV HT1080 GFP+ (A1D9).

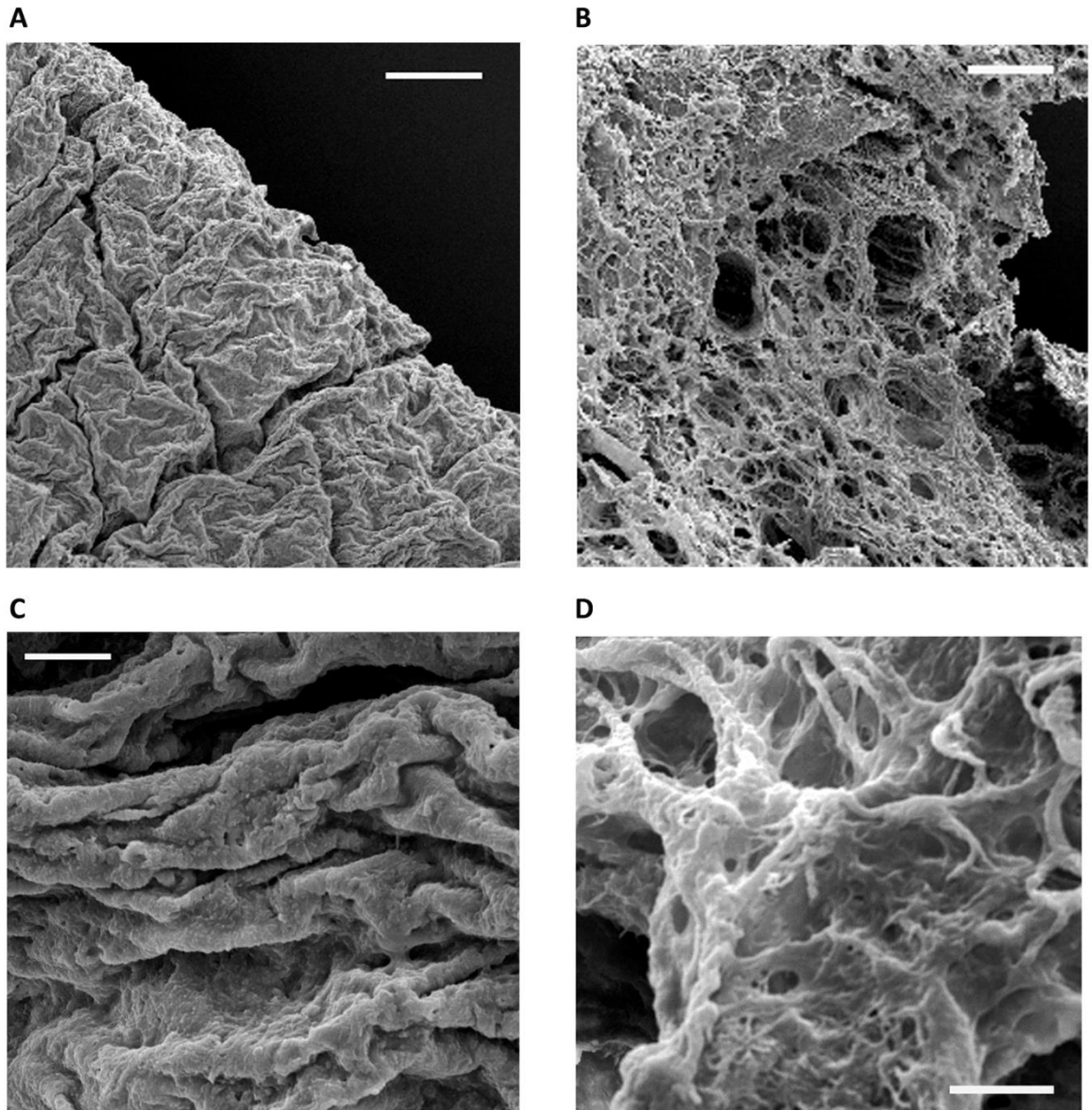


Figure 5.1, Decellularized rat lung. Scanning Electron Microscopy was conducted for two samples of decellularized rat lung using a Quanta FEI. **A, B** Images showing two different surfaces presented by decellularized rat lung. **A** showed a smoother folded surface, which is shown at higher magnification in **C**. **D** shows **B** at higher magnification this being porous and more fibrous in nature. Scale bars: A and B = 200 μ m and C and D = 20 μ m.

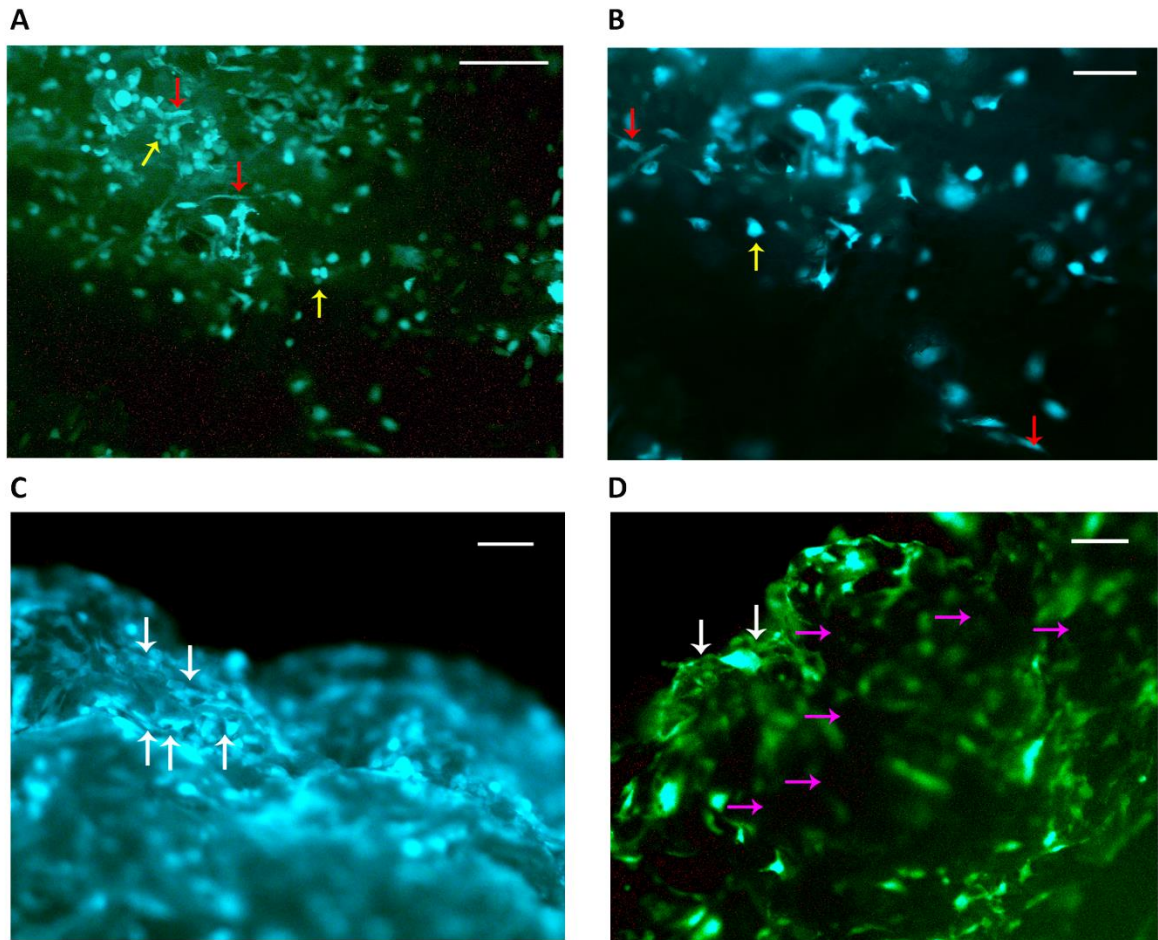


Figure 5.2, MDA-MB-231 GFP+ cells colonizing decellularized rat lung (dLung). **A** MDA cells on rat lung 4 days after seeding (low magnification) and **B** at higher magnification. Cells can be seen to adopt a variety of morphologies at the surface of the dLung. Red arrows indicate elongated cells and yellow arrows indicate rounded cells (A and B). **C** dLung 18 days after MDA GFP+ cells were added was well colonized – white arrows indicate layers of flattened cells forming a covering over the surface. UV light treated sample. **D** Ethanol treated sample took longer to colonize (pink arrows indicate spaces where little or no colonization has taken place). White arrows indicate areas where MDA GFP+ cells have formed layers on dLung surface. Images were taken using a Zeiss Axio Vert Epifluorescence microscope. Scale bars for A, C, D = 100 μ m and B = 50 μ m.

Decellularized rat lung samples harvested after 21 days looked well colonized externally but due to the sample density it was not possible to obtain good images at higher magnification at this stage. Consequently samples were stained, embedded and sectioned for fluorescence microscopy to identify the level of colonization throughout the whole dLung tissue matrix. Figure 5.3 shows a cross section of colonized lung tissue with MDA-MB-231

cells seeded for 21 days and LV HT1080 GFP+ cells added for the last 4 days. Whilst there a number of MDA-MB231 cells had migrated into the lung matrix, there were areas completely un-colonized after three weeks of culture. Higher magnification images in Figure 5.4 show that cells were able to cluster and form tumour type growths with both cell types present. Phalloidin staining showing the acto-cytoskeleton location shows coterminous boundaries for cells which is suggestive of the formation of cell-cell junctions (Figure 5.4 C and D – white arrows).

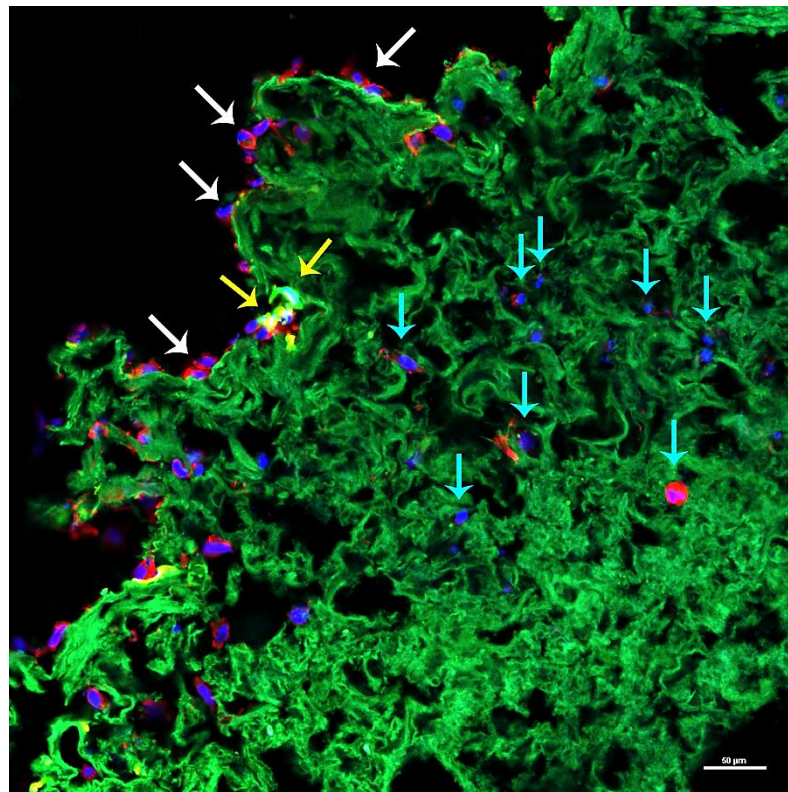


Figure 5.3, Rat dLung co-culture. Confocal microscopy of a decellularized rat lung section colonized with MDA-MB-231 cells (after 21 days) shown with DAPI (nuclei – blue) and phalloidin stain (actin – red) and LV HT1080 GFP+ (A1D9) cells (after 4 days) – green. The dLung matrix also appears green in the image due to autofluorescence of the collagen matrix. MDA-MB-231 cells can be seen both at the outer surface of the dLung (white arrows) and to have moved into the lung tissue (blue arrows) where they can be seen on the many surfaces of the open and porous structure. 2-3 LV HT GFP+ cells are seen to have adhered to the outer surface (yellow arrows). Nikon A1 Plus confocal microscope image. Scale bar = 50μm.

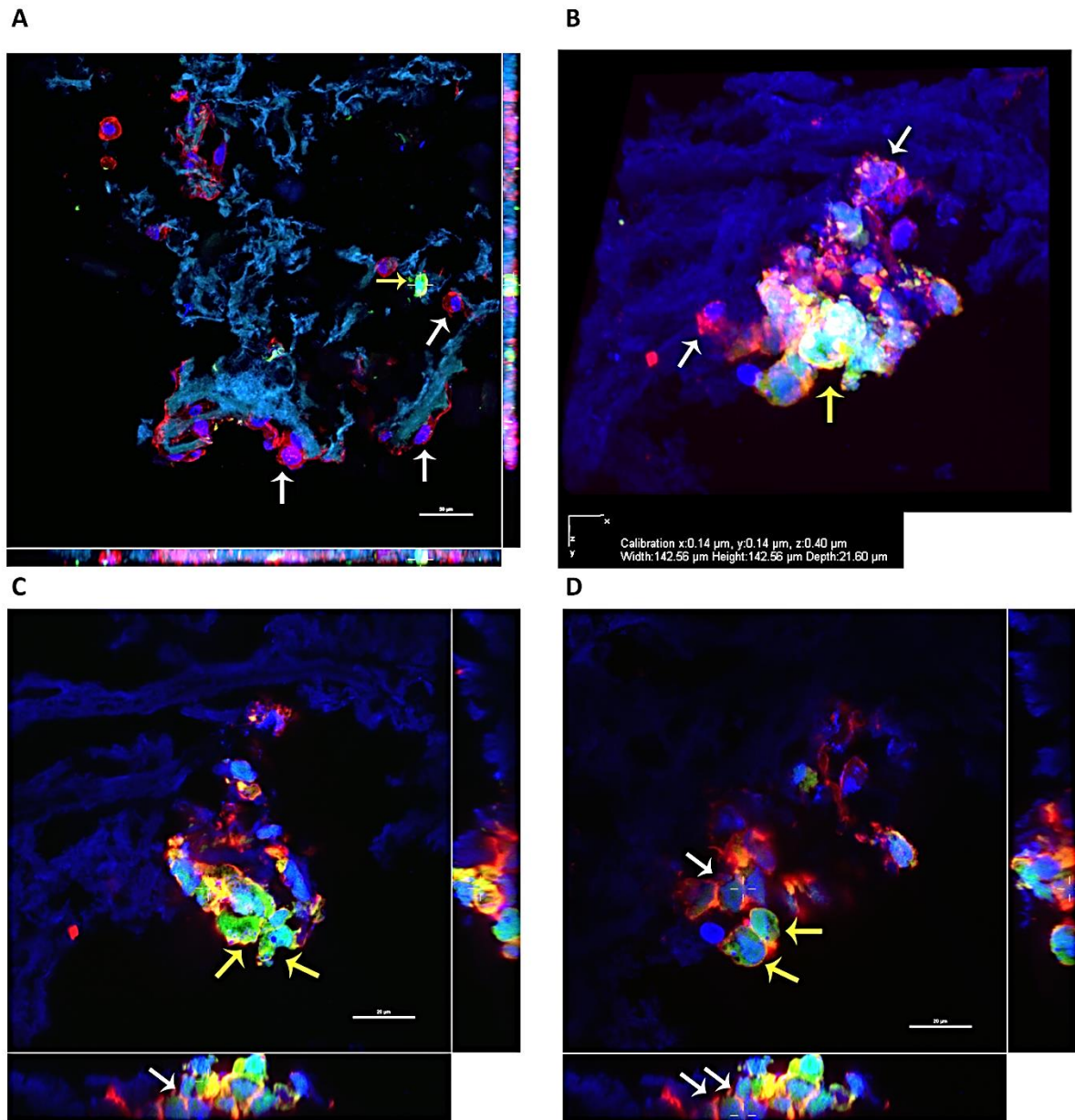


Figure 5.4, Decellularized rat lung co-culture shows cell cluster formation comprising both cell types. MDA-MB-231 (MDA) breast cancer cells were cultured for 17 days then LV HT1080 GFP+ cells (A1D9) were added and cultured for a further 4 days together on decellularized rat lung before fixing, embedding staining and sectioning. Confocal images were taken with a Nikon A1 Plus microscope. A low magnification image showing both MDA cells growing and covering surfaces of dLung. B 3D reconstruction of a group of cells in which both MDA and HT GFP+ cell types appear to be growing together and possibly making cell-cell junctions. For A and B white arrows indicate MDA cells and yellow arrows indicate HT GFP+ cells. C and D show different slice positions of the same z stack shown in B. Yellow arrows indicate HT GFP+ cells and white arrows indicate possible junctions formed between MDA cells. Scale bars: A = 50 μ m and C and D = 20 μ m.

Immuno-staining was conducted on co-culture samples to test this as an approach in the 3D decellularized tissue and to determine whether differences in protein expression could be determined in cells growing within the dLung matrix. Vimentin expression was chosen as this expression is usually a marker for epithelial mesenchymal transition with expression increased in migrating cells. Figure 5.5 shows dLung colonized by MDA-MB-231 and LV HT1080 GFP+ (A1D9) cells stained for vimentin. In Figure 5.5 A and C, two GFP+ cells (green) can be seen within the lung matrix (indicated with white arrows) and MDA cells stained for phalloidin (not green) are seen, indicated with blue arrows. Vimentin expressions appears to be low but visible (Far red laser channel – shown in yellow in B) and is indicated with white arrows for the LV HT GFP+ cells. Vimentin expression in MDA-MB-231 cells is hardly visible in comparison (blue arrows).

Decellularized rat lung tissue thus provided a suitable 3D matrix for cell culture and study using confocal microscopy and immuno-staining and allowed the optimisation both these techniques. Given that the protocol for rat lung decellularization had yielded tissue suitable for successful 3D tissue culture, the decellularization protocol was used as a basis for the decellularization of chorioallantoic membrane of chick.

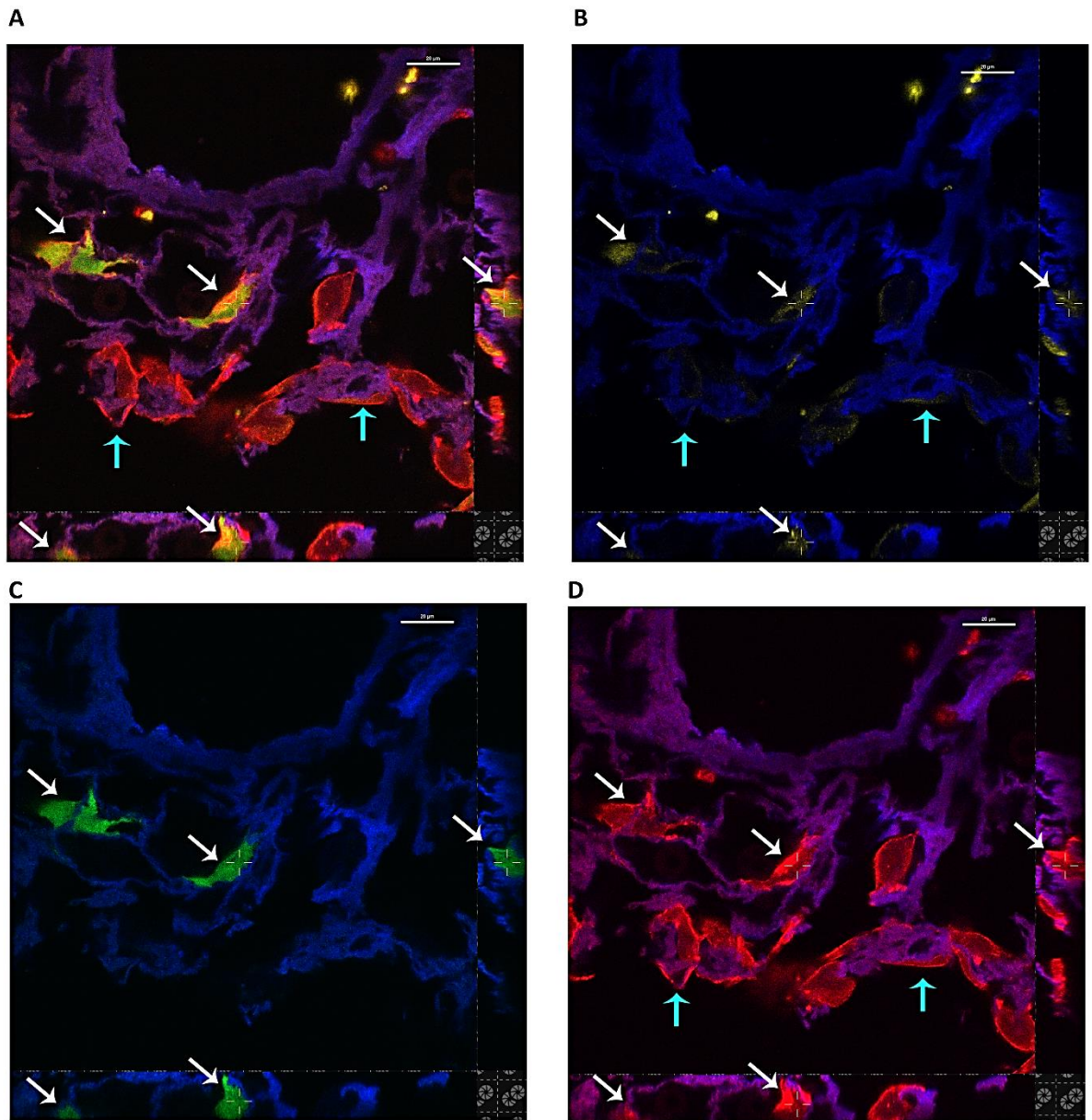


Figure 5.5, Decellularized rat lung colonized with MDA-MB-231 and LV HT1080 GFP+ (A1D9) cells stained for vimentin expression. Phalloidin is shown in the red channel, GFP+ in the green channel and Vimentin in the far red channel – shown yellow. The dLung tissue is blue in these images. White arrows indicate LV HT1080 GFP+ cells in which vimentin expression is clearer and possibly a higher expression levels than in MDA cells is indicated with blue arrows. **A** combined image. **B** vimentin (yellow) and dLung. **C** GFP+ and dLung. **D** phalloidin, red and dLung. Images taken with Nikon A1 Plus confocal microscope. Scale bars = 20µm.

5.3.2. Optimization of decellularization of chick chorioallantoic membrane

The chick chorioallantoic membrane (CAM) is a delicate extracellular tissue comprising three layers and between 30 - 100µm thick (Deryugina and Quigley 2008b). It has been reported that protocols used for decellularization are harsh and can leave damaged material as a result (Balestrini et al. 2015). The approach taken to decellularization of CAM therefore had to be sufficient to remove the cells from the matrix but leave the basic collagen matrix intact to facilitate its use as a 3D biological scaffold for cell culture and study. The Medberry protocol had proved successful with rat lung decellularization and so was used as a starting point for CAM decellularization. The chemicals used in the protocol act to denature proteins (trypsin), break up cell membranes and detach proteins from DNA (detergent: Triton-X 100) and emulsify fat (deoxycholate) and then clear debris from the tissue (peracetic acid). Osmotic pressure also forms part of the protocol with an initial soaking of tissue in water, and later a 1M sucrose step to help further disrupt cell integrity. Whilst the general protocol is given in section 5.2, optimization of the protocol was conducted over a series of experiments, the main details of which are now described.

Frozen CAM tissue (Figure 5.6 A) was used for decellularization, harvested in line with timings for samples used in *in vivo* experiments. CAM tissue was therefore frozen for decellularization at time points 9-11 days into incubation, that is 1-3 days after cells would have been added to the CAM for *in vivo* experiments. All steps from the Medberry protocol used for rat lung decellularization were retained but the exposure times were shortened significantly. After defrosting CAM tissue, the first step was a water soaking/stirring stage. CAM was found to disintegrate if left for more than 2 hours at this stage and too much agitation also caused tissue to break up so the protocol was optimised to start with a soaking

step of just 30 minutes. Initial experiments allowed CAM to free float in each of the treatment solutions but the CAM tissue became difficult to harvest with much tissue lost during the process. To maintain CAM integrity, keeping CAM tissue flat, adding solutions then gently draining them was determined as the best approach. On this basis a series of different receptacles were trialled, the best proving to be a metal colander type sample holder such as that shown in Figure 5.6 B.

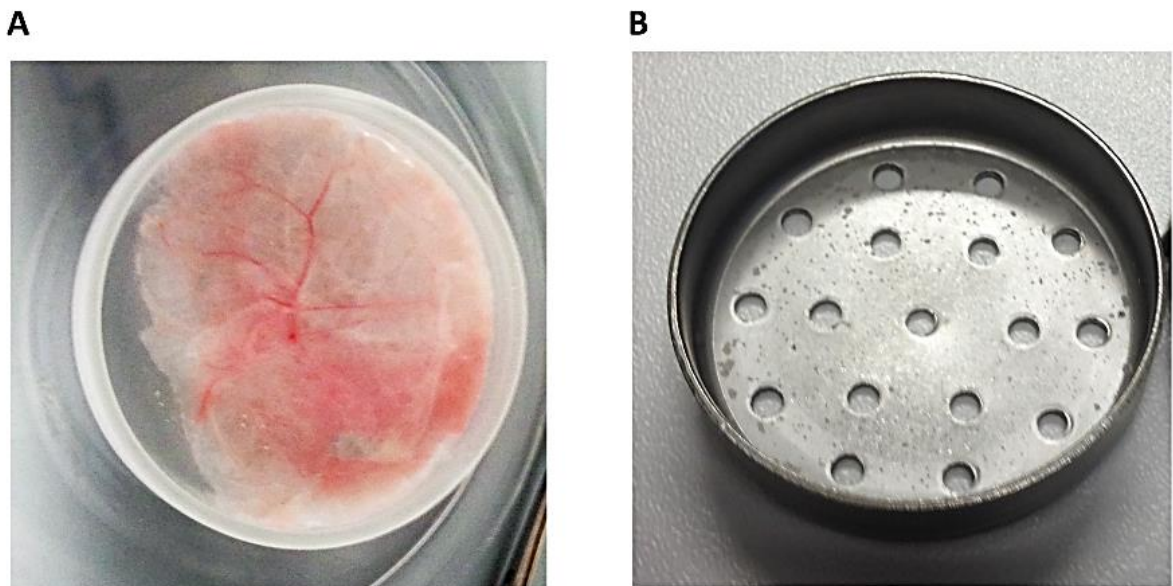


Figure 5.6, Decellularizing CAM. A frozen CAM tissue prior to decellularization.
B Metal sample holder used to freeze and process CAM during decellularization.
Dish diameter = 3.5cm.

Scanning electron microscopy was used to examine decellularized CAM at each stage. Initially dCAM yield was low and dCAM tissue appeared damaged and stringy, Figure 5.7. Keeping the CAM flat whilst treating it and draining it more gently helped to reduce abrasion and damage in subsequent preparations. Staining with DAPI and phalloidin followed by fluorescence microscopy was used to identify the extent of decellularization. Nuclear fragments identified by the DAPI stain (blue) were seen within the decellularized tissue in some samples (Figure 5.7) but no associated cell structure was evident when viewed in the red channel (phalloidin) and green channel (autofluorescence for CAM tissue and cells).

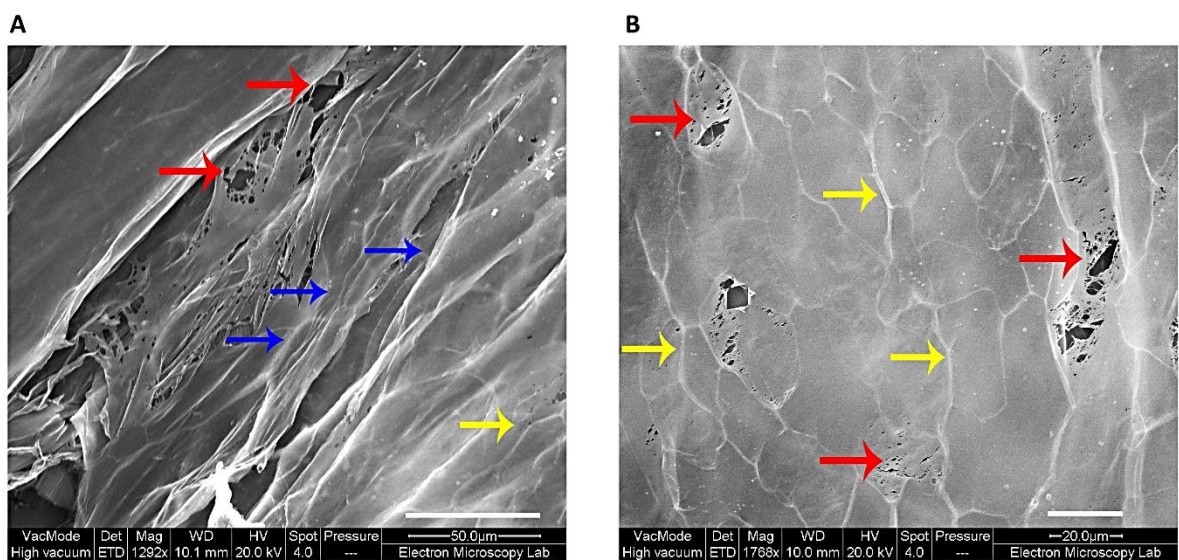


Figure 5.7, Scanning Electron Microscopy for dCAM before protocol optimisation. A Image shows folded and damaged dCAM. **B** Shows a higher resolution image with vascular structure still evident. There also appears to be damage to the surface which looks almost leaf like. Red arrows indicate areas of damage and folded or stringy tissue by blue arrows. Evidence of original vasculature is indicated with yellow arrows. Images taken with an FEI Quanta. Scale bars A = 50µm, B = 20µm.

To ensure decellularization was complete, two treatment steps were optimized: firstly the peracetic acid step, which acts to clear tissue debris. The time for this step was extended so three different soaking times were compared. SEM and staining followed by fluorescence microscopy were used to assess the effects of the different soaking times on the final dCAM (Figure 5.9-10). Results showed that both five and ten minute soaking times gave similar results and were sufficient. The ten minute peracetic acid step was adopted to ensure good clearance of debris. The second optimisation conducted was to increase the trypsinization step, the enzymatic action acting to break up proteins within the tissue by cleaving polypeptide chains. The aim of this was to improve the fragmentation of cellular material prior to clearance.

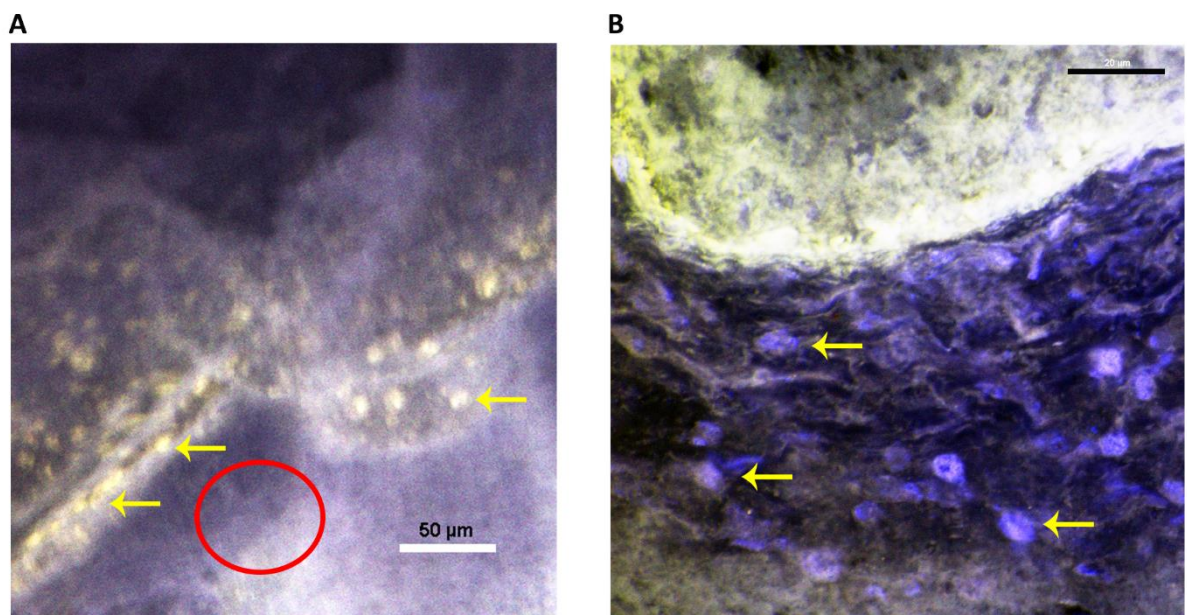


Figure 5.8, Decellularization of CAM – was decellularization complete?

dCAM was stained with phalloidin (actin – red channel) and DAPI (nucleus – blue channel) and confocal / reflectance microscopy used to examine the dCAM tissue to determine the extent of decellularization. **A** shows that whilst many areas appeared acellular (for example within the red ellipse), some cellular material could be present – yellow arrows. **B** examination at higher resolution showed some blue stained material within the remaining dCAM, likely to be nuclear material. However, there was no evidence of phalloidin stained material remaining, this staining for the actin cytoskeleton of cells and no green fluorescence evident which would indicate CAM cellular tissue. Images were taken with a Nikon A1R confocal microscope. Scale bars are A = 50μm and B = 20μm.

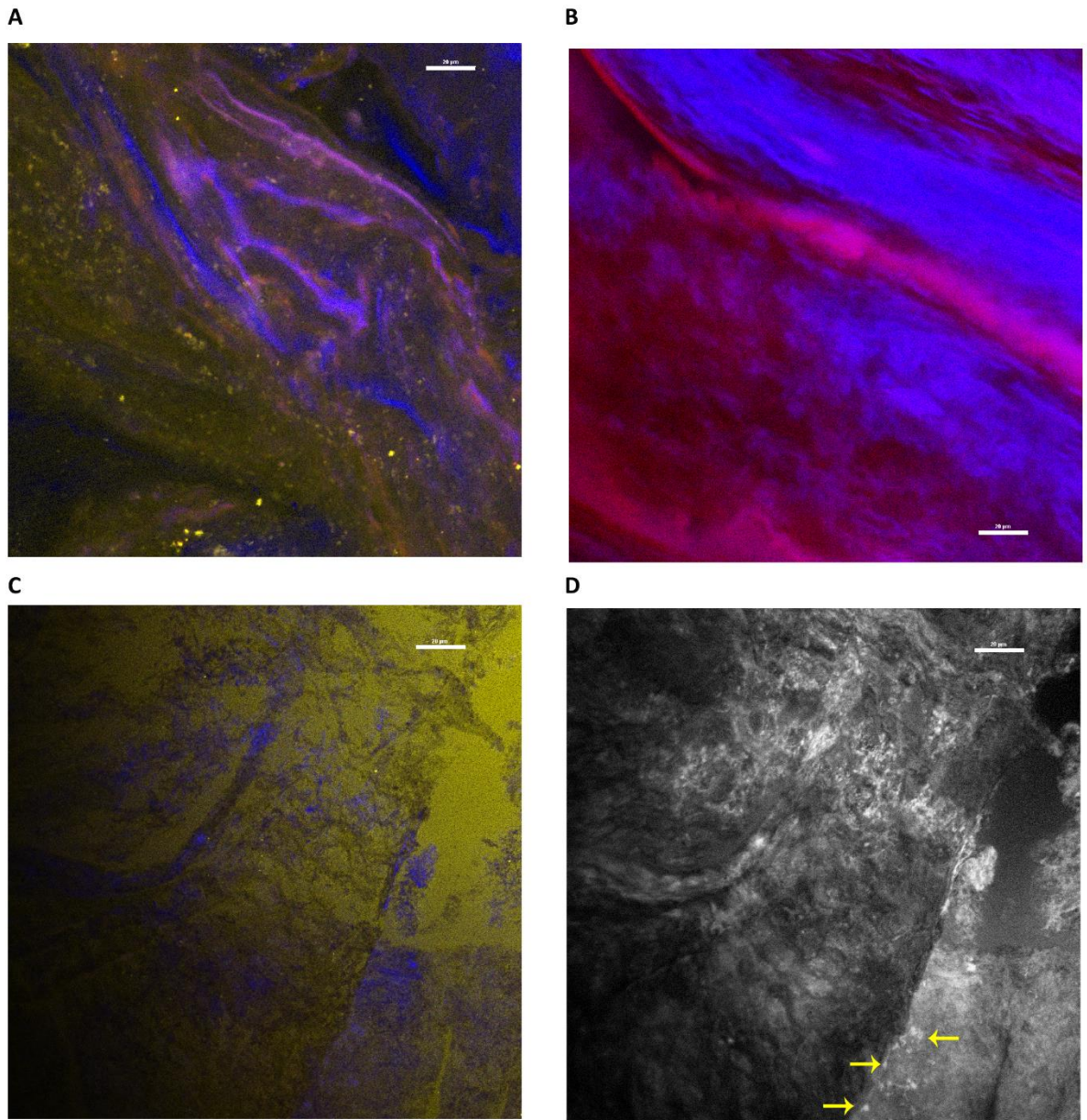


Figure 5.9, Optimization of peracetic acid clearance of CAM tissue during decellularization. Decellularized tissue was stained with DAPI (blue) and phalloidin atto 565 (red). Images were taken with a Nikon A1 Plus confocal microscope using all four laser channels and spectral unmixing conducted using three filters: DAPI, phalloidin and dCAM without stain. Figures **A and B** show dCAM following a full protocol with a 5 peracetic clearance step and **C and D** following the decellularization with a 10 minute clearance with peracetic acid step. **A** shows dCAM using all three filters and **B** DAPI and phalloidin only. **C** shows dCAM with all three filters and **D** shows the blue channel only in which an number of small particles less than $2\mu\text{m}$ can be seen (yellow arrows) but none as large as an intact nucleus. Scale bars = $20\mu\text{m}$.

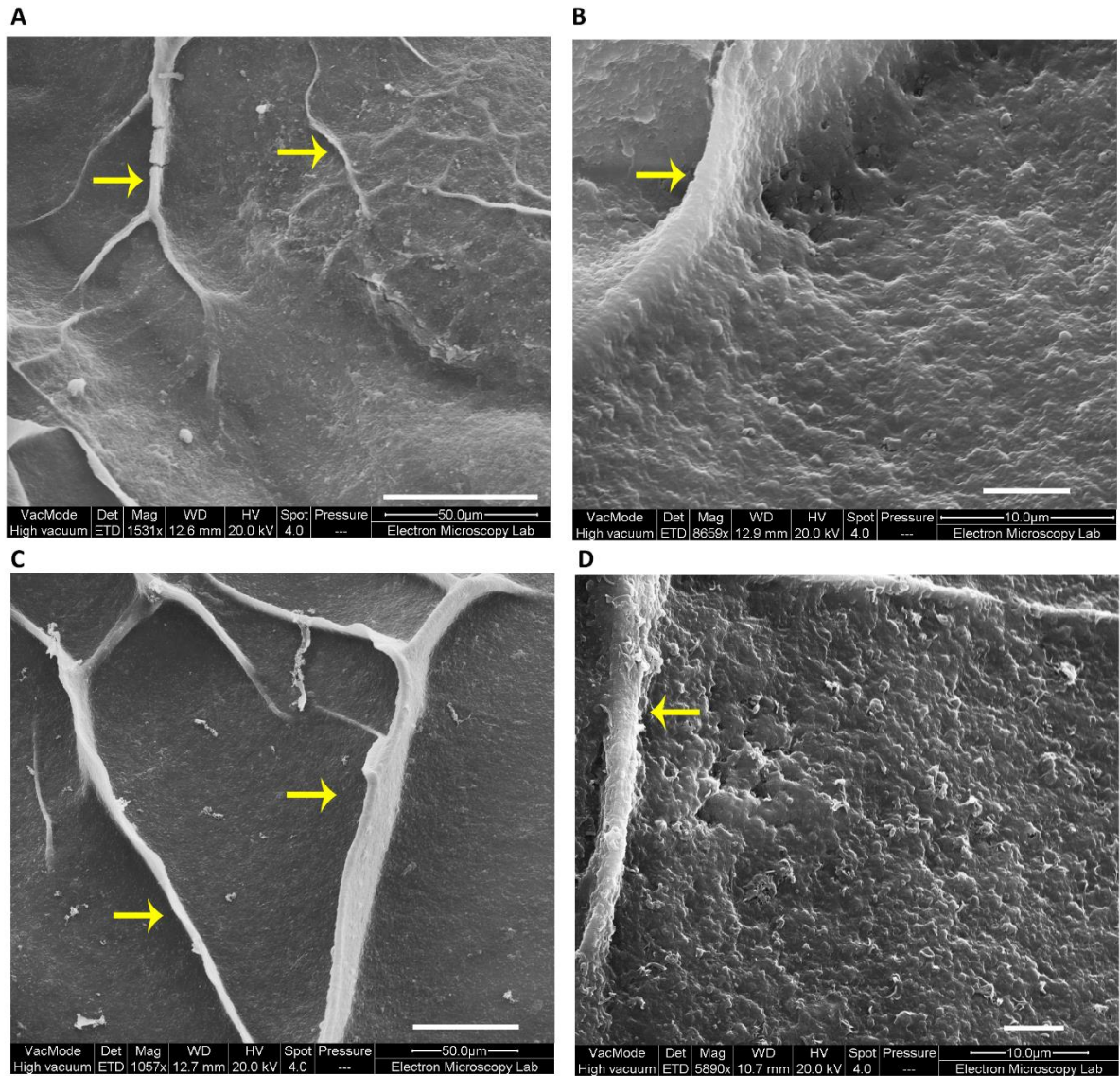


Figure 5.10, Scanning Electron Microscopy images for peracetic acid step optimization. **A** and **B** show images of dCAM following a full decellularization protocol with a 5 minute peracetic acid tissue clearance step. **C** and **D** show images for the same protocol but with a 10 minute peracetic acid step. Yellow arrows indicate remaining vascular structure. dCAM is intact in each case. Scale bars A and C = 50µm, B and D = 5µm. SEM images were taken using a Quanta FEI.

5.3.3. dCAM as a 3D Growth Matrix

CAM was prepared for seeding using the protocol developed and optimized for decellularized rat lung. MDA-MB-231, MCF7 and HT1080 cells were all seeded and cultured on dCAM either individually or as a co-culture. Colonization was easier to monitor with GFP+ cells seeded (Figure 5.11 A v B).

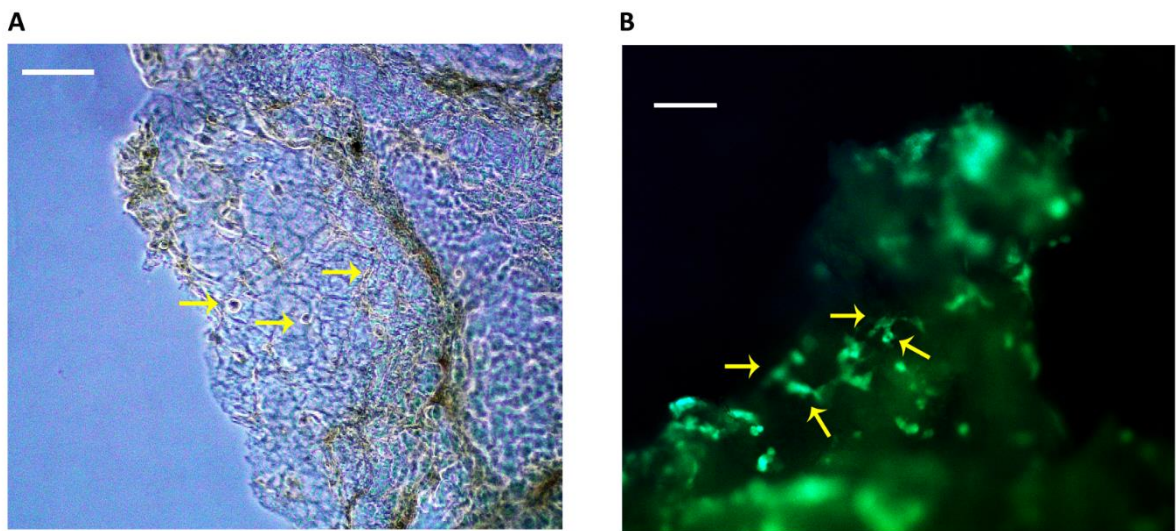


Figure 5.11, Cells seeded on dCAM proliferate over the surface. Cells were seeded on dCAM and survival and proliferation were monitored using an inverted microscope. **A** MDA-MB-231 cells on dCAM 9 days after seeding. **B** MDA-MB-231 cells and MCF7 GFP+ cells on dCAM. Fluorescence shows MCF7 cells in patches on dCAM surface. Images taken using a Zeiss Axiovert inverted microscope using brightfield and epifluorescence. Scale bars = 1mm.

Once harvested and fixed, colonized dCAM could be imaged either intact to investigate interactions between cells or between cells and matrix throughout the tissue or it could be sectioned in a similar way to seeded live CAM. Figure 5.12 shows images of MDA-MB-231 colonized whole dCAM stained with phalloidin (actin cytoskeleton - red) and DAPI (nucleus – blue). Cells had formed layers over the dCAM which appears green in these images.

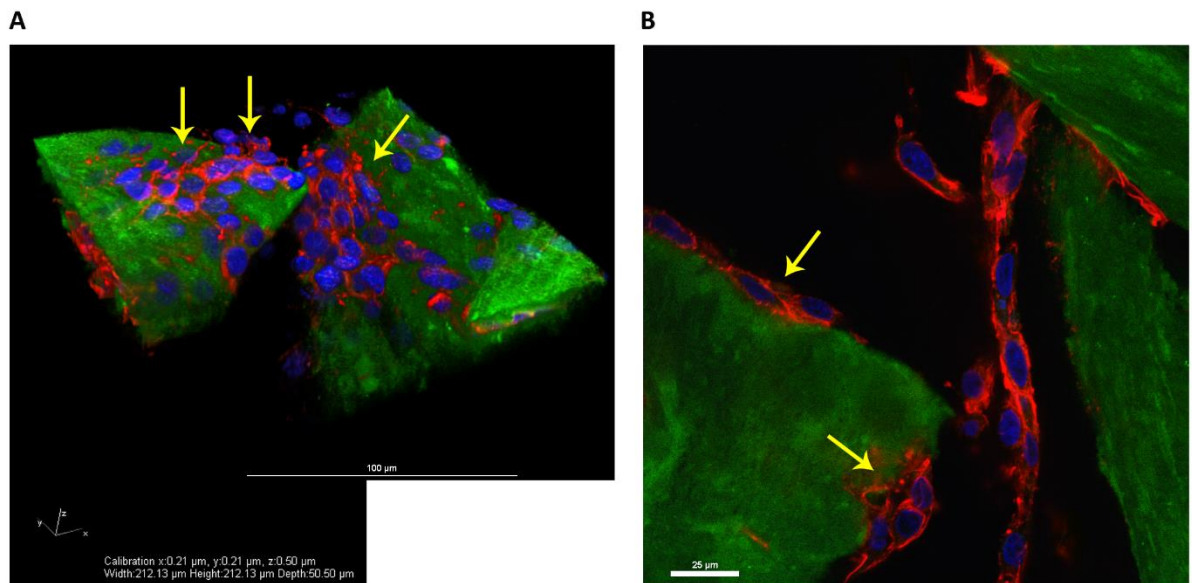


Figure 5.12, MDA-MB-231 cells colonize dCAM. Cells appeared to proliferate over the dCAM surface forming layers of rounded, flattened cells (yellow arrows). Cells were stained with DAPI (nucleus- blue) and phalloidin (actin cytoskeleton- red). Images were taken with a Nikon A1R confocal microscope. **A** 3D reconstruction of MDA cells on dCAM. **B** cross section through tissue in which cells appear as layers. Scale bars: A = 100µm and B = 25µm.

Differences in colonization habit when cells were co-cultured on dCAM could be seen between the two cell lines: MDA-MB-231 and LV MCF7 GFP+ (Figure 5.13). The MCF7 cells formed small groups on dCAM, whereas MDA-MB-231 cells spread out along edges and formed flattened patches. They may also have formed junctions but these were not specifically stained for in these experiments. Cells colonizing dCAM were stained for Ki67, an antigen marker expressed during the active phases of the cell cycle (Jonat and Arnold 2011). Figure 5.14 shows that a large number of cells stained positively for the proliferation marker Ki67, suggesting that these cells were in the active stages of the cell cycle: G1 (Growth 1), S (Synthesis), G2 (Growth 2) and M (Mitosis) phases. Some cells showed no Ki67 nuclear staining which suggested they were quiescent, cell cycle phase: G0 (Growth 0).

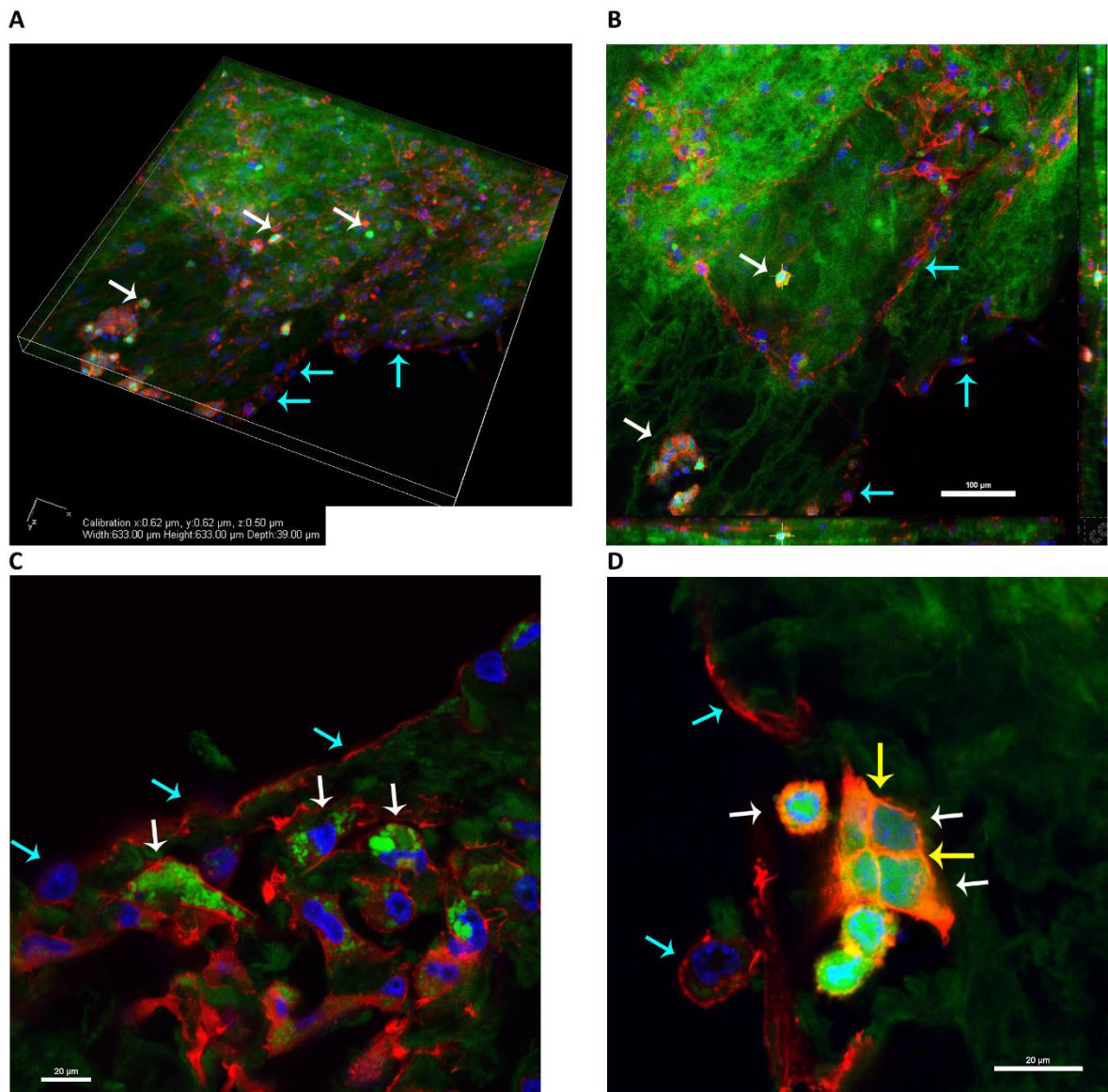


Figure 5.13, dCAM co-culture colonized with MDA-MB-231 and LV MCF7 GFP+ cells. Colonized tissue was fixed and stained after 10 days, stained with phalloidin (actin – red channel) and DAPI (nucleus – blue channel). GFP+ cells appear brighter than autofluorescent dCAM tissue. White arrows indicate GFP+ cells and blue arrows MDA-MB-231 cells. Images taken with a Nikon A1R confocal microscope. **A** 3D reconstruction of colonized dCAM. **B** A slice through the 3D construction shown in A. **C** higher magnification image showing both MDA and MCF7 cells on dCAM. **D** Shows a group of LV MCF7 GFP+ cells which have formed a group and cell-cell interactions (yellow arrows) on dCAM. MDA-MB-231 cells are also present. Scale bars: B = 100µm, C and D = 20µm.

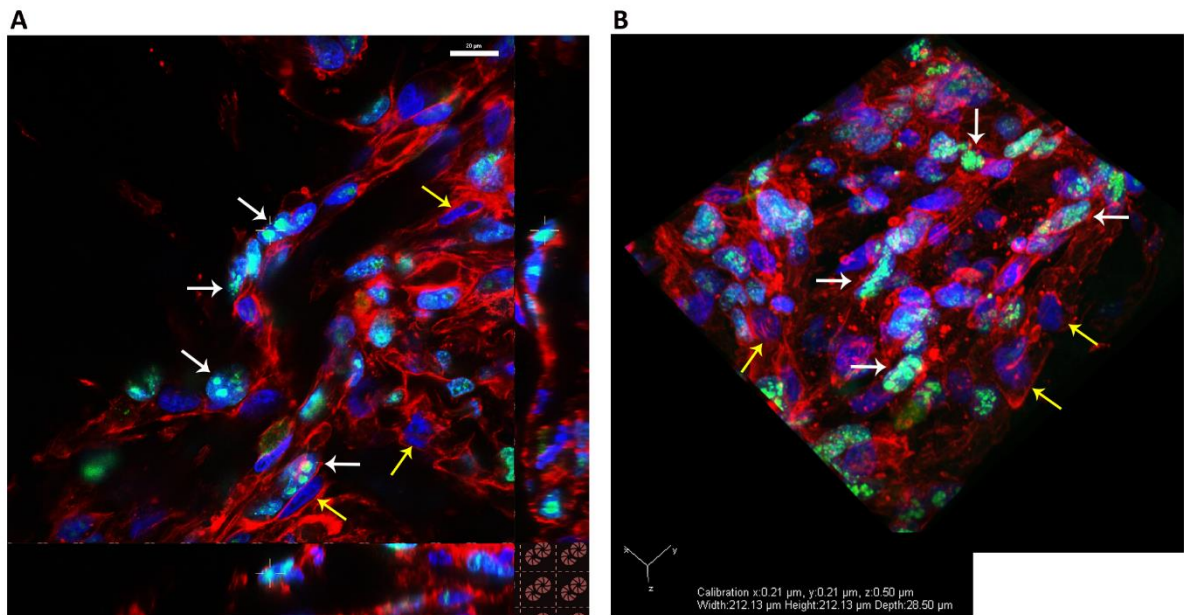


Figure 5.14, HT1080 cells proliferate over dCAM. HT1080 cells colonizing dCAM were fixed and stained: Ki67 protein marker for proliferation (FITC – green), DAPI for nuclei (blue) and phalloidin for actin (red). White arrows indicate cells which are actively proliferating in which green fluorescence highlights nucleosomes in the nucleus. Yellow arrows indicate cells in which this is absent and these cells were not actively proliferating. **A** shows a cross section through a number of cells populating the dCAM surface in which the majority of cells are proliferating. **B** 3D rendered image of cells populating dCAM for the same sample and experiment. Images were taken using a Nikon A1 plus confocal microscope. Scale bar for A = 20 μ m.

The results in this section show that chick chorioallantoic membrane can be decellularized successfully and the product used for 3D cell culture. Cells can be imaged successfully without the need to embed and section tissue, this enabling cell-cell and cell-matrix interactions to be probed without loss of tissue integrity due to the processing associated with embedding and sectioning.

To test the approach further decellularization of a third tissue was investigated, this being rat pup skin, an epithelial tissue which could be of interest for colonisation and as a comparator for dCAM.

5.3.4. Decellularization of rat pup skin (dSkin)

The same basic protocol for decellularization was used for rat skin (Medberry et al. 2013) starting with the original timings and adapting the protocol accordingly. As epithelial tissue is much tougher than CAM, stirring in water overnight was chosen as the first step to start the process. Sample tissue was kept in suspension whilst treated, in comparison to the very careful tissue handling of CAM in which tissue was kept flat and drained during decellularization. SEM images for freeze dried whole rat skin versus the resultant decellularized rat skin are shown in Figure 5.15 and stained, sectioned images in Figure 5.16.

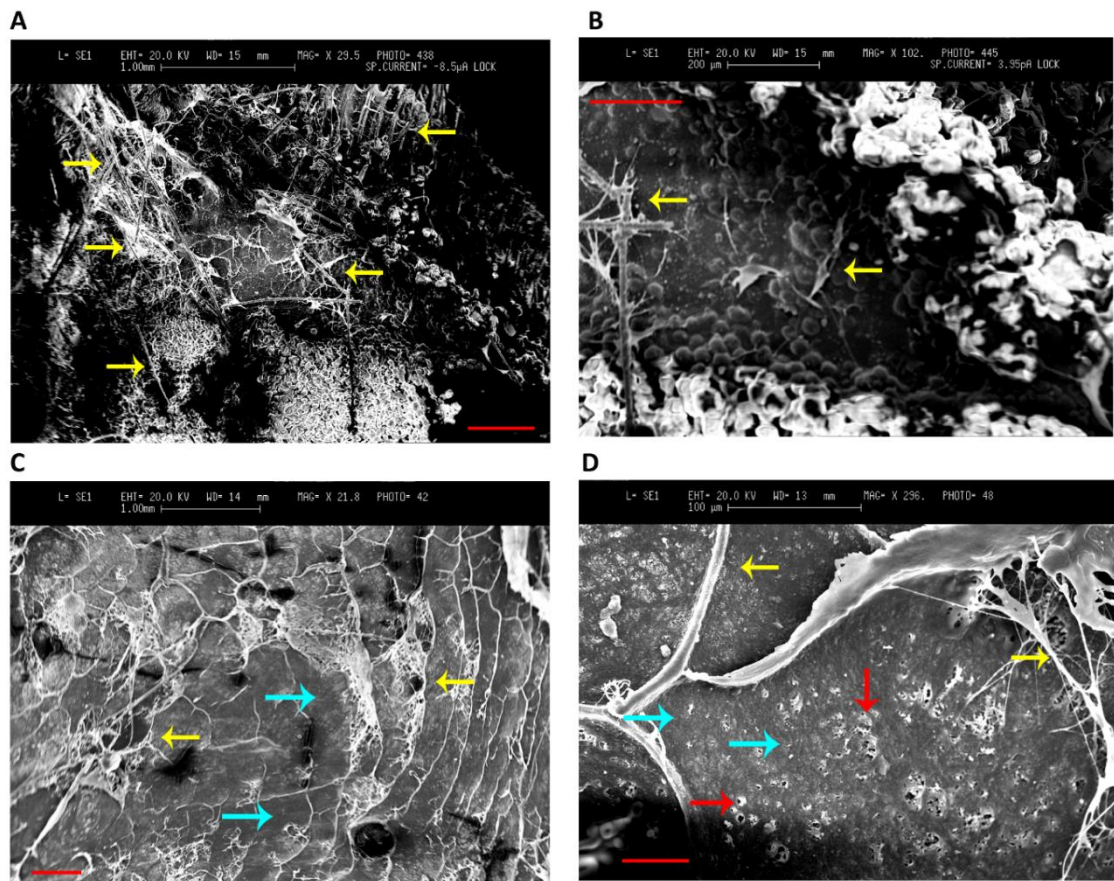


Figure 5.15, Rat skin and decellularized rat skin compared via Scanning Electron Microscopy (SEM). A freeze dried sample of whole and decellularized rat pup skin was compared using SEM. **A** and **B** show images of whole rat skin. Yellow arrows indicate fur. The skin surface appears textured and uneven. **C** and **D** show decellularized rat skin which still shows fibrous material likely to be fur (yellow arrows) but appears smoother (blue arrows) in many places. Red arrows indicate breaks in the tissue which may have occurred during sample preparation. Images were taken using a Cambridge S360 SEM. Scale bars: A and C = 500 µm, B = 200µm, D = 50µm.

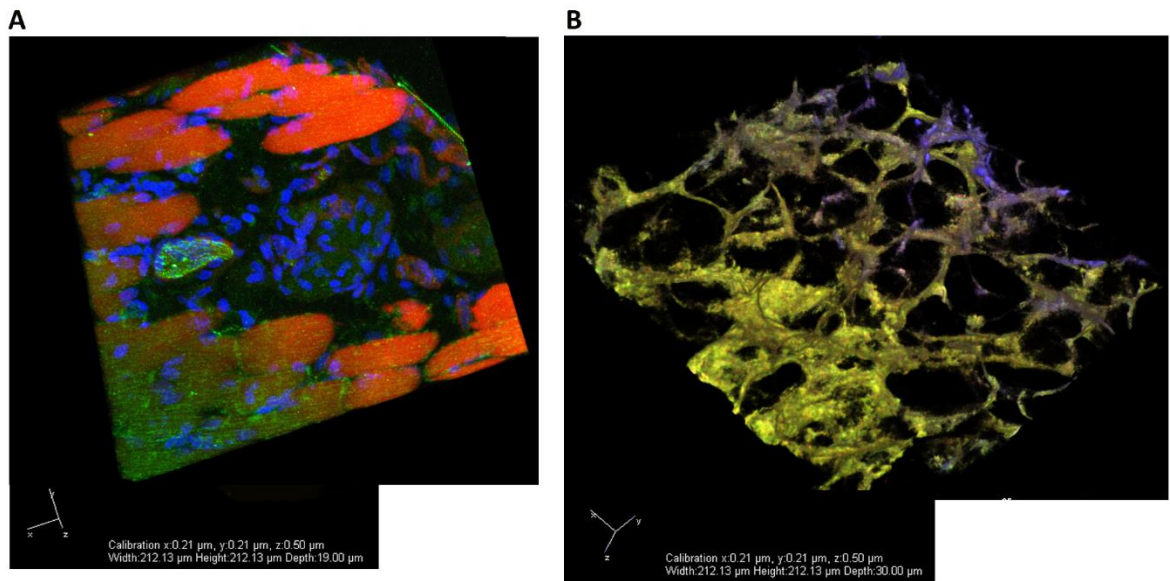


Figure 5.16, Sectioned whole rat pup skin compared with decellularized rat skin.

A 3D rendered image of a section of whole rat skin stained with phalloidin (red) and DAPI (blue). Hair follicles (orange and elongated ovals) and cell nuclei (blue) can be seen clearly within this image. **B** The decellularized structure has an open honeycomb texture and there are no cell nuclei, cells or hair follicles evident in the 3D image. Images taken with a Nikon A1R confocal microscope.

Surface fur was removed from rat skin before decellularization when the protocol was repeated. This allowed SEM images to be taken at closer range due to a more even sample texture. The images in Figure 5.17 show an open meshwork structure similar to that shown in Figure 5.16 B. There was no obvious evidence of cellular material within the sectioned skin sample. Following successful decellularization, attempts were made to use dSkin as a 3D growth matrix. However cell seeding onto dSkin was problematic as samples floated easily and were difficult to cover with cells. dSkin pieces were approximately 1cm² so these were fragmented further to attempt to create a greater surface area.

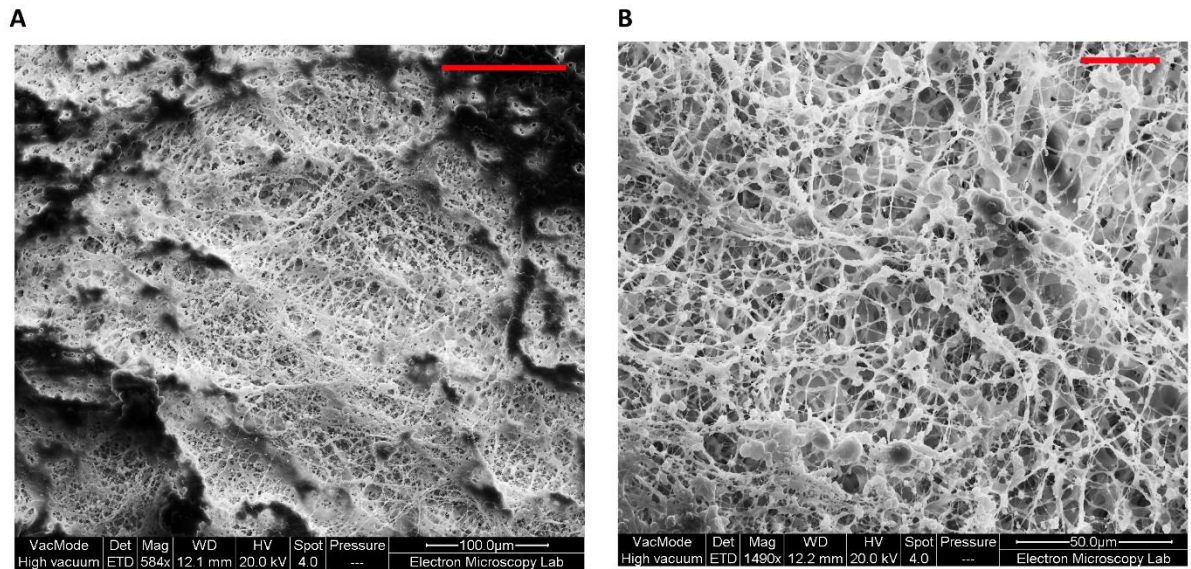


Figure 5.17, Rat skin decellularization with rat pup hair removed first. SEM images taken with FEI Quanta show a meshwork of fibres but no obvious cellular structures within the decellularized tissue. **A** scale = 100µm and **B** scale = 25µm.

Cells were seeded and samples cultured for 3 weeks alongside dLung samples and then harvested, stained, embedded then sectioned. Initial sections made showed no evidence of cell growth within the decellularized matrix however due to the varied surfaces presented within the dSkin samples, it is possible that a small number of cells were present but were sparse and therefore not found in the sections made and viewed.

The results from this section show that decellularized tissue from another host and organ can be decellularized successfully using the protocol adopted for the decellularization of chick chorioallantoic membrane (and rat lung), with adjusted timings. Overall the results reported in this chapter show that decellularized tissue offers an opportunity for 3D cell culture in a structured biologically relevant environment. A range of microscopy images has shown both the structure of the matrix and cells interacting with each other and with the matrix. In particular CAM has been decellularized to provide a novel 3D matrix which can be

imaged intact once colonized. The opportunities and implications for these findings is discussed in detail in the next section.

5.4. Discussion

Cells operate within a tissue context, their behaviour guided by the extracellular matrix structure, mechanical and biological cues from cells and tissue infrastructure and from the soluble factors in which they are bathed. To understand cell behaviour in context, the culture and study of cells thus needs to reflect this rich and complex environment (Baker and Chen 2012, Pampaloni et al. 2007). The construction of a three dimensional cell culture environment has been attempted in a number of ways in recent research, ranging from simple gels using components of the extracellular matrix, through to artificially constructed porous matrix products. However these products lack the natural and varied structure of a native extracellular matrix structure. Recent advances in tissue engineering have explored and exploited the decellularization of organs and tissues allowing their repopulation and use for the development of allografts and xenopants for patients. The opportunity for the use of these products for cell culture has also been explored and extended to 3D tissue culture where they provide a natural and biologically relevant matrix in which to explore and further understand cellular mechanisms in both healthy and diseased tissue (Badylak et al. 2009, Brown et al. 2010, Gilpin et al. 2014, Lu et al. 2014).

The approach to using decellularized tissue within this project enabled the exploration of three different tissue scaffolds as 3D culture matrix environments: rat lung, rat skin and chick chorioallantoic membrane (CAM). Due to this novel *ex vivo* use of the CAM, the protocol for decellularization of chick CAM was developed and optimized for the first time here with a view to the further investigation of behaviours and interactions observed in *in vivo* CAM experiments.

All three tissues were decellularized using a biochemical approach based on the Medberry protocol (Medberry et al. 2013) with adaptation and adjustment to minimize tissue damage yet still achieve an acellular product. Scanning electron microscopy and immuno-staining were used to confirm that resultant matrix products were indeed cell free. Recently published literature shows that other researchers have adopted similar approaches for verifying the absence of cells following decellularization, with the addition in some cases of histological staining such as a trichrome assay or haemotoxylin and eosin staining to identify the tissue components (Balestrini et al. 2015, Xiong et al. 2015). In this work as in other recent research, DAPI staining has typically been used to confirm that cell nuclei (and therefore cells) were absent from the decellularized tissue (Guyette et al. 2014, Xiong et al. 2015). In addition some researchers have used a quantitative DNA assay to assess levels of residual DNA following decellularization (Crapo et al. 2011, Guyette et al. 2014). Residual DNA can result in an inflammatory response from host cells and is particularly important if the decellularized matrix is to be used *in vivo* (Balestrini et al. 2015). During the development of the decellularization protocol in this work, DAPI and phalloidin staining allowed the identification of cell remnants after each trial so that the protocol could be suitably refined enabling an intact acellular tissue to be produced. In their research Xiong et al, reporting a 'DNA smear' in some samples and optimized their protocol to include a DNase wash step to in the breakdown and removal of these. This could be adopted as a further refinement to the protocols used here. (DNase was also reported to help remove any residual detergent which might complicate seeding.)

CAM tissue is delicate and easily disintegrated in the early stages of decellularization when the protocol was in the early stages of development and optimization. Tissue handling proved to be extremely important especially as chemical treatment made the tissue sticky

and as a result it clung both to itself and to anything used to manipulate it. Placing CAM tissue in a suitable receptacle in which it could remain throughout treatment whilst solutions and washes were carefully administered and drained resulted in intact decellularized tissue. Timings for chemical treatment steps were then optimized to ensure that decellularization was complete but using minimum treatment time to avoid unnecessary degradation of the residual ECM structure. Freeze dried and rehydrated dCAM proved relatively easy to seed, providing it was first soaked in medium containing FBS. Balestrini et al have also reported that washing decellularized tissue in serum helped to remove DNA fragments and so a serum wash could be introduced in the preparation of the matrix for cell culture to improve both tissue clearing and the initial adhesion of cells when seeding. dCAM and dLung colonization was successful for all cell types used in this work once cell seeding had been optimized. dLung was well colonized at the surface after 17 days using an initial seeding density of around 1×10^5 cells of however there was still a large amount of uncolonized surface area in the deeper lung tissue. However, Xiong et al achieved a better population rate in just 9 days using twice the number of cells, indicating that denser seeding could improve colonization. One of the great benefits of using decellularized tissue is well illustrated here in that cell population and colonization can continue for as long as is necessary. The extent of colonization can be observed using live microscopy or by harvesting samples in stages to monitor progress. This flexibility in culture time is in sharp contrast to the strictly limited time available in live CAM experiments of just 5 days following cell seeding. In comparison to 2D culture however, proliferation of cells in the 3D decellularized matrices was slower and cell morphology more consistent to that seen *in vivo* (Baker and Chen 2012, Kremmer et al. 1991).

Whilst cells seeded on dLung were able to migrate into the porous structure of the tissue in these experiments, cells colonizing dCAM appeared to colonize in layers or formed small tumours at the surface. As cells preferentially proliferated over the dCAM surface it may be that experiments needed a longer time course to allow cell invasion into the dCAM itself. Ki67 staining suggested that during the colonization of dCAM that many cells were actively proliferating, however some cells seemed to show no Ki67 staining suggesting that they might have entered a quiescent phase of the cell cycle (G0). Ki67 localization to chromosomes in some cells provided evidence of cell mitosis (M) whereas the more general nuclear localization of Ki67 in other cells indicated the transcription of ribosomal RNA during the active growth and DNA synthesis phases of the cell cycle (Bullwinkel et al. 2006, Scholzen and Gerdes 2000). Again this is a more realistic cell cycle profile for cells in a tissue than for that seen in 2D culture where cells are constantly dividing. It is possible that reduced tissue elasticity plays a role in the ability of cells to migrate and invade, however whilst atomic force microscopy measurements have showed a slight reduction in elasticity following decellularization, these matrices are still closer to the live tissue equivalent than gel matrix environments such as collagen (softer) or agarose (stiffer) (Wu et al. 2003, Xiong et al. 2015). It is clear that decellularized tissue architecture provides a structure which carefully seeded cells can inhabit however, in removing the cellular element of the matrix much of the dynamic element and response of the tissue is lost. In live tissue, cells move to accommodate each other, breaking and reconnecting at cell junctions (Yap et al. 2007) so this is absent initially in the decellularized tissue setting. However, with careful and appropriate cell colonization, a dynamic niche could be recreated which could then be used for further studies such as metastatic invasion and colonization. In addition the biochemical components and chemotactic gradients provided within living tissue are also no longer

present. The creation of specific niche environments is very much the focus of tissue engineers in their quest to provide tissue and organ grafts using donor decellularized matrix and patient cells, so much can be learnt as this field matures.

As a model for the study of cell migration and colonization the decellularized tissue allows the quantification of cell behaviour via either live microscopy or by fixing and staining samples for quantification. Cell morphology could be quantified within the decellularized tissue in a similar way to that conducted in the models shown in Chapter 3, by measuring length and width of a number of cells and calculating the aspect ratio. Thus cells seeded onto and colonizing the decellularized tissue could be directly compared with those seeded in both CAM in Chapter 4 and in the simpler *in vitro* models described in Chapter 3 allowing the behaviour of cells from the same cell line to be directly compared for the different model contexts.

Many researchers working with decellularized tissue have reported that damage to the tissue during decellularization process leads to variation in adhesion and colonization as well as on occasion either a stiffer or a weaker resultant matrix (Badylak and Gilbert 2008, Crapo et al. 2011). Producing and optimizing protocols for decellularization is therefore important as is characterizing the matrix produced. Further work to stain and characterize the matrices produced here would provide necessary information to allow further refinement of protocols.

The results presented for the decellularization and colonization of decellularized matrices in this chapter demonstrate the potential of these products as natural 3D scaffolds for tissue culture and the study of disease mechanisms and processes at the cellular level. Table 5.1 summarizes the advantages and disadvantages associated with their use in this context.

The development of a protocol for the decellularization of chick chorioallantoic membrane for the first time allows the further use and exploitation of this well characterized model to be extended in a novel way for the comparison and characterization of cell behaviour in this context. In addition dCAM has the potential to be used for the probing of specific cell behaviours and resultant protein expression as well as to be used as a basis for the *ex vivo* testing of drug compounds (Loessner Daniela et al. 2014).

In the next chapter, dCAM is used as an *ex vivo* comparative assay alongside two *in vitro* assays for the investigation of protein expression and drug response in these three different culture environments.

Table 5.1 Benefits and disadvantages of decellularized tissue for the exploration of cell behaviour

	Advantage	Disadvantage
Preparation	Quick - 48 hours from harvest	Takes time to optimize protocol
Extent of Decellularization	Optimized protocol should provide a good output with controls	Need controls for each batch
Composition	Structural composition can be left intact to enable the study of cell interaction with these components.	Loss of biochemical components and cells means many of the cues stimulating cell behaviour are lost.
Seeding	Different cell types can be introduced either as a monoculture or co-culture.	Each tissue varies. dSkin proved difficult to populate.
Colonization	More realistic proliferation profile and timescales than 2D tissue culture	Where tissue is dense this can be difficult to monitor. Thin sections of tissue (eg rat lung) have been adopted by some researchers (Gilpin et al. 2014).
Experimental versatility	Tractable and easy to use	Batches may vary so need quality control for components present.
Harvesting	Fixing and staining in line with normal tissue culture protocols	Slightly longer times needed and slightly higher background for immunostaining may occur.
<i>In vivo</i> cell morphologies and behaviours replicated?	Yes	
Visualization	More accessible than live tissue and less autofluorescence	Thicker and more densely populated tissue may still need sectioning eg dLung.

6. An Integrated Approach to the Study of Metastatic Mechanisms

6.1. Introduction

In the previous chapters the development of several different 3D growth matrices has been described and presented for the investigation of cell migration and colonisation in the context of metastasis. The 3D contexts developed have included ECM based *in vitro* assays, the *in vivo* chick CAM model and *ex vivo* assays using decellularized tissues. In this chapter three of these assays are used to explore the differential expression of intermediate filaments in the different 3D contexts.

Intermediate filaments are known to contribute to cell structure, morphology and compartmentalization of organelles within the cell (Fuchs and Weber 1994, Kidd et al. 2014, Mendez et al. 2010). Recent research has also indicated their involvement in cell signalling pathways (Ivaska et al. 2007, Kidd et al. 2014). Intermediate filaments play a role in desmosomes, cell-cell junctions which bind cells together enabling tissue to resist shear stress (Fuchs and Weber 1994). In epithelial cells, keratin filaments complex with cadherins to form tight junctions and in cardiac and muscle cells the intermediate filament desmin plays the equivalent role (Lowery et al. 2015). Vimentin filaments on the other hand form a structural network in migrating cells driving their mesenchymal morphology (Mendez et al. 2010) and are involved in anchoring moving cells to a substrate through their role in focal adhesion complex assembly (Leube et al. 2015, Lowery et al. 2015). Cells undergoing epithelial-mesenchymal transition (EMT) frequently show an upregulation in vimentin expression as e-cadherins are lost and cell-cell junctions disrupted (Hanahan and Weinberg 2011, Onder et al. 2008). Filamentous vimentin forms a network which contributes to the cytoskeletal structure enabling the switch from a tissue resident, polarized epithelial cell to

the characteristic elongated mesenchymal morphology of a migrating cell (Lowery et al. 2015, Mendez et al. 2010, Murray et al. 2014). Indeed, vimentin has been identified as a marker of EMT and also endothelial-mesenchymal transition (EndMT) in disease conditions such as cardiac and kidney fibrosis, inflammation and many cancers (Kalluri and Weinberg 2009, Kidd et al. 2014, Thiery 2002). The down regulation of e-cadherin, loss of cell-cell junctions and cell polarity as cells detach from host tissue and invade into surrounding tissue, thus involves changes in the location and function of both keratin and vimentin intermediate filaments. Expression of both vimentin and keratin in these 3D environments provide interesting reporters for cellular response to the 3D matrices compared to a two dimension tissue culture environment.

The involvement of intermediate filaments in cell migration and adhesion gives the further opportunity to test inhibitors against two kinases known to be involved in the regulation of focal adhesions, namely Focal Adhesion Kinase (FAK) and SRC Kinase 1 (SRC) (Huveneers and Danen 2009, Li et al. 2002). Integrin activation of FAK causes auto-phosphorylation of FAK, recruiting SRC to form a FAK-SRC complex, the binding of SRC triggering further phosphorylation and upregulation of FAK (Huveneers and Danen 2009). The FAK-SRC complex drives both focal adhesion (FA) turnover and the phosphorylation of the focal adhesion protein paxillin, which in turn activates Rac1, Cdc42 and other proteins involved in driving the formation and extension of membrane protrusions during cell migration (Huveneers and Danen 2009, Lawson and Schlaepfer 2013). Research also indicates a role for the FAK-SRC complex in the disassembly of e-cadherin at tight junctions during EMT (Schaller 2010). Cell spreading and focal adhesion turnover and maturation are also known to be affected by substrate stiffness (Plotnikov et al. 2012, Schaller 2010, Wehrle-Haller 2012) as is the expression of vimentin within migrating cells (Mendez et al. 2010, Murray et

al. 2014). Vimentin and keratin expression of cancer cells in different 3D contexts in the absence or presence of FAK or SRC inhibitors could therefore help to elucidate cellular responses to different niche environments.

This chapter describes the investigation of vimentin and keratin expression with and without FAK and SRC inhibitors, using two different cell lines and three different 3D matrix environments developed within this project.

6.2. Materials and methods

6.2.1. Inverted invasion assay

Cells were trypsinized then seeded into 3.5cm² microscope dishes (ibitreat – Thistle) and left for 1-2 days until cells were 70-80% confluent. 2mg/ml collagen solution was made using 10X DMEM and 0.5M NaOH to bring to a pH of 7-7.5. Whole growth medium was used to make up the full volume with SRC Kinase 1 inhibitor (Merck Millipore, used at 1µM) or FAK inhibitors (Tocris, used at 1µM) added as appropriate. The concentration for the inhibitors was chosen based on previous work within the lab which investigated the inhibition of invadosome formation in HT1080 cells (Patel 2012). Growth medium was aspirated and collagen was layered over the top of the adherent cells and left to set in a humidified incubator at 37°C, 5% CO₂. Whole medium with/without inhibitors was added to each dish and these were placed in the incubator for either 1 or 2 days depending on the cell line seeded. Cells were then fixed with 4% PFA/PBS, washed with PBS, permeabilized with 0.2% TX-100/PBS then stained with phalloidin atto 565 (1:250) and DAPI (1µg/ml) using the protocol described in section 2.4. Confocal images were taken using a Nikon A1 Plus microscope and images rendered and measurements taken using NIS Elements software. ImageJ software was then used to quantify fluorescence by first summing the protein expression for all slices in the Z stack, defining a specific region of interest (ROI) around a cell then taking the mean fluorescence for that cell. For each image the mean fluorescence for a background sample was also measured and this value was deducted from the fluorescence mean for each cell to give a final corrected value.

6.2.2. SRC and FAK inhibited 2D/3D colonisation assay

A 2D/3D assay (section 3.2.5) was set up by pipetting 2mg/ml collagen at the centre of each well of a 12-well tissue culture plate. Collagen was set up both without inhibitors (control wells) or with FAK inhibitor or SRC Kinase 1 inhibitors added both at 1 μ M (experiment wells). Cells were trypsinized and re-suspended in normal growth medium with or without inhibitors and these were added to the 2D/3D assay to give a 20% initial confluence once cells had settled and adhered. After 2 hours, time-lapse microscopy was set-up to monitor cell proliferation and migration using a Nikon TIE phase contrast microscope with moving stage and environmental chamber as described in section 2.5.

6.2.3. Cell colonization on compressed collagen

Compressed collagen discs were made according to the protocol described in section 3.2.4 either without inhibitors (control) or with either FAK or SRC Kinase 1 inhibitors (both at 1 μ M concentration). Compressed collagen discs were first hydrated in medium (with/without inhibitors) to prepare them for cell seeding. Cells from three cell lines were trypsinized from 25cm² flasks and re-suspended in medium either with or without inhibitors to give a 1:5 concentration (where 1ml contains 1cm² of cells \approx 1.2 x 10⁵ cells). Re-suspended cells were then seeded onto compressed collagen: 200 μ l of HT1080 (around 2.4 x 10⁴ cells) or 250 μ l (around 3 x 10⁴ cells) of either MDA-MB-231 or MCF7 cells. Cells were left to settle for 2 hours then additional medium was added with/without inhibitors. Colonization was monitored and medium changed every 2-3 days. Cells/ compressed collagen were harvested 5 days after seeding, fixed, permeabilized and stained with phalloidin, DAPI and with primary antibodies against specific proteins of interest, these being: vimentin (abcam RV202 ab8978,

1:250) and/or Ki67 (abcam 16667, 1:500) as described in section 5.2.7. Alexafluor 647 was used as a secondary antibody for vimentin and Alexafluor 488 was used for Ki67.

6.2.4. HT1080 colonization of dCAM

dCAM was prepared for seeding as previously described (section 5.2.4). Cells were trypsinized and re-suspended in medium with/without inhibitors. Cells were seeded and left to settle as for the compressed collagen assay described above. Additional medium with/without inhibitors was added and cells left to colonize the dCAM for the required number of days. Medium was replaced every 2-3 days containing inhibitors as required and dCAM/cells were fixed, permeabilized and stained in the same way as for compressed collagen. Primary antibodies were used against: vimentin (abcam RV202 ab8978, 1:250) and/or Ki67 (abcam 16667, 1:500) and keratin (abcam ab118817 1:200). Secondary antibodies used were Alexafluor 647 vimentin/keratin and Alexafluor 488 was used for Ki67.

6.2.5. Statistics

Graphpad Prism 6 was used for statistical analyses. A normality test was conducted to determine whether data distribution fitted a Gaussian curve (normal distribution). The statistical test to be used was then selected, either a One-way ANOVA if Gaussian or a Kruskal-Wallis test as an alternative non- parametric test. Where an equal number of replicates for each condition was available a two-way ANOVA was conducted to take account of variation within each population when comparing replicates within each experiment/condition. Pearson's test for correlation was conducted to determine whether two variables might be correlated: cell aspect ratio and protein expression. Outcomes of statistics are shown in the results section and full tables for each test are shown in Appendix E.

6.3. Results

Cells respond and behave according to their surrounding environment and so research into cell behaviours is only relevant if it can replicate the environmental characteristics that drive the behaviours being studied (Bissell et al. 2003, Hynes 2009). Providing an appropriate context for the study of cell behaviours is therefore important. Due to the complexity and variation within live tissues, not to mention in different disease states and individual patients, it is difficult to determine a specific environment to be used. This section presents the results obtained for three different contexts and two different cell lines.

6.3.1. Cell colonisation and migration in the presence of FAK and SRC kinase 1 inhibitors

The 2D/3D assay was used to determine the effect of FAK or SRC Kinase 1 inhibitors on cell adhesion, colonization and migration for three cell lines: MCF7, MDA-MB-231 and HT1080 cells. Time-lapse movies showed that cells adhered and started to colonize in all cases (Figure 6.1) but differences in the extent of colonization were difficult to detect due to the large area of seeding and difficulty in controlling seeding area so that it was directly comparable. One approach for the comparison of proliferation was to count the number of cell divisions during the 22 hour time-lapse period. However, when this was carried out for a sample of cells for each treatment, most cells divided once and the resulting data was insufficient for meaningful quantification, therefore this approach was not pursued (data not shown). Whilst differences in cell migration could be quantified using cell tracking, this would not necessarily provide data relating to colonization. In order to better quantify invasion and colonization behaviours, the assay was modified to create an inverted invasion assay in which cells were seeded and grown until they were 70-80% confluent and then

collagen layered over the cells into which they could invade. Quantification of invasion could then be specifically measured using z-depth analysis.

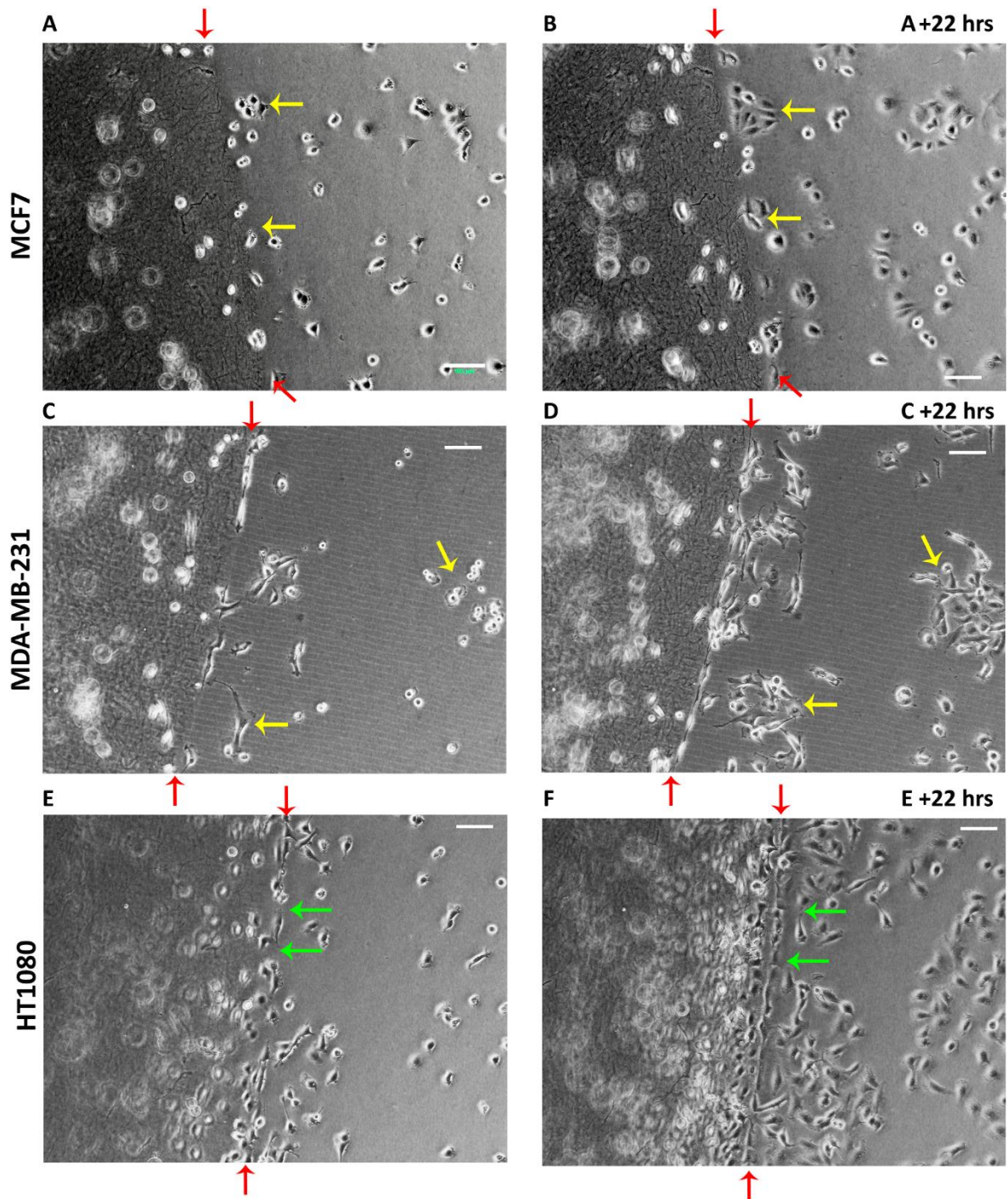


Figure 6.1, Cell colonization of a 2D/3D assay. Cells from three different cell lines were seeded onto a 2D/3D collagen assay either with or without inhibitors for FAK or SRC Kinase 1. Cell migration and division were monitored for 22 hours via time-lapse microscopy using a Nikon TiE with moveable stage and environmental chamber. Images shown are for the start and finish of the 22 hour period for each cell line. **A, B** MCF7 cells, **C, D** MDA-MB-231 cells, **E, F** HT1080 cells. Yellow arrows indicate cell groups which have expanded during the 22 hour period. Green arrows indicate areas now well populated after 22 hours. Red arrows indicate the 2D/3D border. Scale bars = 100 μ m.

6.3.2. Inverting the 2D/3D assay to quantify invasion – inverted invasion assay

MCF7, MDA-MB-231 and HT1080 cells were seeded and allowed to proliferate on the 2D surface until they were at least 70% confluent before layering collagen over the cells and allowing them to invade into it. Invasion into the collagen was then quantified by measuring the height of the top of the nucleus from the base of the dish for each cell type both without inhibitors (controls) and with either FAK or SRC inhibitors. Results for MCF7 cells (Figure 6.2) showed that the height of the top of the nucleus from the base did vary between controls and the experiments with FAK and SRC inhibitors after 2 days, with mean values for 30 cells for each of 3 repeats suggesting that nuclei from inhibited cells had pushed up into the collagen around 1.5 μ m further from the dish base than had controls (control = 10.51 μ m, FAK inhibited = 12.03 μ m, SRC inhibited = 12.08 μ m). However, the measurements and images show that the majority of the cell nuclei were still in touch with the base of the plate and therefore could not be deemed to have migrated. In Figure 6.2 A, nuclei (blue) appear oval and grouped, the phalloidin staining showing cytoskeletal protrusions reaching upwards into the collagen as well as laterally within the cell layer. Figure 6.2 B, shows the confluence of a typical experiment indicating that cells would have little opportunity to move or proliferate in the horizontal plane due to their confluence. For MDA-MB-231 cells (Figure 6.3) measurements of cell nuclei from the baseline for cells invading up into the collagen layer indicated that where SRC inhibitor was present, nuclei and therefore cells were more mobile and had started to invade into the overlying collagen significantly further than control cells (32 cells for each condition were counted and this repeated 3 times, statistical tests giving mean distances: control = 7.95, FAK inhibited = 9.12, SRC inhibited = 10.52). However there was no significant difference seen between control cells measured and cells with FAK inhibitors present in these experiments.

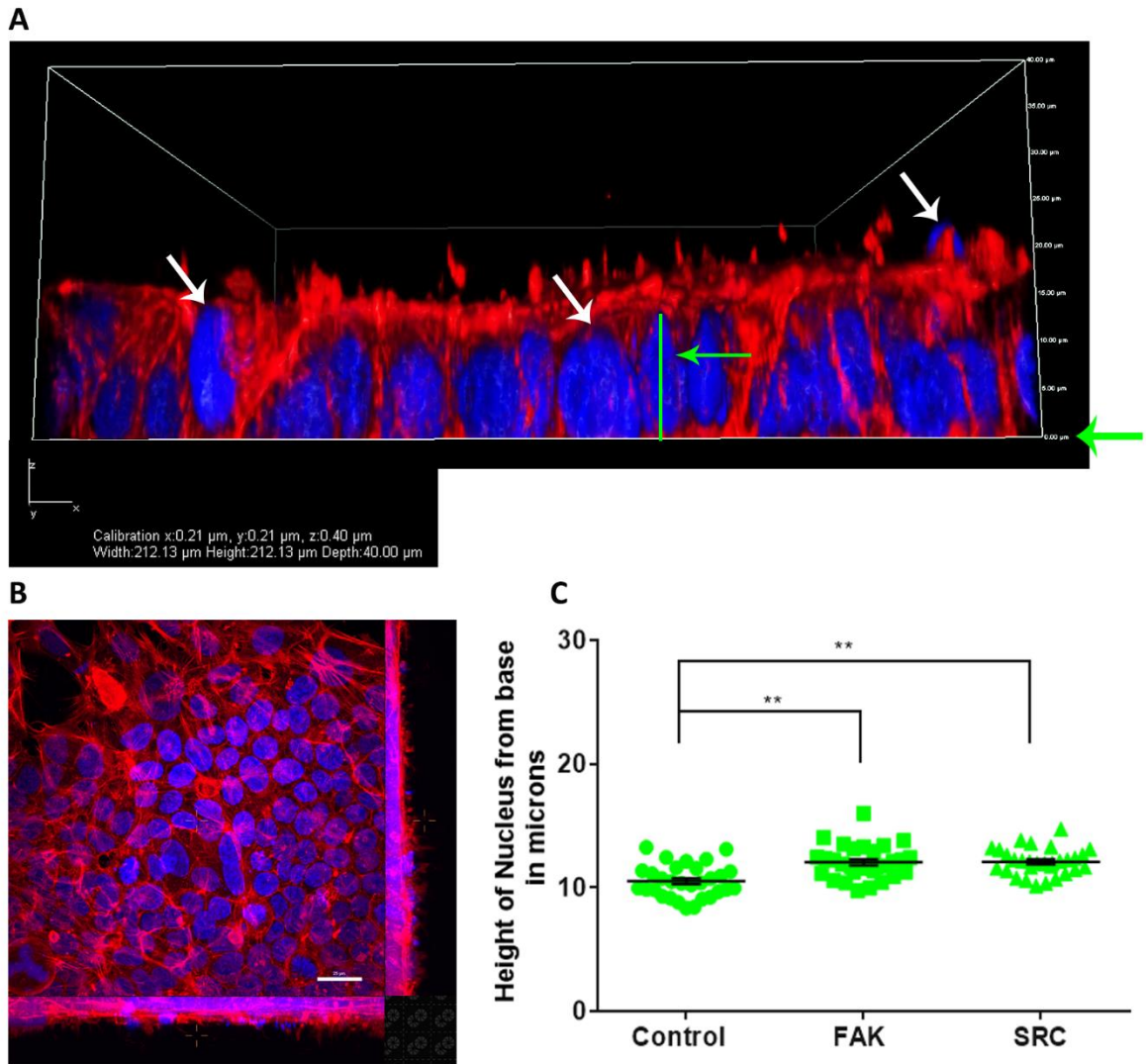


Figure 6.2, MCF7 cell invasion into collagen using an inverted invasion assay. Collagen was layered over growing MCF7 cells. After 2 days, cells were fixed and stained with phalloidin and DAPI and confocal images taken with a Nikon A1 plus microscope with a z-stack totalling 40 μm (0.4 μm slices). NIS elements software was used to render images and measurements of height from base were taken for 30 cells per treatment type for each of 3 separate experiments (n=3). **A**, 3D rendered image showing nuclei stained with DAPI (blue) and the actin cytoskeleton stained with phalloidin (red). Green arrows indicate the base and the measurement of nucleus height from base. **B**, maximum projection image of cells shows that cells formed a layer at the base of the plate. **C**, The height of the nucleus for each of 30 cells for each treatment was measured for each of three experiments. Graphpad Prism 6 was used to generate a two-way ANOVA with Dunn's multiple comparisons test. Significance shown: ** $p \leq 0.01$. Each cell is represented by a point. Error bars show standard error of the mean (SEM). Scale bar in B = 25 μm .

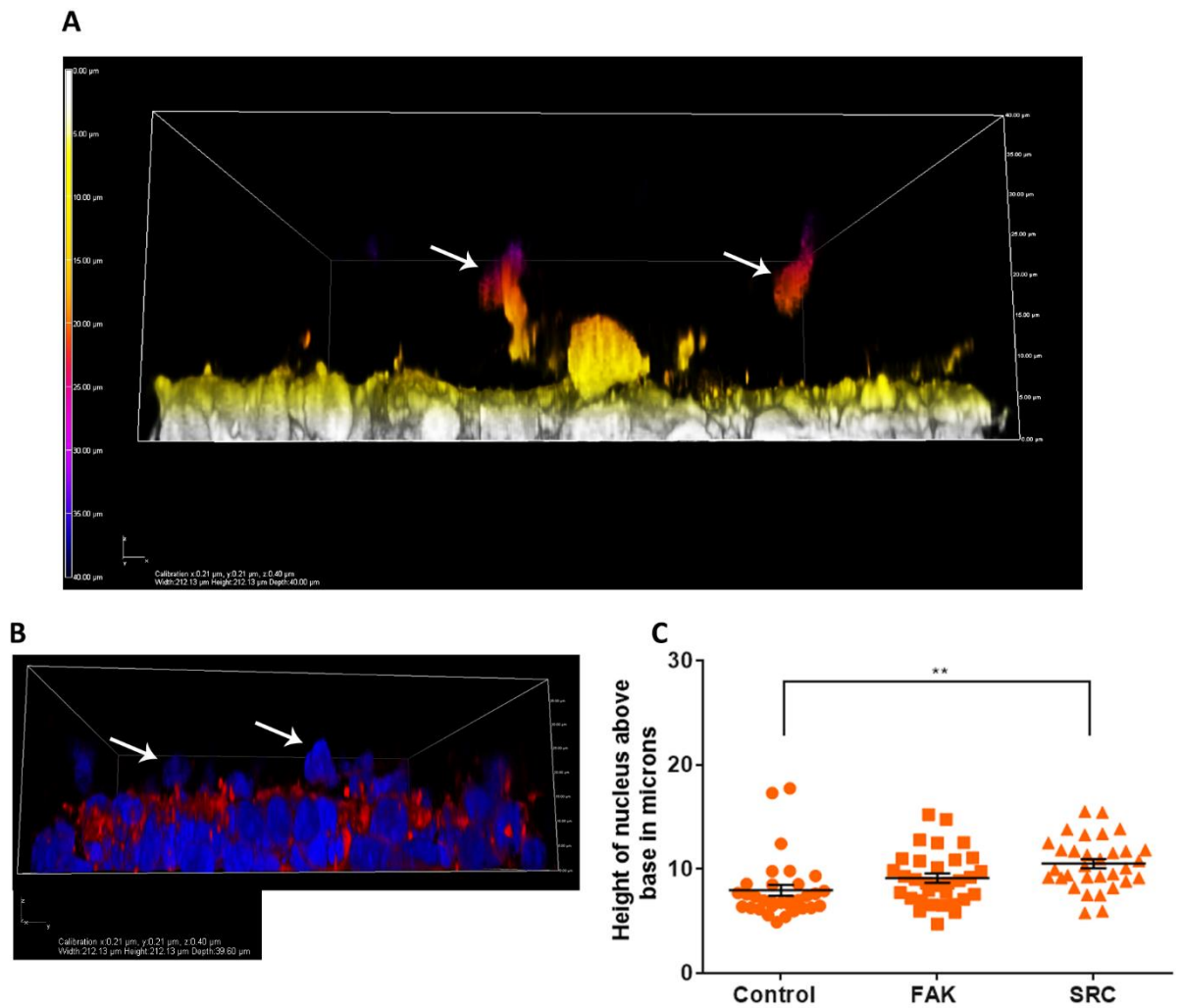


Figure 6.3, MDA-MB-231 cell invasion into collagen measured using an inverted invasion assay. Collagen was layered over growing cells. After 2 days, cells were fixed and stained with phalloidin and DAPI and confocal images taken with a Nikon A1 plus microscope with a z-stack totalling 40 μ m (0.4 μ m slices). NIS elements software was used to render images and measurements of height of the nucleus from the base were taken for 32 cells per treatment type for each of 3 separate experiments (n=3). **A** 3D rendered image using z-depth coding to show the invasion of nuclei upwards into the collagen layer. White arrows show nuclei that have moved 20-30 μ m up into the collagen. **B** 3D rendered image showing nuclei stained with DAPI (blue) and the actin cytoskeleton stained with phalloidin (red). White arrows indicate nuclei which have moved away from the base and up into the collagen layer. **C** Graph to show the height of the nucleus for each cell for each treatment was measured for each of three experiments. Each data point represents one cell. Graphpad Prism 6 was used to generate a two-way ANOVA with Dunn's multiple comparisons test. Significance shown: ** $p \leq 0.01$. Error bars show standard error of the mean.

When the inverted invasion assay was used to compare the invasion of HT1080 cells into collagen in the absence or presence of FAK or SRC Kinase 1 inhibitors, cell invasion was prolific after 2 days and it was therefore difficult to differentiate between individual nuclei so cell invasion was measured after just one day. The z-depth colour coded image shown in Figure 6.4 A, shows the extent of cell migration up into the collagen and blue arrows in Figure 6.4 B, show examples of DAPI stained nuclei and phalloidin stained cytoskeleton for some of these migrating cells. The height of the top of cell nuclei from the baseline was measured for 30 cells for each of three independent experiments. The graph at Figure 6.4 C, shows the results of obtained which suggested that there was a significant difference between control and cell invasion with FAK inhibitors, the nuclei of control cells moving further up into the collagen than those of cells with FAK inhibitors present (means: control = $10.70\mu\text{m}$, FAK inhibited = $7.11\mu\text{m}$, SRC inhibited $11.51\mu\text{m}$). However, when cell nuclei for the control cells and cells with SRC inhibitors present were compared the height of nuclei from base showed a similar pattern of distribution and the difference was not found to be significant.

Investigation into the effects on these cell lines of the FAK and SRC inhibitors was taken further by extending the investigation into the compressed collagen environment.

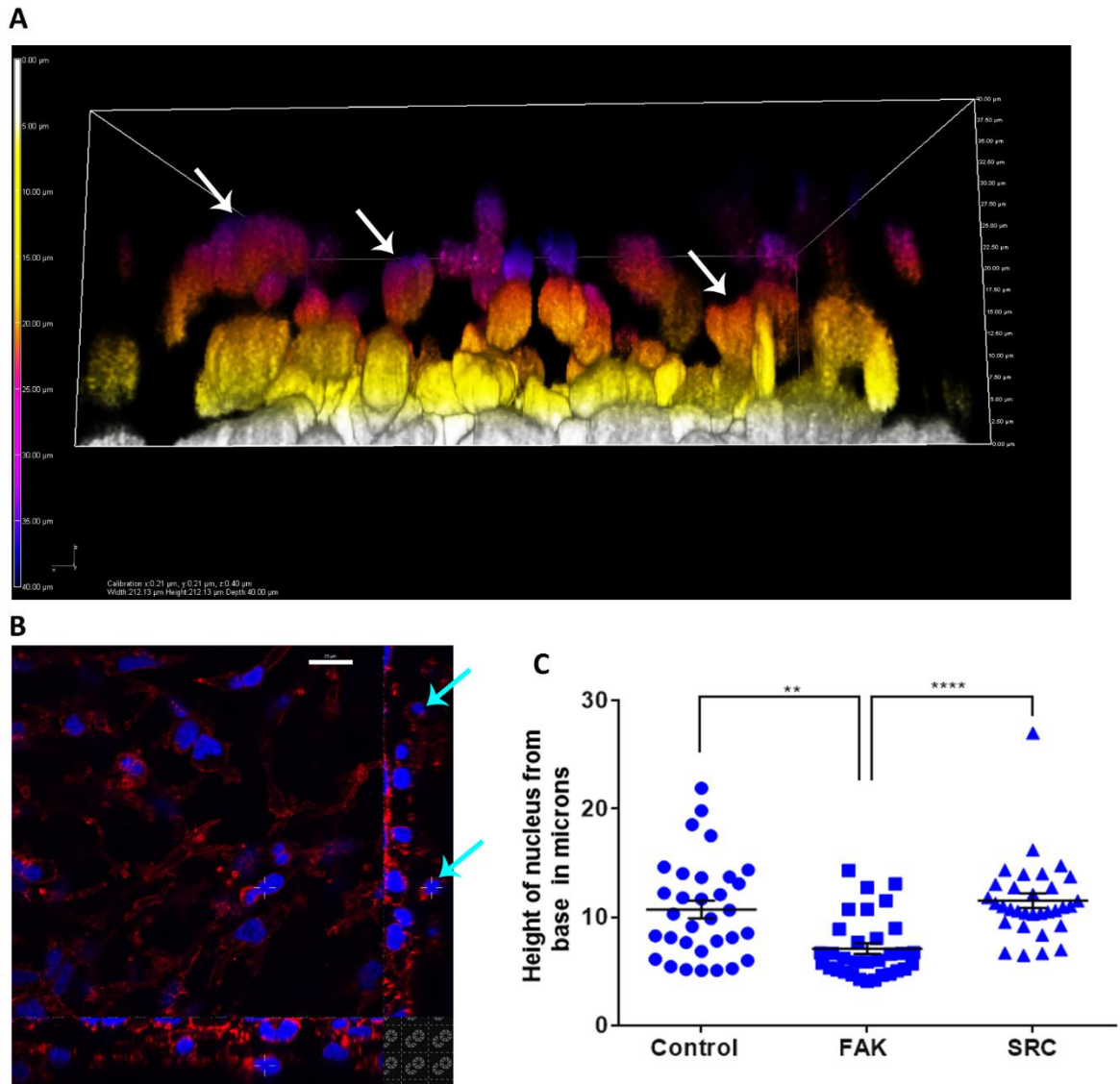


Figure 6.4, HT1080 cell invasion into collagen measured using an inverted invasion assay. Collagen was layered over growing cells. After 1 day, cells were fixed and stained with phalloidin and DAPI and confocal images taken with a Nikon A1 plus microscope with a z-stack totalling 40 μm (0.4 μm slices). NIS elements software was used to render images and measurements of height from base were taken for 32 cells per treatment type for each of 3 separate experiments (n=3). **A**, 3D rendered image using z-depth coding to show the invasion of nuclei upwards into the collagen layer. White arrows show nuclei that have invaded at least 20 μm into the collagen layer. **B**, Image shows a slice through a z-stack showing nuclei stained with DAPI (blue) and the actin cytoskeleton stained with phalloidin (red). Blue arrows indicate nuclei which have invaded right up into the collagen layer. **C**, The height of the nucleus for each cell for each treatment was measured for each of three experiments. Graphpad Prism 6 was used to generate a two-way ANOVA with Dunn's multiple comparisons test. Each cell is represented by one data point. Significance shown: ** $p \leq 0.01$ and **** $p \leq 0.0001$. Errors bars show standard error of the mean. Scale bar in B = 25 μm .

6.3.3. Using the compressed collagen 3D environment to investigate vimentin expression in the absence and presence of FAK and SRC kinase 1 inhibitors

The compressed collagen assay, developed as a novel approach to the investigation of cell behaviour in the 3D environment, was explored further as a 3D *in vitro* assay to investigate the expression of the intermediate filament vimentin in the absence and presence of FAK and SRC kinase 1 inhibitors, these kinases being known to affect cell adhesion, migration and invasion. MDA-MB-231 cells were seeded and allowed to proliferate on compressed collagen discs and the level of expression of vimentin quantified after 5 days (Figure 6.5). Compared to control cells, vimentin expression levels appeared to be higher in the presence of FAK inhibitor (mean and SD values: control: mean, 1994, SD, 1090; FAK: mean, 5168, SD, 3553 Grays) whereas the standard deviation and population distribution for control cells compared to cells in the presence of SRC inhibitor were similar (SRC: mean, 2882, SD, 2215). Cells showed a varied morphology with many rounded cells forming a pavement type arrangement on flat areas of the compressed collagen (blue arrows in Figure 6.5, A-C) and elongated cells stretched out along edges and in between groups of rounded cells (white arrows Figure 6.5, A-C). For comparison, HT1080 cells were also seeded on compressed collagen and results for controls compared with cells with SRC inhibitor present, are shown in Figure 6.6 for two independent experiments (n=2). For the first experiment the mean values and data distribution for vimentin expression were similar between the control and cells in the presence of SRC inhibitor (Con1 mean: 1310 Grays, SD, 596; SRC1 mean: 1241, SD, 360 Grays). In the second experiment, the mean for the vimentin expression in control cells was higher than in the first experiment (Con1: mean: 1310, SD, 596 Grays and Con2 mean, 2034, SD, 850 Grays) and the cells showed a greater variation in vimentin expression. SRC inhibited cells in the second experiment also showed a greater range of vimentin

expression and the mean value suggested that there might be a difference between the control and cells with SRC inhibitor for this experiment (Con2 mean: 2034, SD, 850 Grays; SRC2, mean: 3457, SD, 1762 Grays). In comparison to MDA-MB-231 cells, HT1080 cells appeared to be mainly elongated in regions where they had colonized the compressed collagen surface.

Differential expression of vimentin was further investigated in dCAM colonization experiments to enable the comparison of expression across three different culture environments: 2D tissue culture plastic, compressed collagen and decellularized tissue (dCAM).

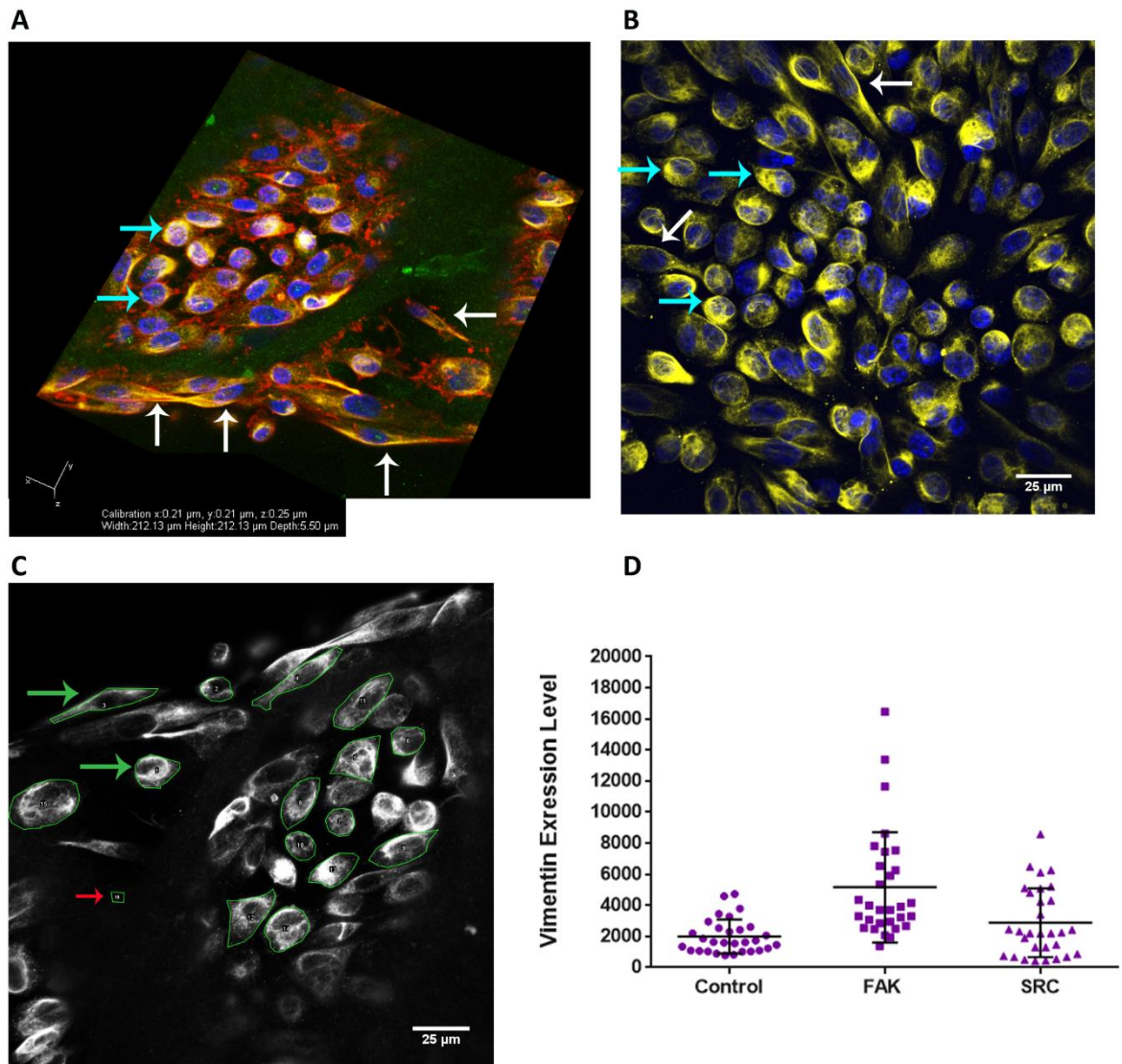


Figure 6.5, Vimentin expression of MDA-MB-231 (MDA) cells on compressed collagen with/without inhibitors for FAK or SRC kinase 1. Cells were seeded onto compressed collagen with/without inhibitors present and allowed to proliferate and colonize the collagen for 5 days. Cells and collagen were fixed, stained with phalloidin (red), DAPI (blue) and for vimentin (yellow). A Nikon A1 confocal plus was used to acquire image stacks. **A** 3D rendered image showing MDA cells colonizing compressed collagen (green due to reflectance at around 500nm). Cells can be seen to adopt both elongated (white arrows) and rounded (blue arrows) morphologies on control samples. **B** The z-stack for each image set was summated using ImageJ so that vimentin fluorescence could be quantified. Cells of rounded (blue arrows) and elongated (white) morphologies are indicated. **C** a region of interest was drawn around each vimentin expressing area for a cell (green arrows indicate green ROIs) and a figure for mean fluorescence was obtained. A background area was selected and the mean fluorescence from this area was deducted for all cells from that image. **D** Fluorescence for 30 cells for each treatment for 1 experiment (n=1) was quantified and the mean and standard deviation (error bars) for each population calculated. Cells with FAK inhibitor showed higher fluorescence than control cells. Fluorescence is measured based on summated pixel intensity in grays (y-axis). Scale bars = 25 μm .

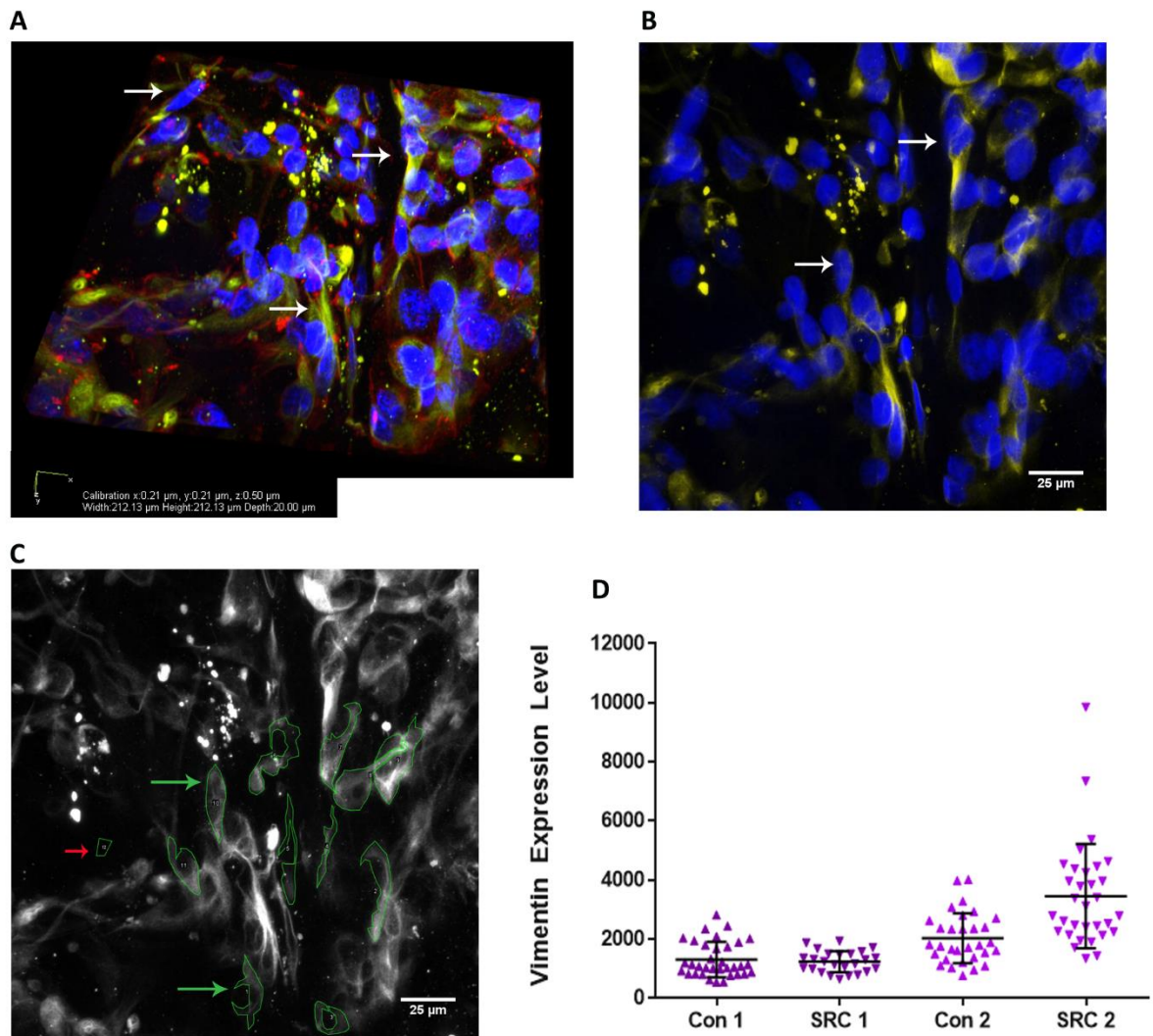


Figure 6.6, HT1080 cell colonization of compressed collagen with/without SRC kinase 1 inhibitor. Cells were left to colonize compressed collagen for 5 days then fixed and stained with phalloidin (red - cytoskeleton) DAPI (blue - nuclei) and vimentin (yellow). Images were taken using a Nikon A1 plus confocal microscope. Vimentin expression was quantified using ImageJ based regions of interest drawn around cells on a summated z-stack for the far red channel. **A** 3D rendered image showing cell colonization – cells were mostly of elongated morphology (white arrows A and B). **B** combined DAPI and vimentin compressed z-stack image. **C** vimentin only compressed image with ROI drawn around cells (green arrows and ROI). Red arrow indicates the control area used to calculate background fluorescence which was then deducted. **D** Graph showing data from two separate experiments (n=2), each with a control and a colonized compressed collagen with SRC inhibitor. Con = Control, SRC = SRC inhibited. Error bars show standard deviation. Fluorescence is measured based on summated pixel intensity in grays (y-axis). Scale bars = 25 μm .

6.3.4. Vimentin expression using dCAM as a 3D matrix

Decellularized tissue was proposed as a second novel biomaterial for the culture and exploration of cell behaviour in Chapter 5. dCAM was used here as a comparative 3D matrix for the exploration of vimentin expression levels in comparison with the compressed collagen assay. Figure 6.7 shows results for the comparison of vimentin expression for cells in 2D, compressed collagen (CC) and on dCAM after deduction for background fluorescence. At least 37 cells were sampled for each environment and mean values and standard deviation (SD) in Grays were as follows: 2D: mean, 3143, SD 2006; CC: mean, 2034, SD, 843.6; dCAM: mean, 7372, SD, 7851. These results suggest that vimentin expression may be increased in the 3D dCAM environment for HT1080 cells.

The response of HT1080 cells to dCAM was further investigated in the absence and presence of the SRC Kinase 1 inhibitor. Figure 6.8 shows results for three independent SRC inhibited experiments in which HT1080 cells were seeded and cultured on dCAM in the presence of 1 μ M of SRC kinase 1 inhibitor for 5 days. A control sample from n3 is included for comparison against all samples. Results for vimentin expression indicated that there was a significant difference between cells measured for the control sample compared to two of the three inhibited samples. Mean values and standard deviation (SD) in Grays were: Control: mean, 7372, SD, 7851; SRC n1, mean, 21825, SD, 9372; SRC n2: mean, 3835, SD, 1551; SRC n3: mean, 14802, SD, 7151. The 3D image (Figure 6.8 A) suggests differential expression of vimentin across the dCAM with some cells expressing high quantities of vimentin (white arrows) and others barely expressing vimentin at all (green arrows).

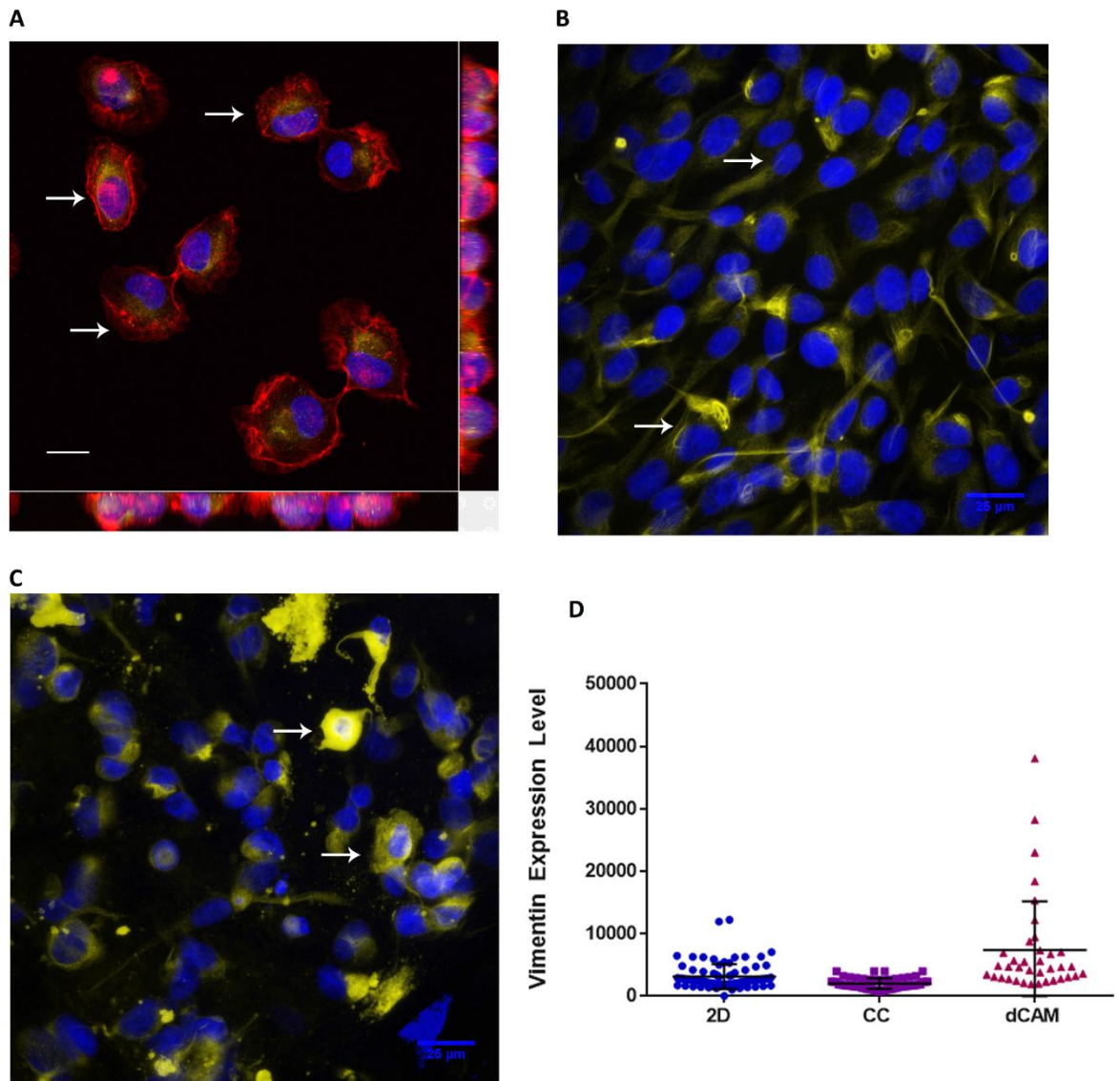


Figure 6.7, Comparison of HT1080 vimentin expression on 2D plastic (2D), compressed collagen (CC) and decellularized chick chorioallantoic membrane (dCAM). Cells were left to colonize CC and dCAM for 5 days then harvested and stained with phalloidin (actin - red), DAPI (nuclei - blue) and vimentin (yellow). 2D cells were fixed and stained 1 day after seeding directly onto plastic microscopy dishes (ibitreat). White arrows indicate examples of cells expressing vimentin in each of A-C. **A** Cells dividing in 2D express vimentin. **B** cells on CC have divided and colonized well and mostly show an elongated cell morphology in this summated z-stack image. **C** cells colonizing dCAM show varied vimentin expression in this summated z-stack image. **D** Graph showing differences in vimentin expression between 2D, CC and dCAM. At least 37 data points are shown for each condition. The results from 2 independent experiments were summated for CC. 2D results were taken from 3 technical replicates from one experiment and dCAM results were taken by sampling several areas of a colonized dCAM from one experiment. Fluorescence is measured based on summated pixel intensity in grays (y-axis). Error bars show standard deviation. Scale bars A-C, 25μm.

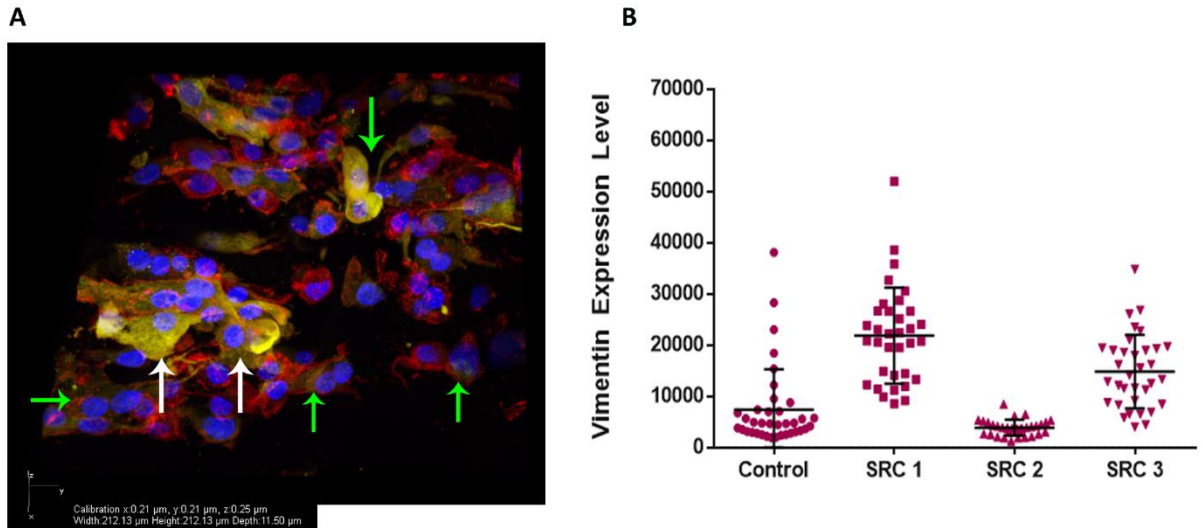


Figure 6.8, HT1080 expression of vimentin on dCAM in the absence and presence of SRC kinase 1 inhibitor. Cells were seeded on prepared dCAM in the absence and presence of SRC Kinase 1 and left to colonize the matrix for 5 days. Harvested samples were stained with phalloidin (actin – red), DAPI (nuclei – blue) and for vimentin (yellow). Image stacks were taken using a Nikon A1 Plus confocal microscope. ImageJ was used to summate the z-stacks and quantify fluorescence. Three independent experiments were conducted (n1-3) and are shown for SRC inhibited samples along with one control sample from experiment 3. The fluorescence for at least 31 cells was quantified for each condition. Error bars show standard deviation. Fluorescence is measured based on summated pixel intensity in grays (y-axis).

Figure 6.9 presents a comparison of results for vimentin expression both with and without SRC across the three different environments: 2D, CC and dCAM in the absence and presence of SRC kinase 1 inhibitor. The mean values and distribution of the data suggest that in the presence of SRC kinase 1 inhibitor, vimentin expression was different when compared across the two 3D environments, CC and dCAM (mean and standard deviation (SD) values in Grays: 2D: mean, 3143, SD, 2006; CC Con: mean, 2034, SD, 843; CC SRC: mean, 2485, SD, 1733; d Con: mean, 7372, SD, 7851; d SRC: mean, 13780, SD, 10081).

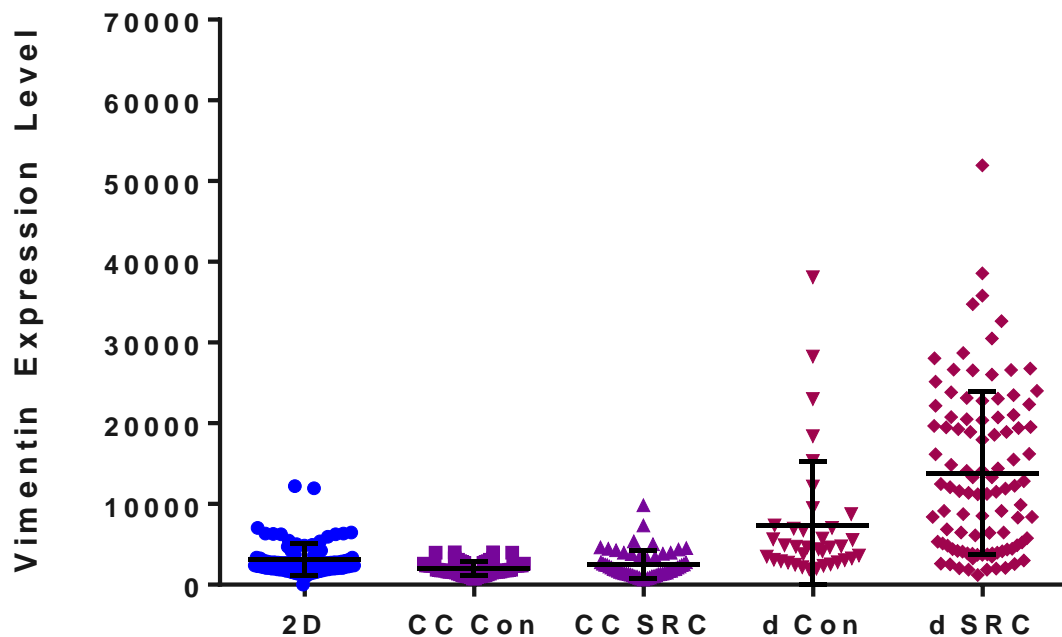


Figure 6.9, Comparison of HT1080 vimentin expression between 2D and 3D environments with and without SRC kinase 1 inhibitor. Vimentin expression for cells seeded on 2D plastic microscope dishes (Ibitreat) are shown as a control '2D'. Controls, with no inhibitors, are shown for both compressed collagen (CC Con) and dCAM (d Con). Cells with SRC inhibitor are shown for both CC (CC SRC) and dCAM (d SRC). (Cell numbers for each condition were: 2D, 82 cells from 3 technical replicates; CC Control, 62 cells and CC SRC 57 cells for 2 independent replicates; d Con, 37 cells for one experiment; d SRC, 99 cells from 3 independent replicates.) Error bars show standard deviation.

To explore the possibility that vimentin expression might reduce over time, a timeline study was conducted for vimentin expression on dCAM. Figure 6.10 shows the vimentin expression results for 4 separate 7 day experiments, compared to one experiment for each a 1 day and 3 day time point. These results are compared to 2D vimentin expression. The difference in mean and population spread suggested that there might be a difference in vimentin expression seen between 2D and day 1 on dCAM and between Day 1 results and results at Day 3 and each result at Day 7 (mean and SD values in Grays: 2D, 2611; Day1, 6944; Day 3, 2550; Day7 n1, 5727, n2 1309, n3 4381, n4 2207 in Grays).

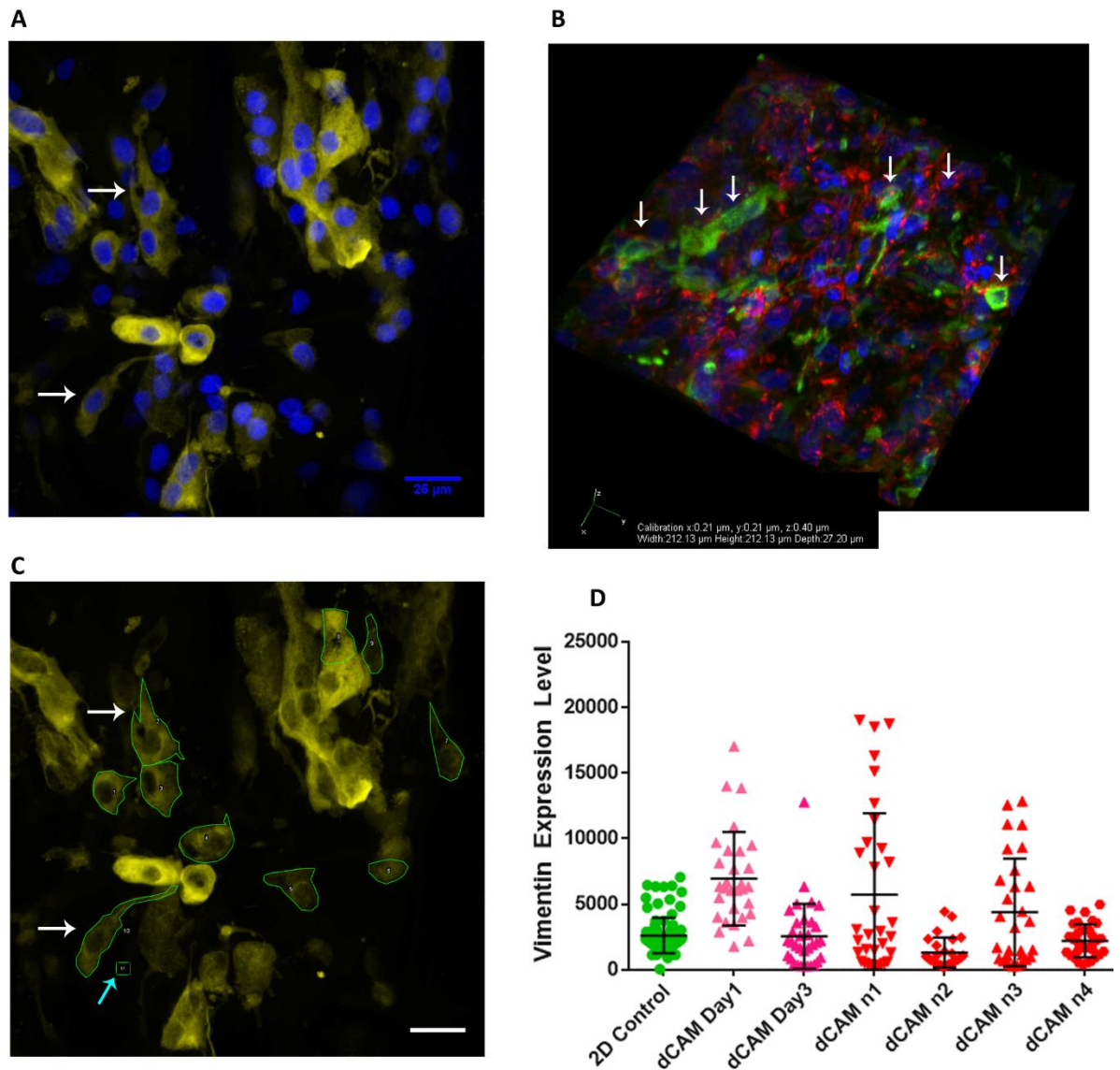


Figure 6.10, Timeline of vimentin expression for HT1080 cells seeded onto dCAM. Cells were seeded and allowed to proliferate on dCAM for either 1 day, 3 days or 7 days (n1-4). Cells and matrix were harvested, stained with DAPI (nuclei-blue), phalloidin (actin-red) and vimentin (yellow) and confocal images taken using a Nikon A1 plus microscope. ImageJ was used to summate the z-stacks and quantify fluorescence based on pixel intensity levels (grays). **A** An example of a summated composite image showing DAPI and vimentin stained cells. White arrows indicate elongated cells expressing vimentin which are defined and quantified at C. **B** 3D rendered RGB image showing vimentin in the green channel. **C** Summated z-stack image for vimentin only shows defined regions of interest which were quantified for this image. Background fluorescence was deducted based on a sample taken which is indicated by the blue arrow. **D** Graphpad6 was used to generate mean and standard deviation values for each experiment (at least 26 cells per experiment). Cells seeded on 2D plastic were used as a control for comparison. Error bars show standard deviation. Scale bars A, C, 25µm.

6.3.4.1. Is vimentin expression related to cell morphology?

The cell morphology of cells inhabiting the different matrix models can be compared with a view to characterisation and identification of differential cell behaviours in each context. Cell morphology was quantified for cells on dCAM expressing vimentin. Aspect ratio was calculated for each cell and the mean fluorescence level, indicating vimentin expression, calculated using ImageJ as shown in Figure 6.10. This was carried out for three independent experiments (n1-3, for 30-33 cells per experiment). The aspect ratio for each cell was plotted against its mean fluorescence value for each experiment and these values plotted as a scatter plot (Figure 6.11). A Pearson's test for correlation was conducted for each cell population to determine whether the aspect ratio and vimentin expression levels might be related. The results suggested that for the cells measured for these experiments that there was no correlation between aspect ratio and vimentin expression level for any of the three populations tested (statistics and confidence intervals (CI) obtained were: n1, Pearson $r = -0.1414$, 95% CI -0.4623 to 0.2122 ; n2, Pearson $r = -0.007052$, 95% CI -0.3664 to 0.3541 ; n3, Pearson $r = -0.1355$, 95% CI -0.4727 to 0.2363 . Results tables are given in Appendix E.)

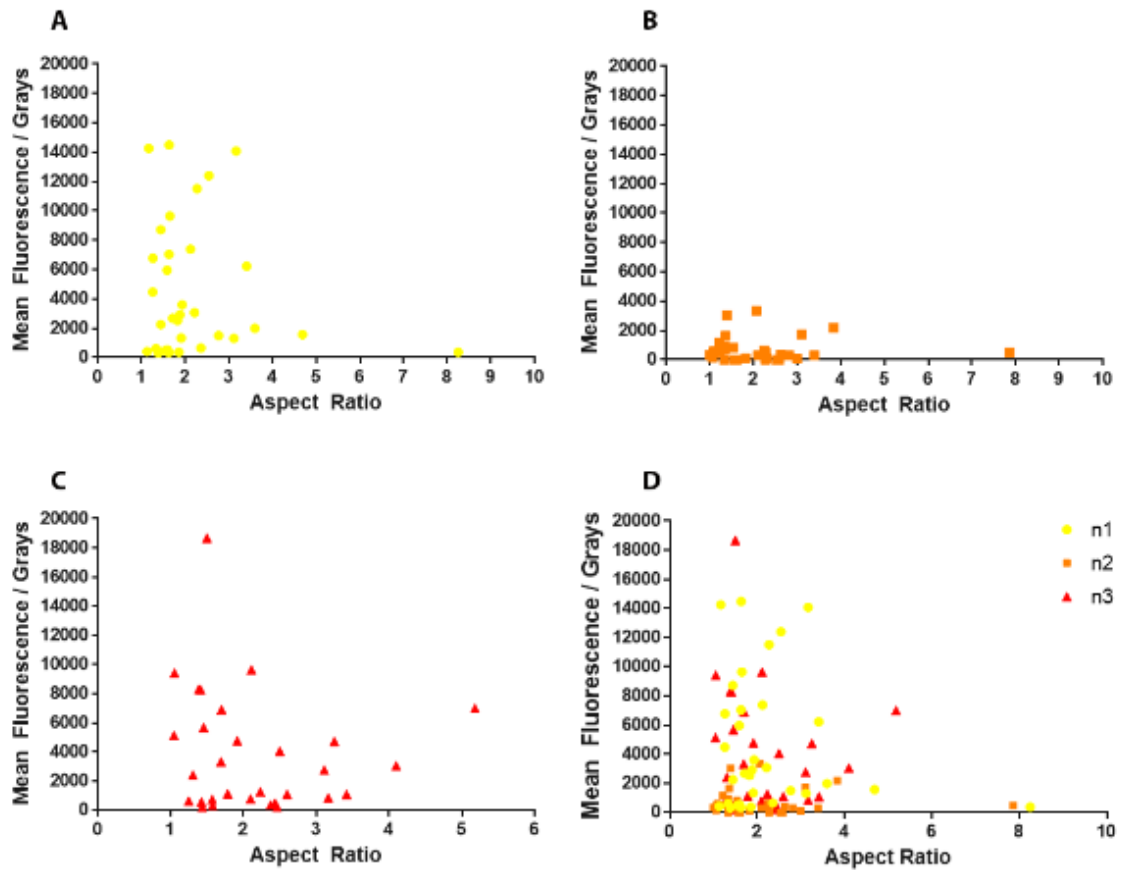


Figure 6.11, Is vimentin expression related to cell morphology? The aspect ratio and vimentin expression level for at least thirty HT1080 cells cultured on dCAM for 7 days was plotted for three independent experiments. **A** n1; **B** n2; **C** n3, **D** n1-3. Each cell is represented by a dot on the scatter plot. There was no correlation found between aspect ratio and mean fluorescence for the populations. Pearson's test for correlation was conducted using Graphpad Prism 6.

6.3.5. Keratin expression in cells seeded on dCAM

As intermediate filament expression is important in many cellular functions relating to cell-cell adhesion and cell migration, the differential expression of keratin was also examined. Keratin expression was compared for cells seeded onto 2D plastic with the 3D, dCAM environment, using one day and seven day time points, Figure 6.12. Images suggested variable expression on dCAM, for example, Figure 6.10 C, and mean and standard deviation statistics suggested that there might be a difference between keratin expression at the one Day time point when compared to three out of four of the seven day experiments (mean and SD values in Grays, 2D: mean, 1896, SD, 1050; 1 Day: mean, 5019, SD, 3506; 7 day n1: mean, 1789, SD, 1166; 7 Day n2: mean, 2971, SD, 3018; 7 Day n3: mean, 925, SD, 732; 7 Day n3: mean, 5489, SD, 4346). Interestingly, two of the day seven experiments showed populations of cells which were generally similarly low in keratin expression (n1, n3) whereas the other two showed a much greater range of keratin expression in cells (n2, n4). Further replicates and time point samples would be needed to establish whether there is indeed a significant difference in expression over time.

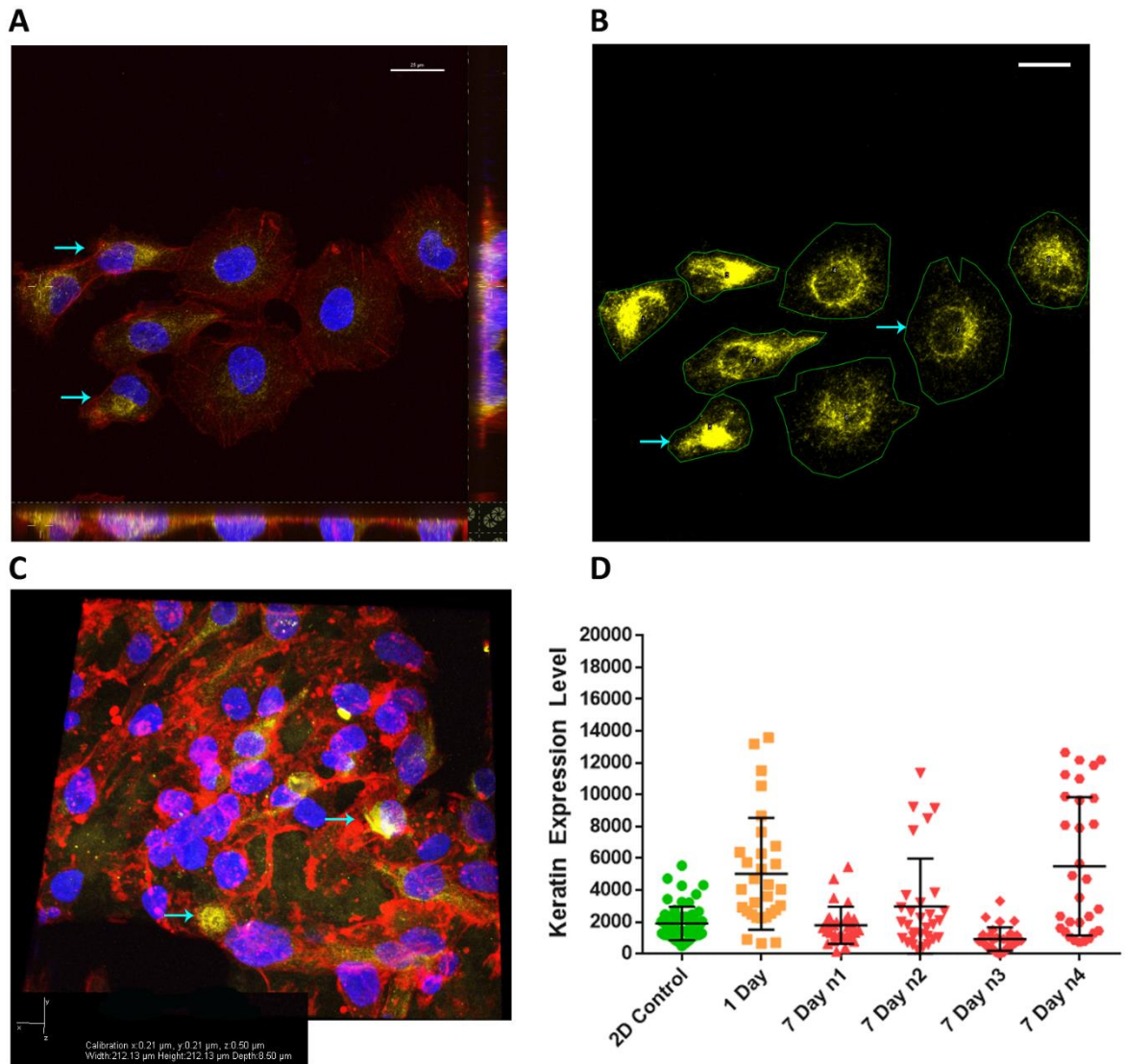


Figure 6.12, Keratin expression in HT1080 cells seeded on dCAM at 1 and 7 days. Cells were seeded and allowed to proliferate on dCAM for either 1 day, or 7 days (n1-4). Cells and matrix were harvested, stained with DAPI (nuclei-blue), phalloidin (actin-red) and keratin (yellow) and confocal images taken using a Nikon A1 plus microscope. ImageJ was used to summate the z-stacks and quantify fluorescence based on pixel intensity levels (grays). **A** Cells seeded in 2D as a control – keratin expression is indicated in cells by blue arrows. **B** An example of a summated z-stack image for cells on dCAM. Blue arrows indicate the region of interest drawn around cells which was then used for quantification of fluorescence for keratin expression levels. **C** 3D rendered image showing keratin expression in some cells (blue arrows). **D** Graphpad prism 6 was used to determine the means and standard deviation for each cell group. 30 cells per experiment and 60 cells for 2D control taken from 2 technical replicates. A difference was suggested between Day 1 samples and all except one of the Day 7 samples at varying levels of significance. There was also a significant difference between 2D and Day 1 experiments. Error bars show standard deviation. Scale bars A, B, 25 μ m.

6.4. Discussion

Cancer metastasis is a complex process involving the escape, transit and colonization of cells at new locations away from the primary site. Metastasizing cells must move through and interact with a number of different and varied contexts. Modelling appropriate conditions in which to study metastasis is therefore challenging as tissue contexts and locations will vary with each cancer and for each patient. However, studying metastasis in a biologically relevant environment which at least represents the three dimensional extracellular matrix structure surrounding cells in tissue, provides a good starting point. The assays developed within this project, three of which are used within this chapter, use ECM materials in different ways to recreate a 3D environment in which to study cell invasion, migration and colonization.

The simple 2D/3D *in vitro* assay was used initially to explore the effects of FAK and SRC inhibitors on three different cell lines: MCF7 and MDA-MB-231 breast cancer cell lines (both samples originating from metastatic sites) and HT1080 fibrosarcoma cells (originating from a primary site). Both FAK and SRC kinase 1 inhibitors from the same source had been titrated and used for cell migration and invasion as part of experiments conducted within the Dash laboratory and so were used here at the concentrations previously determined (Patel 2012). Ideally a fresh titration would have been conducted as part of this work for each cell line, conducted for cells seeded onto and adhering to a thin layer of collagen/fibronectin where focal adhesion turnover would be evident and FAK and SRC would be actively expressed in migrating cells. The effectiveness of the FAK and SRC inhibitors could then have been assessed using western blotting with antibodies used to determine levels of phosphorylation of FAK and SRC in the absence and presence of the inhibitors.

In this work, using the previously determined concentrations of each inhibitor, the aim was to investigate differences in colonization in the absence and presence of FAK or SRC inhibitors, as a means of demonstrating the use of this matrix model in this scenario, by seeding cells on and around collagen and monitoring the progression of colonization. However, whilst time-lapse microscopy provided data for the analysis and comparison of cell migration, it was clear that to monitor colonization required imaging over extensive time periods. Identifying and tracking cells in time-lapse movies as they proliferated to fill the visual field, would make correct identification over these timescales challenging. To enable better quantification of cell behaviour, the assay was inverted, providing a more controlled environment in which cell invasion could be quantified for each condition. This approach is similar in concept to that described by Artym and Matsumoto in which they sandwiched cells between collagen layers creating an enclosed environment in which to observe cell behaviour (Artym and Matsumoto 2010).

The three different cell lines used within this assay showed different invasion characteristics. MCF7 cells which do not typically migrate individually, generally remaining in groups when they proliferate, showed some indication of early invasion, with nuclei pushing upwards into the collagen matrix along with actin protrusions. Nuclear translocation was not evident for cells regardless of the presence or absence of inhibitors, with most cells remaining in contact with the base of the plate. However as these cells are generally invasive rather than migratory and may retain their cell-cell junctions as they move collectively, a longer time point or a timeline would be necessary to investigate invasive behaviour further (Cheung et al. 2013, Friedl and Gilmour 2009). The nuclei of MDA-MB-231 (MDA) cells on the other hand showed evidence of translocation into the overlying collagen layer. MDA cells do not typically form cell-cell junctions however and migrate individually when they interact with a

3D collagen context in comparison with MCF7 cells. Whilst the introduction of both the FAK and SRC inhibitors seemed to encourage a slightly greater thrust of nuclei upwards into the collagen layer for MCF7 cells, a somewhat different response was evident in the MDA cells. In the presence of the SRC inhibitor, MDA cells appeared to commence invasion and migration into the overlying collagen to a greater extent than the control cells, however the introduction of the FAK inhibitor seemed to make no difference to cell migration. As FAK and SRC are known to form a complex which drives cell motility and focal adhesion turnover, one would expect that cell migration might be reduced where both these were inhibited, assuming that these inhibitors were acting on their intended targets in these experiments. However it is possible that whilst still expressed within MDA cells, focal adhesion proteins may not complex to form focal adhesions in the same way as seen on a 2D surface where these proteins are inhibited (Fraleley et al. 2010). If the FAK and SRC inhibitors were effective and on target in this assay, then it is possible then that the FAK-SRC complex was not the driving force for cell migration and invasion in this context and that other drivers of cell migration in 3D may counter the effect of inhibition of either FAK or SRC in this environment. In contrast to the results for the breast cancer cell lines in this assay, nuclei for HT1080 cells with and without SRC inhibitors started to translocate into the overlying collagen layer. On the other hand, where the FAK inhibitor was present cells seemed to be much less mobile suggesting a possible role for FAK in the interaction of HT1080 cells with collagen (Menke et al. 2001, Zhao et al. 2016).

Whilst using the FAK and SRC inhibitors did allow the approach to compound testing using this model to be demonstrated, without a fresh titration and evidence to show that each inhibitor was successfully acting on its target protein, any effects seen cannot be attributed to the inhibition of FAK and SRC in these scenarios but only to their presence.

This model provided a useful means of comparing cell migration and invasion into collagen and it could also be used to quantify cell morphology by measuring the length and width of cells and calculating the aspect ratio. To avoid introducing the confounding factor of cell proliferation, the assay could be limited to a maximum of 24 hours. Cells could also have been seeded onto a thin coating of collagen so that they had adapted to the collagen prior to layering the thick collagen over the top (Sanz-Moreno et al. 2011).

Vimentin, a marker for EMT and a protein frequently upregulated in invasive and metastatic cells, was used as a reporter for metastatic cell behaviour in the compressed collagen and dCAM 3D matrix assays developed within this project. Vimentin expression for MDA cells was similar for control and samples where the SRC inhibitor was present but increased when the FAK inhibitor was introduced. Many of the cells quantified for the MDA control samples had adopted a more rounded morphology and although vimentin still appeared to be filamentous, the filament network seemed to be more compact and focussed around the nucleus. Cells within the samples where the FAK and SRC inhibitors were present had a more mixed morphology and this variation could have affected the fluorescence measurements made. Further work to investigate vimentin expression in these conditions with respect to aspect ratio would help to clarify this relationship. The rounded morphology and close association of cells in a cobbled arrangement suggests that MDA cells could have been settling and beginning to differentiate, undergoing Mesenchymal-epithelial transition (MET) in response to their 3D environment (Kalluri and Weinberg 2009, Radisky 2005). The rounded cell morphology (Figure 6.4) could indicate an intermediate stage in the MET process for these cells, in which the extended filamentous vimentin network characteristic in an elongated migrating cell is broken down into shorter fragments and particulate vimentin (Lowery et al. 2015). When HT1080 cells were allowed to colonize compressed collagen

they adopted the characteristic elongated, mesenchymal morphology typical of fibroblasts. In the presence of the SRC inhibitor, vimentin expression was elevated in the second experiment and there was greater variation of expression in both control and SRC inhibitor experiments for this pair in comparison to the first experiment pair. Whilst further replicates would help to establish the pattern of vimentin expression in this context, it is clear that there was differential vimentin expression even within each context showing variation in intermediate filament dynamics in HT1080 cells as cells responded to their 3D context.

Vimentin expression in HT1080 cells for cells in 2D was much lower compared to cells in the 3D compressed collagen. Cells seeded in 2D were harvested after 1 day and the HT1080 cells were still proliferating, were more rounded than on CC and had in general not developed the elongated and extensive filamentous network evident in these cells on the CC. It has been demonstrated that the form in which vimentin is expressed: particulate, short filaments, long filaments, indicates cell migration behaviour and polarity, particulate vimentin occurring at the leading edge of a migrating cell, smaller filaments close to the nucleus and the elongated fibrous network extending towards the tail of the elongated cell (Lowery et al. 2015). It has recently been discovered that the solubility of vimentin is affected by substrate stiffness and so these two pieces of evidence together suggest that variation in vimentin expression seen here is likely to be directly affected by the interaction of the HT1080 cells with their 3D context. As vimentin filaments directly associate with focal adhesions and focal adhesions vary in response to substrate stiffness, it is likely that both FAK and SRC expression would affect the vimentin expression response in different durotactic conditions (Doyle et al. 2015, Fraley et al. 2010, Leube et al. 2015, Murray et al. 2014, Plotnikov et al. 2012).

On dCAM HT1080 cells showed a range of morphologies and vimentin expression levels.

In the presence of the SRC inhibitor on dCAM, HT1080 cells again displayed differential vimentin expression, with two of the three samples showing a greater range and in general higher vimentin expression level than the control sample. An initial analysis of cell morphology compared with vimentin expression for HT1080 cells suggested that there was no correlation between vimentin expression and aspect ratio, however, there was a great deal of variation for both variables and so a much larger sample size would be needed to clarify this further. Whilst decellularized material used was processed in a similar way it is possible that some variation existed in the % of components present within the matrix both between and with particular samples. Staining for structural components or proteomic analysis would help to quantify this variation and clarify this potential variation further. As variation in component content is inherent within both healthy and diseased ECM (Nelson and Bissell 2006), the dCAM is likely to be more biologically relevant as a context in this respect. However, understanding and controlling for this variation is an important consideration when using the 3D matrix in a culture system.

It is clear from these results however that cells responded in different ways to their 3D matrix context both within and between experimental samples. With a heterogeneous mix of cells seeded at any one time derived from cancer cell lines harbouring a multitude of mutations, cell response to context is likely to vary, just as it would for cells escaping a tumour.

Differences evident from the comparison of HT1080 cell behaviour in the three contexts: 2D, CC and dCAM – in the presence and absence of the SRC inhibitor, provided a clear example of the importance of using different contexts to explore cell behaviour and metastatic

mechanisms in context. Determining a timeline for behaviour for vimentin expression gave an early indication that cells may respond differently to their environment over time and that the CC and dCAM provided a new opportunity for longer studies into expression and inhibition.

The timeline for the expression of the intermediate filament keratin showed some similarities to the pattern seen for vimentin, with an initially elevated expression shown 1 day after seeding followed by downregulation of keratin in some samples. Keratin expression in epithelial cells is generally diffuse and surrounds the nucleus, except where it is involved in desmosomes at cell-cell junctions (Lowery et al. 2015). In fibroblasts however keratin has been shown to exhibit a pattern of expression similar to that of vimentin with a fibrous filamental structure extending behind the nucleus towards the back of the moving cell and particulate keratin at the leading edge (Lowery et al. 2015). Keratin and vimentin have both been identified together within focal adhesions at the leading edge of keratocytes (Velez-delValle et al. 2016) and variable expression of keratin and vimentin within circulating tumour cells has been identified as a reporter of EMT status which may be useful for prognostic testing (Polioudaki et al. 2015).

The results from each of the three assays tested here demonstrate that cell behaviour not only varies between 2D and 3D contexts but that different 3D contexts can trigger the same cell lines to behave differently under similar conditions. The collagen based inverted invasion assay and compressed collagen assay are both similarly homogeneous in content, however the elasticity/rigidity of the CC is known to be closer to that of ECM than that of the soft collagen used in the inverted invasion assay. Both of these matrices however lack the complexity of ECM and in their simplicity are missing many of the binding sites involved in

focal adhesion and integrin binding. dCAM on the other hand is more complex in both its structure and content, with many of the structural components still available for binding (the exact content and percentage remaining needing further quantification via proteomic analysis). Whilst the results shown here for CC and dCAM comprise just a few experiments to demonstrate proof of principle, there is clearly great opportunity to explore protein expression over time within these two assays, allowing as they do for cell culture and colonization over protracted periods on the bioengineered 3D matrices.

7. Discussion

7.1. Background

The mechanisms and progression of cancer metastasis are multi-factorial and complex, taking place within a host over months and years. Given its spontaneity and the temporal nature of the process, metastasis is difficult to investigate, observe and model, occurring as it does within host tissues long before it is usually detected.

7.2. Comparable and compatible models of metastasis

Models of metastasis need to be representative of both the host environment and of the cellular changes which initiate and drive the metastatic process.

This project has sought to develop an approach to modelling metastatic mechanisms in three dimensions *in vitro* using the basic components of the extracellular matrix to create a biologically relevant context as a research tool. In particular the main focus has been on modelling of the primary tumour microenvironment and of the metastatic niche. A unifying pipeline of the models discussed and presented in this thesis is given in Figure 7.1, which aims to show the main structural features of each model along with its suitability for culture and experimentation in order of increasing complexity. A summary of the properties and considerations relating to each level in the diagram is discussed below.

Starting with simple *in vitro* experiments based on ECM extracts, the extent to which metastatic behaviours seen *in vivo* could be represented was explored within these models. In recent research, simple gel like substrates have been used to either encapsulate cancer cells or as a substrate for invasion (Kramer et al. 2013, Sung et al. 2009, Wolf et al. 2009). Whilst the components of these gels have been broadly relevant; collagen, fibronectin and

laminin all being important components of the ECM; the construction of the 3D context has resulted in a soft, unstructured environment. The initial model explored was based on the simple collagen gel invasion assays used by many researchers to explore migration (Kramer et al. 2013, Wolf et al. 2009). By setting ECM components such as collagen or collagen with fibronectin in such a way that cells could be observed from multiple perspectives, invasion and migration could be explored and quantified at several different levels within the same assay: 2D, 3D, 2D to 3D, 3D to 2D and at border zones between the two environments.

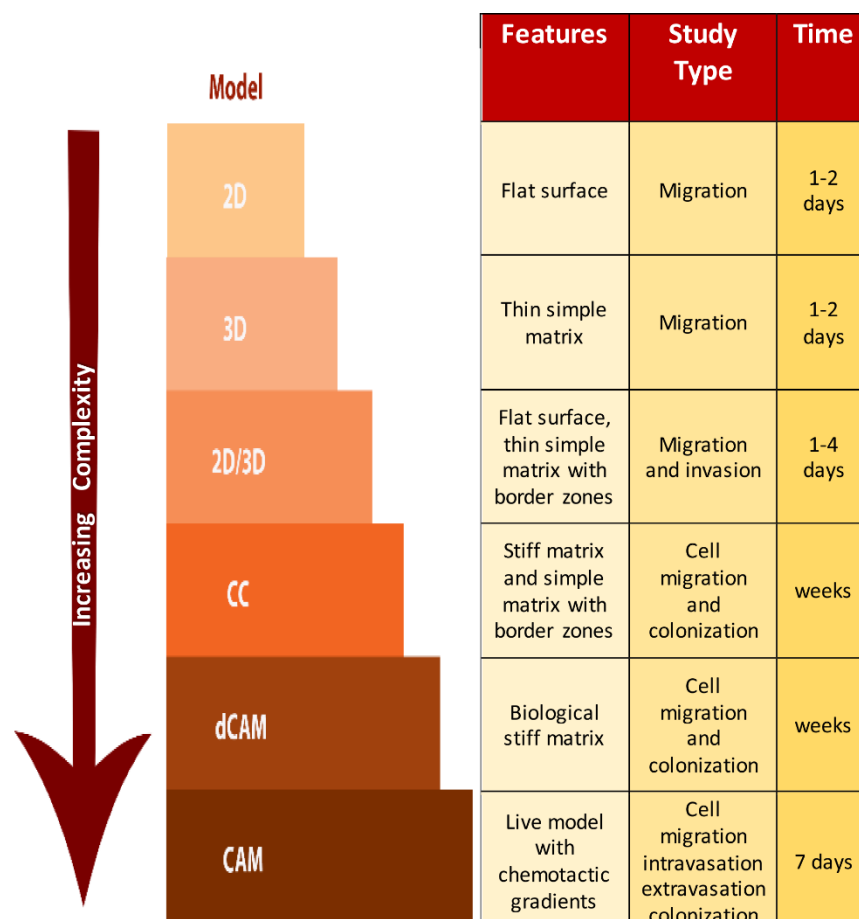


Figure 7.1, A pipeline approach to the experimental modelling of metastasis. Models are presented in increasing complexity: 2D, two dimensional cell migration assay; 3D, three dimensional cell migration assay; 2D/3D assay; CC, compressed collagen assay; dCAM, decellularized chorioallantoic membrane assay; CAM, chorioallantoic membrane assay. The structural features are listed along with the type of study that the model is suitable for and the time frame for its use. The models can either be selected individually or used to compare and contrast cell behaviours accordingly.

Border zones are of great interest when exploring metastatic behaviour as cells invading and migrating out from a primary tumour must emerge and cross through borders into areas of different context and composition. *In vivo*, ECM remodelling in the tumour microenvironment has resulted in a stiffened matrix and the formation of collagen bundles which cells have been seen to use as conduits for escape (Wang et al. 2002). Epithelial-mesenchymal transition results in the upregulation of integrin binding and other adhesion proteins with which cells can attach at collagen binding sites. Bundles of collagen fibres thus provide tracks which cells can attach to and move along as they migrate away from a tumour (Friedl and Wolf 2003).

The compressed collagen assay adapted in this project for the exploration of metastasis, provided a stiffer more complex *in vitro* model as well as a context in which to explore cell behaviours at border zones. In this assay, cells could be observed as they transitioned between regions of different stiffness and context. A variety of cell morphologies was observed ranging from elongated mesenchymal cells to rounded amoeboid morphologies, spanning the range described by Friedl and Wolf in their multiscale tuning model of cell migration (Friedl and Wolf 2009a). Whilst homogeneous in components, the compressed collagen provided a more compact and structured context with a more biologically relevant elasticity and deformability to that of soft uncompressed collagen gels (Artym et al. 2015, Jones et al. 2012). Both the 2D/3D and compressed collagen assay provide a simple highly replicable environment which can be manipulated easily for experimental purposes. However they both lack the deposited structural component of a 3D matrix constructed by cells themselves.

The chick CAM assay, well characterized and explored by many researchers, was explored as a potential *in vivo* assay in which to observe and explore the interaction of cells with ECM as they escaped their encapsulated collagen patch and migrated away, over and into the CAM tissue (Kain et al. 2014, Ribatti 2014). As cell division and colonization at areas within the CAM was observed, mechanisms of colonization relating to a metastatic niche could also be investigated. Whilst this assay had great potential as a tool for investigating the mechanisms of metastasis, there were a number of draw backs. The short development cycle of the chick meant that once cells had seeded there was a period of only 6 days in which to allow cell dissemination and colonization before harvesting. Whilst samples could be harvested and probed, tissue autofluorescence and a lack of human specific antibodies limited the amount of information that could be gleaned directly from this contextual environment. However, taking a tissue engineering approach to extract the cells from the CAM ECM and provide a cell free structure for colonization and study, allowed the study of metastasis in a relevant structural context to be explored for longer periods with better options for visualization and staining.

The use of decellularized tissue for reconstructive surgery and organ replacement has been developed and expanded over recent years due to its natural and biologically relevant structure and reduced immunogenicity (Cheng et al. 2014, Macchiarini et al. 2014, Theodoridis et al. 2015). As a biologically relevant structure to support 3D cell culture it is in many ways ideal, providing it can be decellularized without undue damage and loss of the important matrix components and properties (Balestrini et al. 2015, Crapo et al. 2011). A number of different tissues have been decellularized and used in the medical arena and some researchers have sought to exploit its structure as a scaffold for the investigation of cellular mechanisms and disease conditions (Gonzalez-Andrades et al. 2011, Guyette et al.

2014, Hoshiba et al. 2016, Xiong et al. 2015). Whilst whole organ decellularization allows tissue compartments within to support each other and remain intact, small tissue sections are more vulnerable to abrasive damage as they are processed (Crapo et al. 2011, Guyette et al. 2014). Decellularization of the CAM ECM required a delicate approach but yielded a useful and interesting scaffold for 3D cell culture. The morphological response of cells in this environment was mixed, with both elongated and rounded amoeboid cells observed and from a temporal point of view cell culture of more than 7 days could easily be supported. The material was easy to set up and manipulate and could be used in a similar way to either the compressed collagen or an artificial product such as Alvetex. However, as a naturally derived and highly structured product, the decellularized CAM provides a superior context to the more homogenous compressed collagen or the artificial membrane. Whilst cell colonization seemed to take place primarily at the dCAM surface, full colonization was not observed for the duration of the experiments conducted. Further experiments to establish a timeline for colonization and invasion would help to determine cell colonization behaviours in more detail. Probing for invasive mechanisms and matrix degradation during colonization could help determine how and to what extent migration and invasion is employed by cells as they proliferate and take up residence within the decellularized tissue.

Whilst the elasticity and deformability of the dCAM was not specifically measured as part of this project, from other relevant research it is clear that both the stiffness and elasticity of the matrix is somewhat reduced (Badylak and Gilbert 2008, Crapo et al. 2011). Steric hindrance may also be an issue with nuclear translocation having been identified as a limitation for cells migrating in a constricted environment such as a dense fibrillar collagen network (Lange and Fabry 2013, Wolf et al. 2013). Taking the tissue engineering approach to re-population could provide an excellent basis for co-culture experiments using

decellularized tissue as the platform and seeding with cells of interest to form a tissue section. This approach could potentially restore the elastic and dynamic properties of the ECM allowing it to function as a more relevant biological niche as was recently demonstrated in the repopulation of arterial conduits, heart valves and ECM for cardiovascular tissue engineering (Moroni and Mirabella 2014, Quint et al. 2011).

Whilst the use of stably expressing fluorescent cell lines was important when working *in vivo*, allowing the differentiation between CAM and human cells, this was not a necessity when working with decellularized CAM tissue. Where a co-culture model was set up using a relevant non-fluorescent cell type for repopulation of the matrix, fluorescently labelled cells of interest could be introduced, based on the approaches tested in this project and interactions with the re-populated dCAM could be monitored as a timeline experiment over periods of days and potentially weeks.

7.3. Technical issues and mitigation

A number of technical issues were experienced during the course of the project. Those issues considered to have had a broader impact are discussed here along with their mitigation.

7.3.1. Mycoplasma

A mycoplasma infection was identified in the shared tissue culture facilities in the Hopkins building at University of Reading during the final months of the project during which some experiments were being conducted.

Mycoplasma is a prokaryote and member of the *Mollicutes* which infects human cells and may be either extra-cellular or intra-cellular, the intracellular phase allowing the bacteria to evade both detection and therapies (Drexler and Uphoff 2002). Mycoplasma does not have a cell wall and penicillin is therefore ineffective (Taylor-Robinson and Bebear 1997).

Resistance to other antibiotics is high and whilst treatment may be possible, cells in culture may be adversely affected to the point that they would no longer be viable for experimental purposes (Drexler and Uphoff 2002, Stanbridge 1971). Infection can go undetected during tissue culture as the organisms are small and not readily seen when checking cell cultures under low magnification. Continuously cultured cell lines are more at risk due to protracted culture and the many opportunities for infection to be introduced during the cell passaging process (Freshney 2010, Stanbridge 1971). Usually introduced into incubators and culture hoods via contaminated sources or human exposure, once established mycoplasma infection is very difficult to remove and can easily be transferred from one culture to another (Drexler and Uphoff 2002, Freshney 2010). Where facilities and tissue culture equipment is shared this can be problematic and the infection can spread quickly.

Whilst all infected and potentially infected samples and materials were destroyed, it is possible that some of the work conducted in the preceding 2-3 months could have been contaminated. As the infection is largely silent and difficult to qualify without a specific test it is uncertain which experiments were affected and it was not possible to repeat all work for this period during the timescales available. Possible evidence of infection was spotted during time-lapse quantification of *in vitro* cell migration experiments for the period in question, however cells still proliferated and migrated in a similar way to samples from 12 months earlier. To determine the effect a mycoplasma infection may have had on cell migration, cell tracking and quantification was carried out and compared for MDA-MB-231 cells and HT1080 cells. A set of control samples (30 cells each) for each cell line was tracked from much earlier in the project and these compared with the data from three replicates of 30 cells each conducted in the questionable period before the infection was identified. No significant difference was seen when experiments were compared with controls for either cell line for either speed of migration or for distance from start after 8 hours. (Graphs are shown in Appendix F.)

7.3.2. Microscopy

When observing cell behaviours in context, the properties of the context have an impact on the data acquisition and quantification methods used. Tissue autofluorescence and light scattering were both issues encountered during bright field, phase contrast and confocal microscopy when working with samples and experiments in three dimensions.

Tissue autofluorescence arises from the intrinsic properties of tissues and their bi-products and can be a confounding factor when trying to use fluorophores as markers to identify specific structures and interactions at a cellular and molecular level (Monici 2005).

Autofluorescence can also be increased in some samples dependent on the fixation method used (Williams et al. 2008). When working with densely populated tissues such as the chick chorioallantoic membrane, components of the extracellular matrix as well as the cells contribute to the intrinsic autofluorescence of the tissue. Autofluorescence from collagen and elastin fibres results from light excitation in the 440-480nm range with emission detected in the 470-520nm range which conflicts mainly with the emission spectral profile for enhanced GFP (eGFP - main emission peak at 509nm) (Billinton and Knight 2001). eGFP (adapted from the wild type GFP for excitation at 490nm) was used within this project as a marker to identify either the specific cell type or for the expression of a protein of interest. Due to the high content of collagen in the extracellular matrix or collagen substrates used, autofluorescence of collagen could mean that differentiating cells against background fluorescence was an issue. Approaches used to mitigate this included confocal imaging in a linear rather than parallel fashion for multiple fluorophores, the use of spectral unmixing confocal microscopy and reflectance microscopy. Taking images for each fluorophore using laser channels in turn provided a means of capture of all light emitted for the excitation range for that laser channel, an image being produced for analysis for each channel in question. This method also eliminated the issue of cross talk between channels which can occur when multiple fluorophores are imaged simultaneously. Whilst autofluorescence could occur across all channels, the emission spectra for each fluorophore of interest could be extracted above the background in most cases. Spectral unmixing using Nikon A1 Plus confocal microscopes also enabled specific emission profiles to be extracted. In addition, the emission spectrum for a control tissue sample could be used to determine the peaks in autofluorescence so that they could be deducted or at least considered when analysing data. Reflectance microscopy is a way of specifically detecting and creating an image based on

reflectance or the back scatter of light from tissues and their structures and it could be used to specifically identify components such as collagen to help set cells in context (Artym and Matsumoto 2010). Two different methods of confocal imaging (4 laser channels: blue, green, red, far red) using fluorophores in combination with reflectance enabled cells to be set in context with up to two fluorophores, using the 488nm excitation laser for reflectance rather than to excite fluorophores, thus minimizing background for the 488/green channel. Sample harvesting protocols could also be further optimized to reduce autofluorescence, given that paraformaldehyde can increase autofluorescence in some tissues and cells; for example, alternatives such as a mix of ethanol and methanol could be used for fixation (Aubin 1979, Williams et al. 2008).

When taking images using bright field and phase contrast imaging using an inverted microscope, the appropriate phase ring was employed and settings for light levels, gain and exposure were adjusted to give the best image possible at the focal point selected. With the light source above the matrix and lens inverted, this meant that cells closest to the lens could be seen most clearly however, cells further away from optics and located within the 3D matrix were more difficult to see and light scatter could hinder the collection of cell images with good definition.

7.3.3. Quantification of 3D assays using 2D analytical methods

Throughout the work presented here, the quantification methods used have entailed taking a two dimensional approach to analysis.

Where cell tracking has been conducted, tracking has been measured based on movement in the x,y plane only, so no account has been taken of fluctuations in z-depth. Where cells have moved so far in the z-plane that they could no longer be differentiated from their context

then tracking ceased or they were excluded. This means if anything that cell migration distances have been under reported, however this was consistent throughout the analyses. For confocal microscopy where a z-stack image set was collected and a 3D rendered image obtained, measurement was taken from base to maximum height. Measurements of travel for cells towards the front of a 3D rendered image will therefore be more accurate than for cells towards the rear whose migration distances will be under reported. When quantifying images, mainly cells towards the front of the image were measured for this reason.

Issues relating to the production and quantification of images for cell migration have been highlighted in a recently published review which identifies key considerations for experimental design when seeking the correct means of obtaining images and quantifying events in a 3D environment (Driscoll and Danuser 2015). Certainly as technology to obtain complex 3D data improves, so too should the means to quantify the data in an appropriate manner and these inconsistencies can be removed.

7.4. Further work and potential application of methods

This project allowed the development and novel application of three *in vitro* 3D matrices which have the potential to be used for the exploration and manipulation of cell behaviours in a number of different ways. As demonstrated in Chapter 6, the 2D/3D assay can be used innovatively to investigate cell invasion, migration and proliferation. The compressed collagen assay, a more complex and stiffer substrate, could also be used with an inverted invasion assay approach. Both compressed collagen and decellularized tissue could be used to culture cells as free floating tissue organoids as described here or they could be used as well inserts in a similar way to a Boyden chamber assay. Decellularized tissue could also be anchored into a substrate such as a collagen substrate in a similar way to the approach used to anchor compressed collagen. Flexible arrangements and transfer of set-up attributes between these assays would allow the flexible study of different aspects of cell invasion, migration and colonization relevant to cancer metastasis and other diseases. Population and seeding with different cell lines, including primary cell lines or new tumour samples would enable these matrices to be investigated further as relevant 3D bio-matrices and to glean new insights into the behaviours of cells when interacting in these environments.

The proteomic content and detailed staining of decellularized tissues produced from further optimized protocols, would allow both the tissue composition to be determined and quantified as well as the damage and changes from the decellularization process to be assessed. A first attempt at solubilizing decellularized CAM using the Medberry protocol for hydrogel production (Medberry et al. 2013) yielded partial information of protein content, probably due to problems with protein precipitation encountered when trying to solubilize the dCAM. However other recently published research offers new protocols which could be

explored and optimized to take this work further (Aguado et al. 2016, de Castro Bras et al. 2013).

The assays developed and presented in this work offer the opportunity to take a flexible and integrative approach to the study of cell behaviours in 3D with specific pertinence to the metastatic process, based as they are on the ECM environment, a tissue environment relevant as both a tumour microenvironment and a metastatic niche. The collagen based matrices and the decellularized chorioallantoic chick membrane can all be replicated using simple protocols and readily available materials at relatively low cost or could be adapted to use alternatives as necessary. With the option to select and adapt each assay according to the exact requirement to be tested, a suite of assays can thus be designed to investigate a specific target of interest. For example other ECM materials can be introduced to the compressed collagen and inverted invasion assays at specific percentages to reflect those found through proteomic analysis of dCAM. By manipulating components and content of each assay in the context of metastasis, contextual drivers of cell behaviours could be explored.

Batch processing could allow the use of these assays to be scaled up and potentially automated for use as a pipeline for probing multiple targets of interest or for testing drugs on different combinations of cells in 3D. Once a protocol for production of a dCAM hydrogel was optimized this could be used as either a tissue culture coating (2D or 3D environments) or as a base for the anchorage of whole dCAM to allow further development of the use of whole dCAM sections for longer timescales for the generation of artificial tissue (Decaestecker et al. 2007, Dunne et al. 2014, Edmondson et al. 2014, Loessner et al. 2010).

References

- Aguado BA, Caffè JR, Nanavati D, Rao SS, Bushnell GG, Azarin SM, Shea LD. 2016. Extracellular matrix mediators of metastatic cell colonization characterized using scaffold mimics of the pre-metastatic niche. *Acta Biomaterialia* 33:13-24.
- Alberts B, Johnson A, Lewis J, Raff M, Roberts K, Walter P. 2002. *Molecular Biology of the Cell*. 4th edition. New York: Garland Science.
- Alexander S, Friedl P. 2012. Cancer invasion and resistance: interconnected processes of disease progression and therapy failure. *Trends in Molecular Medicine* 18:13-26.
- Allinen M, Beroukhi R, Cai L, Brennan C, Lahti-Domenici J, Huang H, Porter D, Hu M, Chin L, Richardson A. 2004. Molecular characterization of the tumor microenvironment in breast cancer. *Cancer Cell* 6:17-32.
- Arciero JC, Mi Q, Branca MF, Hackam DJ, Swigon D. 2011. Continuum Model of Collective Cell Migration in Wound Healing and Colony Expansion. *Biophysical Journal* 100:535-543.
- Armstrong PB, Quigley JP, Sidebottom E. 1982. Transepithelial Invasion and Intramesenchymal Infiltration of the Chick Embryo Chorioallantois by Tumor Cell Lines. *Cancer Research* 42:1826-1837.
- Artym VV, Matsumoto K. 2010. Imaging cells in three-dimensional collagen matrix. *Current protocols in cell biology / editorial board, Juan S. Bonifacino ... [et al.] Chapter 10:Unit 10 18 11-20*.
- Artym VV, et al. 2015. Dense fibrillar collagen is a potent inducer of invadopodia via a specific signaling network. *The Journal of Cell Biology* 208:331-350.
- Aubin JE. 1979. Autofluorescence of viable cultured mammalian cells. *The journal of histochemistry and cytochemistry : official journal of the Histochemistry Society* 27:36-43.
- Badylak SF, Freytes DO, Gilbert TW. 2009. Extracellular matrix as a biological scaffold material: Structure and function. *Acta Biomater* 5:1-13.
- Badylak SF, Gilbert TW. 2008. Immune response to biologic scaffold materials. *Semin Immunol* 20:109-116.
- Baker BM, Chen CS. 2012. Deconstructing the third dimension – how 3D culture microenvironments alter cellular cues. *Journal of Cell Science* 125:3015-3024.
- Balda MS, Matter K. 2008. Tight junctions at a glance. *Journal of Cell Science* 121:3677-3682.
- Balestrini JL, et al. 2015. Production of decellularized porcine lung scaffolds for use in tissue engineering. *Integr Biol (Camb)* 7:1598-1610.
- Barry DJ, Durkin CH, Abella JV, Way M. 2015. Open source software for quantification of cell migration, protrusions, and fluorescence intensities. *The Journal of Cell Biology* 209:163-180.
- Bergert M, Chandradossa SD, Desai RA, Paluch E. 2012. Cell mechanics control rapid transitions between blebs and lamellipodia during migration. *Proceedings of the National Academy of Sciences* 109:14434-14439.
- Berginski ME, Vitriol EA, Hahn KM, Gomez SM. 2011. High-resolution quantification of focal adhesion spatiotemporal dynamics in living cells. *PLoS One* 6:e22025.

- Berzat A, Hall A. 2010. Cellular responses to extracellular guidance cues. *The EMBO journal* 29:2734-2745.
- Billinton N, Knight AW. 2001. Seeing the wood through the trees: a review of techniques for distinguishing green fluorescent protein from endogenous autofluorescence. *Analytical biochemistry* 291:175-197.
- Bissell MJ, Radisky DC. 2001. Putting Tumours in Context. *Nature Reviews Cancer* 1:46-54.
- Bissell MJ, Radisky DC, Rizki A, Weaver VM, Petersen OW. 2002. The organizing principle: microenvironmental influences in the normal and malignant breast. *Differentiation; research in biological diversity* 70:537-546.
- Bissell MJ, Rizki A, Mian IS. 2003. Tissue architecture: the ultimate regulator of breast epithelial. *Curr Opin Cell Biol* 15:753-762.
- Borley AC, Hiscox S, Gee J, Smith C, Shaw V, Barrett-Lee P, Nicholson RI. 2008. Anti-oestrogens but not oestrogen deprivation promote cellular invasion in intercellular adhesion-deficient breast cancer cells. *Breast cancer research : BCR* 10:R103.
- Boyden S. 1962. The chemotactic effect of mixtures of antibody and antigen on polymorphonuclear leucocytes. *J Exp Med* 115:453-466.
- Boyer B, Thiery JP. 1993. Epithelium-mesenchyme interconversion as example of epithelial plasticity. *APMIS* 101:257-268.
- Bradbury P, Fabry B, O'Neill GM. 2012. Occupy tissue: The movement in cancer metastasis. *Cell Adhesion & Migration* 6:424-432.
- Bravo-Cordero JJ, Hodgson L, Condeelis J. 2012. Directed cell invasion and migration during metastasis. *Current Opinion in Cell Biology* 24:277-283.
- Bremnes RM, Dønnem T, Al-Saad S, Al-Shibli K, Andersen S, Sirera R, Camps C, Marinez I, Busund L-T. 2011. The Role of Tumor Stroma in Cancer Progression and Prognosis: Emphasis on Carcinoma-Associated Fibroblasts and Non-small Cell Lung Cancer. *Journal of Thoracic Oncology* 6:209-217.
- Brizzi MF, Tarone G, Defilippi P. 2012. Extracellular matrix, integrins, and growth factors as tailors of the stem cell niche. *Current Opinion in Cell Biology* 24:645-651.
- Bross ID, Viadana E, Pickren JW. 1975. The metastatic spread of myeloma and leukemias in men. *Virchows Arch A Pathol Anat Histol* 365:91-101.
- Brown BN, Barnes CA, Kasick RT, Michel R, Gilbert TW, Beer-Stolz D, Castner DG, Ratner BD, Badylak SF. 2010. Surface characterization of extracellular matrix scaffolds. *Biomaterials* 31:428-437.
- Bullwinkel J, Baron-Luhr B, Ludemann A, Wohlenberg C, Gerdes J, Scholzen T. 2006. Ki-67 protein is associated with ribosomal RNA transcription in quiescent and proliferating cells. *J Cell Physiol* 206:624-635.
- Cairns RA, Harris I, McCracken S, Mak TW. 2011. Cancer cell metabolism. *Cold Spring Harb Symp Quant Biol* 76:299-311.
- Calvo F, Sanz-Moreno V, Agudo-Ibanez L, Wallberg F, Sahai E, Marshall CJ, Crespo P. 2011. RasGRF suppresses Cdc42-mediated tumour cell movement, cytoskeletal dynamics and transformation. *Nat Cell Biol* 13:819-826.

- Candido J, Hagemann T. 2012. Cancer-Related Inflammation. *Journal of Clinical Immunology* 33:79-84.
- Canel M, Serrels A, Frame MC, Brunton VG. 2013. E-cadherin-integrin crosstalk in cancer invasion and metastasis. *Journal of Cell Science* 126:393-401.
- Carrel A, Ebeling A. 1923. SURVIVAL AND GROWTH OF FIBROBLASTS IN VITRO. *J Exp Med* 38:487-497.
- Casey T, et al. 2009. Molecular signatures suggest a major role for stromal cells in development of invasive breast cancer. *Breast Cancer Res Treat* 114:47-62.
- Chang Q, et al. 2013. The IL-6/JAK/Stat3 Feed-Forward Loop Drives Tumorigenesis and Metastasis. *Neoplasia* 15:848-IN845.
- Charras GT, Coughlin M, Mitchison TJ, Mahadevan L. 2008. Life and Times of a Cellular Bleb. *Biophysical Journal* 94:1836-1853.
- Chen B, Jones RR, Mi S, Foster J, Alcock SG, Hamley IW, Connon CJ. 2012. The mechanical properties of amniotic membrane influence its effect as a biomaterial for ocular surface repair. *Soft Matter* 8:8379.
- Chen HC. 2005. Boyden chamber assay. *Methods Mol Biol* 294:15-22.
- Cheng CW, Solorio LD, Alsberg E. 2014. Decellularized tissue and cell-derived extracellular matrices as scaffolds for orthopaedic tissue engineering. *Biotechnology advances* 32:462-484.
- Cheung KJ, Gabrielson E, Werb Z, Ewald AJ. 2013. Collective invasion in breast cancer requires a conserved basal epithelial program. *Cell* 155:1639-1651.
- Collins VP, Loeffler RK, Tivey H. 1956. Observations on growth rates of human tumors. *Am J Roentgenol Radium Ther Nucl Med* 76:988-1000.
- Condeelis J, Pollard JW. 2006. Macrophages: Obligate Partners for Tumor Cell Migration, Invasion, and Metastasis. *Cell* 124:263-266.
- Condeelis J, Wyckoff JB, Bailly M, Pestell R, Lawrence D, Backer J, Segall JE. 2001. Lamellipodia in invasion. *Seminars in Cancer Biology* 11:119-128.
- Cox TR, Ertler JT. 2011. Remodeling and homeostasis of the extracellular matrix: implications for fibrotic diseases and cancer. *Disease models & mechanisms* 4:165-178.
- Cox TR, Gartland A, Ertler JT. 2016. Lysyl Oxidase, a Targetable Secreted Molecule Involved in Cancer Metastasis. *Cancer Research* 76:188-192.
- Crapo PM, Gilbert TW, Badylak SF. 2011. An overview of tissue and whole organ decellularization processes. *Biomaterials* 32:3233-3243.
- Cukierman E, Pankov R, Stevens DR, Yamada KM. 2001. Taking Cell-Matrix Adhesions to the Third Dimension. *Science* 294:1708-1712.
- Dadi S, et al. Cancer Immunosurveillance by Tissue-Resident Innate Lymphoid Cells and Innate-like T Cells. *Cell* 164:365-377.
- Davies EJ, et al. 2015. Capturing complex tumour biology in vitro: histological and molecular characterisation of precision cut slices. *Scientific reports* 5:17187.

- de Castro Bras LE, Ramirez TA, DeLeon-Pennell KY, Chiao YA, Ma Y, Dai Q, Halade GV, Hakala K, Weintraub ST, Lindsey ML. 2013. Texas 3-step decellularization protocol: looking at the cardiac extracellular matrix. *J Proteomics* 86:43-52.
- Decaestecker C, Debeir O, Van Ham P, Kiss R. 2007. Can anti-migratory drugs be screened in vitro? A review of 2D and 3D assays for the quantitative analysis of cell migration. *Medicinal research reviews* 27:149-176.
- Deryugina EI, Quigley JP. 2008a. Chapter 2 Chick Embryo Chorioallantoic Membrane Models to Quantify Angiogenesis Induced by Inflammatory and Tumor Cells or Purified Effector Molecules. 444:21-41.
- . 2008b. Chick embryo chorioallantoic membrane model systems to study and visualize human tumor cell metastasis. *Histochemistry and cell biology* 130:1119-1130.
- Discher DE, Jammey P, Wang Y. 2005. Tissue Cells Feel and Respond to the Stiffness of their Substrate *Science* 310:1139-1143.
- Doyle AD, Carvajal N, Jin A, Matsumoto K, Yamada KM. 2015. Local 3D matrix microenvironment regulates cell migration through spatiotemporal dynamics of contractility-dependent adhesions. *Nature communications* 6:8720.
- Doyle AD, Kutys ML, Conti MA, Matsumoto K, Adelstein RS, Yamada KM. 2012. Micro-environmental control of cell migration--myosin IIA is required for efficient migration in fibrillar environments through control of cell adhesion dynamics. *Journal of Cell Science* 125:2244-2256.
- Doyle AD, Petrie RJ, Kutys ML, Yamada KM. 2013. Dimensions in cell migration. *Current Opinion in Cell Biology* 25:642-649.
- Doyle AD, Wang FW, Matsumoto K, Yamada KM. 2009. One-dimensional topography underlies three-dimensional fibrillar cell migration. *The Journal of Cell Biology* 184:481-490.
- Drexler HG, Uphoff CC. 2002. Mycoplasma contamination of cell cultures: Incidence, sources, effects, detection, elimination, prevention. *Cytotechnology* 39:75-90.
- Driscoll MK, Danuser G. 2015. Quantifying Modes of 3D Cell Migration. *Trends in Cell Biology* 25:749-759.
- Dunne LW, Huang Z, Meng W, Fan X, Zhang N, Zhang Q, An Z. 2014a. Human decellularized adipose tissue scaffold as a model for breast cancer cell growth and drug treatments. *Biomaterials* 35:4940-4949.
- Dvorak HF. 1986. Tumors: wounds that do not heal. Similarities between tumor stroma generation and wound healing. *N Engl J Med* 315:1650-1659.
- Edmondson R, Broglie JJ, Adcock AF, Yang L. 2014. Three-dimensional cell culture systems and their applications in drug discovery and cell-based biosensors. *Assay and drug development technologies* 12:207-218.
- Engler AJ, Sen S, Sweeney HL, Discher DE. 2006. Matrix elasticity directs stem cell lineage specification. *Cell* 126:677-689.
- Erler JT, Bennewith KL, Nicolau M, Dornhofer N, Kong C, Le QT, Chi JT, Jeffrey SS, Giaccia AJ. 2006. Lysyl oxidase is essential for hypoxia-induced metastasis. *Nature* 440:1222-1226.

- Evanko SP, Tammi MI, Tammi RM, Wight TN. 2007. Hyaluronan-Dependent Pericellular Matrix *Advanced Drug Delivery Reviews* 10:1351-1365.
- Ewing J. 1928. *Neoplastic Diseases: A Treatise on Tumours*. By James Ewing, A.M., M.D., Sc.D., Professor of Pathology at Cornell University Medical College, N.Y.; Pathologist to the Memorial Hospital. Third edition. Royal 8vo. Pp. 1127, with 546 illustrations. 1928. Philadelphia and London: W. B. Saunders Co. Ltd. 63s. net. *British Journal of Surgery* 16:174-175.
- Fackler OT, Grosse R. 2008. Cell motility through plasma membrane blebbing. *The Journal of Cell Biology* 181:879-884.
- Fidler IJ, Kripke ML. 1977. Metastasis results from preexisting variant cells within a malignant tumor. *Science* 197:893-895.
- Fischbach C, Chen R, Matsumoto T, Schmelzle T, Brugge JS, Polverini PJ, Mooney DJ. 2007. Engineering tumors with 3D scaffolds. *Nature Methods* 4:855-860.
- Fishman JM, et al. 2013. Immunomodulatory effect of a decellularized skeletal muscle scaffold in a discordant xenotransplantation model. *Proc Natl Acad Sci U S A* 110:14360-14365.
- Foster JW, Gouveia RM, Connon CJ. 2015. Low-glucose enhances keratocyte-characteristic phenotype from corneal stromal cells in serum-free conditions. *Scientific reports* 5:10839.
- Foulds L. 1958. The natural history of cancer. *Journal of Chronic Diseases* 8:2-37.
- Fraley SI, Feng Y, Krishnamurthy R, Kim DH, Celedon A, Longmore GD, Wirtz D. 2010. A distinctive role for focal adhesion proteins in three-dimensional cell motility. *Nature Cell Biology* 12:598-604.
- Frantz C, Stewart KM, Weaver VM. 2010. The extracellular matrix at a glance. *Journal of Cell Science* 123:4195-4200.
- Freshney RI. 2010. *Culture of Animal Cells*. Wiley-Blackwell.
- Friedl P, Alexander S. 2011. Cancer Invasion and the Microenvironment: Plasticity and Reciprocity. *Cell* 147:992-1009.
- Friedl P, Gilmour D. 2009. Collective cell migration in morphogenesis, regeneration and cancer. *Nature Reviews. Molecular Cell Biology* 10:445-457.
- Friedl P, Sahai E, Weiss S, Yamada K. 2012. New dimensions in cell migration. *Nature Reviews Molecular Cell Biology* 13:743-747.
- Friedl P, Wolf K. 2003. Tumour-cell invasion and migration: diversity and escape mechanisms. *Nature Reviews Cancer* 3:362-374.
- . 2008. Tube travel: the role of proteases in individual and collective cancer cell invasion. *Cancer Res* 68:7247-7249.
- . 2009a. Plasticity of cell migration: a multiscale tuning model. *The Journal of Cell Biology* 188:11-19.
- . 2009b. Proteolytic interstitial cell migration: a five-step process. *Cancer Metastasis Reviews* 28:129-135.

- Friedl P, Wolf K, von Andrian UH, Harms G. 2007. Biological second and third harmonic generation microscopy. *Current protocols in cell biology* / editorial board, Juan S. Bonifacino ... [et al.] Chapter 4:Unit 4.15.
- Fuchs E, Weber K. 1994. Intermediate filaments: structure, dynamics, function, and disease. *Annu Rev Biochem* 63:345-382.
- Gabrielli MG, Accili D. 2010. The Chick Chorioallantoic Membrane: A Model of Molecular, Structural, and Functional Adaptation to Transepithelial Ion Transport and Barrier Function during Embryonic Development. *Journal of Biomedicine and Biotechnology* 2010 (art. 940741):12.
- Gaggioli C, Hooper S, Hidalgo-Carcedo C, Grosse R, Marshall JF, Harrington K, Sahai E. 2007. Fibroblast-led collective invasion of carcinoma cells with differing roles for RhoGTPases in leading and following cells. *Nature Cell Biology* 9:1392-1400.
- Geiger TR, Peeper DS. 2009. Metastasis mechanisms. *Biochimica et biophysica acta* 1796:293-308.
- Gest C, et al. 2013. Rac3 induces a molecular pathway triggering breast cancer cell aggressiveness: differences in MDA-MB-231 and MCF-7 breast cancer cell lines. *BMC Cancer* 13:1-14.
- Ghosh K, Thodeti CK, Dudley AC, Mammoto A, Klagsbrun M, Ingber DE. 2008. Tumor-derived endothelial cells exhibit aberrant Rho-mediated mechanosensing and abnormal angiogenesis in vitro. *Proceedings of the National Academy of Sciences* 105:11305-11310.
- Gilbert SF. 2010. Lateral Plate Mesoderm and Endoderm. 9th Edition, *Developmental Biology*, Sinauer:480-482.
- Gilpin SE, Ren X, Okamoto T, Guyette JP, Mou H, Rajagopal J, Mathisen DJ, Vacanti JP, Ott HC. 2014. Enhanced lung epithelial specification of human induced pluripotent stem cells on decellularized lung matrix. *Ann Thorac Surg* 98:1721-1729; discussion 1729.
- Gligorijevic B, Condeelis J. 2009. Stretching the timescale of intravital imaging in tumors. *Cell Adh Migr* 3:313-315.
- Gligorijevic B, Wyckoff J, Yamaguchi H, Wang Y, Roussos ET, Condeelis J. 2012. N-WASP-mediated invadopodium formation is involved in intravasation and lung metastasis of mammary tumors. *Journal of Cell Science* 125:724-734.
- Gonzalez-Andrades M, de la Cruz Cardona J, Ionescu AM, Campos A, Del Mar Perez M, Alaminos M. 2011. Generation of bioengineered corneas with decellularized xenografts and human keratocytes. *Invest Ophthalmol Vis Sci* 52:215-222.
- Guyette JP, et al. 2016. Bioengineering Human Myocardium on Native Extracellular Matrix. *Circulation Research* 118:56-72.
- Guyette JP, Gilpin SE, Charest JM, Tapias LF, Ren X, Ott HC. 2014. Perfusion decellularization of whole organs. *Nat. Protocols* 9:1451-1468.
- Haeger A, Wolf K, Zegers MM, Friedl P. 2015. Collective cell migration: guidance principles and hierarchies. *Trends in Cell Biology* 25:556-566.
- Hanahan D, Coussens LM. 2012. Accessories to the Crime: Functions of Cells Recruited to the Tumor Microenvironment. *Cancer Cell* 21:309-322.

- Hanahan D, Weinberg RA. 2011. Hallmarks of cancer: The Next Generation. *Cell* 144:646-674.
- Hegerfeldt Y, Tusch M, Brocker EB, Friedl P. 2002. Collective cell movement in primary melanoma explants: plasticity of cell-cell interaction, beta1-integrin function, and migration strategies. *Cancer Research* 62:2125-2130.
- Hernandez-Caballero ME. 2013. Molecular Mechanisms of Metastasis: Epithelial-Mesenchymal Transition, Anoikis and Loss of Adhesion.
- Hickman JA, Graeser R, de Hoogt R, Vidic S, Brito C, Gutekunst M, van der Kuip H. 2014. Three-dimensional models of cancer for pharmacology and cancer cell biology: capturing tumor complexity in vitro/ex vivo. *Biotechnology journal* 9:1115-1128.
- Hidalgo-Carcedo C, Hooper S, Chaudhry SI, Williamson P, Harrington K, Leitinger B, Sahai E. 2011. Collective cell migration requires suppression of actomyosin at cell-cell contacts mediated by DDR1 and the cell polarity regulators Par3 and Par6. *Nature Cell Biology* 13:49-58.
- Holliday DL, Speirs V. 2011. Choosing the right cell line for breast cancer research. *Breast Cancer Research* 13:215-221.
- Hoshiba T, Chen G, Endo C, Maruyama H, Wakui M, Nemoto E, Kawazoe N, Tanaka M. 2016. Decellularized Extracellular Matrix as an In Vitro Model to Study the Comprehensive Roles of the ECM in Stem Cell Differentiation. *Stem Cells Int* 2016:6397820.
- Hughes CS, Postovit LM, Lajoie GA. 2010. Matrigel: A complex protein mixture required for optimal growth of cell culture. *Proteomics* 10:1886-1890.
- Huveneers S, Danen EHJ. 2009. Adhesion signaling – crosstalk between integrins, Src and Rho. *Journal of Cell Science* 122:1059-1069.
- Hynes RO. 2009. The Extracellular Matrix: Not Just Pretty Fibrils. *Science* 326:1216-1219.
- IARC. 2014. World Cancer Report 2014.
- Ivaska J, Pallari H-M, Nevo J, Eriksson JE. 2007. Novel functions of vimentin in cell adhesion, migration, and signaling. *Experimental Cell Research* 313:2050-2062.
- Jankovic BD, Isakovic K, Markovic BM, M RA. 1977. Immunological capacity of the chicken embryo. II. Humoral immune responses in embryos and young chickens bursectomized and sham-bursectomized at 52--64 h of incubation. *Immunology* 32:689-699.
- Jonat W, Arnold N. 2011. Is the Ki-67 labelling index ready for clinical use? *Annals of Oncology* 22:500-502.
- Jones RR, Hamley IW, Connon CJ. 2012. Ex vivo expansion of limbal stem cells is affected by substrate properties. *Stem cell research* 8:403-409.
- Jonkman J, Brown CM. 2015. Any Way You Slice It—A Comparison of Confocal Microscopy Techniques. *Journal of Biomolecular Techniques : JBT* 26:54-65.
- Joyce JA, Pollard JW. 2008. Microenvironmental regulation of metastasis. *Nature Reviews Cancer* 9:239-252.

- Kain KH, Miller JW, Jones-Paris CR, Thomason RT, Lewis JD, Bader DM, Barnett JV, Zijlstra A. 2014. The chick embryo as an expanding experimental model for cancer and cardiovascular research. *Developmental dynamics : an official publication of the American Association of Anatomists* 243:216-228.
- Kalluri R. 2003. Basement membranes: Structure, assembly and role in tumour angiogenesis. *Nature Reviews Cancer* 3:422-433.
- Kalluri R, Weinberg RA. 2009. The basics of epithelial-mesenchymal transition. *The Journal of clinical investigation* 119:1420-1428.
- Kaplan RN, et al. 2005. VEGFR1-positive haematopoietic bone marrow progenitors initiate the pre-metastatic niche. *Nature* 438:820-827.
- Karnoub AE, Dash AB, Vo AP, Sullivan A, Brooks MW, Bell GW, Richardson AL, Polyak K, Tubo R, Weinberg RA. 2007. Mesenchymal stem cells within tumour stroma promote breast cancer metastasis. *Nature* 449:557-563.
- Katz MJ, Lasek RJ. 1980. Invited review: guidance cue patterns and cell migration in multicellular organisms. *Cell Motil* 1:141-157.
- Kaufman CK, et al. 2016. A zebrafish melanoma model reveals emergence of neural crest identity during melanoma initiation. *Science* 351.
- Kedrin D, Gligorijevic B, Wyckoff J, Verkhusha VV, Condeelis J, Segall JE, van Rheenen J. 2008. Intravital imaging of metastatic behavior through a mammary imaging window. *Nature Methods* 5:1019-1021.
- Keller KE, Doctor ZM, Dwyer ZW, Lee YS. 2014. SAICAR induces protein kinase activity of PKM2 that is necessary for sustained proliferative signaling of cancer cells. *Mol Cell* 53:700-709.
- Kelley LC, Lohmer LL, Hagedorn EJ, Sherwood DR. 2014. Traversing the basement membrane in vivo: a diversity of strategies. *The Journal of Cell Biology* 204:291-302.
- Kerkhoff E, Rapp UR. 1998. Cell cycle targets of Ras/Raf signalling. *Oncogene* 17:1457-1462.
- Khanna C, Hunter K. 2005. Modeling metastasis in vivo. *Carcinogenesis* 26:513-523.
- Kidd ME, Shumaker DK, Ridge KM. 2014. The role of vimentin intermediate filaments in the progression of lung cancer. *Am J Respir Cell Mol Biol* 50:1-6.
- Kim, Wirtz D. 2013. Focal adhesion size uniquely predicts cell migration. *The FASEB Journal* 27:1351-1361.
- Kim MR, Chang HW, Nam HY, Han MW, Moon SY, Kim HJ, Lee HJ, Roh J-L, Kim SW, Kim SY. 2012. Activation of p53-p21 is closely associated with the acquisition of resistance to apoptosis caused by β 1-integrin silencing in head and neck cancer cells. *Biochemical and Biophysical Research Communications* 418:260-266.
- Klingenberg M, Becker J, Eberth S, Kube D, Wilting J. 2014. The chick chorioallantoic membrane as an in vivo xenograft model for Burkitt lymphoma. *BMC Cancer* 14:339.
- Konen J, Wilkinson S, Lee B, Fu H, Zhou W, Jiang Y, Marcus AI. 2016. LKB1 kinase-dependent and -independent defects disrupt polarity and adhesion signaling to drive collagen remodeling during invasion. *Molecular biology of the cell* 27:1069-1084.

- Kramer N, Walzl A, Unger C, Rosner M, Krupitza G, Hengstschlager M, Dolznig H. 2013. In vitro cell migration and invasion assays. *Mutation research* 752:10-24.
- Kraning-Rush CM, Carey SP, Califano JP, Smith BN, Reinhart-King CA. 2011. The role of the cytoskeleton in cellular force generation in 2D and 3D environments. *Physical biology* 8:015009.
- Kremmer T, Palyi I, Daubner D, Boldizsar M, Vincze B, Paulik E, Sugar J, Pokorny E, Tury E. 1991. Comparative studies on the polyamine metabolism and DFMO treatment of MCF-7 and MDA-MB-231 breast cancer cell lines and xenografts. *Anticancer Res* 11:1807-1813.
- Lämmermann T, Sixt M. 2009. Mechanical modes of 'amoeboid' cell migration. *Current Opinion in Cell Biology* 21:636-644.
- Lange JR, Fabry B. 2013. Cell and tissue mechanics in cell migration. *Exp Cell Res* 319:2418-2423.
- Larue L, Bellacosa A. 2005. Epithelial–mesenchymal transition in development and cancer: role of phosphatidylinositol 3' kinase/AKT pathways. *Oncogene* 24:7443-7454.
- Lawson C, Schlaepfer DD. 2013. pHocal adhesion kinase regulation is on a FERM foundation. *The Journal of Cell Biology* 202:833-836.
- Le Clairche C, Carlier M. 2008. Regulation of Actin Assembly Associated With Protrusion and Adhesion in Cell Migration. *Physiology Review* 88:489-513.
- Lecuit T, Yap AS. 2015. E-cadherin junctions as active mechanical integrators in tissue dynamics. *Nature Cell Biology* 17:533-539.
- Lemmon CA, Chen CS, Romer LH. 2008. Cell Traction Forces Direct Fibronectin Matrix Assembly. *Biophysical Journal* 96:729-738.
- Leube RE, Moch M, Windoffer R. 2015. Intermediate filaments and the regulation of focal adhesion. *Current Opinion in Cell Biology* 32:13-20.
- Li L, Okura M, Imamoto A. 2002. Focal Adhesions Require Catalytic Activity of Src Family Kinases To Mediate Integrin-Matrix Adhesion. *Molecular and Cellular Biology* 22:1203-1217.
- Lillie FR. 1919. *The Development of the Chick. An Introduction to Embryology*, 2nd Edition, Henry Holt and Co. New York.
- Loessner D, Holzapfel BM, Clements JA. 2014. Engineered microenvironments provide new insights into ovarian and prostate cancer progression and drug responses. *Advanced Drug Delivery Reviews* 79–80:193-213.
- Loessner D, Stok KS, Lutolf MP, Huttmacher DW, Clements JA, Rizzi SC. 2010. Bioengineered 3D platform to explore cell-ECM interactions and drug resistance of epithelial ovarian cancer cells. *Biomaterials* 31:8494-8506.
- Lokman NA, Elder AS, Ricciardelli C, Oehler MK. 2012. Chick Chorioallantoic Membrane (CAM) Assay as an In Vivo Model to Study the Effect of Newly Identified Molecules on Ovarian Cancer Invasion and Metastasis. *International journal of molecular sciences* 13:9959-9970.
- Lorentzen A, Bamber J, Sadok A, Elson-Schwab I, Marshall CJ. 2011. An ezrin-rich, rigid uropod-like structure directs movement of amoeboid blebbing cells. *Journal of Cell Science* 124:1256-1267.

- Lorusso G, Ruegg C. 2008. The tumor microenvironment and its contribution to tumor evolution toward metastasis. *Histochemistry and cell biology* 130:1091-1103.
- Lowery J, Kuczmarski ER, Herrmann H, Goldman RD. 2015. Intermediate Filaments Play a Pivotal Role in Regulating Cell Architecture and Function. *Journal of Biological Chemistry*.
- Lu H. 2006. Inflammation, a Key Event in Cancer Development. *Molecular Cancer Research* 4:221-233.
- Lu P, Weaver VM, Werb Z. 2012. The extracellular matrix: a dynamic niche in cancer progression. *The Journal of Cell Biology* 196:395-406.
- Lu WD, Zhang L, Wu CL, Liu ZG, Lei GY, Liu J, Gao W, Hu YR. 2014. Development of an acellular tumor extracellular matrix as a three-dimensional scaffold for tumor engineering. *PLoS One* 9:e103672.
- Lucey BP, Nelson-Rees WA, Hutchins GM. 2009. Henrietta Lacks, HeLa Cells, and Cell Culture Contamination. *Arch Pathol Lab Med* 133:1463-1467.
- Macchiarini P, et al. 2014. Clinical transplantation of a tissue-engineered airway. *The Lancet* 372:2023-2030.
- Madar S, Goldstein I, Rotter V. 2013. 'Cancer associated fibroblasts' --more than meets the eye. *Trends in Molecular Medicine* 19:447-453.
- Maddams J, Utley M, Moller H. 2012. Projections of cancer prevalence in the United Kingdom, 2010-2040. *Br J Cancer* 107:1195-1202.
- Madsen CD, Hooper S, Tozluoglu M, Bruckbauer A, Fletcher G, Erler JT, Bates PA, Thompson B, Sahai E. 2015. STRIPAK components determine mode of cancer cell migration and metastasis. *Nat Cell Biol* 17:68-80.
- Magalhaes MAO, Larson DR, Mader CC, Bravo-Cordero JJ, Gil-Henn H, Oser M, Chen X, Koleske AJ, Condeelis J. 2011. Cortactin phosphorylation regulates cell invasion through a pH-dependent pathway. *The Journal of Cell Biology* 195:903-920.
- Malladi S, Macalinao Danilo G, Jin X, He L, Basnet H, Zou Y, de Stanchina E, Massagué J. 2016. Metastatic Latency and Immune Evasion through Autocrine Inhibition of WNT. *Cell* 165:45-60.
- Mani SA, et al. 2008. The Epithelial-Mesenchymal Transition Generates Cells with Properties of Stem Cells. *Cell* 133:704-715.
- Mannherz HG, Mach M, Nowak D, Malicka-Blaszkiewicz M, Mazur A. 2007. Lamellipodia and Amoeboid Cell Locomotion: The Role of Actin-cycling and Bleb Formation. *Biophysical Reviews and Letters* 2:5-22.
- Mantovani A, Allavena P, Sica A, Balkwill F. 2008. Cancer-related inflammation. *Nature* 454:436-444.
- Martin P, Nunan R. 2015. Cellular and molecular mechanisms of repair in acute and chronic wound healing. *Br J Dermatol* 173:370-378.
- Martinez-Outschoorn UE, Pavlides S, Howell A, Pestell RG, Tanowitz HB, Sotgia F, Lisanti MP. 2011. Stromal-epithelial metabolic coupling in cancer: Integrating autophagy and metabolism in the tumor microenvironment. *The International Journal of Biochemistry & Cell Biology* 43:1045-1051.

- Massagué J. 2008. TGF β in Cancer. *Cell* 134:215-230.
- Mazza G, et al. 2015. Decellularized human liver as a natural 3D-scaffold for liver bioengineering and transplantation. *Scientific reports* 5:13079.
- McAllister SS, Weinberg RA. 2014. The tumour-induced systemic environment as a critical regulator of cancer progression and metastasis. *Nature Cell Biology* 16:717-727.
- McCaffrey LM, Macara IG. 2011. Epithelial organization, cell polarity and tumorigenesis. *Trends in Cell Biology* 21:727-735.
- Medberry CJ, et al. 2013. Hydrogels derived from central nervous system extracellular matrix. *Biomaterials* 34:1033-1040.
- Medema RH, Macúrek L. 2011. Checkpoint control and cancer. *Oncogene* 31:2601-2613.
- Mehlen P, Puisieux A. 2006. Metastasis: a question of life or death. *Nature Reviews Cancer* 6:449-458.
- Mendez MG, Kojima S-I, Goldman RD. 2010. Vimentin induces changes in cell shape, motility, and adhesion during the epithelial to mesenchymal transition. *The FASEB Journal* 24:1838-1851.
- Menke A, Philippi C, Vogelmann R, Seidel B, Lutz MP, Adler G, Wedlich D. 2001. Down-regulation of E-cadherin gene expression by collagen type I and type III in pancreatic cancer cell lines. *Cancer Res* 61:3508-3517.
- Momtahan N, Poornejad N, Struk JA, Castleton AA, Herrod BJ, Vance BR, Eatough JP, Roeder BL, Reynolds PR, Cook AD. 2015. Automation of Pressure Control Improves Whole Porcine Heart Decellularization. *Tissue Eng Part C Methods* 21:1148-1161.
- Monici M. 2005. Cell and tissue autofluorescence research and diagnostic applications. *Biotechnol Annu Rev* 11:227-256.
- Moroni F, Mirabella T. 2014. Decellularized matrices for cardiovascular tissue engineering. *American Journal of Stem Cells* 3:1-20.
- Murphy SV, Atala A. 2014. 3D bioprinting of tissues and organs. *Nat Biotech* 32:773-785.
- Murray ME, Mendez MG, Janmey PA. 2014. Substrate stiffness regulates solubility of cellular vimentin. *Molecular biology of the cell* 25:87-94.
- Nelson CM, Bissell MJ. 2006. Of extracellular matrix, scaffolds, and signaling: Tissue architecture regulates development, homeostasis, and cancer. Pages 287-309. *Annual Review of Cell and Developmental Biology*, vol. 22.
- Nguyen-Ngoc K-V, Cheung KJ, Brenot A, Shamir ER, Gray RS, Hines WC, Yaswen P, Werb Z, Ewald AJ. 2012. ECM microenvironment regulates collective migration and local dissemination in normal and malignant mammary epithelium. *Proceedings of the National Academy of Sciences of the United States of America* 109:E2595-E2604.
- Nguyen DX, Bos PD, Massague J. 2009. Metastasis: from dissemination to organ-specific colonization. *Nature reviews. Cancer* 9:274-284.
- Nguyen DX, Massagué J. 2007. Genetic determinants of cancer metastasis. *Nature Reviews Genetics* 8:341-352.
- Nik-Zainal S, et al. 2012. The Life History of 21 Breast Cancers. *Cell* 149:994-1007.

- Novaro V, Roskelley CD, Bissell MJ. 2003. Collagen-IV and laminin-1 regulate estrogen receptor alpha expression and function in mouse mammary epithelial cells. *Journal of Cell Science* 116:2975-2986.
- O'Brien FJ. 2011. Biomaterials & scaffolds for tissue engineering. *Materials Today* 14:88-95.
- Onder TT, Gupta PB, Mani SA, Yang J, Lander ES, Weinberg RA. 2008. Loss of E-Cadherin Promotes Metastasis via Multiple Downstream Transcriptional Pathways. *Cancer Research* 68:3645-3654.
- Onion D, et al. 2016. 3-Dimensional Patient-Derived Lung Cancer Assays Reveal Resistance to Standards-of-Care Promoted by Stromal Cells but Sensitivity to Histone Deacetylase Inhibitors. *Molecular cancer therapeutics*.
- Orgaz JL, et al. 2014. Diverse matrix metalloproteinase functions regulate cancer amoeboid migration. *Nature communications* 5:4255.
- Orimo A, Weinberg RA. 2006. Stromal fibroblasts in cancer - A novel tumor-promoting cell type. *Cell Cycle* 5:1597-1601.
- Oser M, Yamaguchi H, Mader CC, Bravo-Cordero JJ, Arias M, Chen X, DesMarais V, van Rheenen J, Koleske AJ, Condeelis J. 2009. Cortactin regulates cofilin and N-WASp activities to control the stages of invadopodium assembly and maturation. *The Journal of Cell Biology* 186:571-587.
- Otto A, Collins-Hooper H, Patel A, Dash PR, Patel K. 2011. Adult skeletal muscle stem cell migration is mediated by a blebbing/amoeboid mechanism. *Rejuvenation Research* 14:249-260.
- Ouyang L, Shi Z, Zhao S, Wang FT, Zhou TT, Liu B, Bao JK. 2012. Programmed cell death pathways in cancer: a review of apoptosis, autophagy and programmed necrosis. *Cell Prolif* 45:487-498.
- Padua D, Massagué J. 2009. Roles of TGF β in metastasis. *Cell Research* 19:89-102.
- Paget S. 1989. The distribution of secondary growths in cancer of the breast. 1889. *Cancer Metastasis Rev* 8:98-101.
- Paluch E, van der Gucht J, Sykes C. 2006. Cracking up: symmetry breaking in cellular systems. *The Journal of Cell Biology* 175:687-692.
- Pampaloni F, Reynaud EG, Stelzer EH. 2007. The third dimension bridges the gap between cell culture and live tissue. *Nature reviews. Molecular cell biology* 8:839-845.
- Pasapera AM, Plotnikov SV, Fischer RS, Case LB, Egelhoff TT, Waterman CM. 2015. Rac1-dependent phosphorylation and focal adhesion recruitment of myosin IIA regulates migration and mechanosensing. *Current biology : CB* 25:175-186.
- Patel A. 2012. The Identification and regulatory mechanisms of extravillous trophoblast cell invadosomes in a 2 and 3D Extracellular Matrix. PhD Thesis, University of Reading.
- Peela N, Sam FS, Christenson W, Truong D, Watson AW, Mouneimne G, Ros R, Nikkhah M. 2016. A three dimensional micropatterned tumor model for breast cancer cell migration studies. *Biomaterials* 81:72-83.
- Petrie RJ, Doyle AD, Yamada KM. 2009. Random versus directionally persistent cell migration. *Nature Reviews Molecular Cell Biology* 10:538-549.

- Petrie RJ, Gavara N, Chadwick RS, Yamada KM. 2012. Nonpolarized signaling reveals two distinct modes of 3D cell migration. *The Journal of Cell Biology* 197:439-455.
- Petrie RJ, Yamada KM. 2012. At the leading edge of three-dimensional cell migration. *Journal of Cell Science* 125:5917-5926.
- Pinner S, Sahai E. 2008. Imaging amoeboid cancer cell motility in vivo. *J Microsc* 231:441-445.
- Plotnikov Sergey V, Pasapera Ana M, Sabass B, Waterman Clare M. 2012. Force Fluctuations within Focal Adhesions Mediate ECM-Rigidity Sensing to Guide Directed Cell Migration. *Cell* 151:1513-1527.
- Polioudaki H, Agelaki S, Chiotaki R, Politaki E, Mavroudis D, Matikas A, Georgoulas V, Theodoropoulos PA. 2015. Variable expression levels of keratin and vimentin reveal differential EMT status of circulating tumor cells and correlation with clinical characteristics and outcome of patients with metastatic breast cancer. *BMC Cancer* 15:1-10.
- Provenzano PP, Eliceiri KW, Campbell JM, Inman DR, White JG, Keely PJ. 2006. Collagen reorganization at the tumor-stromal interface facilitates local invasion. *BMC Medicine* 4:38.
- Provenzano PP, Inman DR, Eliceiri KW, Knittel JG, Yan L, Rueden CT, White JG, Keely PJ. 2008. Collagen density promotes mammary tumor initiation and progression. *BMC Medicine* 6:11.
- Pylayeva-Gupta Y, Grabocka E, Bar-Sagi D. 2011. RAS oncogenes: weaving a tumorigenic web. *Nature Reviews Cancer* 11:761-774.
- Quail DF, Joyce JA. 2013. Microenvironmental regulation of tumor progression and metastasis. *Nature Medicine* 19:1423-1437.
- Quint C, Kondo Y, Manson RJ, Lawson JH, Dardik A, Niklason LE. 2011. Decellularized tissue-engineered blood vessel as an arterial conduit. *Proceedings of the National Academy of Sciences* 108:9214-9219.
- Radisky DC. 2005. Epithelial-mesenchymal transition. *Journal of Cell Science* 118:4325-4326.
- Radisky DC, et al. 2005. Rac1b and reactive oxygen species mediate MMP-3-induced EMT and genomic instability. *Nature* 436:123-127.
- Räsänen K, Vaheri A. 2010. Activation of fibroblasts in cancer stroma. *Experimental Cell Research* 316:2713-2722.
- Reya T, Morrison SJ, Clarke MF, Weissman IL. 2001. Stem cells, cancer, and cancer stem cells. *Nature* 414:105-111.
- Ribatti D. 2010. *The Chick Embryo Chorioallantoic Membrane in the Study of Angiogenesis and Metastasis*, Springer, London.
- . 2014. The chick embryo chorioallantoic membrane as a model for tumor biology. *Experimental Cell Research* 328:314-324.
- Ribatti D, Vacca A, Ranieri G, Sorino S, Roncali L. 1996. The Chick Embryo Chorioallantoic Membrane as an in vivo Wound Healing Model. *Path. Res. Pract.* 192:1068-1076.
- Ridley AJ. 2011. Life at the leading edge. *Cell* 145:1012-1022.
- Rolli M, Fransvea E, Pilch J, Saven A, Felding-Habermann B. 2003. Activated integrin α v β 3 cooperates with metalloproteinase MMP-9 in regulating migration of

- metastatic breast cancer cells. Proceedings of the National Academy of Sciences of the United States of America 100:9482-9487.
- Romanoff AL. 1960. The Avian Embryo - Structural and Functional Development. Macmillan, New York.
- . 1967. Biochemistry of the Avian Embryo. A Quantitative Analysis of Prenatal Development. J. Wiley and Sons, New York, London and Sydney.
- Rønnevig-Jessen L, Bissell MJ. 2009. Breast cancer by proxy: can the microenvironment be both the cause and consequence? Trends in Molecular Medicine 15:5-13.
- Rørth P. 2012. Fellow travellers: emergent properties of collective cell migration. EMBO reports 13:984-991.
- Rowe RG, Weiss SJ. 2008. Breaching the basement membrane: who, when and how? Trends in Cell Biology 18.
- Sahai E, Marshall CJ. 2003. Differing modes of tumour cell invasion have distinct requirements for Rho/ROCK signalling and extracellular proteolysis. Nature Cell Biology 5:711-719.
- Sanz-Moreno V, Gadea G, Ahn J, Paterson H, Marra P, Pinner S, Sahai E, Marshall CJ. 2008. Rac Activation and Inactivation Control Plasticity of Tumor Cell Movement. Cell 135:510-523.
- Sanz-Moreno V, et al. 2011. ROCK and JAK1 signaling cooperate to control actomyosin contractility in tumor cells and stroma. Cancer Cell 20:229-245.
- Sapudom J, Rubner S, Martin S, Kurth T, Riedel S, Mierke CT, Pompe T. 2015. The phenotype of cancer cell invasion controlled by fibril diameter and pore size of 3D collagen networks. Biomaterials 52:367-375.
- Sapudom J, Rubner S, Martin S, Pompe T. 2016. Mimicking Tissue Boundaries by Sharp Multiparameter Matrix Interfaces. Advanced Health Care Materials.
- Saxena M, Christofori G. 2013. Rebuilding cancer metastasis in the mouse. Molecular Oncology 7:283-296.
- Schafer G, Narasimha M, Vogelsang E, Leptin M. 2014. Cadherin switching during the formation and differentiation of the Drosophila mesoderm - implications for epithelial-to-mesenchymal transitions. Journal of Cell Science 127:1511-1522.
- Schaller MD. 2010. Cellular functions of FAK kinases: insight into molecular mechanisms and novel functions. Journal of Cell Science 123:1007-1013.
- Scheel C, et al. 2011. Paracrine and Autocrine Signals Induce and Maintain Mesenchymal and Stem Cell States in the Breast. Cell 145:926-940.
- Scheel C, Onder T, Karnoub A, Weinberg RA, Talmadge JE. 2007. Adaptation versus Selection: The Origins of Metastatic Behavior. Cancer Research 67:11476-11480.
- Scholzen T, Gerdes J. 2000. The Ki-67 protein: from the known and the unknown. J Cell Physiol 182:311-322.
- Schor SL. 1980. Cell Proliferation and Migration on Collagen Substrata *in vitro*. J Cell Sci 41:159-175.

- Schwarz S, Koerber L, Elsaesser AF, Goldberg-Bockhorn E, Seitz AM, Durselen L, Ignatius A, Walther P, Breiter R, Rotter N. 2012. Decellularized cartilage matrix as a novel biomatrix for cartilage tissue-engineering applications. *Tissue Eng Part A* 18:2195-2209.
- Schweitzer JK, Sedgwick AE, D'Souza-Schorey C. 2011. ARF6-mediated endocytic recycling impacts cell movement, cell division and lipid homeostasis. *Seminars in Cell & Developmental Biology* 22:39-47.
- Schwitalla S, et al. 2013. Intestinal tumorigenesis initiated by dedifferentiation and acquisition of stem-cell-like properties. *Cell* 152:25-38.
- Sebastián C, et al. 2012. The Histone Deacetylase SIRT6 Is a Tumor Suppressor that Controls Cancer Metabolism. *Cell* 151:1185-1199.
- Shafiq MA, Gemeinhart RA, Yue BY, Djalilian AR. 2012. Decellularized human cornea for reconstructing the corneal epithelium and anterior stroma. *Tissue Eng Part C Methods* 18:340-348.
- Shay JW, Wright WE. 2011. Role of telomeres and telomerase in cancer. *Seminars in Cancer Biology* 21:349-353.
- Shioda T, Munn LL, Fenner MH, Jain RK, Isselbacher KJ. 1997. Early Events of Metastasis in the Microcirculation Involve Changes in Gene Expression of Cancer Cells Tracking mRNA Levels of Metastasizing Cancer Cells in the Chick Embryo Chorioallantoic Membrane. *American Journal of Pathology* 150:2099-2112.
- Sixt M. 2012. Cell migration: Fibroblasts find a new way to get ahead. *Journal of Cell Biology* 197:347-349.
- Sleeman JP. 2012. The metastatic niche and stromal progression. *Cancer metastasis reviews* 31:429-440.
- Sleeman JP, Thiery JP. 2011. SnapShot: The Epithelial-Mesenchymal Transition. *Cell* 145:162-162.e161.
- Smith I, Haag M, Ugbode C, Tams D, Rattray M, Przyborski S, Bithell A, Whalley BJ. 2015. Neuronal-glia populations form functional networks in a biocompatible 3D scaffold. *Neuroscience Letters* 609:198-202.
- Song MS, Salmena L, Pandolfi PP. 2012. The functions and regulation of the PTEN tumour suppressor. *Nature Reviews. Molecular Cell Biology* 13:283-296.
- Spaeth E, Klopp A, Dembinski J, Andreeff M, Marini F. 2008. Inflammation and tumor microenvironments: defining the migratory itinerary of mesenchymal stem cells. *Gene Therapy* 15:730-738.
- Stanbridge E. 1971. Mycoplasmas and Cell Cultures. *Bacteriological Reviews* 35:206-227.
- Stewart SA, et al. 2002. Telomerase contributes to tumorigenesis by a telomere length-independent mechanism. *Proceedings of the National Academy of Sciences of the United States of America* 99:12606-12611.
- Stewart TJ, Abrams SI. 2008. How tumours escape mass destruction. *Oncogene* 27:5894-5903.

- Struecker B, et al. 2015. Porcine liver decellularization under oscillating pressure conditions: a technical refinement to improve the homogeneity of the decellularization process. *Tissue Eng Part C Methods* 21:303-313.
- Sung KE, Su G, Pehlke C, Trier SM, Eliceiri KW, Keely PJ, Friedl A, Beebe DJ. 2009. Control of 3-dimensional collagen matrix polymerization for reproducible human mammary fibroblast cell culture in microfluidic devices. *Biomaterials* 30:4833-4841.
- Taubenberger AV, Quent VM, Thibaudeau L, Clements JA, Hutmacher DW. 2013. Delineating breast cancer cell interactions with engineered bone microenvironments. *Journal of bone and mineral research : the official journal of the American Society for Bone and Mineral Research* 28:1399-1411.
- Taylor-Robinson D, Bebear C. 1997. Antibiotic susceptibilities of mycoplasmas and treatment of mycoplasmal infections. *J Antimicrob Chemother* 40:622-630.
- Theodoridis K, Tudorache I, Calistru A, Cebotari S, Meyer T, Sarikouch S, Bara C, Brehm R, Haverich A, Hilfiker A. 2015. Successful matrix guided tissue regeneration of decellularized pulmonary heart valve allografts in elderly sheep. *Biomaterials* 52:221-228.
- Thiery JP. 2002. Epithelial-mesenchymal transitions in tumour progression. *Nat Rev* 2.
- Thiery JP, Acloque H, Huang RY, Nieto MA. 2009. Epithelial-mesenchymal transitions in development and disease. *Cell* 139:871-890.
- Tsai FC, Wang MC, Lo JF, Chou CM, Lin YL. 2012. Spatiotemporal dynamics of the biological interface between cancer and the microenvironment: a fractal anomalous diffusion model with microenvironment plasticity. *Theor Biol Med Model* 9:36.
- Tsai JH, Yang J. 2013. Epithelial-mesenchymal plasticity in carcinoma metastasis. *Genes & development* 27:2192-2206.
- Tulotta C, Stefanescu C, Beletkaia E, Bussmann J, Tarbashevich K, Schmidt T, Snaar-Jagalska BE. 2016. Inhibition of signaling between human CXCR4 and zebrafish ligands by the small molecule IT1t impairs the formation of triple-negative breast cancer early metastases in a zebrafish xenograft model. *Disease models & mechanisms* 9:141-153.
- Uemura M, Refaat MM, Shinoyama M, Hayashi H, Hashimoto N, Takahashi J. 2010. Matrigel supports survival and neuronal differentiation of grafted embryonic stem cell-derived neural precursor cells. *J Neurosci Res* 88:542-551.
- Valastyan S, Weinberg RA. 2011. Tumor metastasis: molecular insights and evolving paradigms. *Cell* 147:275-292.
- Valdes TI, Kreutzer D, Moussy F. 2002. The chick chorioallantoic membrane as a novel in vivo model for testing biomaterials. *J Biomed Mater Res* 62:273-282.
- Vantangoli MM, Madnick SJ, Huse SM, Weston P, Boekelheide K. 2015. MCF-7 Human Breast Cancer Cells Form Differentiated Microtissues in Scaffold-Free Hydrogels. *PLoS One* 10:e0135426.
- Vasaturo A, Caserta S, Russo I, Preziosi V, Ciacci C, Guido S. 2012. A novel chemotaxis assay in 3-D collagen gels by time-lapse microscopy. *PLoS One* 7:e52251.

- Velez-delValle C, Marsch-Moreno M, Castro-Muñozledo F, Galván-Mendoza IJ, Kuri-Harcuch W. 2016. Epithelial cell migration requires the interaction between the vimentin and keratin intermediate filaments. *Scientific reports* 6:24389.
- Vicente-Manzanares M, Webb DJ, Horwitz A. 2005. Cell Migration at a Glance. *Journal of Cell Science* 118:4917-4919.
- Vogelstein B, Fearon ER, Hamilton SR, Kern SE, Preisinger AC, Leppert M, Nakamura Y, White R, Smits AM, Bos JL. 1988. Genetic alterations during colorectal-tumor development. *N Engl J Med* 319:525-532.
- Wang W, Goswami S, Sahai E, Wyckoff JB, Segall JE, Condeelis JS. 2005. Tumor cells caught in the act of invading: their strategy for enhanced cell motility. *Trends Cell Biol* 15:138-145.
- Wang W, et al. 2002. Single Cell Behavior in Metastatic Primary Mammary Tumors Correlated with Gene Expression Patterns Revealed by Molecular Profiling. *Cancer Research* 62:6278-6288.
- Wang Z, et al. 2015. Broad targeting of angiogenesis for cancer prevention and therapy. *Seminars in Cancer Biology* 35, Supplement:S224-S243.
- Wehrle-Haller B. 2012. Structure and function of focal adhesions. *Current Opinion in Cell Biology* 24:116-124.
- Wehrle-Haller B, Inhof BA. 2003. Actin, microtubules and focal adhesion dynamics during cell migration. *The International Journal of Biochemistry & Cell Biology* 35:39-50.
- Weijer CJ. 2009. Collective cell migration in development. *Journal of Cell Science* 122:3215-3223.
- Weis SM, Cheresh DA. 2011. Tumor angiogenesis: molecular pathways and therapeutic targets. *Nat Med* 17:1359-1370.
- Wen JH, Vincent LG, Fuhrmann A, Choi YS, Hribar KC, Taylor-Weiner H, Chen S, Engler AJ. 2014. Interplay of matrix stiffness and protein tethering in stem cell differentiation. *Nat Mater* 13:979-987.
- WHO. 2015. WHO Cancer fact sheet 297.
- Williams Y, Byrne S, Bashir M, Davies A, Whelan A, Gun'ko Y, Kelleher D, Volkov Y. 2008. Comparison of three cell fixation methods for high content analysis assays utilizing quantum dots. *J Microsc* 232:91-98.
- Wolf K, Alexander S, Schacht V, Coussens LM, von Andrian UH, van Rheenen J, Deryugina E, Friedl P. 2009. Collagen-based cell migration models in vitro and in vivo. *Seminars in Cell & Developmental Biology* 20:931-941.
- Wolf K, Mazo I, Leung H, Engelke K, von Andrian UH, Deryugina EI, Strongin AY, Bocker EB, Friedl P. 2003. Compensation mechanism in tumor cell migration: mesenchymal-amoeboid transition after blocking of pericellular proteolysis. *The Journal of Cell Biology* 160:267-277.
- Wolf K, Te Lindert M, Krause M, Alexander S, Te Riet J, Willis AL, Hoffman RM, Figdor CG, Weiss SJ, Friedl P. 2013. Physical limits of cell migration: control by ECM space and nuclear deformation and tuning by proteolysis and traction force. *The Journal of Cell Biology* 201:1069-1084.

- Woodhouse EC, Kelly K. 2011. *Drosophila* and Zebrafish: Genetic Models for Cancer Metastasis. *Cancer and Metastasis Biological Basis and Therapeutics*, Cambridge:15-24.
- Wu J, Rajwa B, Filmer DL, Hoffman CM, Yuan B, Chiang C, Sturgis J, Robinson JP. 2003. Automated quantification and reconstruction of collagen matrix from 3D confocal datasets. *Journal of Microscopy* 210 Pt2:158-165.
- Wyckoff JB, Pinner SE, Gschmeissner S, Condeelis JS, Sahai E. 2006. ROCK- and Myosin-Dependent Matrix Deformation Enables Protease-Independent Tumor-Cell Invasion In Vivo. *Current Biology* 16:1515-1523.
- Wyckoff JB, Wang Y, Lin EY, Li Jf, Goswami S, Stanley ER, Segall JE, Pollard JW, Condeelis J. 2007. Direct Visualization of Macrophage-Assisted Tumor Cell Intravasation in Mammary Tumors. *Cancer Research* 67:2649-2656.
- Xiong G, Flynn TJ, Chen J, Trinkle C, Xu R. 2015. Development of an ex vivo breast cancer lung colonization model utilizing a decellularized lung matrix. *Integr Biol (Camb)* 7:1518-1525.
- Xu W, Yang Z, Lu N. 2015. A new role for the PI3K/Akt signaling pathway in the epithelial-mesenchymal transition. *Cell Adh Migr* 9:317-324.
- Yamada KM, Cukierman E. 2007. Modeling tissue morphogenesis and cancer in 3D. *Cell* 130:601-610.
- Yamaguchi H, Condeelis J. 2007. Regulation of the actin cytoskeleton in cancer cell migration and invasion. *Biochimica et Biophysica Acta (BBA) - Molecular Cell Research* 1773:642-652.
- Yamaguchi H, Wyckoff J, Condeelis J. 2005. Cell migration in tumors. *Current Opinion in Cell Biology* 17:559-564.
- Yap AS, Crampton MS, Hardin J. 2007. Making and breaking contacts: the cellular biology of cadherin regulation. *Curr Opin Cell Biol* 19:508-514.
- Youssef KK, et al. 2012. Adult interfollicular tumour-initiating cells are reprogrammed into an embryonic hair follicle progenitor-like fate during basal cell carcinoma initiation. *Nature Cell Biology* 14:1282-1294.
- Yu X, Machesky LM. 2012. Cells assemble invadopodia-like structures and invade into matrigel in a matrix metalloprotease dependent manner in the circular invasion assay. *PLoS One* 7:e30605.
- Zaman MH, Trapani LM, Sieminski AL, Mackellar D, Gong H, Kamm RD, Wells A, Lauffenburger DA, Matsudaira P. 2006. Migration of tumor cells in 3D matrices is governed by matrix stiffness along with cell-matrix adhesion and proteolysis. *Proceedings of the National Academy of Sciences of the United States of America* 103:10889-10894.
- Zhao XK, et al. 2016. Focal Adhesion Kinase Regulates Fibroblast Migration via Integrin beta-1 and Plays a Central Role in Fibrosis. *Scientific reports* 6:19276.
- Zhu QS, et al. 2011. Vimentin is a novel AKT1 target mediating motility and invasion. *Oncogene* 30:457-470.
- Zijlstra A, Aimes RT, Zhu D, Regazzoni K, Kupriyanova T, Seandel M, Deryugina EI, Quigley JP. 2004. Collagenolysis-dependent angiogenesis mediated by matrix metalloproteinase-13 (collagenase-3). *The Journal of Biological Chemistry* 279:27633-27645.

Zijlstra A, Lewis J, Degryse B, Stuhlmann H, Quigley JP. 2008. The inhibition of tumor cell intravasation and subsequent metastasis via regulation of in vivo tumor cell motility by the tetraspanin CD151. *Cancer Cell* 13:221-234.

Zijlstra A, Seandel M, Kupriyanova TA, Partridge JJ, Madsen MA, Hahn-Dantona EA, Quigley JP, Deryugina EI. 2006. Proangiogenic role of neutrophil-like inflammatory heterophils during neovascularization induced by growth factors and human tumor cells. *Blood* 107:317-327.

Zijlstra Aea. 2002. A Quantitative Analysis of Rate-limiting Steps in the Metastatic Cascade Using Human-specific Real-Time Polymerase Chain Reaction.

Zoltan-Jones A, Huang L, Ghatak S, Toole BP. 2003. Elevated hyaluronan production induces mesenchymal and transformed properties in epithelial cells. *The Journal of Biological Chemistry* 278:45801-45810.

Appendix A

A1. DMEM constituents (DMEM, low glucose with pyruvate – 31885 Thermo Fisher)

Components	Molecular Weight	Concentration (mg/L)	mM
Amino Acids			
Glycine	75.0	30.0	0.4
L-Arginine hydrochloride	211.0	84.0	0.39810428
L-Cystine 2HCl	313.0	63.0	0.20127796
L-Glutamine	146.0	580.0	3.9726028
L-Histidine hydrochloride-H ₂ O	210.0	42.0	0.2
L-Isoleucine	131.0	105.0	0.8015267
L-Leucine	131.0	105.0	0.8015267
L-Lysine hydrochloride	183.0	146.0	0.7978142
L-Methionine	149.0	30.0	0.20134228
L-Phenylalanine	165.0	66.0	0.4
L-Serine	105.0	42.0	0.4
L-Threonine	119.0	95.0	0.79831934

Components	Molecular Weight	Concentration (mg/L)	mM
L-Tryptophan	204.0	16.0	0.078431375
L-Tyrosine	181.0	72.0	0.39779004
L-Valine	117.0	94.0	0.8034188

Vitamins			
Choline chloride	140.0	4.0	0.028571429
D-Calcium pantothenate	477.0	4.0	0.008385744
Folic Acid	441.0	4.0	0.009070295
Niacinamide	122.0	4.0	0.032786883
Pyridoxine hydrochloride	206.0	4.0	0.019417476
Riboflavin	376.0	0.4	0.0010638298
Thiamine hydrochloride	337.0	4.0	0.011869436
i-Inositol	180.0	7.2	0.04

Inorganic Salts			
Calcium Chloride (CaCl ₂ ·2H ₂ O)	147.0	264.0	1.7959183
Ferric Nitrate (Fe(NO ₃) ₃ ·9H ₂ O)	404.0	0.1	2.4752476E-4
Magnesium Sulfate (MgSO ₄ ·7H ₂ O)	246.0	200.0	0.8130081
Potassium Chloride (KCl)	75.0	400.0	5.3333335
Sodium Bicarbonate (NaHCO ₃)	84.0	3700.0	44.04762
Sodium Chloride (NaCl)	58.0	6400.0	110.344826
Sodium Phosphate monobasic (NaH ₂ PO ₄ ·2H ₂ O)	154.0	141.0	0.91558444
Other Components			
D-Glucose (Dextrose)	180.0	1000.0	5.5555553
Phenol Red	376.4	15.0	0.039851222
Sodium Pyruvate	110.0	110.0	1.0

A2. Qiagen mini-prep and giga-prep kits

Qiagen mini-prep kit used: QIAprep Spin Miniprep Kit

The miniprep kit was used according to manufactureres instructions following the Qiagen Qiaprep Miniprep Handbook 2012.

Briefly:

1. Overnight cultures were harvested and the pellet resuspended in resuspension buffer P1.
2. Lysis buffer P2 was added and mixed gently to produce a viscous solution.
3. Precipitation buffer N3 was added and mixed gently but thoroughly.
4. The precipitate solution was centrifuged for 10 minutes at 3000 x g in a spin column and collection tube. This was conducted to pellet separate genomic DNA and cell debris from plasmid DNA.
5. The bound plasmid DNA was washed in the spin tube.
6. The plasmid was eluted from the spin column using double distilled water and stored at -80°C.

Plasmid Giga Kit (12191)

The kit was used according to the manufacturer's instructions contained in the EndoFree Plasmid Purification Handbook provided with the kit (2013).

Briefly:

1. An overnight bacterial culture was harvested by pelleting at 6000 x g for 15 minutes at 4°C.
2. The bacterial pellet was resuspended in buffer P1.
3. Buffer P1 and P2 were mixed in equal quantities at room temperature for 5 minutes to lyse the bacteria. (LyseBlue was added as an indicator to show lysis.)
4. Buffer P3 was used to precipitate the plasmid DNA. It was added, mixed and left to incubate for 30 minutes.
5. The precipitate mix was then filtered to remove cell debris, genomic DNA and other extraneous material. It was added to a filter cartridge, left to incubate for 10 minutes then filtration achieved with the aid of a vacuum pump.
6. The eluent was treated with an endotoxin removal buffer and incubated on ice for 30 minutes.
7. The Qiagen tip was equilibrated with buffer QBT.
8. The supernatant containing plasmid was added to the Qiagen tip and left to bind to the column for 10 minutes.
9. The Qiagen tip and its contents were washed with a wash buffer and then plasmid DNA eluted using an eluting buffer and a vacuum pump.
10. The DNA was precipitated from the eluent using isopropanol followed by centrifugation for 30 minutes at 15,000 x g at 4°C.

11. The supernatant was removed, the pellet washed with 70% ethanol then the pellet air dried.
12. The pellet was re-suspended in TE buffer, aliquoted and frozen at -80°C.

Buffers Used:

P1 – Resuspension Buffer – 50mM Tris-Cl, pH 8.0; 10mM EDTA; 100µg/ml RNase A

P2 – Lysis Buffer – 200mM NaOH, 1% SDS (w/v)

P3 – Neutralization Buffer – 3.0M potassium acetate, pH5.5

Filter Wash Buffer – 1M Potassium acetate pH 5.0

Tip Equilibration Buffer – 750mM NaCl; 50mM MOPS pH 7.0; 15% isopropanol (v/v); 0.15% Triton X-100 (v/v)

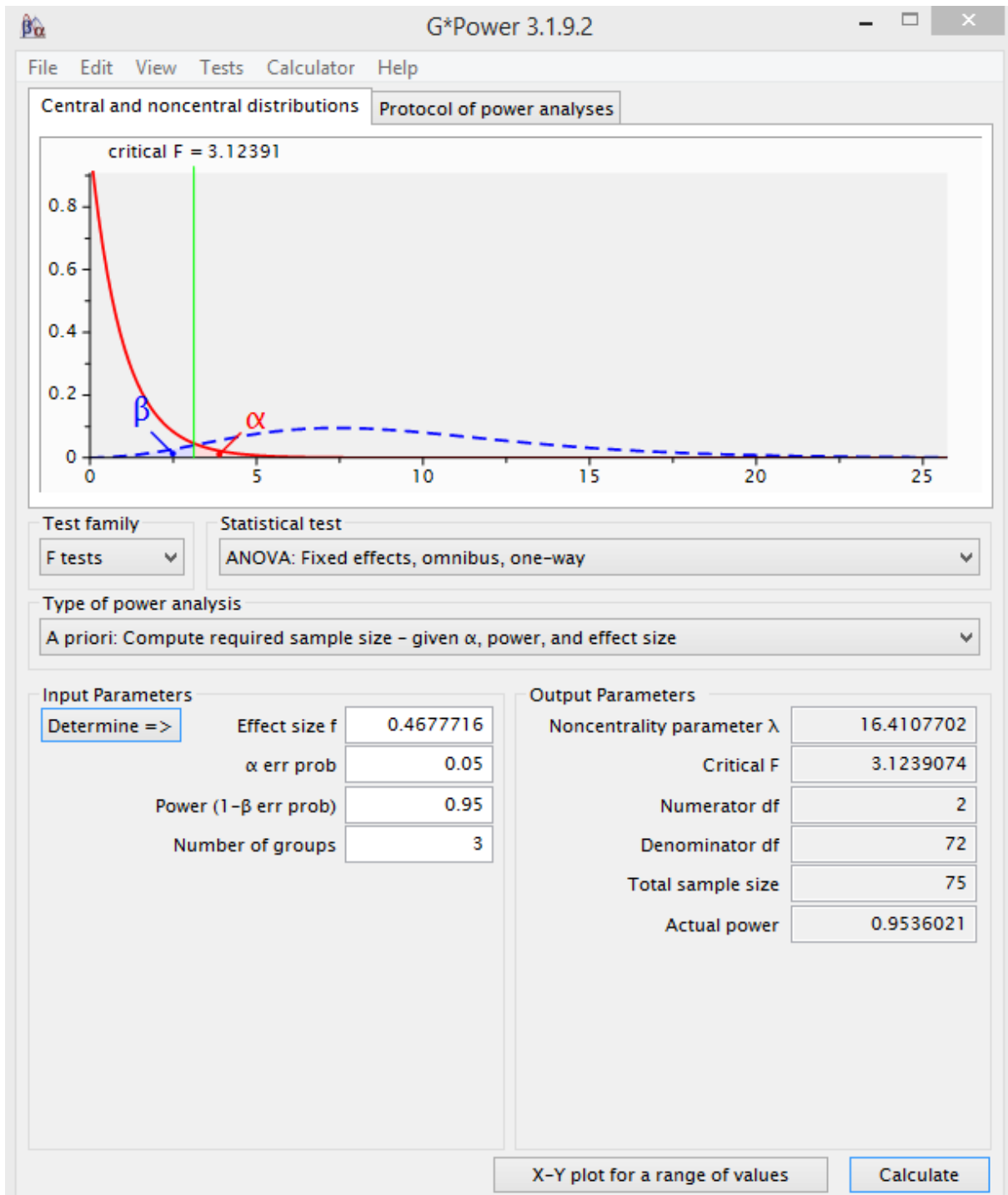
Tip Wash Buffer – 1.0M NaCl; 50mM MOPS pH 7.0; 15% isopropanol (v/v).

Tip Elution buffer – 1.25M NaCl; 50mM TrisCl, pH 8.5; 15% isopropanol (v/v).

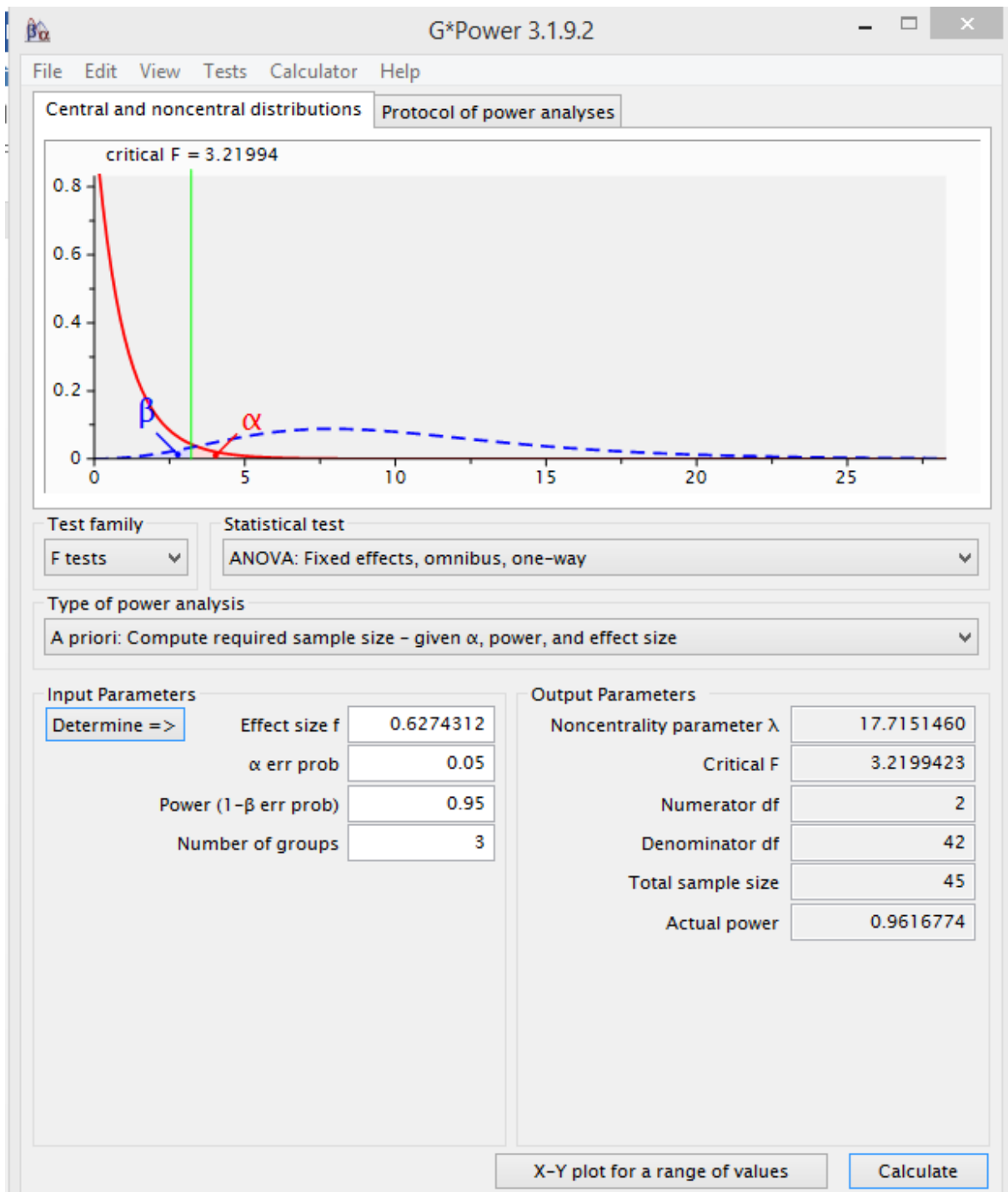
TE Buffer – 10mM Tris-Cl, pH 8.0; 1mM EDTA.

Appendix B

B1. 2D coatings



B2. 3D collagen



B3. Collagen/fibronectin (MDA-MB-231)

G*Power 3.1.9.2

File Edit View Tests Calculator Help

Central and noncentral distributions Protocol of power analyses

critical F = 1.88186

Test family: F tests

Statistical test: ANOVA: Fixed effects, omnibus, one-way

Type of power analysis: A priori: Compute required sample size - given α , power, and effect size

Input Parameters

Determine =>

Effect size f: 0.2901784

α err prob: 0.1

Power (1- β err prob): 0.90

Number of groups: 6

Output Parameters

Noncentrality parameter λ : 14.6514097

Critical F: 1.8818642

Numerator df: 5

Denominator df: 168

Total sample size: 174

Actual power: 0.9090449

Select procedure: Effect size from means

Number of groups: 6

SD σ within each group: 36

Group	Mean	Size
1	65.57	30
2	56.76	30
3	38.94	30
4	40.91	30
5	56.96	30
6	39.34	30

Equal n: 6

Total sample size: 180

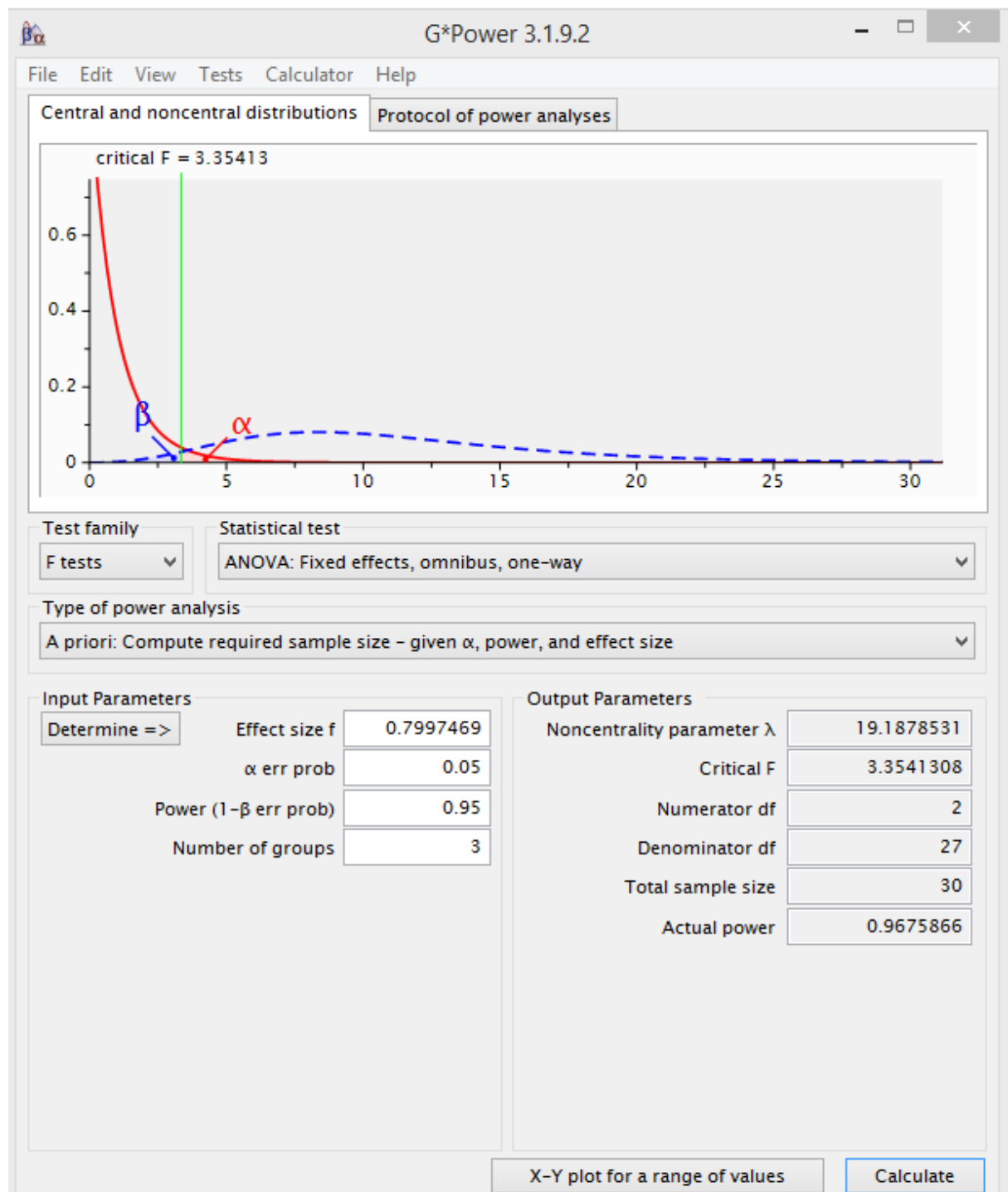
Calculate Effect size f: 0.2901784

Calculate and transfer to main window

Close

X-Y plot for a range of values Calculate

B4. 2D/3D assay



B5. 2D coatings: fibronectin/collagen/Matrigel

MDA-MB-231 Cells – Distance to Start

Table Analyzed	D2S all								
Two-way ANOVA	Ordinary								
Alpha	0.05								
Source of Variation	% of total variation	P value	P value summary	Significant?					
Interaction	28.17	0.0409	*	Yes					
Cells	8.220	0.7080	ns	No					
Coating	7.688	< 0.0001	****	Yes					
ANOVA table	SS	DF	MS	F (DFn, DFd)	P value				
Interaction	177157	58	3054	F (58, 165) = 1.432	P = 0.0409				
Cells	51693	29	1783	F (29, 165) = 0.8359	P = 0.7080				
Coating	48350	2	24175	F (2, 165) = 11.34	P < 0.0001				
Residual	351852	165	2132						
Number of missing values	15								
Compare column means (main column effect)									
Number of families		1							
Number of comparisons per family		3							
Alpha		0.05							
Tukey's multiple comparisons test	Mean Diff.	95% CI of diff.	Significant?	Summary					
Fibronectin vs. Collagen	28.67	11.71 to 45.62	Yes	***					
Fibronectin vs. Matrigel	29.17	13.00 to 45.33	Yes	****					
Collagen vs. Matrigel	0.4985	-16.46 to 17.46	No	ns					
Test details	Mean 1	Mean 2	Mean Diff.	SE of diff.	N1	N2	q	DF	
Fibronectin vs. Collagen	79.60	50.94	28.67	7.191					
Fibronectin vs. Matrigel	79.60	50.44	29.17	6.857	90	90	4.745	180	
Collagen vs. Matrigel	50.94	50.44	0.4985	7.191	90	90	6.531	180	
					90	90	1.786	180	

MDA-MB-231 cells - speed

Table Analyzed	Speed								
Two-way ANOVA	Ordinary								
Alpha	0.05								
Source of Variation	% of total variation	P value	P value summary	Significant?					
Interaction	6.304	< 0.0001	****	Yes					
Cells	0.9150	0.1285	ns	No					
Coating	38.39	< 0.0001	****	Yes					
ANOVA table	SS	DF	MS	F (DFn, DFd)	P value				
Interaction	0.5086	4	0.1272	F (4, 246) = 7.128	P < 0.0001				
Cells	0.07383	2	0.03691	F (2, 246) = 2.069	P = 0.1285				
Coating	3.098	2	1.549	F (2, 246) = 86.82	P < 0.0001				
Residual	4.388	246	0.01784						
Number of missing values	15								
Compare column means (main column effect)									
Number of families	1								
Number of comparisons per family	3								
Alpha	0.05								
Tukey's multiple comparisons test	Mean Diff.	95% CI of diff.	Significant?	Summary					
Fibronectin vs. Collagen	0.1947	0.1454 to 0.2439	Yes	****					
Fibronectin vs. Matrigel	0.2625	0.2156 to 0.3095	Yes	****					
Collagen vs. Matrigel	0.06788	0.01865 to 0.1171	Yes	**					
Test details	Mean 1	Mean 2	Mean Diff.	SE of diff.	N1	N2	d	DF	
Fibronectin vs. Collagen	0.4446	0.2499	0.1947	0.02088	90	90	8.799	180	
Fibronectin vs. Matrigel	0.4446	0.1820	0.2625	0.01991	90	90	11.50	180	
Collagen vs. Matrigel	0.2499	0.1820	0.06788	0.02088	90	90	2.697	180	

MDA-MB-231 cells – aspect ratio

Table Analyzed	Aspect Ratio							
Two-way ANOVA	Ordinary							
Alpha	0.05							
Source of Variation	% of total variation	P value	P value summary		Significant?			
Interaction	12.36	0.4411	ns		No			
Cells	7.037	0.2683	ns		No			
Coating	48.84	<0.0001	****		Yes			
ANOVA table	SS	DF	MS		F (DFn, DFd)	P value		
Interaction	95.12	58	1.640		F (58, 165) = 1.025	P = 0.4411		
Cells	54.17	29	1.868		F (29, 165) = 1.167	P = 0.2683		
Coating	376.0	2	188.0		F (2, 165) = 117.5	P < 0.0001		
Residual	264.0	165	1.600					
Number of missing values	15							
Compare column means (main column effect)								
Number of families	1							
Number of comparisons per family	3							
Alpha	0.05							
Tukey's multiple comparisons test	Mean Diff.	95% CI of diff.	Significant?	Summary				
Fibronectin vs. Collagen	-2.151	-2.619 to -1.683	Yes	****				
Fibronectin vs. Matrigel	0.7487	0.3027 to 1.195	Yes	***				
Collagen vs. Matrigel	2.900	2.432 to 3.367	Yes	****				
Test details	Mean 1	Mean 2	Mean Diff.	SE of diff.	N1	N2	q	DF
Fibronectin vs. Collagen	1.953	4.104	-2.151	0.1978	90	75	15.38	165
Fibronectin vs. Matrigel	1.953	1.205	0.7487	0.1886	90	90	5.615	165
Collagen vs. Matrigel	4.104	1.205	2.900	0.1978	75	90	20.73	165

HT1080 cells - distance to start

Table Analyzed	HT1080 D2S							
Two-way ANOVA	Ordinary							
Alpha	0.05							
Source of Variation	% of total variation	P value	P value summary	Significant?				
Interaction	20.51	0.3170	ns	No				
Cells	14.18	0.0534	ns	No				
Coating	7.338	< 0.0001	****	Yes				
ANOVA table	SS	DF	MS	F (DFn, DFd)			P value	
Interaction	83594	58	1441	F (58, 180) = 1.098			P = 0.3170	
Cells	57795	29	1993	F (29, 180) = 1.518			P = 0.0534	
Coating	29911	2	14956	F (2, 180) = 11.39			P < 0.0001	
Residual	236310	180	1313					
Number of missing values	0							
Compare column means (main column effect)								
Number of families	1							
Number of comparisons per family	3							
Alpha	0.05							
Tukey's multiple comparisons test	Mean Diff.	95% CI of diff.	Significant?	Summary				
Fibronectin vs. Collagen	18.12	5.357 to 30.89	Yes	**				
Fibronectin vs. Matrigel	24.94	12.18 to 37.71	Yes	****				
Collagen vs. Matrigel	6.820	-5.944 to 19.58	No	ns				
Test details	Mean 1	Mean 2	Mean Diff.	SE of diff.	N1	N2	q	DF
Fibronectin vs. Collagen	64.62	46.50	18.12	5.401	90	90	4.745	180
Fibronectin vs. Matrigel	64.62	39.68	24.94	5.401	90	90	6.531	180
Collagen vs. Matrigel	46.50	39.68	6.820	5.401	90	90	1.786	180

HT1080 cells - speed

Table Analyzed	HT1080 Speed							
Two-way ANOVA	Ordinary							
Alpha	0.05							
Source of Variation	% of total variation	P value	P value summary	Significant?				
Interaction	10.98	0.9926	ns	No				
Cells	5.673	0.9519	ns	No				
Coating	23.88	< 0.0001	****	Yes				
ANOVA table	SS	DF	MS	F (DFn, DFd)		P value		
Interaction	0.6117	58	0.01055	F (58, 180) = 0.5730		P = 0.9926		
Cells	0.3161	29	0.01090	F (29, 180) = 0.5921		P = 0.9519		
Coating	1.331	2	0.6653	F (2, 180) = 36.14		P < 0.0001		
Residual	3.313	180	0.01841					
Number of missing values	0							
Compare column means (main column effect)								
Number of families	1							
Number of comparisons per family	3							
Alpha	0.05							
Tukey's multiple comparisons test	Mean Diff.	95% CI of diff.	Significant?	Summary				
Fibronectin vs. Collagen	0.1258	0.07804 to 0.1736	Yes	****				
Fibronectin vs. Matrigel	0.1644	0.1166 to 0.2122	Yes	****				
Collagen vs. Matrigel	0.03857	-0.009225 to 0.08637	No	ns				
Test details	Mean 1	Mean 2	Mean Diff.	SE of diff.	N1	N2	q	DF
Fibronectin vs. Collagen	0.3728	0.2470	0.1258	0.02022	90	90	8.799	180
Fibronectin vs. Matrigel	0.3728	0.2084	0.1644	0.02022	90	90	11.50	180
Collagen vs. Matrigel	0.2470	0.2084	0.03857	0.02022	90	90	2.697	180

HT1080 cells - aspect ratio

Table Analyzed	HT1080 Aspect Ratio					
Two-way ANOVA	Ordinary					
Alpha	0.05					

Source of Variation	% of total variation	P value	P value summary	Significant?				
Interaction	13.79	0.9043	ns	No				
Cells	3.510	0.9985	ns	No				
Coating	25.20	< 0.0001	****	Yes				
ANOVA table	SS	DF	MS	F (DFn, DFd)	P value			
Interaction	105.7	58	1.822	F (58, 180) = 0.7444	P = 0.9043			
Cells	26.89	29	0.9273	F (29, 180) = 0.3790	P = 0.9985			
Coating	193.1	2	96.55	F (2, 180) = 39.46	P < 0.0001			
Residual	440.5	180	2.447					
Number of missing values	0							
Compare column means (main column effect)								
Number of families	1							
Number of comparisons per family	3							
Alpha	0.05							
Tukey's multiple comparisons test	Mean Diff.	95% CI of diff.	Significant?	Summary				
Fibronectin vs. Collagen	-1.883	-2.434 to -1.332	Yes	****				
Fibronectin vs. Matrigel	-0.1942	-0.7453 to 0.3569	No	ns				
Collagen vs. Matrigel	1.689	1.138 to 2.240	Yes	****				
Test details	Mean 1	Mean 2	Mean Diff.	SE of diff.	N1	N2	q	DF
Fibronectin vs. Collagen	1.663	3.546	-1.883	0.2332	90	90	11.42	180
Fibronectin vs. Matrigel	1.663	1.857	-0.1942	0.2332	90	90	1.177	180
Collagen vs. Matrigel	3.546	1.857	1.689	0.2332	90	90	10.24	180

HT1080 v MDA-MB-231 speed comparison

Table Analyzed		Speed Comparison HT and MDA				
Kruskal-Wallis test						
P value		0.0011				
Exact or approximate P value?		Approximate				
P value summary		**				
Do the medians vary signif. (P < 0.05)		Yes				
Number of groups		4				
Kruskal-Wallis statistic		16.10				
Data summary						
Number of treatments (columns)		4				
Number of values (total)		225				
Number of families	1					
Number of comparisons per family	2					
Alpha	0.05					
Dunn's multiple comparisons test	Mean rank diff.	Significant?	Summary			
HT Control vs. HT N1-3	8.767	No	ns			A-B
MDA Control vs. MDA N1-3	16.71	No	ns			C-D
Test details	Mean rank 1	Mean rank 2	Mean rank diff.	n1	n2	
HT Control vs. HT N1-3	104.2	95.47	8.767	30	90	
MDA Control vs. MDA N1-3	142.5	125.8	16.71	30	75	

B6. 3D collagen assay for HT1080, MDA-MB-231 and MCF7 cells

Cell length

Table Analyzed	cell length n1-3					
Two-way ANOVA	Ordinary					
Alpha	0.05					
Source of Variation	% of total variation	P value	P value summary	Significant?		
Interaction	13.10	0.4256	ns	No		
Cells	4.220	0.0049	**	Yes		
Cell in Matrix	51.17	< 0.0001	****	Yes		
ANOVA table	SS	DF	MS	F (DFn, DFd)	P value	
Interaction	83464	245	340.7	F (245, 600) = 1.019	P = 0.4256	
Cells	26878	49	548.5	F (49, 600) = 1.640	P = 0.0049	
Cell in Matrix	325953	5	65191	F (5, 600) = 194.9	P < 0.0001	
Residual	200658	600	334.4			
Number of missing values	0					
Compare column means (main column effect)						
Number of families	1					
Number of comparisons per family	15					
Alpha	0.05					
Tukey's multiple comparisons test	Mean Diff.	95% CI of diff.	Significant?	Summary		
MCF7 1mg/ml vs. MCF7 2mg/ml	4.000	-2.037 to 10.04	No	ns		
MCF7 1mg/ml vs. MDA 1mg/ml	-32.82	-38.86 to -26.78	Yes	****		
MCF7 1mg/ml vs. MDA 2mg/ml	-28.31	-34.34 to -22.27	Yes	****		
MCF7 1mg/ml vs. HT 1mg/ml	-45.86	-51.90 to -39.82	Yes	****		
MCF7 1mg/ml vs. HT 2mg/ml	-39.47	-45.50 to -33.43	Yes	****		
MCF7 2mg/ml vs. MDA 1mg/ml	-36.82	-42.86 to -30.78	Yes	****		
MCF7 2mg/ml vs. MDA 2mg/ml	-32.31	-38.34 to -26.27	Yes	****		
MCF7 2mg/ml vs. HT 1mg/ml	-49.86	-55.90 to -43.82	Yes	****		
Tukey's multiple comparisons test	Mean Diff.	95% CI of diff.	Significant?	Summary		
MCF7 2mg/ml vs. HT 2mg/ml	-43.47	-49.50 to -37.43	Yes	****		
MDA 1mg/ml vs. MDA 2mg/ml	4.513	-1.524 to 10.55	No	ns		
MDA 1mg/ml vs. HT 1mg/ml	-13.04	-19.08 to -7.003	Yes	****		

MDA 1mg/ml vs. HT 2mg/ml	-6.647	-12.68 to -0.6096	Yes	*				
MDA 2mg/ml vs. HT 1mg/ml	-17.55	-23.59 to -11.52	Yes	****				
MDA 2mg/ml vs. HT 2mg/ml	-11.16	-17.20 to -5.123	Yes	****				
HT 1mg/ml vs. HT 2mg/ml	6.393	0.3562 to 12.43	Yes	*				
Test details	Mean 1	Mean 2	Mean Diff.	SE of diff.	N1	N2	q	DF
MCF7 1mg/ml vs. MCF7 2mg/ml	31.30	27.30	4.000	2.112	150	150	2.679	600
MCF7 1mg/ml vs. MDA 1mg/ml	31.30	64.12	-32.82	2.112	150	150	21.98	600
MCF7 1mg/ml vs. MDA 2mg/ml	31.30	59.61	-28.31	2.112	150	150	18.96	600
MCF7 1mg/ml vs. HT 1mg/ml	31.30	77.16	-45.86	2.112	150	150	30.71	600
MCF7 1mg/ml vs. HT 2mg/ml	31.30	70.77	-39.47	2.112	150	150	26.43	600
MCF7 2mg/ml vs. MDA 1mg/ml	27.30	64.12	-36.82	2.112	150	150	24.66	600
MCF7 2mg/ml vs. MDA 2mg/ml	27.30	59.61	-32.31	2.112	150	150	21.64	600
MCF7 2mg/ml vs. HT 1mg/ml	27.30	77.16	-49.86	2.112	150	150	33.39	600
MCF7 2mg/ml vs. HT 2mg/ml	27.30	70.77	-43.47	2.112	150	150	29.11	600
MDA 1mg/ml vs. MDA 2mg/ml	64.12	59.61	4.513	2.112	150	150	3.023	600
MDA 1mg/ml vs. HT 1mg/ml	64.12	77.16	-13.04	2.112	150	150	8.733	600
MDA 1mg/ml vs. HT 2mg/ml	64.12	70.77	-6.647	2.112	150	150	4.451	600
MDA 2mg/ml vs. HT 1mg/ml	59.61	77.16	-17.55	2.112	150	150	11.76	600
MDA 2mg/ml vs. HT 2mg/ml	59.61	70.77	-11.16	2.112	150	150	7.474	600
HT 1mg/ml vs. HT 2mg/ml	77.16	70.77	6.393	2.112	150	150	4.282	600

Aspect ratio

Table Analyzed	aspect ratio n1-3			
Tw o-way ANOVA	Ordinary			
Alpha	0.05			
Source of Variation	% of total variation	P value	P value summary	Significant?
Interaction	21.22	0.2457	ns	No
cell	6.017	0.0144	*	Yes

Cell and matrix	24.42	< 0.0001	****	Yes				
ANOVA table	SS	DF	MS	F (DFn, DFd)	P value			
Interaction	1279	245	5.219	F (245, 600) = 1.075	P = 0.2457			
cell	362.6	49	7.401	F (49, 600) = 1.524	P = 0.0144			
Cell and matrix	1471	5	294.3	F (5, 600) = 60.59	P < 0.0001			
Residual	2914	600	4.857					
Number of missing values	0							
Compare column means (main column effect)								
Number of families	1							
Number of comparisons per family	15							
Alpha	0.05							
Tukey's multiple comparisons test	Mean Diff.	95% CI of diff.	Significant?	Summary				
MCF7 1mg/ml vs. MCF7 2mg/ml	0.1576	-0.5699 to 0.8851	No	ns				
MCF7 1mg/ml vs. MDA 1mg/ml	-1.104	-1.831 to -0.3764	Yes	***				
MCF7 1mg/ml vs. MDA 2mg/ml	-1.780	-2.508 to -1.053	Yes	****				
MCF7 1mg/ml vs. HT 1mg/ml	-3.353	-4.081 to -2.626	Yes	****				
MCF7 1mg/ml vs. HT 2mg/ml	-2.578	-3.305 to -1.850	Yes	****				
MCF7 2mg/ml vs. MDA 1mg/ml	-1.261	-1.989 to -0.5340	Yes	****				
MCF7 2mg/ml vs. MDA 2mg/ml	-1.938	-2.665 to -1.210	Yes	****				
MCF7 2mg/ml vs. HT 1mg/ml	-3.511	-4.239 to -2.784	Yes	****				
MCF7 2mg/ml vs. HT 2mg/ml	-2.735	-3.463 to -2.008	Yes	****				
MDA 1mg/ml vs. MDA 2mg/ml	-0.6762	-1.404 to 0.05130	No	ns				
MDA 1mg/ml vs. HT 1mg/ml	-2.250	-2.977 to -1.522	Yes	****				
Tukey's multiple comparisons test	Mean Diff.	95% CI of diff.	Significant?	Summary				
MDA 1mg/ml vs. HT 2mg/ml	-1.474	-2.201 to -0.7462	Yes	****				
MDA 2mg/ml vs. HT 1mg/ml	-1.573	-2.301 to -0.8458	Yes	****				
MDA 2mg/ml vs. HT 2mg/ml	-0.7975	-1.525 to -0.06992	Yes	*				
HT 1mg/ml vs. HT 2mg/ml	0.7759	0.04832 to 1.503	Yes	*				
Test details	Mean 1	Mean 2	Mean Diff.	SE of diff.	N1	N2	q	DF
MCF7 1mg/ml vs. MCF7 2mg/ml	1.996	1.839	0.1576	0.2545	150	150	0.8759	600
MCF7 1mg/ml vs. MDA 1mg/ml	1.996	3.100	-1.104	0.2545	150	150	6.135	600
MCF7 1mg/ml vs. MDA 2mg/ml	1.996	3.776	-1.780	0.2545	150	150	9.893	600
MCF7 1mg/ml vs. HT 1mg/ml	1.996	5.350	-3.353	0.2545	150	150	18.64	600
MCF7 1mg/ml vs. HT 2mg/ml	1.996	4.574	-2.578	0.2545	150	150	14.32	600

MCF7 2mg/ml vs. MDA 1mg/ml	1.839	3.100	-1.261	0.2545	150	150	7.011	600
MCF7 2mg/ml vs. MDA 2mg/ml	1.839	3.776	-1.938	0.2545	150	150	10.77	600
MCF7 2mg/ml vs. HT 1mg/ml	1.839	5.350	-3.511	0.2545	150	150	19.51	600
MCF7 2mg/ml vs. HT 2mg/ml	1.839	4.574	-2.735	0.2545	150	150	15.20	600
MDA 1mg/ml vs. MDA 2mg/ml	3.100	3.776	-0.6762	0.2545	150	150	3.758	600
MDA 1mg/ml vs. HT 1mg/ml	3.100	5.350	-2.250	0.2545	150	150	12.50	600
MDA 1mg/ml vs. HT 2mg/ml	3.100	4.574	-1.474	0.2545	150	150	8.190	600
MDA 2mg/ml vs. HT 1mg/ml	3.776	5.350	-1.573	0.2545	150	150	8.743	600
MDA 2mg/ml vs. HT 2mg/ml	3.776	4.574	-0.7975	0.2545	150	150	4.432	600
HT 1mg/ml vs. HT 2mg/ml	5.350	4.574	0.7759	0.2545	150	150	4.312	600

Speed

Table Analyzed	Speed All Summary Values				
Two-way ANOVA	Ordinary				
Alpha	0.05				
Source of Variation	% of total variation	P value	P value summary	Significant?	
Interaction	3.506	< 0.0001	****	Yes	
Cell and Matrix	56.88	< 0.0001	****	Yes	
Replicates	3.470	< 0.0001	****	Yes	
ANOVA table	SS	DF	MS	F (DFn, DFd)	P value
Interaction	1.274	10	0.1274	F (10, 1782) = 17.29	P < 0.0001
Cell and Matrix	20.66	5	4.133	F (5, 1782) = 560.9	P < 0.0001
Replicates	1.261	2	0.6303	F (2, 1782) = 85.55	P < 0.0001
Residual	13.13	1782	0.007368		
Number of missing values	0				
Compare row means (main row effect)					
Number of families	1				
Number of comparisons per family	15				
Alpha	0.05				
Tukey's multiple comparisons test	Mean Diff.	95% CI of diff.	Significant?	Summary	
MCF-7 1mg/ml vs. MCF-7 2mg/ml	0.02736	0.007371 to 0.04736	Yes	**	
MCF-7 1mg/ml vs. MDA-MB-231 1mg/ml	-0.1531	-0.1731 to -0.1331	Yes	****	
MCF-7 1mg/ml vs. MDA-MB-231 2mg/ml	-0.09373	-0.1137 to -0.07373	Yes	****	
MCF-7 1mg/ml vs. HT1080 1mg/ml	-0.2693	-0.2893 to -0.2493	Yes	****	
MCF-7 1mg/ml vs. HT1080 2mg/ml	-0.2134	-0.2334 to -0.1934	Yes	****	
MCF-7 2mg/ml vs. MDA-MB-231 1mg/ml	-0.1805	-0.2005 to -0.1605	Yes	****	
MCF-7 2mg/ml vs. MDA-MB-231 2mg/ml	-0.1211	-0.1411 to -0.1011	Yes	****	
MCF-7 2mg/ml vs. HT1080 1mg/ml	-0.2967	-0.3167 to -0.2767	Yes	****	
MCF-7 2mg/ml vs. HT1080 2mg/ml	-0.2408	-0.2608 to -0.2208	Yes	****	
MDA-MB-231 1mg/ml vs. MDA-MB-231 2mg/ml	0.0594	0.03941 to 0.07939	Yes	****	
MDA-MB-231 1mg/ml vs. HT1080 1mg/ml	-0.1162	-0.1362 to -0.09622	Yes	****	
Tukey's multiple comparisons test	Mean Diff.	95% CI of diff.	Significant?	Summary	

MDA-MB-231 1mg/ml vs. HT1080 2mg/ml	-0.06028	-0.08027 to -0.04029	Yes	****	
MDA-MB-231 2mg/ml vs. HT1080 1mg/ml	-0.1756	-0.1956 to -0.1556	Yes	****	
MDA-MB-231 2mg/ml vs. HT1080 2mg/ml	-0.1197	-0.1397 to -0.09969	Yes	****	
HT1080 1mg/ml vs. HT1080 2mg/ml	0.05593	0.03594 to 0.07593	Yes	****	
Test details	Mean 1	Mean 2	Mean Diff.	SE of diff.	N1
MCF-7 1mg/ml vs. MCF-7 2mg/ml	0.1113	0.08392	0.02736	0.007009	300
MCF-7 1mg/ml vs. MDA-MB-231 1mg/ml	0.1113	0.2644	-0.1531	0.007009	300
MCF-7 1mg/ml vs. MDA-MB-231 2mg/ml	0.1113	0.2050	-0.09373	0.007009	300
MCF-7 1mg/ml vs. HT1080 1mg/ml	0.1113	0.3806	-0.2693	0.007009	300
MCF-7 1mg/ml vs. HT1080 2mg/ml	0.1113	0.3247	-0.2134	0.007009	300
MCF-7 2mg/ml vs. MDA-MB-231 1mg/ml	0.08392	0.2644	-0.1805	0.007009	300
MCF-7 2mg/ml vs. MDA-MB-231 2mg/ml	0.08392	0.2050	-0.1211	0.007009	300
MCF-7 2mg/ml vs. HT1080 1mg/ml	0.08392	0.3806	-0.2967	0.007009	300
MCF-7 2mg/ml vs. HT1080 2mg/ml	0.08392	0.3247	-0.2408	0.007009	300
MDA-MB-231 1mg/ml vs. MDA-MB-231 2mg/ml	0.2644	0.2050	0.0594	0.007009	300
MDA-MB-231 1mg/ml vs. HT1080 1mg/ml	0.2644	0.3806	-0.1162	0.007009	300
MDA-MB-231 1mg/ml vs. HT1080 2mg/ml	0.2644	0.3247	-0.06028	0.007009	300
MDA-MB-231 2mg/ml vs. HT1080 1mg/ml	0.2050	0.3806	-0.1756	0.007009	300
MDA-MB-231 2mg/ml vs. HT1080 2mg/ml	0.2050	0.3247	-0.1197	0.007009	300
HT1080 1mg/ml vs. HT1080 2mg/ml	0.3806	0.3247	0.05593	0.007009	300

Distance to start

Table Analyzed	All D2S n1-3				
Two-way ANOVA	Ordinary				
Alpha	0.05				
Source of Variation	% of total variation	F value	P value summary	Significant?	
Interaction	17.48	0.5827	ns	No	

Cell	3.461	0.5551	ns	No	
Cell and Matrix	35.96	0.0001	****	Yes	
ANOVA table	SS	DF	MS	F (DFn, DFd)	P value
Interaction	1.286e+006	495	2598	F (495, 1200) = 0.9835	P = 0.5827
Cell	254595	99	2572	F (99, 1200) = 0.9736	P = 0.5551
Cell and Matrix	2.645e+006	5	528971	F (5, 1200) = 200.3	P < 0.0001
Residual	3.170e+006	1200	2641		
Number of missing values	0				
Number of comparisons per family	15				
Alpha	0.05				
Tukey's multiple comparisons test	Mean Diff.	95% CI of diff.	Significant?	Summary	
MCF7 1mg/ml vs. MCF7 2mg/ml	7.461	-4.517 to 19.44	No	ns	
MCF7 1mg/ml vs. MDA 1mg/ml	-67.66	-79.64 to -55.68	Yes	****	
MCF7 1mg/ml vs. MDA 2mg/ml	-35.96	-47.94 to -23.98	Yes	****	
MCF7 1mg/ml vs. HT 1mg/ml	-97.04	-109.0 to -85.06	Yes	****	
MCF7 1mg/ml vs. HT 2mg/ml	-72.19	-84.17 to -60.21	Yes	****	
MCF7 2mg/ml vs. MDA 1mg/ml	-75.12	-87.10 to -63.14	Yes	****	
MCF7 2mg/ml vs. MDA 2mg/ml	-43.42	-55.40 to -31.45	Yes	****	
MCF7 2mg/ml vs. HT 1mg/ml	-104.5	-116.5 to -92.52	Yes	****	
MCF7 2mg/ml vs. HT 2mg/ml	-79.65	-91.63 to -67.67	Yes	****	
MDA 1mg/ml vs. MDA 2mg/ml	31.70	19.72 to 43.67	Yes	****	
MDA 1mg/ml vs. HT 1mg/ml	-29.38	-41.36 to -17.40	Yes	****	
MDA 1mg/ml vs. HT 2mg/ml	-4.531	-16.51 to 7.446	No	ns	
MDA 2mg/ml vs. HT 1mg/ml	-61.08	-73.05 to -49.10	Yes	****	
MDA 2mg/ml vs. HT 2mg/ml	-36.23	-48.21 to -24.25	Yes	****	
HT 1mg/ml vs. HT 2mg/ml	24.85	12.87 to 36.83	Yes	****	

Test details	Mean 1	Mean 2	Mean Diff.	SE of diff.	N1	N2	q	DF
MCF7 1mg/ml vs. MCF7 2mg/ml	19.49	12.02	7.461	4.196	300	300	2.515	1200
MCF7 1mg/ml vs. MDA 1mg/ml	19.49	87.14	-67.66	4.196	300	300	22.80	1200
MCF7 1mg/ml vs. MDA 2mg/ml	19.49	55.45	-35.96	4.196	300	300	12.12	1200

MCF7 1mg/ml vs. HT 1mg/ml	19.49	116.5	-97.04	4.196	300	300	32.70	1200
MCF7 1mg/ml vs. HT 2mg/ml	19.49	91.68	-72.19	4.196	300	300	24.33	1200
MCF7 2mg/ml vs. MDA 1mg/ml	12.02	87.14	-75.12	4.196	300	300	25.32	1200
MCF7 2mg/ml vs. MDA 2mg/ml	12.02	55.45	-43.42	4.196	300	300	14.63	1200
MCF7 2mg/ml vs. HT 1mg/ml	12.02	116.5	-104.5	4.196	300	300	35.22	1200
MCF7 2mg/ml vs. HT 2mg/ml	12.02	91.68	-79.65	4.196	300	300	26.84	1200
MDA 1mg/ml vs. MDA 2mg/ml	87.14	55.45	31.70	4.196	300	300	10.68	1200
MDA 1mg/ml vs. HT 1mg/ml	87.14	116.5	-29.38	4.196	300	300	9.901	1200
MDA 1mg/ml vs. HT 2mg/ml	87.14	91.68	-4.531	4.196	300	300	1.527	1200
MDA 2mg/ml vs. HT 1mg/ml	55.45	116.5	-61.08	4.196	300	300	20.58	1200
MDA 2mg/ml vs. HT 2mg/ml	55.45	91.68	-36.23	4.196	300	300	12.21	1200
HT 1mg/ml vs. HT 2mg/ml	116.5	91.68	24.85	4.196	300	300	8.374	1200

B7. 3D collagen with fibronectin

Distance to start

Table Analyzed	D2S							
Two-way ANOVA	Ordinary							
Alpha	0.05							
Source of Variation	% of total variation	P value	P value summary	Significant?				
Interaction	19.69	0.9850	ns	No				
Row Factor	3.604	0.9045	ns	No				
Column Factor	9.889	< 0.0001	****	Yes				
ANOVA table	SS	DF	MS	F (DFn, DFd)	P value			
Interaction	670609	145	4625	F (145, 360) = 0.7317	P = 0.9850			
Row Factor	122738	29	4232	F (29, 360) = 0.6696	P = 0.9045			
Column Factor	336780	5	67356	F (5, 360) = 10.66	P < 0.0001			
Residual	2.275e+006	360	6320					
Number of missing values	0							
Compare column means (main column effect)								
Number of families	1							
Number of comparisons per family	15							
Alpha	0.05							
Tukey's multiple comparisons test	Mean Diff.	95% CI of diff.	Significant?	Summary				
Col 1mg vs. Col 1+5F	23.32	-10.64 to 57.27	No	ns				
Col 1mg vs. Col 1+10F	21.75	-12.21 to 55.70	No	ns				
Col 1mg vs. Col 2mg	66.74	32.79 to 100.7	Yes	****				
Col 1mg vs. Col 2+5F	59.96	26.00 to 93.91	Yes	****				
Col 1mg vs. Col 2+10F	60.66	26.70 to 94.61	Yes	****				
Col 1+5F vs. Col 1+10F	-1.567	-35.52 to 32.39	No	ns				
Col 1+5F vs. Col 2mg	43.43	9.470 to 77.38	Yes	**				
Col 1+5F vs. Col 2+5F	36.64	2.688 to 70.60	Yes	*				
Col 1+5F vs. Col 2+10F	37.34	3.384 to 71.29	Yes	*				
Col 1+10F vs. Col 2mg	44.99	11.04 to 78.95	Yes	**				
Col 1+10F vs. Col 2+5F	38.21	4.255 to 72.17	Yes	*				
Col 1+10F vs. Col 2+10F	38.91	4.951 to 72.86	Yes	*				
Col 2mg vs. Col 2+5F	-6.783	-40.74 to 27.17	No	ns				
Col 2mg vs. Col 2+10F	-6.086	-40.04 to 27.87	No	ns				
Col 2+5F vs. Col 2+10F	0.6963	-33.26 to 34.65	No	ns				
Test details	Mean 1	Mean 2	Mean Diff.	SE of diff.	N1	N2	q	DF
Col 1mg vs. Col 1+5F	128.4	105.1	23.32	11.85	90	90	2.782	360
Col 1mg vs. Col 1+10F	128.4	106.6	21.75	11.85	90	90	2.595	360
Col 1mg vs. Col 2mg	128.4	61.65	66.74	11.85	90	90	7.964	360
Col 1mg vs. Col 2+5F	128.4	68.43	59.96	11.85	90	90	7.155	360
Col 1mg vs. Col 2+10F	128.4	67.74	60.66	11.85	90	90	7.238	360
Col 1+5F vs. Col 1+10F	105.1	106.6	-1.567	11.85	90	90	0.1870	360
Col 1+5F vs. Col 2mg	105.1	61.65	43.43	11.85	90	90	5.182	360
Col 1+5F vs. Col 2+5F	105.1	68.43	36.64	11.85	90	90	4.373	360
Col 1+5F vs. Col 2+10F	105.1	67.74	37.34	11.85	90	90	4.456	360
Col 1+10F vs. Col 2mg	106.6	61.65	44.99	11.85	90	90	5.369	360
Col 1+10F vs. Col 2+5F	106.6	68.43	38.21	11.85	90	90	4.560	360
Col 1+10F vs. Col 2+10F	106.6	67.74	38.91	11.85	90	90	4.643	360
Col 2mg vs. Col 2+5F	61.65	68.43	-6.783	11.85	90	90	0.8094	360
Col 2mg vs. Col 2+10F	61.65	67.74	-6.086	11.85	90	90	0.7263	360
Col 2+5F vs. Col 2+10F	68.43	67.74	0.6963	11.85	90	90	0.08309	360

Speed

Table Analyzed		Speed							
Two-way ANOVA		Ordinary							
Alpha		0.05							
Source of Variation		% of total variation	P value	P value summary	Significant?				
Interaction		12.10	> 0.9999	ns	No				
Cell speed		1.445	> 0.9999	ns	No				
Matrix		19.62	< 0.0001	****	Yes				
ANOVA table		SS	DF	MS	F (DFn, DFd)		P value		
Interaction		2.044	145	0.01410	F (145, 360) = 0.4497		P > 0.9999		
Cell speed		0.2440	29	0.008412	F (29, 360) = 0.2684		P > 0.9999		
Matrix		3.313	5	0.6627	F (5, 360) = 21.14		P < 0.0001		
Residual		11.29	360	0.03135					
Number of missing values		0							
Number of comparisons per family		15							
Alpha		0.05							
Tukey's multiple comparisons test		Mean Diff.	95% CI of diff.	Significant?	Summary				
Col 1mg vs. Col 1+5F		0.07194	-0.003677 to 0.1476	No	ns				
Col 1mg vs. Col 1+10F		0.03256	-0.04306 to 0.1082	No	ns				
Col 1mg vs. Col 2mg		0.1973	0.1216 to 0.2729	Yes	****				
Col 1mg vs. Col 2+5F		0.1891	0.1135 to 0.2647	Yes	****				
Col 1mg vs. Col 2+10F		0.1683	0.09271 to 0.2439	Yes	****				
Col 1+5F vs. Col 1+10F		-0.03938	-0.1150 to 0.03624	No	ns				
Col 1+5F vs. Col 2mg		0.1253	0.04970 to 0.2009	Yes	****				
Col 1+5F vs. Col 2+5F		0.1171	0.04151 to 0.1928	Yes	***				
Col 1+5F vs. Col 2+10F		0.09638	0.02076 to 0.1720	Yes	**				
Col 1+10F vs. Col 2mg		0.1647	0.08908 to 0.2403	Yes	****				
Col 1+10F vs. Col 2+5F		0.1565	0.08090 to 0.2321	Yes	****				
Col 1+10F vs. Col 2+10F		0.1358	0.06015 to 0.2114	Yes	****				
Col 2mg vs. Col 2+5F		-0.008184	-0.08381 to 0.06744	No	ns				
Col 2mg vs. Col 2+10F		-0.02893	-0.1046 to 0.04669	No	ns				
Col 2+5F vs. Col 2+10F		-0.02075	-0.09637 to 0.05487	No	ns				
Test details		Mean 1	Mean 2	Mean Diff.	SE of diff.	N1	N2	q	DF
Col 1mg vs. Col 1+5F		0.3998	0.3278	0.07194	0.02639	90	90	3.855	360
Col 1mg vs. Col 1+10F		0.3998	0.3672	0.03256	0.02639	90	90	1.745	360
Col 1mg vs. Col 2mg		0.3998	0.2025	0.1973	0.02639	90	90	10.57	360
Col 1mg vs. Col 2+5F		0.3998	0.2107	0.1891	0.02639	90	90	10.13	360
Col 1mg vs. Col 2+10F		0.3998	0.2314	0.1683	0.02639	90	90	9.019	360
Col 1+5F vs. Col 1+10F		0.3278	0.3672	-0.03938	0.02639	90	90	2.110	360
Col 1+5F vs. Col 2mg		0.3278	0.2025	0.1253	0.02639	90	90	6.715	360
Col 1+5F vs. Col 2+5F		0.3278	0.2107	0.1171	0.02639	90	90	6.276	360
Col 1+5F vs. Col 2+10F		0.3278	0.2314	0.09638	0.02639	90	90	5.164	360
Col 1+10F vs. Col 2mg		0.3672	0.2025	0.1647	0.02639	90	90	8.825	360
Col 1+10F vs. Col 2+5F		0.3672	0.2107	0.1565	0.02639	90	90	8.386	360
Col 1+10F vs. Col 2+10F		0.3672	0.2314	0.1358	0.02639	90	90	7.275	360
Col 2mg vs. Col 2+5F		0.2025	0.2107	-0.008184	0.02639	90	90	0.4385	360
Col 2mg vs. Col 2+10F		0.2025	0.2314	-0.02893	0.02639	90	90	1.550	360
Col 2+5F vs. Col 2+10F		0.2107	0.2314	-0.02075	0.02639	90	90	1.112	360

Track length

Table Analyzed	Distance Travelled								
Tw o-way ANOVA	Ordinary								
Alpha	0.05								
Source of Variation	% of total variation		P value	P value summary	Significant?				
Interaction	12.10		> 0.9999	ns	No				
Cell track	1.445		> 0.9999	ns	No				
Matrix	19.62		< 0.0001	****	Yes				
ANOVA table	SS		DF	MS	F (DFn, DFd)				P value
Interaction	2.993e+006		145	20640	F (145, 360) = 0.4497				P > 0.9999
Cell track	357183		29	12317	F (29, 360) = 0.2684				P > 0.9999
Matrix	4.851e+006		5	970212	F (5, 360) = 21.14				P < 0.0001
Residual	1.652e+007		360	45896					
Number of missing values	0								
Compare column means (main column effect)									
Number of families	1								
Number of comparisons per family	15								
Alpha	0.05								
Tukey's multiple comparisons test	Mean Diff.	95% CI of diff.	Significant?	Summary					
Col 1mg vs. Col 1+5F	87.05	-4.450 to 178.6	No	ns					
Col 1mg vs. Col 1+10F	39.40	-52.10 to 130.9	No	ns					
Col 1mg vs. Col 2mg	238.7	147.2 to 330.2	Yes	****					
Col 1mg vs. Col 2+5F	228.8	137.3 to 320.3	Yes	****					
Col 1mg vs. Col 2+10F	203.7	112.2 to 295.2	Yes	****					
Col 1+5F vs. Col 1+10F	-47.65	-139.2 to 43.85	No	ns					
Col 1+5F vs. Col 2mg	151.6	60.13 to 243.1	Yes	****					
Col 1+5F vs. Col 2+5F	141.7	50.23 to 233.2	Yes	***					
Col 1+5F vs. Col 2+10F	116.6	25.12 to 208.1	Yes	**					
Col 1+10F vs. Col 2mg	199.3	107.8 to 290.8	Yes	****					
Col 1+10F vs. Col 2+5F	189.4	97.88 to 280.9	Yes	****					
Col 1+10F vs. Col 2+10F	164.3	72.78 to 255.8	Yes	****					
Col 2mg vs. Col 2+5F	-9.903	-101.4 to 81.60	No	ns					
Col 2mg vs. Col 2+10F	-35.01	-126.5 to 56.49	No	ns					
Col 2+5F vs. Col 2+10F	-25.10	-116.6 to 66.40	No	ns					
Test details	Mean 1	Mean 2	Mean Diff.	SE of diff.	N1	N2	q	DF	
Col 1mg vs. Col 1+5F	483.7	396.7	87.05	31.94	90	90	3.855	360	
Col 1mg vs. Col 1+10F	483.7	444.3	39.40	31.94	90	90	1.745	360	
Col 1mg vs. Col 2mg	483.7	245.0	238.7	31.94	90	90	10.57	360	
Col 1mg vs. Col 2+5F	483.7	254.9	228.8	31.94	90	90	10.13	360	
Col 1mg vs. Col 2+10F	483.7	280.0	203.7	31.94	90	90	9.019	360	
Col 1+5F vs. Col 1+10F	396.7	444.3	-47.65	31.94	90	90	2.110	360	
Col 1+5F vs. Col 2mg	396.7	245.0	151.6	31.94	90	90	6.715	360	
Col 1+5F vs. Col 2+5F	396.7	254.9	141.7	31.94	90	90	6.276	360	
Col 1+5F vs. Col 2+10F	396.7	280.0	116.6	31.94	90	90	5.164	360	
Col 1+10F vs. Col 2mg	444.3	245.0	199.3	31.94	90	90	8.825	360	
Col 1+10F vs. Col 2+5F	444.3	254.9	189.4	31.94	90	90	8.386	360	
Col 1+10F vs. Col 2+10F	444.3	280.0	164.3	31.94	90	90	7.275	360	
Col 2mg vs. Col 2+5F	245.0	254.9	-9.903	31.94	90	90	0.4385	360	
Col 2mg vs. Col 2+10F	245.0	280.0	-35.01	31.94	90	90	1.550	360	
Col 2+5F vs. Col 2+10F	254.9	280.0	-25.10	31.94	90	90	1.112	360	

Aspect ratio

Table Analyzed	Aspect Ratio				
Tw o-way ANOVA	Ordinary				

Alpha	0.05								
Source of Variation	% of total variation	P value	P value summary	Significant?					
Interaction	25.56	0.6356	ns	No					
Cell	5.873	0.3440	ns	No					
Matrix	1.778	0.0908	ns	No					
ANOVA table	SS	DF	MS	F (DFn, DFd)	F value				
Interaction	824.1	145	5.683	F (145, 360) = 0.9501	P = 0.6356				
Cell	189.4	29	6.530	F (29, 360) = 1.092	P = 0.3440				
Matrix	57.33	5	11.47	F (5, 360) = 1.917	P = 0.0908				
Residual	2154	360	5.982						
Number of missing values	0								
Compare column means (main column effect)									
Number of families	1								
Number of comparisons per family	15								
Alpha	0.05								
Tukey's multiple comparisons test	Mean Diff.	95% CI of diff.	Significant?	Summary					
Col 1mg vs. Col 1+5F	0.4965	-0.5482 to 1.541	No	ns					
Col 1mg vs. Col 1+10F	-0.2691	-1.314 to 0.7755	No	ns					
Col 1mg vs. Col 2mg	0.6132	-0.4314 to 1.658	No	ns					
Col 1mg vs. Col 2+5F	0.5944	-0.4502 to 1.639	No	ns					
Col 1mg vs. Col 2+10F	0.2620	-0.7826 to 1.307	No	ns					
Col 1+5F vs. Col 1+10F	-0.7656	-1.810 to 0.2791	No	ns					
Col 1+5F vs. Col 2mg	0.1168	-0.9279 to 1.161	No	ns					
Col 1+5F vs. Col 2+5F	0.09798	-0.9467 to 1.143	No	ns					
Col 1+5F vs. Col 2+10F	-0.2344	-1.279 to 0.8102	No	ns					
Col 1+10F vs. Col 2mg	0.8824	-0.1623 to 1.927	No	ns					
Col 1+10F vs. Col 2+5F	0.8636	-0.1811 to 1.908	No	ns					
Col 1+10F vs. Col 2+10F	0.5311	-0.5135 to 1.576	No	ns					
Col 2mg vs. Col 2+5F	-0.01880	-1.063 to 1.026	No	ns					
Col 2mg vs. Col 2+10F	-0.3512	-1.396 to 0.6934	No	ns					
Col 2+5F vs. Col 2+10F	-0.3324	-1.377 to 0.7122	No	ns					
Test details	Mean 1	Mean 2	Mean Diff.	SE of diff.	N1	N2	q	DF	
Col 1mg vs. Col 1+5F	4.239	3.743	0.4965	0.3646	90	90	1.926	360	
Col 1mg vs. Col 1+10F	4.239	4.508	-0.2691	0.3646	90	90	1.044	360	
Col 1mg vs. Col 2mg	4.239	3.626	0.6132	0.3646	90	90	2.379	360	
Col 1mg vs. Col 2+5F	4.239	3.645	0.5944	0.3646	90	90	2.306	360	
Col 1mg vs. Col 2+10F	4.239	3.977	0.2620	0.3646	90	90	1.016	360	
Col 1+5F vs. Col 1+10F	3.743	4.508	-0.7656	0.3646	90	90	2.969	360	
Col 1+5F vs. Col 2mg	3.743	3.626	0.1168	0.3646	90	90	0.4529	360	
Col 1+5F vs. Col 2+5F	3.743	3.645	0.09798	0.3646	90	90	0.3800	360	
Col 1+5F vs. Col 2+10F	3.743	3.977	-0.2344	0.3646	90	90	0.9093	360	
Col 1+10F vs. Col 2mg	4.508	3.626	0.8824	0.3646	90	90	3.422	360	
Col 1+10F vs. Col 2+5F	4.508	3.645	0.8636	0.3646	90	90	3.349	360	
Col 1+10F vs. Col 2+10F	4.508	3.977	0.5311	0.3646	90	90	2.060	360	
Col 2mg vs. Col 2+5F	3.626	3.645	-0.01880	0.3646	90	90	0.07292	360	
Col 2mg vs. Col 2+10F	3.626	3.977	-0.3512	0.3646	90	90	1.362	360	
Col 2+5F vs. Col 2+10F	3.645	3.977	-0.3324	0.3646	90	90	1.289	360	

Cell length

Table Analyzed	Cell Length				
Two-way ANOVA	Ordinary				
Alpha	0.05				
Source of Variation	% of total variation	P value	P value summary	Significant?	
Interaction	24.46	0.7560	ns	No	

Cells	7.526	0.0894	ns	No				
Matrix	0.9044	0.4359	ns	No				
ANOVA table	SS	DF	MS	F (DFn, DFd)	P value			
Interaction	79009	145	544.9	F (145, 360) = 0.9048	P = 0.7560			
Cells	24312	29	838.4	F (29, 360) = 1.392	P = 0.0894			
Matrix	2922	5	584.3	F (5, 360) = 0.9702	P = 0.4359			
Residual	216803	360	602.2					
Number of missing values	0							
Compare column means (main column effect)								
Number of families	1							
Number of comparisons per family	15							
Alpha	0.05							
Tukeys multiple comparisons test	Mean Diff.	95% CI of diff.	Significant?	Summary				
Col 1mg vs. Col 1+5F	3.567	-6.915 to 14.05	No	ns				
Col 1mg vs. Col 1+10F	7.422	-3.059 to 17.90	No	ns				
Col 1mg vs. Col 2mg	2.856	-7.626 to 13.34	No	ns				
Col 1mg vs. Col 2+5F	4.844	-5.637 to 15.33	No	ns				
Col 1mg vs. Col 2+10F	1.878	-8.604 to 12.36	No	ns				
Col 1+5F vs. Col 1+10F	3.856	-6.626 to 14.34	No	ns				
Col 1+5F vs. Col 2mg	-0.7111	-11.19 to 9.770	No	ns				
Col 1+5F vs. Col 2+5F	1.278	-9.204 to 11.76	No	ns				
Col 1+5F vs. Col 2+10F	-1.689	-12.17 to 8.793	No	ns				
Col 1+10F vs. Col 2mg	-4.567	-15.05 to 5.915	No	ns				
Col 1+10F vs. Col 2+5F	-2.578	-13.06 to 7.904	No	ns				
Col 1+10F vs. Col 2+10F	-5.544	-16.03 to 4.937	No	ns				
Col 2mg vs. Col 2+5F	1.989	-8.493 to 12.47	No	ns				
Col 2mg vs. Col 2+10F	-0.9778	-11.46 to 9.504	No	ns				
Col 2+5F vs. Col 2+10F	-2.967	-13.45 to 7.515	No	ns				
Test details	Mean 1	Mean 2	Mean Diff.	SE of diff.	N1	N2	q	DF
Col 1mg vs. Col 1+5F	59.89	56.32	3.567	3.658	90	90	1.379	360
Col 1mg vs. Col 1+10F	59.89	52.47	7.422	3.658	90	90	2.869	360
Col 1mg vs. Col 2mg	59.89	57.03	2.856	3.658	90	90	1.104	360
Col 1mg vs. Col 2+5F	59.89	55.04	4.844	3.658	90	90	1.873	360
Col 1mg vs. Col 2+10F	59.89	58.01	1.878	3.658	90	90	0.7259	360
Col 1+5F vs. Col 1+10F	56.32	52.47	3.856	3.658	90	90	1.490	360
Test details	Mean 1	Mean 2	Mean Diff.	SE of diff.	N1	N2	q	DF
Col 1+5F vs. Col 2mg	56.32	57.03	-0.7111	3.658	90	90	0.2749	360
Col 1+5F vs. Col 2+5F	56.32	55.04	1.278	3.658	90	90	0.4940	360
Col 1+5F vs. Col 2+10F	56.32	58.01	-1.689	3.658	90	90	0.6529	360
Col 1+10F vs. Col 2mg	52.47	57.03	-4.567	3.658	90	90	1.765	360
Col 1+10F vs. Col 2+5F	52.47	55.04	-2.578	3.658	90	90	0.9965	360
Col 1+10F vs. Col 2+10F	52.47	58.01	-5.544	3.658	90	90	2.143	360
Col 2mg vs. Col 2+5F	57.03	55.04	1.989	3.658	90	90	0.7689	360
Col 2mg vs. Col 2+10F	57.03	58.01	-0.9778	3.658	90	90	0.3780	360
Col 2+5F vs. Col 2+10F	55.04	58.01	-2.967	3.658	90	90	1.147	360

HT1080 aspect ratio

Table Analyzed		Aspect Ratio HT1080 n1			
Kruskal-Wallis test					
P value		0.1732			
Exact or approximate P value?		Approximate			
P value summary		ns			
Do the medians vary signif. (P < 0.05)		No			
Number of groups		6			
Kruskal-Wallis statistic		7.707			
Data summary					
Number of treatments (columns)		6			
Number of values (total)		180			
Number of families	1				
Number of comparisons per family	15				
Alpha	0.05				
Dunn's multiple comparisons test	Mean rank diff.	Significant?	Summary		
Col 1mg vs. Col 1+5F	10.48	No	ns		A-B
Col 1mg vs. Col1+10F	-7.183	No	ns		A-C
Col 1mg vs. Col 2mg	27.25	No	ns		A-D
Col 1mg vs. Col 2+5F	7.500	No	ns		A-E
Col 1mg vs. Col2+10F	1.950	No	ns		A-F
Col 1+5F vs. Col1+10F	-17.67	No	ns		B-C
Col 1+5F vs. Col 2mg	16.77	No	ns		B-D
Col 1+5F vs. Col 2+5F	-2.983	No	ns		B-E
Col 1+5F vs. Col2+10F	-8.533	No	ns		B-F
Col1+10F vs. Col 2mg	34.43	No	ns		C-D
Col1+10F vs. Col 2+5F	14.68	No	ns		C-E
Col1+10F vs. Col2+10F	9.133	No	ns		C-F
Col 2mg vs. Col 2+5F	-19.75	No	ns		D-E
Col 2mg vs. Col2+10F	-25.30	No	ns		D-F
Col 2+5F vs. Col2+10F	-5.550	No	ns		E-F
Test details	Mean rank 1	Mean rank 2	Mean rank diff.	n1	n2
Col 1mg vs. Col 1+5F	97.17	86.68	10.48	30	30
Col 1mg vs. Col1+10F	97.17	104.4	-7.183	30	30
Col 1mg vs. Col 2mg	97.17	69.92	27.25	30	30
Col 1mg vs. Col 2+5F	97.17	89.67	7.500	30	30
Col 1mg vs. Col2+10F	97.17	95.22	1.950	30	30
Col 1+5F vs. Col1+10F	86.68	104.4	-17.67	30	30
Col 1+5F vs. Col 2mg	86.68	69.92	16.77	30	30
Col 1+5F vs. Col 2+5F	86.68	89.67	-2.983	30	30
Col 1+5F vs. Col2+10F	86.68	95.22	-8.533	30	30
Col1+10F vs. Col 2mg	104.4	69.92	34.43	30	30
Col1+10F vs. Col 2+5F	104.4	89.67	14.68	30	30
Col1+10F vs. Col2+10F	104.4	95.22	9.133	30	30
Col 2mg vs. Col 2+5F	69.92	89.67	-19.75	30	30
Col 2mg vs. Col2+10F	69.92	95.22	-25.30	30	30
Col 2+5F vs. Col2+10F	89.67	95.22	-5.550	30	30

HT1080 cell length

Table Analyzed		Cell Length HT1080 n1			
Kruskal-Wallis test					
P value		< 0.0001			
Exact or approximate P value?		Approximate			
P value summary		****			
Do the medians vary signif. (P < 0.05)		Yes			
Number of groups		6			
Kruskal-Wallis statistic		32.68			
Data summary					
Number of treatments (columns)		6			
Number of values (total)		180			
Number of families	1				
Number of comparisons per family	15				
Alpha	0.05				
Dunn's multiple comparisons test	Mean rank diff.	Significant?	Summary		
Col 1mg vs. Col 1+5F	33.57	No	ns		A-B
Col 1mg vs. Col1+10F	0.4833	No	ns		A-C
Col 1mg vs. Col 2mg	63.95	Yes	****		A-D
Col 1mg vs. Col 2+5F	37.75	No	ns		A-E
Col 1mg vs. Col2+10F	26.25	No	ns		A-F
Col 1+5F vs. Col1+10F	-33.08	No	ns		B-C
Col 1+5F vs. Col 2mg	30.38	No	ns		B-D
Col 1+5F vs. Col 2+5F	4.183	No	ns		B-E
Col 1+5F vs. Col2+10F	-7.317	No	ns		B-F
Col1+10F vs. Col 2mg	63.47	Yes	****		C-D
Col1+10F vs. Col 2+5F	37.27	No	ns		C-E
Col1+10F vs. Col2+10F	25.77	No	ns		C-F
Col 2mg vs. Col 2+5F	-26.20	No	ns		D-E
Col 2mg vs. Col2+10F	-37.70	No	ns		D-F
Col 2+5F vs. Col2+10F	-11.50	No	ns		E-F
Test details	Mean rank 1	Mean rank 2	Mean rank diff.	n1	n2
Col 1mg vs. Col 1+5F	117.5	83.93	33.57	30	30
Col 1mg vs. Col1+10F	117.5	117.0	0.4833	30	30
Col 1mg vs. Col 2mg	117.5	53.55	63.95	30	30
Col 1mg vs. Col 2+5F	117.5	79.75	37.75	30	30
Col 1mg vs. Col2+10F	117.5	91.25	26.25	30	30
Col 1+5F vs. Col1+10F	83.93	117.0	-33.08	30	30
Col 1+5F vs. Col 2mg	83.93	53.55	30.38	30	30
Col 1+5F vs. Col 2+5F	83.93	79.75	4.183	30	30
Col 1+5F vs. Col2+10F	83.93	91.25	-7.317	30	30
Col1+10F vs. Col 2mg	117.0	53.55	63.47	30	30
Col1+10F vs. Col 2+5F	117.0	79.75	37.27	30	30
Col1+10F vs. Col2+10F	117.0	91.25	25.77	30	30
Col 2mg vs. Col 2+5F	53.55	79.75	-26.20	30	30
Col 2mg vs. Col2+10F	53.55	91.25	-37.70	30	30
Col 2+5F vs. Col2+10F	79.75	91.25	-11.50	30	30

HT1080 distance to start

Table Analyzed		d2S HT1080 n1
Kruskal-Wallis test		
P value		0.0002

Exact or approximate P value?	Approximate				
P value summary	***				
Do the medians vary signif. (P < 0.05)	Yes				
Number of groups	6				
Kruskal-Wallis statistic	24.67				
Data summary					
Number of treatments (columns)	6				
Number of values (total)	180				
Number of families	1				
Number of comparisons per family	3				
Alpha	0.05				
Dunn's multiple comparisons test	Mean rank diff.	Significant?	Summary		
Col 1mg vs. Col 2mg	40.93	Yes	**		A-D
Col 1+5F vs. Col 2+5F	43.15	Yes	**		B-E
Col1+10F vs. Col2+10F	27.25	No	ns		C-F
Test details	Mean rank 1	Mean rank 2	Mean rank diff.	n1	n2
Col 1mg vs. Col 2mg	106.1	65.13	40.93	30	30
Col 1+5F vs. Col 2+5F	112.2	69.08	43.15	30	30
Col1+10F vs. Col2+10F	108.9	81.62	27.25	30	30

HT1080 speed

Table Analyzed		Speed HT1080 n1			
Kruskal-Wallis test					
P value		< 0.0001			
Exact or approximate P value?		Approximate			
P value summary		****			
Do the medians vary signif. (P < 0.05)		Yes			
Number of groups		6			
Kruskal-Wallis statistic		53.67			
Data summary					
Number of treatments (columns)		6			
Number of values (total)		180			
Number of families		1			
Number of comparisons per family		7			
Alpha		0.05			
Dunn's multiple comparisons test	Mean rank diff.	Significant?	Summary		
Col 1mg vs. Col 2mg	46.17	Yes	**		A-D
Col 1mg vs. Col 1+5F	0.4333	No	ns		A-B
Col 1+5F vs. Col1+10F	-11.17	No	ns		B-C
Col 1+5F vs. Col 2+5F	63.73	Yes	****		B-E
Col1+10F vs. Col2+10F	55.10	Yes	***		C-F
Col 2mg vs. Col 2+5F	18.00	No	ns		D-E
Col 2+5F vs. Col2+10F	-19.80	No	ns		E-F
Test details	Mean rank 1	Mean rank 2	Mean rank diff.	n1	n2
Col 1mg vs. Col 2mg	114.6	68.40	46.17	30	30
Col 1mg vs. Col 1+5F	114.6	114.1	0.4333	30	30
Col 1+5F vs. Col1+10F	114.1	125.3	-11.17	30	30
Col 1+5F vs. Col 2+5F	114.1	50.40	63.73	30	30
Col1+10F vs. Col2+10F	125.3	70.20	55.10	30	30
Col 2mg vs. Col 2+5F	68.40	50.40	18.00	30	30
Col 2+5F vs. Col2+10F	50.40	70.20	-19.80	30	30

Distance from start comparison between HT1080 and MDA-MB-231

Table Analyzed	D2S comparison				
Kruskal-Wallis test					
P value	< 0.0001				
Exact or approximate P value?	Approximate				
P value summary	****				
Do the medians vary signif. (P < 0.05)	Yes				
Number of groups	12				
Kruskal-Wallis statistic	113.5				
Data summary					
Number of treatments (columns)	12				
Number of values (total)	720				
Number of families	1				
Number of comparisons per family	3				
Alpha	0.05				
Dunn's multiple comparisons test	Mean rank diff.	Significant?	Summary		
MDA Col 1mg vs. HT Col 1mg	169.8	Yes	***		A-B
MDA Col1+5F vs. HT Col 1+5F	80.93	No	ns		C-D
MDA Col1+10F vs. HT Col1+5F	59.69	No	ns		E-F
Test details	Mean rank 1	Mean rank 2	Mean rank diff.	n1	n2
MDA Col 1mg vs. HT Col 1mg	495.6	325.7	169.8	90	30
MDA Col1+5F vs. HT Col 1+5F	431.3	350.4	80.93	90	30
MDA Col1+10F vs. HT Col1+5F	419.9	360.2	59.69	90	30

HT1080 and MDA-MB-231 cells: control group v n1-3 cells on collagen

Table Analyzed	D2S Comparison HT and MDA				
Kruskal-Wallis test					
P value	0.0149				
Exact or approximate P value?	Approximate				
P value summary	*				
Do the medians vary signif. (P < 0.05)	Yes				
Number of groups	4				
Kruskal-Wallis statistic	10.48				
Data summary					
Number of treatments (columns)	4				
Number of values (total)	225				
Number of families	1				
Number of comparisons per family	2				
Alpha	0.05				
Dunn's multiple comparisons test	Mean rank diff.	Significant?	Summary		
HT Control vs. HT N1-3	2.650	No	ns		A-B
MDA Control vs. MDA N1-3	21.60	No	ns		C-D
Test details	Mean rank 1	Mean rank 2	Mean rank diff.	n1	n2
HT Control vs. HT N1-3	103.5	100.8	2.650	30	90
MDA Control vs. MDA N1-3	141.6	120.0	21.60	30	75

B8. 2D/3D assay

MDA-MB-231 n1-3 - speed

Table Analyzed	MDA 3 cols						
Two-way ANOVA	Ordinary						
Alpha	0.05						
Source of Variation	% of total variation	P value	P value summary	Significant?			
Interaction	7.545	0.9719	ns	No			
Cell speed	5.295	0.7765	ns	No			
Location	30.10	0.0001	< ****	Yes			
ANOVA table	SS	DF	MS	F (DFn, DFd)	P value		
Interaction	0.5194	18	0.02886	F (18, 60) = 0.4408	P = 0.9719		
Cell speed	0.3645	9	0.04050	F (9, 60) = 0.6186	P = 0.7765		
Location	2.072	2	1.036	F (2, 60) = 15.82	P < 0.0001		
Residual	3.928	60	0.06547				
Number of missing values	0						
Compare column means (main column effect)							
Number of families	1						
Number of comparisons per family	3						
Alpha	0.05						
Tukey's multiple comparisons test	Mean Diff.	95% CI of diff.	Significant?	Summary			
2D vs. Border	-0.1253	-0.2841 to 0.03348	No	ns			
2D vs. 3D	0.2404	0.08159 to 0.3991	Yes	**			
Border vs. 3D	0.3657	0.2069 to 0.5244	Yes	****			
Test details	Mean 1	Mean 2	Mean Diff.	SE of diff.	N1	N2	q DF
2D vs. Border	0.5254	0.6507	-0.1253	0.06607	30	30	2.682 60
2D vs. 3D	0.5254	0.2851	0.2404	0.06607	30	30	5.145 60
Border vs. 3D	0.6507	0.2851	0.3657	0.06607	30	30	7.827 60

HT1080 2D/3D assay - speed

Table Analyzed	HT 3 cols								
Two-way ANOVA	Ordinary								
Alpha	0.05								
Source of Variation	% of total variation	P value	P value summary	Significant?					
Interaction	10.13	0.7284	ns	No					
Cell speed	7.060	0.3984	ns	No					
Location	38.80	< 0.0001	****	Yes					
ANOVA table	SS	DF	MS	F (DFn, DFd)	P value				
Interaction	0.2651	18	0.01473	F (18, 60) = 0.7668	P = 0.7284				
Cell speed	0.1848	9	0.02054	F (9, 60) = 1.069	P = 0.3984				
Location	1.016	2	0.5078	F (2, 60) = 26.44	P < 0.0001				
Residual	1.152	60	0.01921						
Number of missing values	0								
Compare column means (main column effect)									
Number of families		1							
Number of comparisons per family		3							
Alpha		0.05							
Tukey's multiple comparisons test		Mean Diff.	95% CI of diff.	Significant?	Summary				
2D vs. Border		-0.1380	-0.2240 to -0.05202	Yes	***				
2D vs. 3D		0.1220	0.03605 to 0.2080	Yes	**				
Border vs. 3D		0.2600	0.1741 to 0.3460	Yes	****				
Test details		Mean 1	Mean 2	Mean Diff.	SE of diff.	N1	N2	q	DF
2D vs. Border		0.2547	0.3927	-0.1380	0.03578	30	30	5.455	60
2D vs. 3D		0.2547	0.1326	0.1220	0.03578	30	30	4.823	60
Border vs. 3D		0.3927	0.1326	0.2600	0.03578	30	30	10.28	60

Appendix C

MCF7 and GFP clones comparison

Table Analyzed	Aspect Ratio MCF7							
Two-way ANOVA	Ordinary							
Alpha	0.05							
Source of Variation	% of total variation	P value	P value summary	Significant?				
Interaction	23.39	0.4540	ns	No				
Cells	6.517	0.5705	ns	No				
Cell Type	2.144	0.4752	ns	No				
ANOVA table	SS	DF	MS	F (DFn, DFd)		P value		
Interaction	15.38	27	0.5695	F (27, 80) = 1.020		P = 0.4540		
Cells	4.284	9	0.4760	F (9, 80) = 0.8527		P = 0.5705		
Cell Type	1.409	3	0.4697	F (3, 80) = 0.8415		P = 0.4752		
Residual	44.66	80	0.5582					
Number of missing values	0							
Compare column means (main column effect)								
Number of families	1							
Number of comparisons per family	6							
Alpha	0.05							
Tukey's multiple comparisons test	Mean Diff.	95% CI of diff.	Significant?	Summary				
MCF7 3D vs. DPF5	1.661	-10.19 to 13.51	No	ns				
MCF7 3D vs. D6F2	4.968	-6.881 to 16.82	No	ns				
MCF7 3D vs. D1B6	-1.681	-13.53 to 10.17	No	ns				
DPF5 vs. D6F2	3.306	-8.543 to 15.16	No	ns				
DPF5 vs. D1B6	-3.342	-15.19 to 8.506	No	ns				
D6F2 vs. D1B6	-6.649	-18.50 to 5.200	No	ns				
Test details	Mean 1	Mean 2	Mean Diff.	SE of diff.	N1	N2	q	DF
MCF7 3D vs. DPF5	23.79	22.13	1.661	4.516	30	30	0.5203	80
MCF7 3D vs. D6F2	23.79	18.82	4.968	4.516	30	30	1.556	80
MCF7 3D vs. D1B6	23.79	25.47	-1.681	4.516	30	30	0.5265	80
DPF5 vs. D6F2	22.13	18.82	3.306	4.516	30	30	1.035	80
DPF5 vs. D1B6	22.13	25.47	-3.342	4.516	30	30	1.047	80
D6F2 vs. D1B6	18.82	25.47	-6.649	4.516	30	30	2.082	80

Table Analyzed	Distance from Start MCF7								
Two-way ANOVA	Ordinary								
Alpha	0.05								
Source of Variation	% of total variation	P value	P value summary		Significant?				
Interaction	24.69	0.3198	ns		No				
Cells	9.195	0.2646	ns		No				
Cell TYpe	1.901	0.5034	ns		No				
ANOVA table	SS	DF	MS	F (DFn, DFd)	P value				
Interaction	9408	27	348.5	F (27, 80) = 1.139	P = 0.3198				
Cells	3504	9	389.3	F (9, 80) = 1.273	P = 0.2646				
Cell TYpe	724.3	3	241.4	F (3, 80) = 0.7893	P = 0.5034				
Residual	24471	80	305.9						
Number of missing values	0								
Compare column means (main column effect)									
Number of families	1								
Number of comparisons per family	6								
Alpha	0.05								
Tukey's multiple comparisons test	Mean Diff.	95% CI of diff.	Significant?	Summary					
MCF7 3D vs. DPF5	1.661	-10.19 to 13.51	No	ns					
MCF7 3D vs. D6F2	4.968	-6.881 to 16.82	No	ns					
MCF7 3D vs. D1B6	-1.681	-13.53 to 10.17	No	ns					
DPF5 vs. D6F2	3.306	-8.543 to 15.16	No	ns					
DPF5 vs. D1B6	-3.342	-15.19 to 8.506	No	ns					
D6F2 vs. D1B6	-6.649	-18.50 to 5.200	No	ns					
Test details	Mean 1	Mean 2	Mean Diff.	SE of diff.	N1	N2	q	DF	
MCF7 3D vs. DPF5	23.79	22.13	1.661	4.516	30	30	0.5203	80	
MCF7 3D vs. D6F2	23.79	18.82	4.968	4.516	30	30	1.556	80	
MCF7 3D vs. D1B6	23.79	25.47	-1.681	4.516	30	30	0.5265	80	
DPF5 vs. D6F2	22.13	18.82	3.306	4.516	30	30	1.035	80	
DPF5 vs. D1B6	22.13	25.47	-3.342	4.516	30	30	1.047	80	
D6F2 vs. D1B6	18.82	25.47	-6.649	4.516	30	30	2.082	80	

MDA-MB-231 v GFP+ clones

Table Analyzed	Aspect Ratio MDA							
Two-way ANOVA	Ordinary							
Alpha	0.05							
Source of Variation	% of total variation	P value	P value summary	Significant?				
Interaction	17.14	0.7805	ns	No				
Row Factor	9.563	0.2602	ns	No				
Column Factor	6.939	0.0459	*	Yes				
ANOVA table	SS	DF	MS	F (DFn, DFd)	P value			
Interaction	94.00	27	3.482	F (27, 80) = 0.7653	P = 0.7805			
Row Factor	52.45	9	5.827	F (9, 80) = 1.281	P = 0.2602			
Column Factor	38.06	3	12.69	F (3, 80) = 2.789	P = 0.0459			
Residual	363.9	80	4.549					
Number of missing values	0							
Compare column means (main column effect)								
Number of families	1							
Number of comparisons per family	6							
Alpha	0.05							
Tukey's multiple comparisons test	Mean Diff.	95% CI of diff.	Significant?	Summary				
MDA vs. XB5	-1.465	-2.910 to -0.02042	Yes	*				
MDA vs. YA1	-1.213	-2.658 to 0.2318	No	ns				
MDA vs. ZB2	-1.126	-2.571 to 0.3185	No	ns				
XB5 vs. YA1	0.2522	-1.193 to 1.697	No	ns				
XB5 vs. ZB2	0.3389	-1.106 to 1.784	No	ns				
YA1 vs. ZB2	0.08669	-1.358 to 1.532	No	ns				
Test details	Mean 1	Mean 2	Mean Diff.	SE of diff.	N1	N2	q	DF
MDA vs. XB5	2.293	3.758	-1.465	0.5507	30	30	3.763	80
MDA vs. YA1	2.293	3.506	-1.213	0.5507	30	30	3.115	80
MDA vs. ZB2	2.293	3.420	-1.126	0.5507	30	30	2.893	80
XB5 vs. YA1	3.758	3.506	0.2522	0.5507	30	30	0.6477	80
XB5 vs. ZB2	3.758	3.420	0.3389	0.5507	30	30	0.8703	80
YA1 vs. ZB2	3.506	3.420	0.08669	0.5507	30	30	0.2226	80

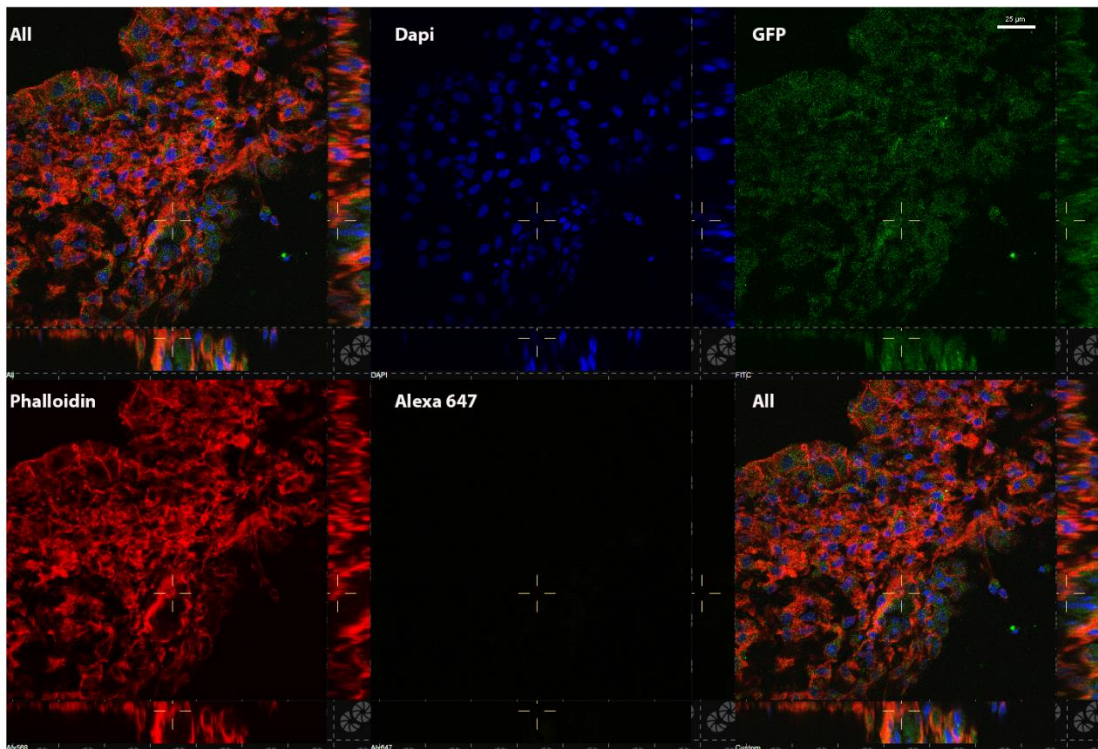
Table Analyzed	Distance from Start MDA							
Two-way ANOVA	Ordinary							
Alpha	0.05							
Source of Variation	% of total variation	P value	P value summary	Significant?				
Interaction	24.07	0.3951	ns	No				
Cell distance	2.003	0.9817	ns	No				
Cell TType	7.245	0.0402	*	Yes				
ANOVA table	SS	DF	MS	F (DFn, DFd)		P value		
Interaction	138680	27	5136	F (27, 80) = 1.070		P = 0.3951		
Cell distance	11537	9	1282	F (9, 80) = 0.2670		P = 0.9817		
Cell TType	41736	3	13912	F (3, 80) = 2.897		P = 0.0402		
Residual	384141	80	4802					
Number of missing values	0							
Compare column means (main column effect)								
Number of families	1							
Number of comparisons per family	6							
Alpha	0.05							
Tukey's multiple comparisons test	Mean Diff.	95% CI of diff.	Significant?	Summary				
MDA vs. XB5	-7.716	-54.66 to 39.23	No	ns				
MDA vs. YA1	38.31	-8.639 to 85.25	No	ns				
MDA vs. ZB2	25.52	-21.42 to 72.47	No	ns				
XB5 vs. YA1	46.02	-0.9226 to 92.97	No	ns				
XB5 vs. ZB2	33.24	-13.71 to 80.19	No	ns				
YA1 vs. ZB2	-12.78	-59.73 to 34.16	No	ns				
Test details	Mean 1	Mean 2	Mean Diff.	SE of diff.	N1	N2	q	DF
MDA vs. XB5	94.48	102.2	-7.716	17.89	30	30	0.6099	80
MDA vs. YA1	94.48	56.18	38.31	17.89	30	30	3.028	80
MDA vs. ZB2	94.48	68.96	25.52	17.89	30	30	2.017	80
XB5 vs. YA1	102.2	56.18	46.02	17.89	30	30	3.638	80
XB5 vs. ZB2	102.2	68.96	33.24	17.89	30	30	2.627	80
YA1 vs. ZB2	56.18	68.96	-12.78	17.89	30	30	1.010	80

HT1080 cells v lentiviral GFP+ clones

Table Analyzed	Distance from start HT1080								
Two-way ANOVA	Ordinary								
Alpha	0.05								
Source of Variation	% of total variation	P value	P value summary	Significant?					
Interaction	14.68	0.9975	ns	No					
Row Factor	7.567	0.6281	ns	No					
Column Factor	6.806	0.0002	***	Yes					
ANOVA table	SS	DF	MS	F (DFn, DFd)				P value	
Interaction	68377	78	876.6	F (78, 216) = 0.5732				P = 0.9975	
Row Factor	35236	26	1355	F (26, 216) = 0.8862				P = 0.6281	
Column Factor	31689	3	10563	F (3, 216) = 6.907				P = 0.0002	
Residual	330332	216	1529						
Number of missing values	0								
Compare column means (main column effect)									
Number of families		1							
Number of comparisons per family		6							
Alpha		0.05							
Tukey's multiple comparisons test	Mean Diff.	95% CI of diff.	Significant?	Summary					
HT1080 vs. A1D9	26.47	10.56 to 42.38	Yes	***					
HT1080 vs. B696	19.35	3.437 to 35.26	Yes	*					
HT1080 vs. ZB5	19.89	3.977 to 35.80	Yes	**					
A1D9 vs. B696	-7.124	-23.03 to 8.786	No	ns					
A1D9 vs. ZB5	-6.584	-22.49 to 9.326	No	ns					
B696 vs. ZB5	0.5401	-15.37 to 16.45	No	ns					
Test details	Mean 1	Mean 2	Mean Diff.	SE of diff.	N1	N2	q	DF	
HT1080 vs. A1D9	63.33	36.86	26.47	6.145	81	81	6.092	216	
HT1080 vs. B696	63.33	43.99	19.35	6.145	81	81	4.453	216	
HT1080 vs. ZB5	63.33	43.45	19.89	6.145	81	81	4.577	216	
A1D9 vs. B696	36.86	43.99	-7.124	6.145	81	81	1.640	216	
A1D9 vs. ZB5	36.86	43.45	-6.584	6.145	81	81	1.515	216	
B696 vs. ZB5	43.99	43.45	0.5401	6.145	81	81	0.1243	216	

Table Analyzed	Aspect Ratio							
Two-way ANOVA	Ordinary							
Alpha	0.05							
Source of Variation	% of total variation	P value	P value summary	Significant?				
Interaction	20.66	0.8755	ns	No				
Cells	10.88	0.1062	ns	No				
Cell type	0.6462	0.3856	ns	No				
ANOVA table	SS	DF	MS	F (DFn, DFd)	P value			
Interaction	341.0	117	2.914	F (117, 320) = 0.8331	P = 0.8755			
Cells	179.6	39	4.604	F (39, 320) = 1.316	P = 0.1062			
Cell type	10.67	3	3.556	F (3, 320) = 1.016	P = 0.3856			
Residual	1119	320	3.498					
Number of missing values	0							
Compare column means (main column effect)								
Number of families	1							
Number of comparisons per family	6							
Alpha	0.05							
Tukey's multiple comparisons test	Mean Diff.	95% CI of diff.	Significant t?	Summary				
HT1080 vs. A1D9	0.05334	-0.5703 to 0.6769	No	ns				
HT1080 vs. B696	-0.1263	-0.7499 to 0.4973	No	ns				
HT1080 vs. ZB5	0.2853	-0.3383 to 0.9089	No	ns				
A1D9 vs. B696	-0.1796	-0.8032 to 0.4440	No	ns				
A1D9 vs. ZB5	0.2319	-0.3917 to 0.8555	No	ns				
B696 vs. ZB5	0.4115	-0.2121 to 1.035	No	ns				
Test details	Mean 1	Mean 2	Mean Diff.	SE of diff.	N1	N2	q	DF
HT1080 vs. A1D9	3.940	3.887	0.05334	0.2415	120	120	0.3124	320
HT1080 vs. B696	3.940	4.066	-0.1263	0.2415	120	120	0.7395	320
HT1080 vs. ZB5	3.940	3.655	0.2853	0.2415	120	120	1.671	320
A1D9 vs. B696	3.887	4.066	-0.1796	0.2415	120	120	1.052	320
A1D9 vs. ZB5	3.887	3.655	0.2319	0.2415	120	120	1.358	320
B696 vs. ZB5	4.066	3.655	0.4115	0.2415	120	120	2.410	320

A



B

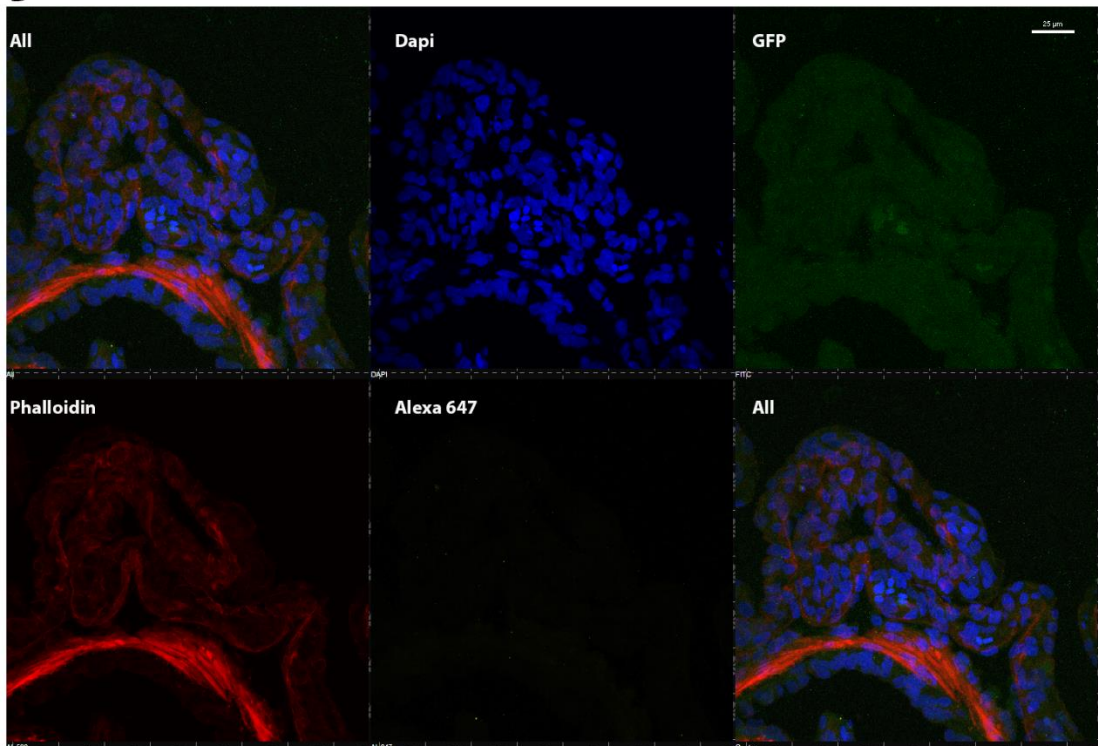


Figure C1. Immuno-staining controls for GFP antibody on CAM. A CAM section stained with DAPI, phalloidin and anti-GFP antibody. **B** Secondary antibody only on CAM with phalloidin and DAPI stains. Images taken with a Nikon A1 Plus confocal microscope using NIS Elements software. Scale bars = 25µm.

Appendix D

HT1080 on dCAM – vimentin expression

Table Analyzed	Final Comparison One Control					
Kruskal-Wallis test						
P value	< 0.0001					
Exact or approximate P value?	Approximate					
P value summary	****					
Do the medians vary signif. (P < 0.05)	Yes					
Number of groups	7					
Kruskal-Wallis statistic	61.58					
Data summary						
Number of treatments (columns)	7					
Number of values (total)	277					
Number of families	1					
Number of comparisons per family	6					
Alpha	0.05					
Dunn's multiple comparisons test	Mean rank diff.	Significant?	Summary		A-?	
2D Control vs. 3D dCAM n1	-12.79	No	ns		B	3D dCAM n1
2D Control vs. 3D dCAM n2	69.47	Yes	***		C	3D dCAM n2
2D Control vs. 3D dCAM n3	-7.172	No	ns		D	3D dCAM n3
2D Control vs. 3D dCAM n4	19.24	No	ns		E	3D dCAM n4
2D Control vs. dCAM Day1	-88.92	Yes	****		F	dCAM Day1
2D Control vs. dCAM Day3	20.76	No	ns		G	dCAM Day3
Test details	Mean rank 1	Mean rank 2	Mean rank diff.	n1	n2	
2D Control vs. 3D dCAM n1	138.2	151.0	-12.79	95	33	
2D Control vs. 3D dCAM n2	138.2	68.77	69.47	95	26	
2D Control vs. 3D dCAM n3	138.2	145.4	-7.712	95	29	
2D Control vs. 3D dCAM n4	138.2	119.0	19.24	95	31	
2D Control vs. dCAM Day1	138.2	227.2	-88.92	95	30	
2D Control vs. dCAM Day3	138.2	117.5	20.76	95	33	

Appendix E

Inverted invasion assay

Table Analyzed	MCF7 Inverted Invasion								
Two-way ANOVA	Ordinary								
Alpha	0.05								
Source of Variation	% of total variation	P value	P value summary	Significant?					
Interaction	8.496	> 0.9999	ns	No					
nucleus height	10.32	0.6759	ns	No					
Treatments	6.655	0.0005	***	Yes					
ANOVA table	SS	DF	MS	F (DFn, DFd)					P value
Interaction	182.9	58	3.153	F (58, 180) = 0.3537					P > 0.9999
nucleus height	222.1	29	7.659	F (29, 180) = 0.8592					P = 0.6759
Treatments	143.3	2	71.63	F (2, 180) = 8.036					P = 0.0005
Residual	1605	180	8.914						
Number of missing values	0								
Compare column means (main column effect)									
Number of families		1							
Number of comparisons per family		3							
Alpha		0.05							
Tukey's multiple comparisons test	Mean Diff.	95% CI of diff.	Significant?	Summary					
Control vs. FAK	-1.523	-2.575 to - 0.4711	Yes	**					
Control vs. SRC	-1.567	-2.618 to - 0.5148	Yes	**					
FAK vs. SRC	-0.04367	-1.096 to 1.008	No	ns					
Test details	Mean 1	Mean 2	Mean Diff.	SE of diff.	N1	N2	q	DF	
Control vs. FAK	10.51	12.03	-1.523	0.4451	90	90	4.839	180	
Control vs. SRC	10.51	12.08	-1.567	0.4451	90	90	4.978	180	
FAK vs. SRC	12.03	12.08	-0.04367	0.4451	90	90	0.138	180	

Table Analyzed	MDA Inverted Invasion							
Two-way ANOVA	Ordinary							
Alpha	0.05							
Source of Variation	% of total variation	P value	P value summary	Significant?				
Interaction	18.17	0.8150	ns	No				
Nucleus	8.955	0.7524	ns	No				
Treatment	4.396	0.0025	**	Yes				
ANOVA table	SS	DF	MS	F (DFn, DFd)	P valu e			
Interaction	1310	62	21.14	F (62, 192) = 0.8218	P = 0.81 50			
Nucleus	645.8	31	20.83	F (31, 192) = 0.8099	P = 0.75 24			
Treatment	317.0	2	158.5	F (2, 192) = 6.162	P = 0.00 25			
Residual	4938	192	25.72					
Number of missing values	0							
Compare column means (main column effect)								
Number of families	1							
Number of comparisons per family	3							
Alpha	0.05							
Tukey's multiple comparisons test	Mean Diff.	95% CI of diff.	Significant?	Summary				
Control vs. FAK	-1.165	-2.894 to 0.5644	No	ns				
Control vs. SRC	-2.566	-4.295 to -0.8372	Yes	**				
FAK vs. SRC	-1.402	-3.131 to 0.3274	No	ns				
Test details	Mean 1	Mean 2	Mean Diff.	SE of diff.	N1	N2	q	DF
Control vs. FAK	7.953	9.117	-1.165	0.7320	96	96	2.250	192
Control vs. SRC	7.953	10.52	-2.566	0.7320	96	96	4.958	192
FAK vs. SRC	9.117	10.52	-1.402	0.7320	96	96	2.708	192

Table Analyzed	HT Inverted Invasion								
Two-way ANOVA	Ordinary								
Alpha	0.05								
Source of Variation	% of total variation	P value	P value summary	Significant?					
Interaction	15.64	0.9223	ns	No					
Nucleus height	11.18	0.4056	ns	No					
Treatment	7.163	< 0.0001	****	Yes					
ANOVA table	SS	DF	MS	F (DFn, DFd)	P value				
Interaction	2300	62	37.09	F (62, 192) = 0.7335	P = 0.9223				
Nucleus height	1643	31	53.01	F (31, 192) = 1.048	P = 0.4056				
Treatment	1053	2	526.7	F (2, 192) = 10.42	P < 0.0001				
Residual	9709	192	50.57						
Number of missing values	0								
Compare column means (main column effect)									
Number of families	1								
Number of comparisons per family	3								
Alpha	0.05								
Tukey's multiple comparisons test	Mean Diff.	95% CI of diff.	Significant?	Summary					
Control vs. FAK	3.588	1.163 to 6.012	Yes	**					
Control vs. SRC	-0.8153	-3.240 to 1.609	No	ns					
FAK vs. SRC	-4.403	-6.827 to -1.978	Yes	****					
Test details	Mean 1	Mean 2	Mean Diff.	SE of diff.	N1	N2	q	DF	
Control vs. FAK	10.70	7.108	3.588	1.026	96	96	4.943	192	
Control vs. SRC	10.70	11.51	-0.8153	1.026	96	96	1.123	192	
FAK vs. SRC	7.108	11.51	-4.403	1.026	96	96	6.066	192	

**Aspect Ratio
vs.
Mean Fluorescence**

Correlation n1

Pearson r	
r	-0.1414
95% confidence interval	-0.4623 to 0.2122
R squared	0.01999
P value	
P (two-tailed)	0.4326
P value summary	ns
Significant? (alpha = 0.05)	No
Number of XY Pairs	33

**Aspect Ratio
vs.
Mean Fluorescence**

Correlation n2

Pearson r	
r	-0.007052
95% confidence interval	-0.3664 to 0.3541
R squared	4.973e-005
P value	
P (two-tailed)	0.9705
P value summary	ns
Significant? (alpha = 0.05)	No
Number of XY Pairs	30

**Aspect Ratio
vs.
Mean Fluorescence**

Correlation n3

Pearson r	
r	-0.1355
95% confidence interval	-0.4727 to 0.2363
R squared	0.01836
P value	
P (two-tailed)	0.4753
P value summary	ns
Significant? (alpha = 0.05)	No
Number of XY Pairs	30

Appendix F

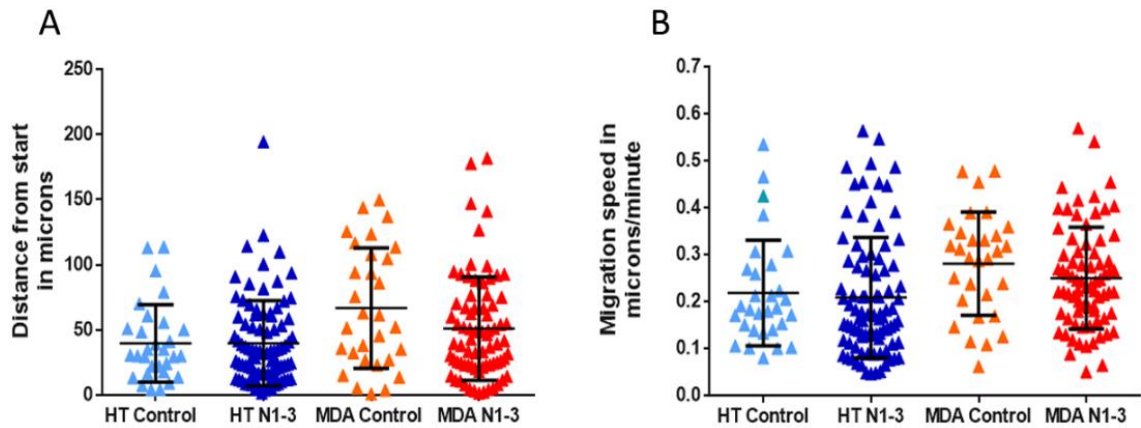


Figure A.7, Comparison of HT-1080 (HT) and MDA-MB-231 (MDA) migrating on 2mg/ml collagen for an 8 hour period from time-lapse images taken at 10 minute intervals. Control groups containing 30 cells from an earlier experiment were compared with grouped cells for N1-3 (30 cells in each group). No significant difference was evident for either cell migration distance from start (**A**) or cell migration speed (**B**) between control groups and N1-3 cell experiments. A Kruskal-Wallis ANOVA with Dunn's test for multiple comparisons was used to test for significant differences between each control and N1-3 pair. The table for this is given on the next page.

Table Analyzed	D2S Comparison HT and MDA				
Kruskal-Wallis test					
P value	0.0149				
Exact or approximate P value?	Approximate				
P value summary	*				
Do the medians vary signif. (P < 0.05)	Yes				
Number of groups	4				
Kruskal-Wallis statistic	10.48				
Data summary					
Number of treatments (columns)	4				
Number of values (total)	225				
Number of comparisons per family	1				
Alpha	2				
	0.05				
Dunn's multiple comparisons test					
	Mean rank diff.	Significant?	Summary		
HT Control vs. HT N1-3					
MDA Control vs. MDA N1-3	2.650	No	ns		A-B
	21.60	No	ns		C-D
Test details					
	Mean rank 1	Mean rank 2	Mean rank diff.	n1	n2
HT Control vs. HT N1-3					
MDA Control vs. MDA N1-3	103.5	100.8	2.650	30	90
	141.6	120.0	21.60	30	75

Table Analyzed	Speed Comparison HT and MDA				
Kruskal-Wallis test					
P value	0.0011				
Exact or approximate P value?	Approximate				
P value summary	**				
Do the medians vary signif. (P < 0.05)	Yes				
Number of groups	4				
Kruskal-Wallis statistic	16.10				
Data summary					
Number of treatments (columns)	4				
Number of values (total)	225				
Number of families	1				
Number of comparisons per family	2				
Alpha	0.05				
Dunn's multiple comparisons test	Mean rank diff.	Significant?	Summary		
HT Control vs. HT N1-3	8.767	No	ns		A-B
MDA Control vs. MDA N1-3	16.71	No	ns		C-D
Test details	Mean rank 1	Mean rank 2	Mean rank diff.	n1	n2
HT Control vs. HT N1-3	104.2	95.47	8.767	30	90
MDA Control vs. MDA N1-3	142.5	125.8	16.71	30	75